Additive Fabrication of Silicon Pillars on Monocrystalline Silicon by Direct Laser Melting

THÈSE N^{O} 8827 (2018)

PRÉSENTÉE LE 27 AOÛT 2018
À LA FACULTÉ DES SCIENCES ET TECHNIQUES DE L'INGÉNIEUR
LABORATOIRE DES MATÉRIAUX PHOTONIQUES ET CARACTÉRISATION
PROGRAMME DOCTORAL EN PHOTONIQUE

ÉCOLE POLYTECHNIQUE FÉDÉRALE DE LAUSANNE

POUR L'OBTENTION DU GRADE DE DOCTEUR ÈS SCIENCES

PAR

Marie Camille Laëtitia LE DANTEC

acceptée sur proposition du jury:

Prof. O. Martin, président du jury
Prof. P. Hoffmann, directeur de thèse
Dr Y. Champion, rapporteur
Dr C. Reimann, rapporteur
Prof. R. Logé, rapporteur

ÉCOLE POLYTECHNIQUE
FÉDÉRALE DE LAUSANNE
Suisse
2018

Acknowledgments

First, I would like to thank my PhD supervisor Prof. Dr. Patrik Hoffmann for giving me the chance to work in a very multi-disciplinary and international research environment, and for trusting me in bringing this project to a successful conclusion. This opportunity allowed me to considerably broaden my knowledge by learning from him and from others, both scientifically and personally. I am extremely grateful to Dr. Marc Leparoux, for his support through this PhD, his feedback, discussions, and advice, which considerably helped me getting through difficulties and learning useful skills.

I would like to especially thank Dr. Toni Ivas for the computation of the FEM simulations of this work and his support. I was very impressed with his multiphysics knowledge and learned a lot through our discussions. Many thanks to Dr. Mustafa Abdulstaar, together with I got started with the DLM machine and got the first success of this project. I also would like to thank Dr. Xavier Maeder for his help with the EBSD measurements and the scientific discussions around silicon growth. I also thank Carlos Guerra for the Raman spectroscopy measurements.

I would like to thank Prof. Olivier Martin from EPFL, Prof. Roland Logé from EPFL, Dr. Yannick Champion from SiMAP (Grenoble, France) and Dr. Christian Reimann from the Fraunhofer Institute of Technology IISB (Erlangen, Germany) for their kind acceptance as jury members of my PhD defense.

My special thanks go to Dr. Sébastien Vaucher, who guided me two years on a microwave project, for his constant support and friendship, and the fruitful scientific and personal discussions. Together with Arnaud Mader (who I also thank), he also greatly participated to the discovery of my artistic self ☺. I received great support from my friends and colleagues Dr. Matthias Leistner, and the soon-to-be Dr. Lucas Güniat, with who I also obtained my first positive results on silicon powders. I am also very grateful to Prof. Olivier Martin, who took time for me during challenging times.

I would like to particularly thank Christoph Amsler, Mehari Asfaha, Bernhard von Gunten, who participated to the development of the DLM machine, and were always available to make modifications or helping solve a problem. I thank Peter Ramseier for his help in sample polishing. Many thanks to Hans-Rudolf Sieber and Anton Böll as well.

I would like to warmly thank my partners in diverse crimes: Dr. Briac Lanfant, Dr. Valentina Dinca (Tina), Dr. Fatemeh Saeidi, Dr. Sriharitha Rowthu, for their incredible moral support and friendship, the very useful scientific and personal discussions all along this PhD. Without you, I would not have made it!

Thank you to the “Surface Chemistry” team: Dr. Michael Reinke, Seyedpayam Vahdati, Benoît Huguet and Daniel Infante. It was great working with you! Special thoughts to Daniel, who went through a triple iron man marathon: you are incredibly strong and keep the positive thinking attitude!

Thank you to Eveline Straubhaar, Katrin Gurtner and Sandra Beer, who were always extremely friendly and helpful all along my stay at Empa.

Thank you to the hiking team buddies and beautiful friendships built over the years: Rachel, Aidan, Arnaud, Gaylord, Kaspar, Aurore, Guillaume, Charlotte, Eva, Agnieszka, and to the music lovers James and Mikhail. Thank you for your constant support and I spent really great moments with you. Thanks to my friends Aurélie, Guillaume, Mounir, Mish, who are always there for me.

I would like to thank all the members of Abteilung 204 “Advanced Materials Processing” and Abteilung 206 “Mechanics of Materials and Nanostructures” for their support, their help, and the scientific discussions. I was very glad to pursue my doctoral studies in such an open and friendly environment. All of you participated to this success and it was wonderful meeting you! Special thanks to Dr. Bastian Meylan, who helped me finalizing some of the chapters of this work. Many thanks to Dr. Kilian Wasmer as well, for his support and advice.

I am thankful to my family, and especially my parents and my siblings who are always supporting me and are always there for me, through my decisions, through the good and bad times. Last but probably the most important, I am extremely grateful to my best partner in life, Keith Thomas, for his love, kindness and patience. Your strength, happiness and positive attitude gave me the confidence that I could make it and gave me the strength to fight through this!

Marie Le Dantec, 26.07.2018

Abstract

Additive Manufacturing (AM) is an emerging part production technology that offers many advantages such as high degree of customization, material savings and design of 3D highly complex structures. However, AM is a complex multiphysics process. Therefore, only a limited number of materials can already be commercially used to produce parts and a handful of others are being studied or developed for such process. Consequently, limited knowledge on this process is available, especially concerning materials that present thermomechanical challenges such as brittle materials.

The present research focuses on additive fabrication of silicon pillars on a monocrystalline silicon wafer by Direct Laser Melting (DLM) with a pulsed 1064 nm laser beam. The simple geometry of pillars allowed for the first determining steps into process understanding.

Several results were achieved through this PhD work.

First, crack-free silicon pillars were successfully built onto monocrystalline silicon wafers. With the help of in-situ process monitoring and sample characterization, wafer substrate temperature and laser repetition rate were found to be the main influential parameters to obtain crack-free samples, as minimum substrate temperature of 730°C and a minimum repetition rate of 100 Hz were necessary to reach this goal (for a feed rate of 15 g/min and a pulse duration of 1 ms). The influence of secondary process parameters such as feed rate and energy per pulse were also discussed. A simple Finite Element Modeling (FEM) model validated by the experiments was used to explain crack propagation in the samples.

Then, process monitoring of the DLM process was realized. High-speed camera image analysis revealed that vertical stage speed and powder feed rate should match to obtain a constant pillar building rate. As all pillars presented necking at their base, estimations of the thermal characteristics of the pillar during growth were carried out by FEM simulations. They were additionally used to explain the pillar final shape.

Finally, the microstructure of the pillars built was characterized by the Electron Back-Scattering Diffraction (EBSD) technique. In the conditions presented in this work, the microstructure of the pillar was found to be in the columnar growth mode. The feed rate was identified as the most influential parameter on the microstructure, followed by the stage speed, the impurity content of the powder and the crystallographic orientation of the substrate. Epitaxial growth was achieved on more than 1 mm with a feed rate of 1.0 g/min, a stage speed of 0.1 mm/s, a powder with purity of 4N and a <111> oriented wafer substrate.

This work could be further continued by making improvements to the DLM setup, studying the influence of additional process parameters on the thermomechanical behavior and the microstructure control of the pillars, and/or using these results to realize more complicated shapes, either with this setup or by using a powder bed technique.

Keywords

Additive fabrication, direct laser melting, silicon, powders, pulsed laser, crack propagation, FEM modeling, epitaxial growth

Résumé

La fabrication additive (AM) est une technique de production émergente qui offre de nombreux avantages tels qu'une grande capacité de personnalisation des pièces produites, l'économie de matériau, et le design de structures 3D complexes. Cependant, AM est un procédé pluridisciplinaire complexe. Ainsi, seulement un nombre limité de matériaux est déjà utilisé pour la production commerciale de pièces par AM, et une poignée d'autres est actuellement étudiée ou en cours de développement, pour leur adaptation à ce procédé. En conséquence, les connaissances sur l'AM sont limitées, surtout concernant les matériaux qui présentent des challenges thermomécaniques tels que les matériaux fragiles.

Le présent travail de recherche se concentre sur la fabrication additive de piliers en silicium déposés sur des wafers monocristallins en silicium par fusion de poudres (DLM) grâce à un laser de longueur d'onde 1064 nm. Le choix d'une géométrie simple telle que des piliers a permis de réaliser les premiers pas déterminants dans la compréhension du procédé AM adapté au silicium.

Ce travail de thèse présente plusieurs résultats majeurs.

Pour commencer, des piliers en silicium sans fissures ont pu être déposés avec succès sur des wafers de silicium monocristallins. Grâce à des techniques d'observation in-situ et à la caractérisation des échantillons, la température du substrat de silicium et le taux de répétition du laser ont été identifiés comme les paramètres les plus influents sur l'obtention de piliers sans fissures. Pour atteindre ce but, la température minimum du wafer devait atteindre 730°C et le taux de répétition du laser devait être supérieur ou égal à 100 Hz (pour un taux d'injection des poudres de 15 g/min et une durée d'impulsion du laser de 1 ms). L'influence de paramètres secondaires tels que le taux d'injection des poudres et l'énergie par impulsion laser est aussi commentée. Un modèle simple basé sur la méthode des éléments finis a été utilisé pour expliquer la propagation des fissures dans les échantillons pendant le procédé.

Ensuite, le monitorage du procédé de DLM a été effectué. L'analyse d'images enregistrées par une caméra à haute vitesse a montré que la vitesse de l'étage mobile et le taux d'injection des poudres devaient être coordonnés pour obtenir une vitesse de construction du pilier constante. Comme tous les piliers présentaient un rétrécissement du diamètre à leur base, les caractéristiques thermiques du pilier pendant sa construction ont été estimées par la méthode des éléments finis. Ces calculs ont été utilisés pour expliquer la forme finale des piliers.

Enfin, la microstructure des piliers construits a été caractérisée par la technique de diffraction d'électrons rétrodiffusés. Dans les conditions présentées dans ce travail, la microstructure des piliers était toujours de mode colonnaire. Le taux d'injection des poudres a été identifié comme ayant le plus d'influence sur la microstructure des piliers, suivi par la vitesse de l'étage mobile, le taux d'impureté des poudres et l'orientation cristallographique du substrat. Une croissance épitaxiale a pu être accomplie sur plus d'1 mm de la hauteur du pilier avec un taux d'injection des poudres d'1 g/min, une vitesse d'étage de 0.1 mm/s, une poudre de pureté 4N et un wafer orienté dans la direction cristallographique <111>.

Ce travail peut être continué en améliorant la machine DLM, en étudiant l'influence des paramètres expérimentaux peu ou non discutés dans ce travail sur le comportement thermomécanique et le contrôle de la microstructure des piliers, et/ou en utilisant ces résultats pour réaliser des structures plus complexes, soit avec cette installation expérimentale, soit avec une technique de fusion de lit de poudres.

Mots-Clefs

Fabrication additive, fusion laser, silicium, poudres, laser pulsé, propagation des fissures, méthode des éléments finis, croissance épitaxiale

Contents

Acknowledgments .... **i**

Abstract .... **iii**

Keywords iv

Résumé .... **v**

Mots-Clefs vi

Contents .... **vii**

List of Figures .... **xi**

List of Tables .... **xix**

Nomenclature .... **xxi**

Greek Letters xxiii

Acronyms xxiii

Chapter 1. Introduction **1**

Chapter 2. State-of-the-Art Review **5**

2.1. 3D Silicon Structures 5

2.2. Direct Laser Melting: A Direct Energy Deposition AM Process 6

2.3. Additive Manufacturing and Soldering of Semiconductors 9

2.3.1. Additive Manufacturing of Brittle Materials 9

2.3.2. AM of Semiconductors 10

2.3.3. Silicon Soldering 11

2.4. Epitaxial Growth in Powder AM and Epitaxial Growth of Silicon 11

2.4.1. Fundamentals of Epitaxial Growth and Solidification 12

2.4.2. Microstructure Control in AM and Crystal Growth Techniques Applied to the Si Case ... 15

2.4.3. Review of Epitaxial Growth of Materials Processed by Additive Manufacturing 20

2.4.4. Epitaxial Growth of Silicon: A Review of the Current Techniques 22

2.5. Silicon Properties Relevant for DLM Processing 24

2.5.1. Silicon Mechanical Properties 24

2.5.2. Silicon Thermal Properties 28
2.5.3. Silicon Optical Properties 30
Chapter 3. Materials and Methods 35
3.1. Materials 35
3.1.1. Wafers 35
3.1.2. Powders 36
3.2. Direct Laser Melting Process 37
3.2.1. Configuration 37
3.2.2. Chamber 38
3.2.3. Laser 39
3.2.4. Moving Stages 40
3.2.5. Nozzle 40
3.2.6. Heating Plate 40
3.2.7. Heat Controller and Temperature Measurements 41
3.2.8. Powder Feeding System 43
3.2.9. Remote Control and Code 45
3.2.10. Printed Structures 45
3.3. In-Situ Observations 46
3.3.1. High-Speed Imaging 46
3.4. Powder Characterization 52
3.4.1. Particle Size Analysis 52
3.4.2. Particle Morphology 53
3.4.3. Powder Flowability 53
3.4.4. Impurities 53
3.5. Pillar Characterization 54
3.5.1. Preparation for Observations of Pillar Cross-Section: Embedding 54
3.5.2. Preparation for Observations of Pillar Cross-Sections: Grinding and Polishing 54
3.5.3. Scanning Electron Microscope (SEM) Observations 54
3.5.4. Energy Dispersive X-ray Spectroscopy (EDX) 55
3.5.5. Electron Back Scatter Diffraction (EBSD) 55
3.5.6. Stress Measurement: Raman Spectroscopy 55
3.6. Modeling of the Laser Heating and Building process 56
3.6.1. Configuration 1: Si wafer Illuminated Perpendicularly with a Laser Beam 56
3.6.2. Configuration 2: Build-Up of Si Pillars 62

Chapter 4. Crack Formation During Pillar Building 65
4.1. Results 65
4.1.1. Cracking Behavior on Silicon Wafers 65
4.1.2. Working Conditions: Crack Formation and Propagation During Pillar Building 78
4.1.3. Cracking in the Pillar Body 83
4.2. Discussion 85
4.2.1. Wafer Surface Temperature 85
4.2.2. Cracking Behavior in a Monocrystalline Wafer Solely Illuminated by the Laser 86
4.2.3. Crack Formed During Pillar Building 87
4.2.4. Mechanism of Crack Initiation and Propagation 89
4.2.5. Cracking Due to Geometry 91
4.2.6. Cracking in the Silicon Pillar Body 92
4.3. Conclusions and Summary 92
Chapter 5. Process Monitoring During Pillar Growth 95
5.1. Feed Rate and Pillar Building 95
5.1.1. Results 95
5.1.2. Discussion 104
5.1.3. Conclusion 111
5.2. Thermal History of the Process and Pillar Shape 112
5.2.1. Results 112
5.2.2. Discussion 115
5.3. Remarks on the Relevance of the Native Oxide for DLM Processing 117
5.4. Conclusions and Perspectives 118
Chapter 6. Pillars Microstructure and Epitaxial Growth 119
6.1. Results 121
6.1.1. Influence of Feed Rate and Stage Speed 121
6.1.2. Influence of Impurities 126
6.1.3. Influence of the Wafer Substrate Crystallographic Orientation 130
6.2. Discussion 131
6.2.1. On the Shape of the Pillars 131
6.2.2. Achievement of Epitaxial Growth: Growth Velocity, Thermal gradients and Feed Rate 132
6.2.3. Loss of Epitaxial Growth 134
6.2.4. Effect of Powder Impurities 134

6.2.5. Effect of Substrate Orientation 135
6.3. Conclusions and Perspectives 136
Chapter 7. Conclusions and Outlooks 137
7.1. Summary 137
7.2. Outlooks 139
Appendix A – Coding Interface used to Build a Pillar 143
Appendix B – Simulation Hypotheses 145
Appendix C – Limit of Detection of the Optical Method of Powder Burst Weight Quantification 147
Appendix D – Microscope Images Used to Plot the Working Window to Build Crack-Free Pillars 149
D.1. Feed rate 15.0 g/min 149
D.2. Feed rate 1.0 g/min 152
Appendix E – On the importance of the oxygen content of the powder raw material in case of powder bed processing – Paper draft 153
References 169
CV 179

List of Figures

Figure 2-1. Diagram showing the two families of single steps AM processing for metals and ceramics currently used, and their subsequent classification. The circle shows to which branch of the family DLM belongs. 8

Figure 2-2. Schematic of the balance of forces at a nucleus formation (adapted from [39]) 13

Figure 2-3. Schematic representation of (a) rough and (b) smooth solid/liquid interfaces[43] δ_i is defined as the interface thickness. 16

Figure 2-4. Mechanism of parallel twin formation at the solid/liquid interface during Si crystal growth. If a twin boundary is unintentionally formed at the interface, another twin boundary forms parallel to the first one upon lateral growth of the original crystal[45]. 16

Figure 2-5. Microstructure map calculated for the Ni superalloy CMSX-4 as a function of growth velocity V (m/s) and thermal gradients G (K/m). The thin black lines represent the CET, with φ the proportion of equiaxed grain required for the microstructure to be considered fully equiaxed (φ=49%) or under which it is considered fully columnar (φ=0.66%). The square represent the range of conditions used during laser processing[48]. 18

Figure 2-6. Microstructure maps of Ni-superalloy for different laser parameters[50]. 18

Figure 2-7. Microstructure maps for the model using thermal rough equiaxed dendrites. (a) Undercooling necessary for the nucleation of equiaxed grains on impurities < 1K, low particle density and (b) Undercooling necessary for the nucleation of equiaxed grains on impurities < 1K and high particle density. The plain line represents the thermal gradient for which the grains are always equiaxed. The dashed line represents the thermal gradient for which the growth is always columnar. 19

Figure 2-8. Schematic of the Verneuil process as described by its author[53]. Fig. 1 describes the Verneuil furnace. Fig. 2, 3, 4, 5 and 6 show different stages of the growing crystal in time. 21

Figure 2-9. Schematic of the PLEG principle 24

Figure 2-10. Silicon crystallization system[73] 25

Figure 2-11. Schematic of (a) brittle and (b) ductile fractures. The arrows indicate the direction of the applied tensile stress. 26

Figure 2-12. BDT of Silicon as function of temperature measured by Brede et al. on pure silicon doped with $5.2.10^4$ boron atoms/cm^3 (Float zone process, < 10^{15} oxygen atoms/cm^3, loading rate 5.5 µm/min, $K^a_{Ico} = 0.88 \pm 0.07$ MPa.$m^{1/2}$) [80] 27

Figure 2-13. Stress-strain curves for Si <100> single crystal measured by micropillar compression at different temperatures[76] 28

Figure 2-14. Density of solid and liquid silicon as a function of temperature as measured and fitted by Ohsaka et al.[85] 29

Figure 2-15. Thermal properties of crystalline and liquid silicon as a function of temperature: (a) thermal capacity[86], (b) thermal conductivity[87 88] 30
Figure 2-16. Absorption coefficient of silicon at λ=1152 nm (plain line) and λ=1064 nm (dotted line) calculated and fitted with experimental data[90]. 31
Figure 2-17. Spectral emissivity of bulk silicon by Sato[94] 32
Figure 2-18. Emissivity of silicon in the solid and the liquid phase from 200 to 2600 nm measured by various authors 33
Figure 3-1. Photo of the resistivity measurement system 36
Figure 3-2. Schematic of the principle of DLM 38
Figure 3-3. Photo of the metallic chamber used for the DLM process 38
Figure 3-4. Reduced intensity beam profile in and out of focus for the pulsed 1064 nm Nd:YAG solid state laser (SLS 200 from LASAG AG, Switzerland) 39
Figure 3-5. Photo of the DLM setup inside the chamber 41
Figure 3-6. Temporal temperature fluctuations of the heating plate for several set temperature values when no protective gas is blowing 42
Figure 3-7. Average temperature measured by the thermocouples placed under the heating plate, on a wafer surface with and without the argon shielding gas of 14 L/min 42
Figure 3-8. Photo of the powder feeding system 43
Figure 3-9. Powder feeder program in function of time over one cycle of 200 ms 44
Figure 3-10. Schematic of the powder feeder system principle 45
Figure 3-11. Spectral response of the camera sensor (copied from Videal (Motion Pro Y4 series) 46
Figure 3-12. Schematic of the setup configuration for observation of the melt pool on a Si wafer during laser irradiation (a) side view and (b) region of interest recorded by the camera, from the point of view of the camera and (c) typical melt pool image, with indication of time (in ms). 47
Figure 3-13. Transmission spectrum of the hard-coated shortpass filter FESH1000 48
Figure 3-14. Schematic examples of a laser melt pool illuminated by the laser at different times. The pixel chosen for the analysis was located at the center of the melt pool. As temperature increases, the brightness of the pixel increases as well 48
Figure 3-15. Schematic of the high speed camera configuration during pillar building observation... 49
Figure 3-16. Typical high speed camera image taken during pillar building 50
Figure 3-17. Schematic top view of the experimental configuration inside and outside the chamber. The high speed camera was set at 90° angle compared to the nozzle axis. The lighting system was set up through another observation port of the chamber 51
Figure 3-18. (a) Schematic of the region of interest (ROI) selected on the camera image to record the movies. (b) Typical picture obtained with the camera recording. The red box indicates the area for which the light intensity profile taken into account during the powder burst for image analysis 51
Figure 3-19. Typical plot of pixel intensity vs. frame number during image analysis. Areas with powder bursts were measured and individual powder burst weight was calculated. 52
Figure 3-20. Photo of a pillar embedded in resin, grinded and polished to reveal its cross-section. .. 54
Figure 3-21. Schematic of the silicon wafer illuminated by the laser. r_0 is the laser beam radius, d is the thickness of the wafer, l is the total diameter of the wafer piece. The model is axisymmetrial around the z axis. 56
Figure 3-22. The element name identifies the primary element characteristics 61
Figure 3-23. Schematic of the interface between active and inactive elements showing activation of elements using birth element method[103] 62

Figure 4-1. Optical microscope pictures showing cross-sections of wafers illuminated for 2s with the following laser conditions: (a) 50 Hz – 405 mJ – 1ms – substrate at ambient temperature, (b) 200 Hz – 160 mJ – 1 ms – substrate at ambient temperature (c) 50 Hz – 405 mJ – 1ms – substrate surface preheated to 730°C and (d) 200 Hz –160 mJ – 1ms – substrate surface preheated to 730°C. 66
Figure 4-2. High-speed camera recordings of the signals showing the temperature variations in function of time at the center of the melt pool for a Si wafer illuminated by the laser at different conditions (a) 50 Hz and 405 mJ (b) 100 Hz and 285 mJ (c) 200 Hz and 160 mJ. The graphs on the right show a zoom on the more general graphs in order to see the shape of the emitted light intensity variations. The areas highlighted in red represent the time zones when the laser is illuminating the sample. 68
Figure 4-3. High-speed camera signals recorded for different conditions of illumination of the wafer substrate at the side of the melt pool. (a) 50 Hz - 405 mJ, (b) 100 Hz - 285 mJ and (c) 200 Hz - 160 mJ. The graphs displayed on the right show a zoom of the general graphs to be able to visualize the shape of the emitted light intensity variations. The areas highlighted in red represent the time zones when the laser is illuminating the sample 69
Figure 4-4. Grey level of a pixel taken in the center of the melt pool plotted in function of time for 2 different conditions (a) 50 Hz 405 mJ and (b) 200 Hz 160 mJ. In both cases, the substrate was at room temperature and the signal was recorded 1 to 2 s after the laser was on. The filter blocking the wavelength of the laser was not used in these measurements, therefore the signal always saturates at 255 when the laser is illuminating the wafer. The time zone when the laser is illuminating the wafer is indicated by the red areas. 70
Figure 4-5. Simulation of temperature variations calculated by FEM during pulsing of the laser for 0.5 s using the conditions (a) 50 Hz – 405 mJ (b) 100 Hz – 285 mJ and (c) 200 Hz – 160 mJ. The substrate bottom temperature was 980°C. 72
Figure 4-6. FEM calculation of the temperature profile as a function of time for the conditions 200 Hz – 160 mJ, with different substrate boundary conditions. 72
Figure 4-7. Maximum melt pool size and temperature field around the melt pool calculated after 0.5 s of laser illumination. The substrate bottom temperature was 980°C, corresponding to a surface temperature of 900°C. (a) 50 Hz – 405 mJ, (b) 100 Hz – 285 mJ (c) 200 Hz – 160 mJ. The grey area stands for temperatures higher than the melting point (liquid phase). 73
Figure 4-8. Typical Raman spectra for a stress-free Si wafer, silicon in compressive stress and silicon in tensile stress. The vertical lines correspond to the position of the maxima of the peaks: blue for compressive stress, red for free of stress and red for tensile stress. 74
Figure 4-9. Optical images of the top view of a wafer surface after illumination for 1.5 s with (a) 200 Hz 160 mJ and (c) 50 Hz 405 mJ. The samples were etched with HNA reagent. (b) Raman shift measured and calculated by FEM along the HAZ radius presented in the optical microscopy pictures for the conditions 50 Hz – 405 mJ and (d) for the conditions 200 Hz – 160 mJ. 76
Figure 4-10. FEM stress calculations for 50 Hz – 405 mJ (a) radial stress during the laser heating phase (b) hoop stress during the laser heating phase (c) radial stress during the cooling phase and (d) hoop stress during the cooling phase 77
Figure 4-11. (a) Crack-free wafer after laser illumination at 50 Hz 405 mJ for 1.5 s. (b) Crack (indicated by a red arrow) induced by adding less than 1 second of powder to the melt pool formed by 50 Hz and 405 mJ laser illumination conditions, (c) Crack-free wafer after laser illumination at 200Hz – 160 mJ for 1.5 s. (d) crack-free wafer with addition of less than 1 s of powder to the melt pool formed with 200 Hz and 160 mJ. The feed rate was 15.0 g/min. 78

Figure 4-12. Optical microscope pictures of cross-section of pillars built on (a) Si wafers at 50 Hz – 405 mJ – 1ms – substrate at ambient temperature, (b) 50 Hz – 405 mJ – 1ms - substrate heated to 730°C (c) 200Hz – 160 mJ – 1 ms – substrate at ambient temperature (d) 200 Hz –160 mJ – 1ms – substrate heated to 730°C. The red arrows indicate the location of a crack on the picture. The feed rate was 15.0 g/min.......... 79
Figure 4-13. Optical microscope images of Si structures built on a Si wafer at different substrate temperature for the condition 200 Hz – 160 mJ. In all the temperature measurements, the argon shielding gas was ON. The temperature measurement does not take into account powder blowing. 80
Figure 4-14. Working window for crack-free DLM processing of Si for a feed rate of 15.0 g/min, a stage speed of 0.1 mm/s and a substrate temperature of 730°C (a) Energy vs repetition rate (samples made with varying pulse duration and power) and (b) Average power vs. repetition rate. The green dots and the green area indicate conditions where the pillar could be built without cracks. The red dots and the red area indicate conditions where the pillars were built with cracking. The blue dots and the blue area stand for the conditions where no attachment to the wafer was possible. 82
Figure 4-15. (a) Optical microscope image of a pillar built with 50 Hz – 405 mJ (b) SEM image of the crack close to the wafer surface (c) SEM image of the crack tip, about 200 µm under the wafer surface.......... 83
Figure 4-16. (a) SEM image of a typical surface of a cross-section of a pillar built with Si_4N. (b) SEM picture of the cross-section of a pillar built with Si_98%. Micro-cracks are indicated by red arrows on the picture. (c) EDX spectrum upon analysis of impurity precipitates.......... 85
Figure 4-17. Schematic of the proposed mechanism of crack formation in function of substrate temperature and laser conditions. The figures are represented in top view, except for the last row, represented in cross-section. These sequences represent the beginning of the pillar building process. The thickness of the arrows represents the relative stress intensity. 91
Figure 5-1. Particle size distribution and corresponding image used in image analysis of (a) Si-4N and (b) Si_98%.......... 96
Figure 5-2. SEM image of Si_4N at different zoom magnitudes. 96
Figure 5-3. SEM image of Si_98% at different zoom magnitudes.......... 96
Figure 5-4. Mass per burst as a function of time for different feed rates monitored by different cell opening times during powder suction. 98
Figure 5-5. Reproducibility of the measurement of pillar height as a function of processing time for a feed rate of 1.0 g/min and a stage speed of 0.1 mm/s. The straight blue line would show the theoretical pillar height vs. processing time if the building rate was controlled by the stage speed of 0.1 mm/s. 99
Figure 5-6. High-speed camera imaging of a pillar during its building at a stage speed of 0.3 mm/s and a feed rate of 15.0 g/min. The numbers in the top left corner indicate the recording time during the process. The yellow area indicates approximately the area of the powder stream.......... 100
Figure 5-7. High-speed camera imaging of a pillar during its building at a stage speed of 0.1 mm/s and a feed rate of 1.0 g/min. The numbers in the top left corner indicate the recording time during the process. The yellow area indicates approximately the area of the powder stream.......... 101
Figure 5-8. High-speed camera imaging of a pillar during its building at a stage speed of 0.0167 mm/s and a feed rate of 15.0 g/min. The numbers in the top left corner indicate the recording time during the process. The yellow area indicates approximately the area of the powder stream. 101
Figure 5-9. High-speed camera imaging of a pillar during its building at a stage speed of 0.3 mm/s and a feed rate of 1.0 g/min. The numbers in the top left corner indicate the recording time during the process. The yellow area indicates approximately the area of the powder stream.......... 102

Figure 5-10. (a) Pillar height as a function of processing time for different stage speeds. The feed rate is 15.0 g/min. (b) Pillar height as a function of processing time for different stage speeds. The feed rate is 1.0 g/min. The dashed black line indicates the expected height of the pillar at the end of the process. For measurements at a stage speed of 0.0167 mm/s, only a third of the process is shown as the time was too long to be able to record it with the camera. 103

Figure 5-11. Pillar height as a function of processing time for a stage speed of 0.0167 mm/s for different feed rates. The plain blue lines would show the theoretical pillar height vs. processing time if the building rate was controlled by the stage speed indicated in the legend. The vertical lines delimitate the regions 1, 2 and 3 for each case. 104

Figure 5-12. Schematic summarizing the building of a pillar built at low feed rate at an optimized stage speed. (1) Formation of a silicon droplet on top of the wafer (2) Tipping of the droplet due to powder and argon gas blowing (3) rapid building due to focused large powder stream. The vertical red lines delimitate the regions 1, 2 and 3. 106

Figure 5-13. Photo of the trace left by the powder jet on a wafer. 107

Figure 5-14. Schematic of the two phenomena occurring during pillar building not taken into account in the theoretical calculations. (a) Laser shielding by light diffusion, scattering or absorption in the powder at the top of the powder burst. (b) The particles arriving at the melt pool can ripple on the partially incorporated particles. 110

Figure 5-15. (a) Geometrical model of the pillar used to model the Si pillar building. The red line indicates the path used to plot thermal gradient. (b)Temperature along the path for different pillar heights (for building times ranging from 1 to 6 s). The building rate was 0.1 mm/s. 113

Figure 5-16. Results of the simulation using FEM showing the radial (left side) component and vertical (right side) components (denoted by HFL1 and HFL3 of the heat flow throughout the pillar structure for different heights assuming a constant speed of 0.1 mm/s (a) (d) after 0.1 mm, (b) (e) after 0.3 mm and (c) (f) after 0.6 mm. 114

Figure 5-17. Typical shape of a silicon pillar built on a silicon wafer (a) built with a feed rate of 15.0 g/min and a stage speed of 0.3 mm/s, laser parameters 200 Hz – 160 mJ. (b) Pillar built with a feed rate of 1.0 g/min and a stage speed of 0.1 mm/s, laser parameters 200 Hz – 160 mJ. (c) Photo of a cross-section of a pillar built with a feed rate of 1.0 g/min and a stage speed of 0.1 mm/s, laser parameters 50 Hz – 405 mJ 115

Figure 5-18. Schematic of the growing pillar showing the pillar diameter broadening. The blue arrows indicate the radial heat flux induced by the diameter broadening around the melt pool. 117

Figure 6-1. Schematic of microstructure map for Si as a function of growth rate and thermal gradients. The red zone corresponds to equiaxed dendritic growth mode, the blue zone corresponds to columnar faceted growth and the white zone is an intermediate zone. The blue and red lines delimitate the CET and equiaxed zone as calculated by Mangelinck et al.[51] The dotted white line represents the shift of CET at higher impurity concentrations. Delimitation of the zones above 10^3 K/m are only extrapolations of the CET calculated by Mangelinck-Noël et al. for Si and by Kurz et al.[48] for E-LMF of nickel-based superalloy and are only represented to give an idea of the process map at high thermal gradients. DS: directional solidification, CZ: Czochralski. 120

Figure 6-2. EBSD crystal orientation mapping of pillar cross-sections built with the powder Si_4N, with the following conditions: frequency 200Hz, 160 mJ, pulse duration 1 ms, stage speed 0.1 mm/s, (a) feed rate 47.5 g/min, (b) feed rate 2.4 g/min and (c) feed rate 1.0 g/min. The pillars were built on a <100> wafer. The grains appearing in the black zone are artefacts measured on the silver paste and the resin used in the experiments. The white line indicates the wafer upper surface. The IPF color scale shows the crystal orientations in the pillar growth direction. 122

Figure 6-3. EBSD pattern quality and grain boundaries maps showing the nature of the grain boundaries in the pillar cross-sections built with the powder Si_4N, with the following conditions: frequency 200Hz, 160 mJ, pulse duration 1 ms, stage speed 0.1 mm/s, (a) feed rate 47.5 g/min, (b) feed rate 2.4 g/min and (c) feed rate 1.0 g/min. The pillars were built on a <100> wafer. The crack appearing at the base of the pillar in (a) appeared during the polishing step. The colored lines represent the different coincident lattice sites (CSL): red for twin boundaries (∑3), green for ∑9 boundaries and black for random grain boundaries. The crack appearing at the base of the pillar in (a) appeared during the polishing step. The grains appearing in the black zone are artefacts measured on the silver paste and the resin used in the experiments. The white line indicates the wafer upper surface. 122

Figure 6-4. EBSD mapping of the cross-sections of pillars built with the powder Si_4N with the following conditions: frequency 200 Hz, 160 mJ, pulse duration 1 ms, feed rate 1.0 g/min, built on a <100> wafer substrate, stage speed (a) 0.0083 mm/s (b) 0.0167 mm/s, (c) 0.05 mm/s and (d) 0.1 mm/s. The grains appearing in the black zone are artefacts measured on the silver paste and the resin used in the experiments. The white line indicates the wafer upper surface. The IPF color scale shows the crystal orientations in the pillar growth direction. 124

Figure 6-5. EBSD mapping of the cross-sections of pillars built with the powder Si_4N with the following conditions: frequency 200 Hz, 160 mJ, pulse duration 1 ms, feed rate 15.0 g/min, built on a <100> wafer substrate, stage speed (a) 0.1 mm/s and (b) 0.3 mm/s. The grains appearing in the black zone are artefacts measured on the silver paste and the resin used in the experiments. The white line indicates the wafer upper surface. The IPF color scale shows the crystal orientations in the pillar growth direction. 125

Figure 6-6. EBSD map showing the microstructure of a pillar built with a feed rate of 1.0 g/min, stage speed of 0.05 mm/s and laser parameters 200 Hz – 160 mJ. The epitaxial front is circled in black. The black arrows indicate the growth direction of the polycrystalline grains. The white line indicates the wafer upper surface. The IPF color scale shows the crystal orientations in the pillar growth direction. 126

Figure 6-7. EBSD mapping of cross-sections of pillars built with 100 Hz, 285 mJ, stage speed 0.13 mm/s, feed rate 1.0 g/min for two different powder purities: (a) Si_4N and (b) Si_98%. The area circled in black corresponds to an area where liquid silicon probably dropped off the melt pool along the side of the pillar. (c) and (d) are the IQ map of (a) and (b) showing the different boundary types across the EBSD map. Red lines indicate twin boundaries. Green lines indicate Σ9 boundaries. Black lines indicate random boundaries. The grains appearing in the black zone are artefacts measured on the silver paste and the resin used in the experiments. The white line indicates the wafer upper surface. 127

Figure 6-8. EBSD mapping of the cross-section of pillars built with the following conditions: frequency 200Hz, 160 mJ, pulse duration 1 ms, stage speed 0.1 mm/s and feed rate 47.5 g/min (a) pillar built with the powder Si_98% and (b) pillar built with the powder Si_4N. Smaller grains can be observed in the microstructure of the pillar built with the metallurgical grade powder. Randomly oriented grains are also more present. Red lines represent twin boundaries, green lines represent Σ9 boundaries and black lines stand for randomly oriented grains. The grains appearing in the black zone are artefacts measured on the silver paste and the resin used in the experiments. The white line indicates the wafer upper surface. 128

Figure 6-9. Optical microscope pictures of cross-sections of pillars built with 100 Hz, 285 mJ, stage speed 0.13 mm/s, feed rate 1.0 g/min (a) with Si_98% and (b) Si_4N. Some of the visible impurity precipitates are shown with arrows........ 129

Figure 6-10. Optical microscope picture of pillar cross-sections polished. The pillars were built with the following conditions: feed rate 47.5 g/min, stage speed 0.1 mm/s, repetition rate 200 Hz, energy per pulse 160 mJ. (a) Pillar built with the powder Si_98% and (b) pillar built with the powder Si_4N. Some of the visible impurity precipitates are shown with arrows. 130
Figure 6-11. (a) SEM picture of the cross-section of a silicon pillar Si_98% and showing impurity inclusions (b) EDX analysis of the impurity inclusions. EDX analysis shows that the inclusions are due to Fe and Al metallic impurities, mixed with Si. The inclusions tend to segregate at the grain boundaries.. 130
Figure 6-12. EBSD mapping of pillars built with the powder Si_4N with the following conditions: pulse duration 1 ms, feed rate 1.0 g/min, stage speed 0.0167 mm/s, frequency 200 Hz, power 160 mJ, (a) substrate orientation <111> (b) <100>. The area circled in black corresponds to liquid silicon that dropped off the melt pool along the pillar side during the process. The grains appearing in the black zone are artefacts measured on the silver paste and the resin used in the experiments. The white line indicates the wafer upper surface. The IPF color scale shows the crystal orientations in the pillar growth direction.. 131
Figure A-1. Typical code to build a pillar. The sentences in green are comments on the command. 143
Figure B-1. Net material evaporation flux as function of temperature, calculated for silicon........... 145
Figure B-2. Temporal temperature profile of the center of the melt pool calculated for different convection coefficients h corresponding to the argon shielding gas.. 146
Figure C-1. Mass per burst in function of time (a) for different cell opening times and the same cell pressure, (b) for the same cell opening time but different cell pressures....................................... 148
Figure D-1. Optical microscope images of pillars built at different laser conditions, for a substrate surface temperature of 730°C. These images were used to establish the working window presented in Chapter 4.1.2. 151
Figure D-2. Optical microscope images of pillars built at different laser conditions, for a substrate surface temperature of 730°C. These images were used to establish the working window presented in Chapter 4.1.2. 152
Figure E-1. Dedicated setup for laser-material interactions. The chamber is equipped with a 1064 nm pulsed Nd:YAG laser and several ports to observe laser-material interactions in-situ. Among them, a mass spectrometer is controlling the atmosphere inside the chamber, a spectrometer records the optical emission of the plume, and a high speed camera allows observing spattering and plume formation... 158
Figure E-2. Schematic of the in-situ observation of the plume with a high speed camera. The plume is observed on the side at a 90° angle with respect to the laser beam.. 158
Figure E-3. (a) Observation of silicon powders by SEM, as-received from the manufacturer, (b) Silicon powder pellet of diameter 10 mm, thickness 950 µm and density 60% obtained by hydraulic pressing of the initial powders, and (c) schematic of the process under investigation: a laser beam is moved on a straight line across the pellet to form a Si molten track. 159
Figure E-4. Particle size measurement in volume of the silicon powder used in the process. We found D10=0.53 µm, D50=3.09 µm and D90=10.58 µm.. 159
Figure E-6. (a) SEM picture of the track made from powder containing 2.6 wt% oxygen. (b) EDX spectrum of the oxidation trace. The trace is composed of Si and O in similar atomic quantity....... 161
Figure E-7. (a) Optical microscope picture of the cross-section of a melted silicon track processed with powders containing 0.1 wt% oxygen. (b) Detail of the track observed by SEM, enhancing the grain contrast. Smaller equiaxed grains can be observed at the bottom of the track due to nucleation

and larger elongated grains can be observed at the top of the track due to the upwards movement of the solidification front. 161

Figure E-8. In-situ high speed camera observations of a single laser shot on silicon powder pellets of different oxygen contents: (a) 2.6 wt% and (b) less than 0.1 wt%. The shot was made with a power of 333 W and a pulse duration of 1 ms. The pellet containing 2.6 wt% oxygen exhibits strong evaporation and spattering during laser processing, whereas the pellet containing less than 0.1 wt% exhibits no spattering and very little evaporation. 162

Figure E-9. (a)Thermal diffusivity measurements for silicon powder pellets of different oxygen content. The measurement has been done by laser flash analysis. Thermal diffusivity of deoxidized silicon powders are 3 orders of magnitude below the one of a monocrystalline silicon wafer. The more oxidized the powders, the lower the thermal diffusivity. (b) Thermal diffusivity measurements for bulk silicon (calculated from the data of Shanks et al.[144]) and silicon powder consolidated by SPS (Ashby et al.[145]). 163

Figure E-10. Molten silicon track on pellets of decreasing densities. (a) 61% (b) 58% (c) 54% (d) 51%. The molten track sinks down into the pellet. 164

Figure E-11. (a) Optical microscopy photo of the cross-section of a track and (b) area of the melted track and total area affected by the laser for pellets of different densities. The less dense the pellet, the deeper the molten track. 164

Figure E-12. Optical microscope picture of silicon tracks produced by SLM (top view). The thickness of the powder bed was 90 µm. The laser powder was 200W at 200 mm/s. 166

Figure E-13. SEM picture of the cross-section of the produced tracks. The heat affected zone can be pictured by a round crack. Pore formation is most likely due to the fact that the melt has a higher density than the bulk material, creating voids during cooling. 167

Figure E-14. EBSD mapping of the cross-section of the track. Silicon recrystallized epitaxially in the same orientation as the wafer. The sample is tilted at 70° angle, hence the distorted view. 167

List of Tables

Table 2-1. Typical range of values for the main parameters of PBF and DED[18] 9
Table 3-1. List of properties of the wafers used as substrates in this study.. 35
Table 3-2. Wafer resistivity measurement for the two batches used in this thesis 36
Table 3-3. List of properties for the 2 types of powders used in this study. 37
Table 3-4. Amount of impurities contained in the powder Si_4N as given by the manufacturer in ppmw.. 37
Table 3-5. Geometrical considerations of the experimental configuration... 58
Table 3-6. Properties of the argon protective gas... 58
Table 4-1. Impurity content measured by GDMS in Si_4N and Si_98% in ppmw. The frames highlighted in red show the main metallic impurities. The frames highlighted in green show the dopants.. 84
Table 5-1. Theoretical bulk silicon layer thickness per burst calculated for the feed rates 1.0 and 15.0 g/min. 108
Table 5-2. expected building rates calculated for the feed rates 1.0 and 15.0 g/min. The expected building rate for a feed rate of 1 g/min is limited by the amount of powder reaching the melt pool and the expected building rate for a feed rate of 15 g/min is limited by the amount of powder that can be incorporated into the melt pool (melt pool size and energy) 108
Table 5-3. Oxygen measurements by combustion and infrared analysis for Si_4N and Si_98%........ 118

Nomenclature

A	Total area under a burst signal [s^{-1}]
a	Half the length of a surface crack [µm]
$A(T)$	Arrhenius type function
A_i	Individual area under a burst signal [s^{-1}]
A_{laser}	Laser beam area [m^{2}]
A_{mp}	Melt pool area [m^{2}]
$\boldsymbol{A_N}$	New area created at the interface between the solid nucleus and the liquid [m^{2}]
$C_{P(liq)}$	Heat capacity of liquid silicon [J/K]
$C_{P(sol)}$	Heat capacity of solid silicon [J/K]
$C_{P_{Ar}}$	Heat capacity of argon [J/K]
C_P	Heat capacity of silicon [J/K]
C_0	Nominal alloy composition [m^{-3}]
C_L	Concentration of impurities in the liquid phase [m^{-3}]
d	Thickness of the wafer [µm]]
D_h	Hydraulic diameter [m]
E	Elastic modulus [GPa]
$E_{[hkl]}$	Crystallographic orientation dependent elastic modulus [GPa]
F	Powder flow rate [g/cm^{2}s]
f	Repetition rate [Hz]
$g(r)$	Spatial distribution of the laser beam
$\boldsymbol{G_V^L}$	Free energy per unit volume of the liquid [J/m^{3}]
$\boldsymbol{G_V^S}$	Free energy per unit volume of the solid [J/m^{3}]
$\Delta \boldsymbol{G_V}$	Free energy change per unit volume provoked by the nucleus formation (liquid to solid transformation) [J/m^{3}]
$\Delta \boldsymbol{G_{het}}$	Gibbs energy for heterogeneous nucleation [J/m^{3}]
$\Delta \boldsymbol{G_{het}^*}$	Gibbs energy for heterogeneous nucleation at the critical radius (energy barrier to overcome to promote heterogeneous nucleation)
H	Distance nozzle-wafer surface [mm]
$H(T)$	Enthalpy [J/mol]
h	Coefficient of convection [W/m^{2}K]
ΔH_f, L or L_{fus}	Fusion enthalpy [J/mol or J/kg]]
$\Delta \boldsymbol{H_V}$	Difference of enthalpy between solid and liquid [J/mol]
$\Delta \boldsymbol{H_V^m}$	Difference of enthalpy between solid and liquid at the melting temperature [J/mol]
$i(t)$	Temporal distribution of the laser beam
K	Curvature [m^{-1}]
k_B	Boltzmann constant [J/K]
k_n	Thermal conductivity in the direction r, θ or z [W/mK]
k_r	Thermal conductivity in the radial direction [W/mK]
k_z	Thermal conductivity in the vertical direction [W/mK]
k_θ	Thermal conductivity in the hoop direction [W/mK]
K_c	Fracture Toughness [Pa.m$^{0.5}$]
K_{Ic}	Fracture toughness for mode I fracture [Pa.m$^{0.5}$]
$K_{Ic(hkl)}$	Fracture toughness for mode I fracture with crystallographic orientation dependence [Pa.m$^{0.5}$]
m	Total powder burst mass [mg]
m_i	Individual powder burst mass [mg]

m_l	Slope of the liquidus of the alloy [K.m^3]
m_{max}	Maximum mass per burst reaching the melt pool [g]
n	Direction r, θ or z
Nu	Nusselt number
P	Laser Peak Power [W]
Pr	Prandlt number
$Q(r,\theta,z,t)$	Total heat loss [W/m^2]
Q_c	Activation energy for creep mechanism [J/mol]
Q_{cond}	Heat loss by conduction [W/m^2]
Q_{conv}	Heat loss by convection [W/m^2]
Q_{laser}	Laser Energy Input [W/m^2]
Q_l	Energy necessary to melt 1 gram of silicon [J]
Q_{rad}	Heat loss by radiation [W/m^2]
r	Radial cylindrical coordinate
r^*	Critical radius [m]
R	Gas constant [J/molK]
Re	Reynolds number
r_c	Radius of the wafer region cooled by the argon shielding gas [m]
r_n	Radius of curvature of the solid nucleus [m]
r_0	Radius of the laser beam [µm]
$S(r,\theta,z,t)$	Heat source or heat sink [W/m^3]
$S(\varphi)$	Shape factor depending on the contact angle
$S_c(x,y,z,t)$	Volumetric laser heat source [¦W/m^3]
$S_l(r)$	Surface laser heat source [W/m^2]
ΔS_M	Melting entropy [J/molK]
ΔS_V	Difference of entropy between solid and liquid [J/molK]
ΔS_V^m	Difference of entropy between solid and liquid at the melting temperature [J/molK]
t	Time [s]
t_b	Powder burst duration [s]
T	Temperature [K]
T_0	Ambient temperature [K]
$T_1(x,y,z,t)$	Temperature field at the boundary [K]
T_b	Temperature at the bottom of the wafer [°C]
T_{bulk}	Temperature of the bulk [K]
T_e	Temperature at which solidification starts [K]
T_m	Melting Temperature [K]
ΔT_c	Constitutional undercooling [K]
ΔT_k	Kinetic undercooling [K]
ΔT_r	Curvature undercooling [K]
ΔT_t	Thermal undercooling [K]
ΔT_{tot}	Total undercooling [K]
ΔT	Interval of temperature over which the phase change (solid-liquid) occurs [K]
U_{jet}	Argon jet speed [m/s]
V	Overall solidification velocity [m/s]
V_C	Speed of sound [m/s]
V_N	Volume of solid nucleus [m^3]
Y	Fracture toughness parameter depending on crack and sample geometries, and load application
y	Creep law exponent depending on the creep mechanism characteristics
z	Vertical cylindrical coordinate
Z	Total number of nearest atomic neighbors in the interface layer

Greek Letters

α_{abs}	Absorption coefficient [m^{-1}]
α	Jackson's factor
$\alpha(T)$	Linear thermal expansion coefficient of silicon [K^{-1}]
$\gamma_{(hkl)}$	Crystallographic plane energy [J/m^2]
γ_s	Specific surface energy [J/m^2]
γ_{NL}	Interfacial energy between the nucleus and the liquid phase [N/m]
γ_{NS}	Interfacial energy between the nucleus and the substrate [N/m]
γ_{SL}	Interfacial energy between the substrate and the liquid phase [N/m]
Γ	Gibbs-Thomson coefficient [K.m]
δ_{ij}	Kronecker symbol
ε	Emissivity
$\dot{\varepsilon}^{cr}$	Uniaxial equivalent creep strain rate [s^{-1}]
$\dot{\varepsilon}_{ij}$	Strain rate [s^{-1}]
$\dot{\varepsilon}_{ij}^{E}$	Elastic strain rate [s^{-1}]
$\dot{\varepsilon}_{ij}^{P}$	Plastic strain rate [s^{-1}]
$\dot{\varepsilon}_{ij}^{T}$	Temperature strain rate [s^{-1}]
$\dot{\varepsilon}_{ij}^{cr}$	Creep strain rate [s^{-1}]
η_1	Number of nearest neighboring atoms in the interface layer
ρ_t	Radius of curvature of the crack tip [m]
σ	Applied stress [MPa]
σ_{SB}	Stefan-Boltzmann constant [W/m^2K^4]
σ_c	Critical stress [MPa]
σ_{ij}	Stress applied in the directions i j [MPa]
σ_m	Maximum stress at a crack tip [MPa]
σ_0	Nominal applied stress [MPa]
θ	Hoop cylindrical coordinate
μ	Argon kinematic viscosity [Pa.s]
ρ	Density of argon [kg/m^3]
τ	Laser heating cycle period [s]
υ	Poisson's ratio
φ	Contact angle [°]
Ω	FEM domain

Acronyms

AM	Additive Manufacturing
BDT	Brittle-to-Ductile Transition
CAD	Computer-Aided Design
CET	Columnar-to-Equiaxed Transition
CVD	Chemical Vapor Deposition
d_{10}	particle diameter at which 10% of the sample's mass is comprised of particles with a diameter less than this value [µm]
d_{50}	particle diameter at which 50% of the sample's mass is comprised of particles with a diameter less than this value [µm]
d_{90}	particle diameter at which 90% of the sample's mass is comprised of particles with a diameter less than this value [µm]
DED	Direct Energy Deposition
DLM	Direct Laser Melting

DMD	Direct Metal Deposition
DRIE	Deep Reactive Ion Etching
EBSD	Electron Backscatter Diffraction
EDX	Energy-Dispersive X-ray Spectroscopy
E-LMF	Epitaxial Laser Metal Forming
FDM	Fused Deposition Modeling
FEM	Finite Element Modeling
FIB	Focused Ion Beam
G	Thermal Gradient
GDMS	Glow-Discharge Mass Spectroscopy
Q-factor	Quality Factor
HAZ	Heat Affected Zone
HF	Hydrofluoric Acid
HR-SEM	High-Resolution Scanning Electron Microscopy
I/O	Input/Output
IR	Infrared
L	Liquid
LBM	Laser Beam Melting
LCVD	Laser-Assisted Chemical Vapor Deposition
LENS	Laser Engineered Net Shaping
LPCVD	Low Pressure Chemical Vapor Deposition
LPE	Liquid Phase Epitaxy
MBE	Molecular Beam Epitaxy
MEMS	Micro-Electro-Mechanical System
N	Nucleus
PBF	Power Bed Fusion
PECVD	Plasma-Enhanced Chemical Vapor Deposition
PID	Proportional-Integral-Derivative Controller
PLEG	Pulsed-Laser-Induced Epitaxial Growth
RF	Radio Frequency
ROI	Region of Interest
S	Substrate
SEM	Scanning Electron Microscopy
Si_4N	Silicon Powder of purity 4N
Si_98%	Silicon Powder of purity 98%
SLM	Selective Laser Melting
SOI	Silicon-on-Insulator
SPE	Solid Phase Epitaxy
TE_{01}	Transverse electric 01 mode
V	Growth Rate
VPE	Vapor Phase Epitaxy

Chapter 1. Introduction

Additive manufacturing (AM) is an innovative layer by layer fabrication technology which has drastically developed in the course of a few years. It offers various advantages over conventional manufacturing, including high degree of customization, reduction of material wastes, design of complex structures and development of lightweight parts. Therefore, this technology holds promise in a wide diversity of domains such as aerospace and defense, medical applications and automotive industries.

Only a limited number of materials can already be processed by AM. Thus, many aspects of the fundamental understanding of AM processes are still lacking. Therefore, there is a need to widen those processes to other materials in order to increase process comprehension, be able to select appropriate methods and implement the correct improvements necessary to extend AM to any desired material in a short time frame. In this work, we propose to extend AM to silicon, the most used semiconductor material. Studying silicon as a potential material for AM gives more fundamental knowledge about AM processing of brittle materials and materials which hold similar solidification characteristics. Indeed, silicon is difficult to process by welding or additive manufacturing because of the residual stress built during part production. Moreover, contrary to most of the metallic materials, silicon grows with a faceted solid/liquid interface.

Currently, only 2.5D silicon structures can be made, mostly through subtractive procedures such as photolithography and etching. More complicated Silicon-on-insulator (SOI) technologies have to be used to obtain 3D structures. AM can be a potential answer to 3D stacks of electronics devices needed for a higher level of integration. Other than for its electrical properties, silicon could be printed for its mechanical properties and used to build micro-opto-electro-mechanical systems with more freedom of design. Additionally, AM of silicon can be interesting in producing watch parts. Indeed, Zaugg et al.[1] filed a patent for the company Breguet, where they describe a silicon-based overcoil balance spring that has to be mounted in several flat parts made independently, because “it is not currently possible to make silicon parts with several levels”. Those parts are currently usually made by Deep Reactive Ion Etching (DRIE). Moreover, being able to make monocrystalline silicon parts by AM would open the doors to integration of this process into cleanroom procedures. For example, in the case of a small number of high aspect ratio structures to be built on a silicon wafer, material waste caused by extensive etching could be reduced, as well as the use of harmful chemicals such as HF.

To the knowledge of the author, up to now, silicon on its own has not yet been proposed as a possible material for AM, neither in powder-bed or a direct energy deposition (DED) approach. Thus, as a first step towards AM of silicon, it is essential to find a working window where the process is realizable. Furthermore, it is necessary to understand how the process parameters influence the building and the microstructure of silicon structures from powders. These are some of the main goals of this PhD thesis. In this work, Direct Laser Melting (DLM), a flexible research installation part of the DED family, was chosen to study the feasibility of AM of silicon. Silicon pillars were built on monocrystalline silicon wafers. This simple geometry was considered best for preliminary experimental investigations.

The objectives of this thesis were multiple. The first goal was to determine experimental conditions leading to crack-free pillar building and understanding the reasons why cracks form. Observations of the melt pool temperature have been carried out with a high speed camera. Stress measurements were carried out by Raman spectroscopy. Both these techniques were complemented by FEM simulations and characterization by microscopy. Proper identification and control of key parameters such as substrate temperature, repetition rate, energy per pulse, and feed rate helped us understand which conditions led to cracking of the part and which had the main influence on the thermomechanical behavior of the built pillar. Based on the FEM simulations validated by experimental results, a mechanism for the crack initiation and propagation is proposed.

The second goal was to realize process monitoring of the DLM process. Monitoring of the powder feed rate and the pillar building speed as a function of process parameters such as feed rate and stage speed was realized thanks to high speed camera observations. Estimations of the thermal characteristics of the pillar during growth were carried out with Finite Element Modeling (FEM) simulations and were used to explain the pillar shape, together with high speed camera observations.

Finally, the last goal was to control certain experimental parameters to obtain epitaxial growth of the pillar from the underlying silicon wafer. The microstructure of the pillars built was characterized by the Electron Back-Scattering Diffraction (EBSD) technique. Control of parameters such as feed rate, stage speed, powder impurity content and crystallographic orientation of the substrate allowed for the control of the pillar microstructure. Epitaxial growth of silicon pillars on a monocrystalline silicon wafer was achieved, and its quality is discussed as a function of the mentioned processing parameters. Careful control of process parameters is needed to achieve the desired pillar microstructure with the optimum growth rate.

This dissertation gives insights into powder feed processes, as DLM has two major alternative features compared to conventional AM processes: a pulsed laser illumination and a pulsed powder feeding system allowing the transport of poorly flowable powders. It additionally gives knowledge in AM processes of materials solidifying with a faceted solid/liquid interface, as well as AM of brittle materials. This thesis also provides additional understanding of thermal management in pulsed laser processes, especially with the help of FEM modelling combined with experimental results.

This manuscript is divided into 7 different sections.

Chapter 1 was an introduction to the idea behind this thesis and stated its objectives. Potential applications for the proposed idea are discussed and the thesis outline is given. Chapter 2 describes the background necessary to approach the present study. A reminder of the basic theories in nucleation and fracture mechanics is presented. It provides the reader with an overview of the work already carried out in the field of additive manufacturing of brittle materials and epitaxial growth in AM, as well as their challenges. It also presents the main characteristics of silicon and the state-of-the-art in silicon epitaxial growth. The details about the experimental procedures, methodologies and simulations are provided in Chapter 3. A detailed description of the DLM machine is provided. Chapter 4 discusses the process conditions under which crack-free pillars can be built on a monocrystalline Si wafer. A mechanism for the crack formation is proposed based on experimental observations and finite element modeling. In Chapter 5, the process is monitored and characterized in details. The pillar building speed and the pillar final shapes are studied in function of the main process parameters. In Chapter 6, epitaxial growth of silicon pillars built on monocrystalline Si wafers is presented. The possibility and the quality of the epitaxial growth are studied in function of different process parameters. Finally, Chapter 7 gives a brief summary of the conclusions related to this manuscript, and recommendations for future studies are proposed. Appendices provide additional information and studies about the experiments displayed in this manuscript.

Chapter 2. State-of-the-Art Review

This chapter gives an overview of the state-of-the-art and background necessary to prepare this thesis. It is organized in several parts. First, a short overview of existing techniques to produce complex 3D silicon shapes is given. Secondly, a general description of Additive Manufacturing (AM) processing techniques is presented, centered on Direct Energy Deposition (DED), the technique used in this PhD work. Then, a review of AM and soldering of semiconductors is provided, presenting the main challenges encountered in AM processing of brittle materials and the solutions achieved in this domain. Subsequently, epitaxial growth and microstructure control in powder AM are introduced, with examples from the literature. A short review of silicon epitaxial growth current methods is added. Finally, fundamental silicon material properties used in this thesis and relevant for the DLM process are described.

2.1. 3D Silicon Structures

As already evoked in the introduction, realizing fully 3D shapes in silicon could have various advantages, especially in the design of MEMS and watch parts. It could also be a solution to 3D stacking of electronic devices in response to the need of higher level of integration.

Currently, simple 3D silicon shapes are realized with classic cleanroom processes. A 2D pattern is realized thanks to photolithography, and the 3rd dimension is created by selectively etching parts of the wafer. More complex Si 3D structures can also be produced by these processes, but with difficulty. Lin et al.[2] have built photonics crystals structures by successive SiO_2 deposition, followed by selective etching. The trenches formed were filled with polycrystalline silicon and the final layer was flattened by chemical mechanical polishing. The process was repeated several times. Final etching in HF was necessary to remove the SiO_2 and obtain the final Si structure.

However, fully 3D Si shapes could be realized thanks to other techniques. Xu et al.[3] managed to create fully 3D shapes out of silicon by using compressive buckling of silicon ribbons transferred to an elastomer substrate. The silicon ribbons were designed with varying radius in the curve of their shapes, and selectively exposed to ozone to create hydroxyl group at specific location of their surface. The elastomer substrate was uniaxially stretched and the silicon micro-ribbons were transferred onto it. Relaxing the elastomer created silicon 3D shapes by compressive buckling. Fischer et al.[4] also realized Si polycrystalline structures on silicon by an additive process. A 40-70 nm layer of silicon was deposited by chemical vapor deposition (CVD). Then, Ga^+ ions were selectively implanted in the silicon layer by FIB writing. The process was repeated until the structure was built. The material having Ga^+ implanted was removed by wet etching.

A few other different techniques have led to production of monocrystalline 3D silicon structures on silicon.

Some of those techniques are based on a raw material provided in a gas phase. Bäuerle et al.[5] used Laser-induced chemical vapor deposition (LCVD) to grow a silicon needle onto a silicon wafer. In LCVD, material can be deposited at localized places thanks to the heat confinement induced by the laser beam size. The needle was found to be the same crystalline orientation as the wafer substrate. Westberg et al.[6] managed to build silicon 3D structures like needles and coils by LCVD. Their substrate was mounted on a 3 linear axis stage supplemented by a rotating goniometer, which allowed them to build 3D silicon shapes. The growth rate of the process was in the range of 1 µm/s. Structures of several mm height and around 130 µm width were produced. The needle structures were found to be monocrystalline. However, this was not the case for helicoidal structures, for which the internal microstructure alternated between polycrystalline and monocrystalline due to temperature fluctuations.

Using another strategy, Takahashi et al.[7] managed to build a silicon needle on a silicon wafer (up to 14 µm height) by using optical vortex created by a picosecond laser pulse. The silicon needle was found to have exactly the same orientation as the wafer substrate. Nevertheless, other 3D shapes cannot be realized with this technique. Moreover, the material used was part of the wafer substrate, which excludes it from additive processes.

However, all those techniques are limited, either by their complexity, the degree of freedom that they provide or a slow deposition rate. Hence the idea of using an AM process.

2.2. Direct Laser Melting: A Direct Energy Deposition AM Process

According to ISO/ASTM 17296 standard on Additive Manufacturing Technologies, AM is defined as a "process of joining materials to make objects from three-dimensional (3D) model data, usually layer by layer, as opposed to subtractive manufacturing and formative manufacturing methodologies"[8]. AM is attractive as complex structures with unique properties can be produced with very little waste (raw material recycling). It also provides a high level of customization and allows for on demand production. Therefore, the parts do not have to be stored.

Two categories of AM processes are defined: the single and the multiple step processes. In a single step process, no additional procedure is needed beyond the basic additive manufacturing process to achieve the desired basic shape and material properties (i.e. further steps like surface finishing is not taken into account). In a multiple step process, additional operations are necessary to reach the basic finished part (typically curing or debinding). This manuscript focuses on single step processes.

In this case, two large families of AM processes exist: powder bed fusion (PBF) and directed energy deposition (DED) processes. The two families and their sub-categories are presented in Figure 2-1. Details of each sub-category are provided by Deckers et al.[9] and Sames et al. [10]. In PBF, parts of a powder bed are selectively melted or sintered by a laser or electron beam. After the first layer has been selectively melted or sintered, another layer of powder is added to the previous one. The process is repeated until the full part is produced. In DED, the raw material (powder or wire) is directly added to the melt pool created by a heat source. In this technique, the raw material is always intended to be melted.

The process used in this thesis, called Direct Laser Melting (DLM), is part of the DED family (circled in Figure 2-1) and uses powder as raw material and a laser beam as a heat source. The full description of our system is displayed in Chapter 3.2.

Different names are used to describe processes of the DED family: Laser Cladding[11], Direct Metal Deposition (DMD)[12] [13], Laser Engineer Net Shaping (LENS)[14] among others[15]. Even if the details and the capabilities of the technology slightly vary from one another (precision, surface finish…), all those processes have the same working principle. The powder delivery is carried out through one or multiple nozzles. The nozzle(s) can be placed coaxially to the laser head, or with an angle. Powders are supplied either by gravity feed or with an inert carrier gas[16]. The powder flow is generally protected by a shielding gas to prevent oxidation of the melt pool. The powders can be heated by the laser beam in flight but do not usually reach the fusion temperature. They melt during their incorporation into the melt pool to form a new layer[11] [17]. In most methods, the part to be printed is fixed to an x-y-z stage, and the laser head and powder nozzle move across the built surface to deposit material. The part is generally created and sliced in layers using computer-aided design (CAD).

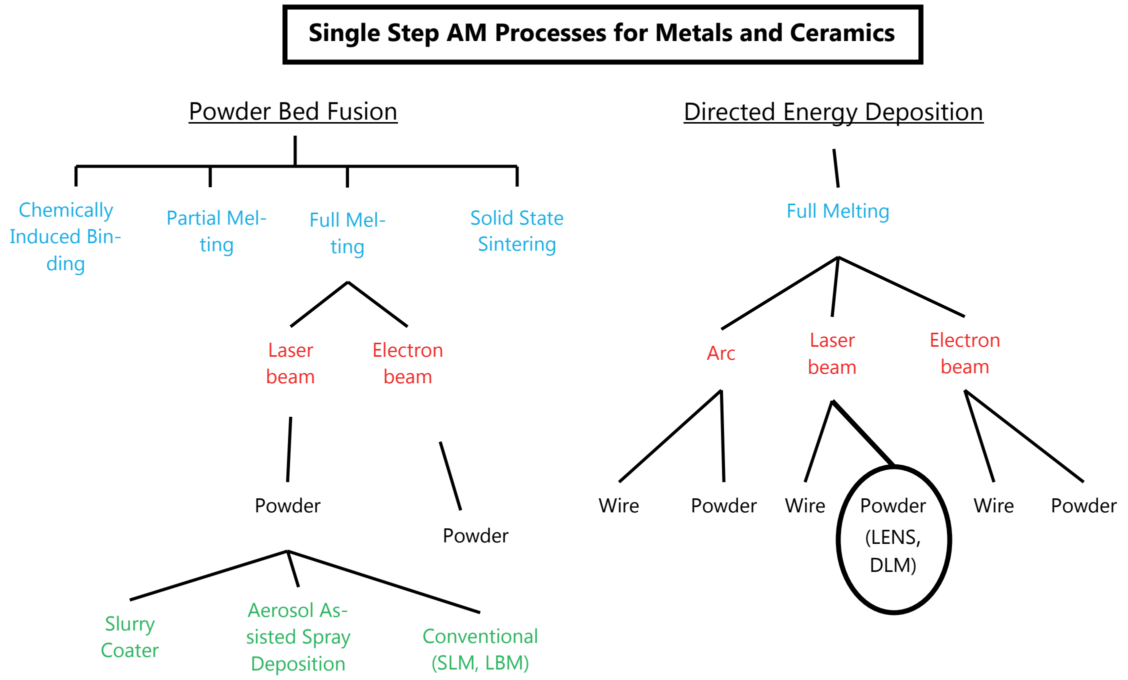
Single Step AM Processes for Metals and Ceramics
Powder Bed Fusion
Directed Energy Deposition
Chemically Induced Binding
Partial Melting
Full Melting
Solid State Sintering
Laser beam
Electron beam
Powder
Powder
Slurry Coater
Aerosol Assisted Spray Deposition
Conventional (SLM, LBM)
Full Melting
Arc
Laser beam
Electron beam
Wire
Powder
Wire
Powder (LENS, DLM)
Wire
Powder

Figure 2-1. Diagram showing the two families of single steps AM processing for metals and ceramics currently used, and their subsequent classification. The circle shows to which branch of the family DLM belongs.

DED has shown promising results, especially in the following applications[15]:

- Rapid prototyping of metallic components
- Fabrication of custom designed complex pieces
- Alternative repair technique for components that cannot be repaired otherwise

DED holds potential for graded materials and in-situ alloy fabrication, and allows fabrication of larger pieces and faster building times than PBF [18]. However, DED is currently inferior to PBF in terms of resolution and precision. The typical values for the main parameters are compared in Table 2-1 for PBF (SLM) and DED[18]. Although the scanning speed of SLM is higher than DED, the total build time of DED is faster because the powder coating step between subsequent layers is inexistent. Moreover, DED offers more flexibility in the choice of powder delivery methods, as more solutions can be imagined in terms of transport of poor flowability powders (cf. Chapter 3). This is the main reason why DED was chosen over SLM to study AM of silicon.

	PBF (SLM)	**DED**
Thickness of layers	10-100 µm	40 µm-1 mm
Typical laser spot size	50-180 µm	300 µm-3 mm
Scan speed	< 15 m/s	2.5-25 mm/s
Feed Rate (when applicable)		4-30 g/min

Table 2-1. Typical range of values for the main parameters of PBF and DED[18]

2.3. Additive Manufacturing and Soldering of Semiconductors

As no literature could be found concerning the building of 3D structures with SLM or DED technologies, it can be interesting to anticipate Si behaviour when processed by DED by comparing our case with 3D printing of material with similar properties to Si. Therefore, this part aims at giving an overview of what has been studied and achieved in SLM and DED of brittle and semiconductor materials. Through examples from the literature, this overview gives an idea of the challenges encountered in these fields, as well as the solutions proposed by the authors to overcome the difficulties. In the same goal, as AM is a type of welding, a state-of-the-art of silicon welding is also proposed.

2.3.1. Additive Manufacturing of Brittle Materials

AM remains challenging for brittle materials, mostly because they tend to crack due to several major reasons:

- High cooling rates due to laser local processing and fast scan speeds
- High thermal gradients across the structure
- High residual stress in the structure
- Thermal shocks due to arrival of cold powder on the preheated structure

However, difficulties can be overcome by applying an appropriate thermal treatment during and after processing. As AM of semiconductors is a relatively new field, most of the publications concerning AM of brittle materials found in the literature are currently focused on metals and ceramics.

In Laser Material Deposition (LMD) of single crystal sapphire conducted by Wilms et al.[19], the brittleness of the material led to cracking during the final cooling down, and during constant powder supply of cold powder to the melt pool. The problem was overcome by carrying out the process at 1550°C, slowly cooling down the furnace at a rate of 5°C/min after part printing and feeding powders at 0.5 g/min for 1 min every 5 min to let the time for the powder to melt between two powder bursts. Rotation of the sample was carried out for more homogenous spreading of the powders. Crack-free single crystal alumina was successfully grown.

Luo et al.[20] performed AM of soda lime glass. They found that substrate heating to 530°C as well as slow cooling were necessary to avoid cracking in the part. Rittinghaus et al.[21] showed that crack-free TiAl bulk samples could be built by LMD if the temperature of the substrate was heated above its brittle-to-ductile transition (BDT) of 700°C and if the part was cooled slowly (5°C/min). Rolink et al.[22] showed that preheating the substrate above the BDT of the material was necessary to obtain crack-free Fe-28at% Al parts. Moreover, notches were avoided by building smooth lateral surfaces. Hagedorn et al.[23] managed to process Al_2O_3-ZrO_2 powders by SLM. They reduced the thermal stress by preheating the structure with a CO_2 laser to 1600°C, slightly below the melting point of the material (1860°C). Li et al.[24] used a double scanning strategy to avoid crack propagation throughout the structure due to thermal stress in SLM of $Al_{85}Ni_5Y_6Co_2Fe_2$.

Consequently, literature shows that most of the cracking problems in AM of brittle materials can be solved using a correct thermal management.

2.3.2. AM of Semiconductors

So far, very few publications have been released in the field of additive manufacturing of semiconductors. Concerning single step processes, only one team has been found to work from semiconductor powders. El-Desouky et al.[25] [26] studied SLM of the thermoelectric semiconductor Bi_2Te_3 with pulsed and continuous lasers. They used powder compacts instead of powder layers because the lack of flowability of the powder used in the experiments prevented it to spread properly in the SLM system. Pores were found after observing cross-sections of the melted tracks. During their first trials, cracks formed at the surface of the tracks due to thermal stress built during laser processing of this brittle material.

The group Hitachi recently declared that they are developing a new 3D printing technology for semiconductors. Their process was based on Focused Ion Beam (FIB) with a plasma ion gun. The raw material was supplied in gas phase[27]. No details on the performance of the process were provided. However, the FIB process is expensive and time consuming.

A few other publications relate to inkjet printing. Kim et al.[28] fabricated a thin-film transistor by using a layer of printed organic semiconductor. Tran et al.[29] developed a Zinc Oxide solution that could be used for inkjet printing to fabricate additively manufactured UV photodetectors. Salea et al.[30] proposed to use Fused Deposition Modeling (FDM) to print semiconductor material. FDM is a common AM technique in which a thermoplastic filament is heated to its melting point to be extruded and deposited layer by layer to form a 3D object. In their work, they use CuO powder mixed with Polylactic acid to form the filament to be extruded. Additional annealing steps are needed to get rid of the polymer and sinter CuO particles. The final product has a very low density and high resistivity, even if it is in the same range as intrinsic Si. Halevi et al.[31] printed single crystal organic semiconductors using inkjet printing.

No work concerning AM of silicon from powders was found in the literature.

2.3.3. Silicon Soldering

Similarly, only a few examples of semiconductor soldering can be found in the literature. Some teams report successful semiconductor-metal/glass soldering. For example, Tamaki et al.[32] demonstrated that welding of borosilicate glass and silicon was possible by focusing a long wavelength femtosecond laser at the materials interface. The short high power pulse allowed non-linear absorption to occur at the interface, which enabled the bonding of the two materials through plasma formation. They claimed that this dissimilar material joining can be extended to silicon-silicon welding provided that the laser focal point can be properly visualized and placed at the silicon-silicon junction. Ultrasonic welding of metals on silicon has also been reported[33]. Using another strategy, Talapin et al.[34] developed compounds composed of Cd, Pb and Bi to apply as a paste or liquid to solder semiconductors at several hundred degrees without losing their electrical properties. They claimed that this paste could be used to realize AM of semiconductors while still delivering good electrical properties.

More important in the frame of this study, Zehavi et al. filed several patents[35] [36] [37] where they claimed a successful welding of silicon wafers without cracking. The pieces were traversed by an electrical current to be resistively heated. Argon was supplied to the welding region to avoid contamination by the environment. The area to be welded was exposed to a plasma or electrical arc welding tip. Sometimes, additional material was provided through a silicon rod to complete the welding process. They reported that moving the welding tip further from the already welded area caused the latter to rapidly cool down and crack. The stress was due to the large difference of temperature between the locally melted silicon and the surroundings of the melt pool. Therefore, according to the authors, the silicon pieces should be heated between 600 and 900°C, and should preferentially be of high purity grade. They claimed that silicon rods of 1 cm thickness could be welded on at least 25 µm depth by this method, without cracking. Therefore, cracking reduction is expected upon heating silicon pieces to more than 600°C.

2.4. Epitaxial Growth in Powder AM and Epitaxial Growth of Silicon

One of the interests in the fabrication of Si parts by AM, and a goal of this present work, is being able to grow Si epitaxially from a substrate to produce monocrystalline structures. Therefore, this part provides the fundamental background to understand in which conditions this goal can be realized. It also provides a review of materials epitaxial growth realized by AM, as well as the conditions required to achieve it. Finally, current processes used to achieve epitaxial growth of silicon are presented.

2.4.1. Fundamentals of Epitaxial Growth and Solidification

2.4.1.1. Nucleation [38]

The term epitaxy designates the growth of a crystalline material on a crystalline substrate. Epitaxial growth carried out on a substrate of the same material is called “homoepitaxy”. Epitaxial growth carried out on a substrate made of a different material is called “heteroepitaxy”.

Epitaxy is the result of a heterogeneous nucleation process. Therefore, grain nucleation takes place from the material liquid phase on the substrate solid surface. In our case, this surface is a monocrystalline silicon wafer. This process is opposed to homogeneous nucleation, which occurs directly in the liquid phase and always results in a polycrystalline microstructure.

In order to trigger solidification, it is needed to ensure a reduction of the system energy upon nucleus formation. That means that the reduction of energy induced by the phase transformation should be more than the increase in energy associated by the nucleus surface creation. ΔG_V is the free energy change per unit volume provoked by the nucleus formation (liquid to solid transformation):

$$\Delta G_V = G_V^L - G_V^S \qquad (2\text{-}1)$$

With G^L_V free energy per unit volume of the liquid and G^S_V free energy per unit volume of the solid. Another expression of ΔG_V is the following:

$$\Delta G_V = \Delta H_V - T\Delta S_V \qquad (2\text{-}2)$$

With ΔH_V difference of enthalpy between solid and liquid and ΔS_V difference of entropy between solid and liquid.

At the melting temperature T_m:

$$\Delta G_V^m = \Delta H_V^m - T_m \Delta S_V^m = 0 \qquad (2\text{-}3)$$

With ΔH_V^m difference of enthalpy between solid and liquid at T_m and ΔS_V^m difference of entropy between solid and liquid at T_m.

For a small undercooling ΔT_{tot}:

$$\Delta G_V \approx \Delta H_V^m - T\Delta S_V^m = \Delta H_V^m - \frac{T\Delta H_V^m}{T_m} = \frac{\Delta H_V^m \Delta T_{tot}}{T_m} \qquad (2\text{-}4)$$

With $\Delta T_{tot} = T_m - T$ the undercooling of the liquid.

At T<Tm, equation (2-4) becomes positive and, as the solid phase becomes more energetically favorable ($G^S_V < G^L_V$) [38].

When a nucleus forms at the solid/liquid interface, its shape is hemispherical as it minimizes the total interfacial free energy of the system. The following equation governs the balance of interfacial forces:

$$\gamma_{SL} = \gamma_{NS} + \gamma_{NL}\cos(\varphi) \qquad (2\text{-}5)$$

With γ_{SL} interfacial free energy between the substrate and the liquid, γ_{NS} interfacial free energy between the solid nucleus and the substrate, γ_{NL} the interfacial free energy between the solid nucleus and the liquid and ϕ the contact angle formed by the nucleus on the solid substrate. Figure 2-2 gives a schematic of the situation.

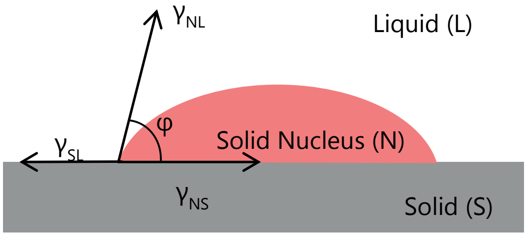

Figure 2-2. Schematic of the balance of forces at a nucleus formation (adapted from [39])

In the frame of this thesis, as in many AM systems, the solid nucleus and the solid phase are constituted of the same material. Therefore, the following approximations can be made:

$$\gamma_{NS} \approx 0 \qquad (2\text{-}6)$$

$$\gamma_{SL} \approx \gamma_{NL} \qquad (2\text{-}7)$$

Therefore,

$$\varphi \to 0 \qquad (2\text{-}8)$$

The difference ΔG_{het} in free energy undergone by the system as it creates a solid nucleus of radius of curvature r_n is:

$$\Delta G_{het} = -V_N\Delta G_V + A_N\gamma_{NL} = S(\varphi)\left[-\frac{4}{3}\pi {r_n}^3\Delta G_V + 4\pi {r_n}^2\gamma_{NL}\right] \qquad (2\text{-}9)$$

Where ΔG_V is the free energy change per unit volume provoked by the nucleus formation (liquid to solid transformation), V_N is the volume of the solid nucleus, A_N is the new area created at the interface between the solid nucleus and the liquid, S(ϕ) is a shape factor dependent on cos(ϕ).

$$S(\varphi) = \frac{[2+\cos(\varphi)][1-\cos(\varphi)]^2}{4} \qquad (2\text{-}10)$$

The critical nucleus radius r* necessary to favor nucleation is the solution to the following equation:

$$\frac{d\Delta G_{het}}{dr_n} = 0 \qquad (2\text{-}11)$$

The result is

$$r^* = \left|\frac{2\gamma_{NL}}{\Delta G_V}\right| \qquad (2\text{-}12)$$

Therefore, the energy barrier to overcome to promote heterogeneous nucleation is

$$\Delta G_{het}^* = \frac{16\pi}{3}\frac{\gamma_{NL}^3}{\Delta G_V^2} S(\varphi) \quad (2\text{-}13)$$

And the critical radius decreases if the undercooling increases.

In the case of epitaxial solidification, S(ϕ) tend to 0, therefore, the energy barrier to overcome in order to promote epitaxial growth is relatively small. This assertion is even truer as the liquid and the substrate are the same material, as γ_{NL} is small in this case. Therefore, in DED and PBF system, epitaxy happens immediately from the substrate or the previous deposited layer. Partial remelting of the substrate is necessary to ensure good adhesion to the substrate and avoid contamination introduced by the surface of the previous layer (for example oxide or small randomly nucleated grains)[39].

2.4.1.2. Different Types of Undercooling[40]

There are several contributions to undercooling which can be summarized by the following equation:

$$\Delta T_{tot} = \Delta T_t + \Delta T_k + \Delta T_c + \Delta T_r \qquad (2\text{-}14)$$

ΔT_t is the thermal undercooling, ΔT_k is the kinetic undercooling, ΔT_c is the constitutional undercooling, and ΔT_r is the curvature undercooling.

The curvature undercooling is defined by the following equation:

$$\Delta T_r = \Gamma K \qquad (2\text{-}15)$$

with Γ the Gibbs-Thomson coefficient, which is a measure of the amount of energy required to form a new surface, and K the curvature (variation of surface area with respect to variation of volume). The melting temperature is decreased by increasing the surface-to-volume ratio. This term is only important for shapes for which the radius is smaller than 10 µm.

The thermal undercooling is defined by the following equation:

$$\Delta T_t = T_s - T_{bulk} \qquad (2\text{-}16)$$

Where T_{bulk} is the melting temperature of the bulk and T_s the temperature at which solidification actually starts. With the presence of a thermal gradient in the liquid, thermal undercooling occurs when nucleation is difficult or when the latent heat of solidification cannot be easily transported away from the interface. In silicon, the large latent heat of fusion can lead to difficult evacuation of heat.

The constitutional undercooling is defined by the following equation:

$$\Delta T_c = -m_l(C_L - C_0) \qquad (2\text{-}17)$$

Where m_l is the liquidus slope of the alloy system, C_L is the composition of the liquid at the interface and C_0 is the nominal composition of the alloy. The segregation of the alloying elements ahead of the solidification front widens the freezing range of the alloy by lowering its melting point. In pure silicon, this type of undercooling can be neglected.

The kinetic undercooling is defined by the following equation:

$$\Delta T_k = \frac{R T_s^2 V}{\Delta H_f V_C} \qquad \text{(2-18)}$$

with V overall solidification velocity (rate of solidification – rate of melting), T_s temperature at which solidification starts, ΔH_f fusion enthalpy, R gas constant, and V_C speed of sound. Kinetic undercooling is induced by the fact that, to achieve solidification, more atoms should jump from the liquid to the solid phase than the contrary. For this condition to be fulfilled, the interface should be undercooled. This type of undercooling is the main undercooling present in our case, as further presented in the microstructure maps in Section 2.4.2.3.

2.4.2. Microstructure Control in AM and Crystal Growth Techniques Applied to the Si Case

In the frame of this work, it is essential to understand the process conditions under which epitaxial growth can be achieved and controlled. Therefore, the next paragraphs are dedicated to describe the solidification of silicon at the micro and macroscopic level, as well as the combination of experimental parameters to be controlled to reach epitaxial growth.

2.4.2.1. Solid/Liquid Interface Morphology during Si Crystal Growth

The Jackson's α-factor is used to assess if a plane is atomically smooth or not at the solid/liquid interface at the atomic level[41] :

$$\alpha = \frac{\eta_1 L}{Z k_B T_m} = \frac{\eta_1 \Delta S_M}{Z k_B} \qquad \text{(2-19)}$$

With η_1 number of nearest neighboring atoms in the interface layer, Z total number of nearest neighbors, L latent heat of fusion, k_B is the Boltzmann constant, T_M is the melting temperature and ΔS_M is the melting entropy. The quantity $L/k_B T_M$ is a measure of the ease to create disorder at the interface[42]. If $\alpha>2$, the interface is smooth, and if $\alpha<2$, the interface is rough. For metals, $L/k_B T_M$ is usually small, of the order of 0.8-1.5. Therefore, the solid/liquid metallic interfaces are usually atomically rough. For silicon, $L/k_B T_M=3.6$ and $\eta_1/Z=0.75$ for {111} and less or equal to 0.5 for the other planes. Therefore, the (111) plane is smooth and all the other ones are rough. A schematic representation of a rough and smooth solid/liquid interface is presented in Figure 2-3.

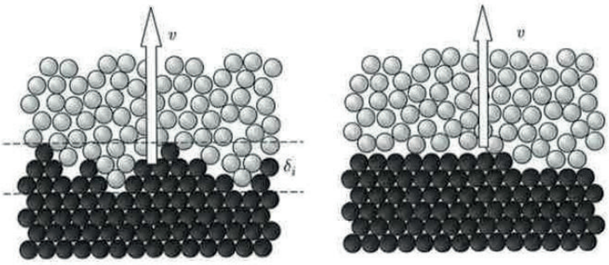

Figure 2-3. Schematic representation of (a) rough and (b) smooth solid/liquid interfaces[43] δ_i is defined as the interface thickness.

Smooth and rough planes obey to different growth velocity models. A smooth plane grows layer by layer and follows a 2D growth model. Its growth is controlled by the nucleation of new layers. Therefore, the growth velocity exponentially depends on the inverse of the undercooling. A rough plane can grow from all directions of space and follows a 3D growth model. Its growth is controlled by the diffusion of atoms at the solid/liquid interface. Its growth velocity is linearly dependent on the undercooling[44]. It follows that rough planes have higher growth velocities than smooth planes. The {111} plane of silicon is also known to have the lowest surface energy. Therefore, the {111} plane always grows with a planar liquid/solid interface, whereas other planes grow with a faceted interface, delimited by {111} planes at the atomic level.

Twin boundaries are also easily formed on the faceted {111} delimited interfaces, as described by Figure 2-4 [45]. Therefore, they are expected to easily form during crystal growth of all planes except for {111}.

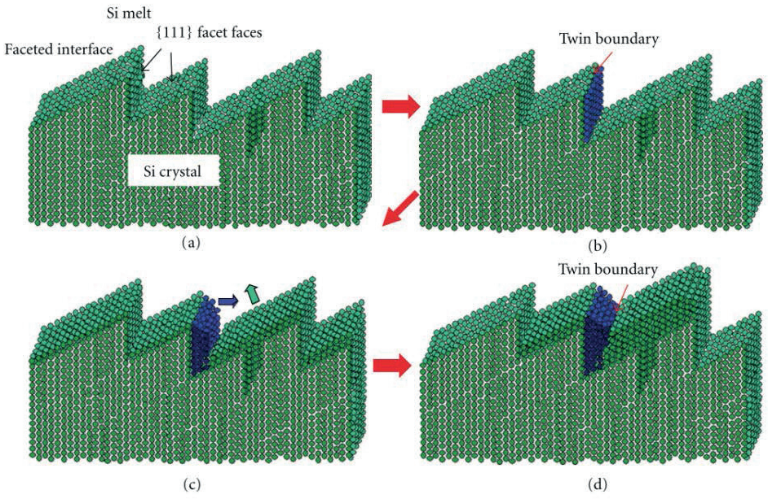

Figure 2-4. Mechanism of parallel twin formation at the solid/liquid interface during Si crystal growth. If a twin boundary is unintentionally formed at the interface, another twin boundary forms parallel to the first one upon lateral growth of the original crystal[45].

At microscopic scale, Tokairin et al.[46] experimentally observed a change from a smooth to a faceted interface delimited by (111) planes, at a critical growth velocity of 147 µm/s for a thermal gradient of 8.10^3 K/m in the furnace. They attributed this change to the instability created by the difficulty of evacuating the latent heat produced during the solid/liquid phase change at high velocities. This phenomenon led to the apparition of a negative gradient ahead of the crystallization front. They also noticed that the critical growth velocity decreased when the thermal gradients along the growth direction decreased.

2.4.2.2. Microstructure-Process Maps: Columnar-to-equiaxed transition (CET) in metal AM

Hunt[47] developed a first model to draw microstructure maps as a function of process parameters such as thermal gradients and growth rate. Kurz et al.[48] adapted it to welding type processes. As silicon AM microstructure maps cannot be found in literature, a microstructure map for the nickel alloy CMSX-4 is shown on as an example in Figure 2-5. This map gives a first hint of the microstructural behavior of materials in AM type processes. In the case of CMSX-4, three types of microstructures could be distinguished, depending on the thermal gradients G and growth velocity V:

- Planar front growth for High G/V ratios
- Columnar dendritic growth for intermediate G/V ratios
- Equiaxed dendritic growth for low G/V ratios

In order to achieve epitaxial growth from the substrate, the growth mode should be columnar, and the transition from the columnar to the equiaxed growth mode should be avoided. During solidification, equiaxed grains are formed if the local heat flux is isotropic, and columnar growth occurs if the local heat flux is oriented. The transition occurs when equiaxed grains nucleate in the liquid ahead of the columnar zone. The processing maps differ depending on the alloy, but several trends are common.

- High thermal gradients G and low speeds V are required to maintain a columnar growth
- Higher thermal gradients are required if the quantity of impurities (nucleation sites) increase

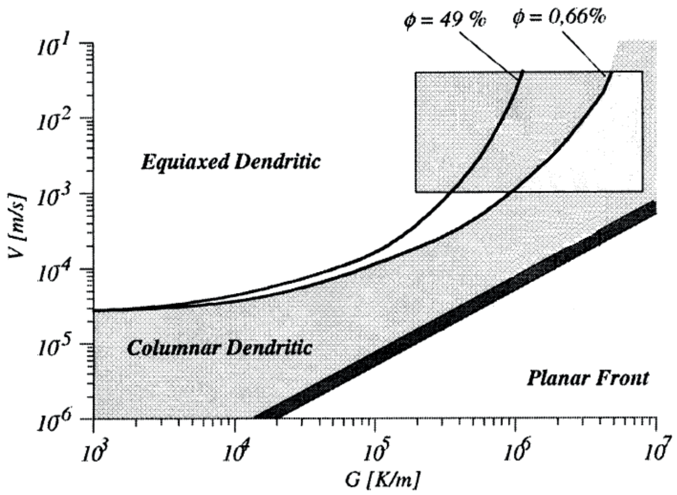

Figure 2-5. Microstructure map calculated for the Ni superalloy CMSX-4 as a function of growth velocity V (m/s) and thermal gradients G (K/m). The thin black lines represent the CET, with φ the proportion of equiaxed grain required for the microstructure to be considered fully equiaxed (φ=49%) or under which it is considered fully columnar (φ=0.66%). The square represent the range of conditions used during laser processing[48].

G and V depend on the laser parameters, mainly power, scan speed, substrate temperature and beam diameter. If the substrate temperature increases, G decreases. This has to be compensated by a decrease in power to maintain high thermal gradients and epitaxial growth. The use of large beam diameter is limited because a larger power has to be used to ensure remelting of the substrate (or previous layer). Therefore, small beam diameters are preferential[49]. Gäumann et al.[50] plotted microstructure maps as a function of laser power and beam diameter for two preheating temperatures, for laser cladding applications (Figure 2-6). They showed that a threshold fluence was necessary to remelt the previous layer, and that small diameters and low powers enabled them to maintain a columnar growth when the substrate was heated.

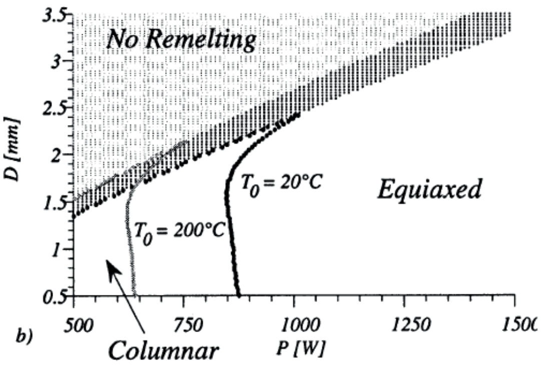

Figure 2-6. Microstructure maps of Ni-superalloy for different laser parameters[50].

2.4.2.3. Microstructures-Process Maps for Silicon: Columnar-to-Equiaxed Transition (CET) as a function of process parameters

Similarly, several types of microstructures can be observed in silicon, depending on the undercooling (or growth rate), thermal gradients across the material and impurity content.

- Columnar faceted growth
- Faceted dendritic/equiaxed growth
- Planar amorphous growth

Unlike alloys, silicon does not present any planar front growth, because the interface is always faceted, as mentioned in the previous paragraph. It is necessary to stay in columnar faceted growth mode to maintain a proper epitaxial growth.

Mangelinck-Noël et al.[51] developed a model in which a faceted-to-equiaxed transition (FET) is introduced in the case of silicon crystal growth, similarly to the columnar-to-equiaxed transition (CET) introduced by Hunt[47] for the growth of metals and alloys. This model was first introduced to explain the formation of small grains in silicon ingots during the Czochralski process, where slow growth velocity and low thermal gradients take place. The model was based on the assumption that kinetic undercooling is the dominant mechanism responsible for undercooling and solidification, contrary to the model used for alloys that assumes constitutional undercooling. They considered the transition to occur when the volume occupied by the equiaxed grain reaches a critical value compared to the one occupied by the columnar grains. The formation of equiaxed dendrites was assumed to be triggered by the precipitation of impurities in the undercooled melt ahead of the liquid/solid interface at a certain undercooling, lower than the kinetic undercooling. As silicon has rough and faceted planes, two models were used for the growth of equiaxed dendrites: thermal rough equiaxed dendrites and faceted equiaxed grains. The results of their calculations (Figure 2-7) were microstructure maps as a function of thermal gradients, impurity content and growth rate during the process.

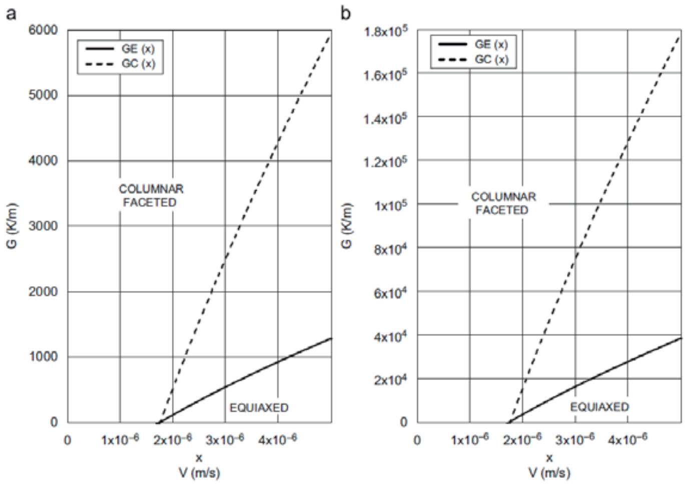

Figure 2-7. Microstructure maps for the model using thermal rough equiaxed dendrites. (a) Undercooling necessary for the nucleation of equiaxed grains on impurities < 1K, low particle density and (b) Undercooling necessary for the nucleation of equiaxed grains on impurities < 1K and high particle density. The plain line represents the thermal gradient for which the grains are always equiaxed. The dashed line represents the thermal gradient for which the growth is always columnar.

Comparatively to metal processing, the same tendency can be drawn for Si: at high G/V ratio, the growth is columnar, and at sufficiently low G/V ratio, the growth is equiaxed. It is interesting to notice that higher thermal gradients are necessary to maintain the columnar growth for a material that contains more impurities. Brynjulfsen et al.[52] observed the formation of dendrites at high pulling rate (5 cm/min) during Bridgman process, but none appeared at low pulling rates (0.2 mm/min).

Thus, careful adjustment of the ratio G/V as a function of processing parameters is expected in order to be able to achieve epitaxial growth of silicon on silicon by DLM.

2.4.3. Review of Epitaxial Growth of Materials Processed by Additive Manufacturing

This section gives an overview of the cases of epitaxial growth accomplished by AM.

First, it is interesting to mention the Verneuil process, which also aims at producing single crystals from powders. The Verneuil process[53] is mostly used to produce rubies (Al_2O_3 single crystals). In this process, the raw material should be more than 6N pure. It is grinded until it is turned into a very fine powder. Powder preparation is crucial as the material should be of a good flowability[54]. The powder is then placed in a container inside a so-called Verneuil furnace. The container is vibrated to let the powder flow along a thin tube set at the bottom of the container, together with oxygen gas. Hydrogen is supplied into an outer tube. Combustion occurs at the outlet of the inner tube, and melts the powder into thin droplets to a temperature of about 2000°C. The droplets drop onto a support rod and form a sintered cone. The tip of the cone is close enough to the flame to remain in liquid state: that is where the crystal forms. As the rod is slowly moved down, a crystal *boule* solidifies on top of the rod. A schematic of the Verneuil process is displayed in Figure 2-8. The process typically produces sapphire cylinders of 13 mm diameter and 25 to 50 mm length in 2.5 hours. Typical growth rates lie between a few microns to a few dozens of microns per second.

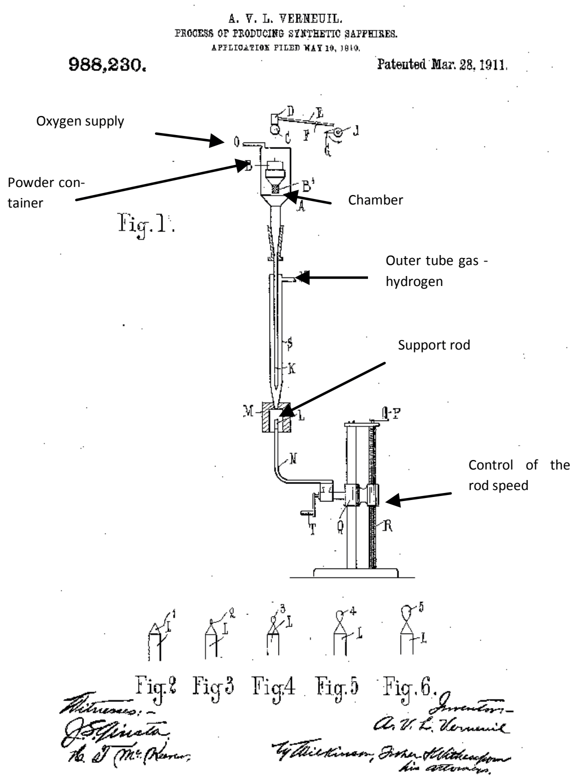
A. V. L. VERNEUIL.
PROCESS OF PRODUCING SYNTHETIC SAPPHIRES.
APPLICATION FILED MAY 19, 1910.
988,230.
Patented Mar. 28, 1911.
Oxygen supply
Powder container
Chamber
Fig. 1.
Outer tube gas - hydrogen
Support rod
Control of the rod speed
Fig.2
Fig.3
Fig.4
Fig.5
Fig.6.

Figure 2-8. Schematic of the Verneuil process as described by its author[53]. Fig. 1 describes the Verneuil furnace. Fig. 2, 3, 4, 5 and 6 show different stages of the growing crystal in time.

Epitaxial growth is usually observed at least on a short range at the interface between the substrate and the clad when both of them are the same material. For example this is the case in additive manufacturing of CoCrMo by the LENS technique[55]. More complete epitaxial growth of several materials has been achieved using DED processes. As evoked in the previous paragraph, Wilms et al.[19] also successfully grew single crystal alumina of diameter 30 mm and height 3.5 mm by LMD. Gäumann et al.[56] produced single crystals of a commercial Ni-based superalloy (CMSX-4) by E-LMF (Epitaxial Laser Metal Forming), which is a derivative of the laser cladding technique. They successfully repaired a turbin blade by depositing tracks of several mm height and width.

Hetero epitaxial growth can also be achieved by AM. Cu-30Ni layers were grown on a rolled C71500 (Cu-Ni alloy) plate by DMD[57] and epitaxy of dendrites were observed at the substrate/clad interface. Bezençon et al.[58] managed to achieve hetero-epitaxial growth of a MCrAlY coating on a Ni-based superalloy using the laser cladding technique. Santos et al.[59] managed to produce a multilayer epitaxial clad of the Ni-based alloy Rene N4 on a CMSX-4 single crystal substrate on about 40% of the clad thanks to high G/V ratios. However, epitaxial growth was lost at the top of the clad due to a decreasing G/V ratio and passing the CET. Vilar et al.[60] demonstrated the epitaxial growth of NiCrAlY on (100) single crystal substrates of a Ni-based superalloy by laser cladding.

2.4.4. Epitaxial Growth of Silicon: A Review of the Current Techniques

Many methods already exist to grow silicon epitaxially. This section gives an overview of these techniques. It gives the reader a starting point for comparison with the DLM process.

2.4.4.1. Epitaxial Growth for Ingot Production

The most well-known of these processes are the ones used for silicon crystal ingot growth for solar cells and electronics such as Czochralski, float-zone and directional growth processes. All of them use a monocrystalline piece of silicon as seed to set the crystalline orientation of the final ingot.

In the Czochralski process, the feedstock material is melted in a quartz crucible into a vacuum chamber. Silicon is heated to its melting point, and the heat is transmitted through a graphite container placed between the crucible and the heaters. A monocrystalline seed is then introduced into the melt and is gradually pulled up at a speed of a few cm/h. Liquid silicon is crystallizing around it, in the same crystallographic orientation[61]. In the float-zone process, a monocrystalline seed is set at the top of a polycrystalline ingot. The ingot is then locally melted by a RF coil. The heat causes the atoms to rearrange in the orientation of the crystal seed, forming monocrystalline silicon. The melting zone is moved along the entire ingot until the latter becomes completely monocrystalline.

Directional growth can also be used to produce monocrystalline silicon. This technique is called quasi-mono or mono-like silicon growth. In this technique, silicon is epitaxially grown from several monocrystalline seeds set at the bottom of a crucible. The liquid silicon is cooled down by controlling the speed at which the crucible is taken out of the heat zone. The growth speeds of this method are similar to the Czochralski growth process[62].

Keck et al.[63] fabricated polycrystalline silicon *boules* by Tip Fusion Method. This method was a hybrid between the Verneuil process (explained in a previous section) and the float-zone method. In this process, the tip of a polycrystalline seed was melted with an induction coil into a sessile drop. Silicon powder was fed into the melt at a weak feed rate. Polycrystalline silicon boules were produced with a growth rate of about 7 µm/s.

However, all of these processes produce large-scale ingots, which differ greatly from AM processes. Nevertheless, useful comparisons can be drawn between the two types of silicon directional crystal growth processes, as discussed in Chapter 6.

2.4.4.2. Epitaxial Growth for thin film production

Processes to grow silicon epitaxial on a substrate are numerous: Liquid Phase Epitaxy (LPE), vapor Phase Epitaxy (VPE), Molecular Beam Epitaxy (MBE), Solid Phase Epitaxy (SPE). However, these methods are restricted to thin-film technologies. Therefore, the layers produced range commonly from a few nm to a few microns in thickness. They are reviewed in this section.

Vapour Phase Epitaxy[64] is a modified CVD. In VPE, Si is deposited epitaxially onto Si substrates by controlling the deposition of Si atoms decomposing from precursors introduced in a chamber in a gas phase. Diverse precursors can be used for Si deposition: Silicon tetrachloride ($SiCl_4$), Dichlorosilane (SiH_2Cl_2), Trichlorosilane ($SiHCl_3$), Silane (SiH_4). VPE enables the growth of silicon films of thickness about 1 to 100 µm at rate > 1 µm/min. Too high growth rates would result in obtaining polycrystalline silicon instead of monocrystalline silicon. VPE usually takes place at temperatures as high as 1200°C.

Liquid Phase Epitaxy of Si [65] allows the growth of Si from a monocrystalline Si seed (wafer), from a metallic solution. The semiconductor is dissolved into the melt of another metallic compound. The most common metals used in solutions for Si growth are Sn and Ga. The deposition happens at a temperature well below the melting point of silicon, and at a lower temperature than for VPE. The metallic solution is saturated with Si, and a diffusion process driven by a concentration gradient due to the melt saturation enables the deposition of Si onto Si wafer, with the same crystallographic orientation as the latter. The metals used as a solution for the Si deposition are incorporated as dopants into the deposited Si during the process.

In Solid Phase Epitaxy[66], a layer of amorphous Si is either deposited or produced by ion implantation on top of a monocrystalline Si substrate. Then, low temperature (~ 600°C) heating causes the atoms of the amorphous film to rearrange in the same crystallographic orientation as the substrate. The heat can be produced in an oven or with a localized heat source such as a laser[67].

Molecular Beam Epitaxy of silicon[68] is a thin-film growth method taking place in Ultra High Vacuum. The material to be deposited is either heated until sublimation, sputtered or pyrolysis of Si compounds such as SiH_4. It is then deposited onto the substrate by condensation. The temperature of the growth is relatively low (750-1000°C), but the deposition rate is very slow (typically 3 nm/h and less). However, this technique enables the control of the film layer by layer and achieves the highest purity.

More recently, Pulsed-laser-induced epitaxial growth (PLEG)[69] has been developed in the scope of 3D circuit integration. Indeed, to stay in phase with the more and more demanding “Moore” law, which predicts the decrease in size of the transistors used in the integrated circuit technology year by year, the trend leads to 3D circuits where transistors could be stacked on one another and separated by a layer of insulating material. The main problem in this case is to grow silicon epitaxially without heating too much the underlying circuits. PLEG could solve this problem by offering local heating thanks to a pulsed laser. In PLEG, a layer of SiO_2 is deposited by Plasma enhanced chemical vapor deposition (PECVD) on top of a monocrystalline wafer. Dry etching is required on the regions that are designated to be seeding regions (see Figure 2-9). The process is repeated twice to adjust the size of the opening. Then, a layer of a-Si is deposited by LPCVD. Finally, an excimer laser is used to recrystallize a-Si from the seeds formed by the wafer, in a SPE fashion, as the substrate is heated to 400°C. The crystallized Si also grows epitaxially laterally on top of the deposited SiO_2.

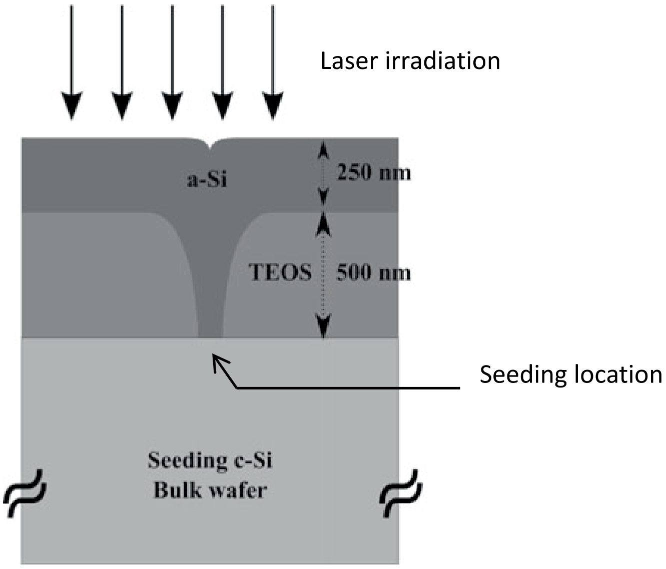

Figure 2-9. Schematic of the PLEG principle

Si homoepitaxy can also be achieved by ion sputtering[70]. The process is carried out in Ultra High Vacuum (UHV). In this process, the Si atoms are sputtered onto a monocrystalline silicon substrate by primary ions accelerated towards the Si target. The Si thin films are typically deposited at a temperature of 700-1000°C at a rate of few Å to a few dozens of Å/min[71 72].

2.5. Silicon Properties Relevant for DLM Processing

AM is a complex process that involve careful knowledge in the processed material's properties. Localized laser heating and powder supply induce changes in the materials properties during processing. Those changes are highly implicated in the production of crack-free silicon parts and microstructure control. Therefore, a good knowledge of multiphysics silicon properties is essential to understand experimental results. It also constitutes a vital part of FEM modeling. Therefore, in the next paragraphs, mechanical, thermal and optical properties of silicon in the solid and liquid states will be reviewed.

2.5.1. Silicon Mechanical Properties

At ambient pressure and temperature, silicon crystallizes in the same crystallographic system as cubic diamond (see Figure 2-10). Silicon is an anisotropic material, which means its mechanical properties will be different according to the orientation of the crystal lattice.

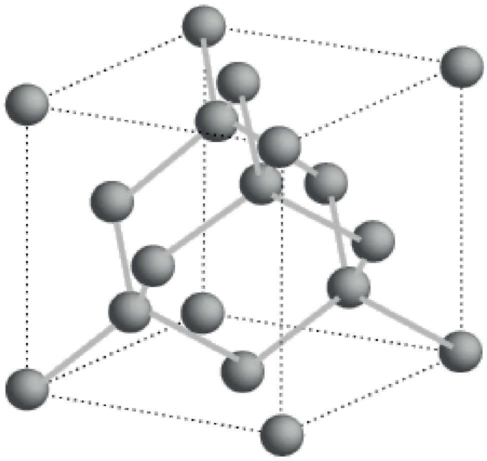

Figure 2-10. Silicon crystallization system[73]

The resistance of a material to brittle fracture in the presence of a crack is described by the fracture toughness K_c[74].

$$K_c = Y\sigma\sqrt{\pi a} \qquad (2\text{-}20)$$

Where Y is a parameter that depends on crack and sample geometries, and load application, σ is the applied stress and a is the length of an internal crack or half the length of a surface crack. For a plate of infinite width and a crack propagating into its thickness (such as a silicon wafer), Y ≈ 1. When the thickness of the plate is large compared to the length of the crack, it is assumed that no strain component is located perpendicular to the front and the back face. Then K_{Ic} is defined to describe such situation, and is called plane strain fracture toughness (the I stands for the mode I of crack surface displacement, which occurs by opening of the material).

$$K_{Ic} = Y\sigma\sqrt{\pi a} \qquad (2\text{-}21)$$

K_{Ic} is small for brittle materials and rather large for ductile materials. It mostly depends on temperature, strain rate and microstructure.

The fracture toughness K_{Ic} of monocrystalline silicon depends on its crystallographic orientation.

$$K_{Ic(hkl)} = \sqrt{2\gamma_{(hkl)}E_{[hkl]}} \qquad (2\text{-}22)$$

Silicon has two main cleavage planes: {111} and {110}, with {111} being the easiest of all. Reported values for fracture toughness of silicon at room temperature are in the range 0.62 to 1.22 MPa.m$^{1/2}$ for {111}, 0.68 to 1.19 MPa.m$^{1/2}$ for {110} and 0.75 to 1.29 MPa.m$^{1/2}$ for {100}[75].

Fracture strength of silicon depends on many parameters such as the type of test, the impurity concentration, temperature, defect size and specimen size. In monocrystalline Si micropillar compression tests, Wheeler et al.[76] found up to 7 GPa before fracture of the base of the pillar at room temperature. 3-point bent tests were carried out by Wu et al.[77] on silicon wafers of different characteristics. They measured fracture strengths ranging from about 200 to 600 MPa. Fracture strength decreases considerably with increase in surface flaws. Barredo et al.[78] also found that a stress of about 225 MPa was necessary to reach a fracture probability of more than 60% with a bending test. Pertersen[79] evokes a very high tensile yield strength for silicon of 6.9 GPa. However, this value can be considerably decreased by the presence of crystallographic or surface defects.

Elastic constants of silicon also depend on the crystallographic orientation. Young's modulus are reported to be between 130 and 190 GPa[75].

The fracture of a solid phase involves crack formation and crack propagation due to applied stress[74]. Applied stresses can be of different nature: tensile, compressive, shear or torsional. By convention, tensile stresses are positive and compressive stresses are negative. Cracking will result in the separation of the material in several pieces. There are two possible fracture types: brittle and ductile. They are both illustrated in Figure 2-11. A brittle fracture is characterized by crack formation, rapid propagation, and no material deformation. The cleavage usually shows sharp edges and facets. On the contrary, the ductile fracture is occurring thanks to the formation of voids that coalesce and form an elliptic crack. The crack propagates thanks to the coalescence of voids formed ahead of the crack tip. The fracture shows plastic deformation of the material.

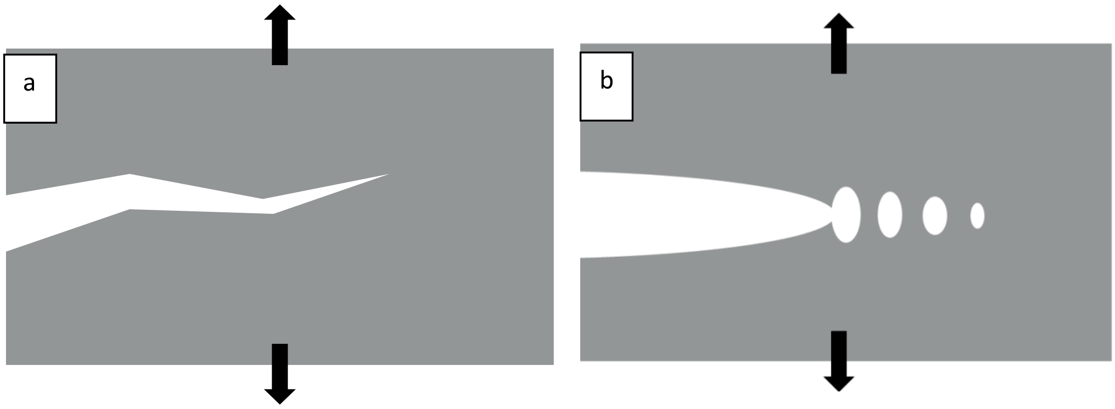

Figure 2-11. Schematic of (a) brittle and (b) ductile fractures. The arrows indicate the direction of the applied tensile stress.

When a crack is initiated by a stress, the stress at the tip of the crack can be largely amplified depending on its orientation and geometry. Away from the crack, the stress corresponds to the nominal applied stress. However, stress concentration occurs at the tip of the crack, and the maximum stress is approximated by

$$\sigma_m = 2\,\sigma_0 \sqrt{\frac{a}{\rho_t}} \qquad \text{(2-23)}$$

Where σ_0 is the applied nominal stress, ρ_t is the radius of the curvature of the crack tip, a is the length of a surface crack or half the length of a crack if it is located in the bulk.

Stress concentration at a crack tip is more important in brittle than in ductile materials. Indeed, for the latter, plastic deformation occurs when $\sigma_m$becomes higher than the yield strength. The stress will then be more uniformly distributed around the crack (stress raiser), and finally leads to σ_m smaller than the theoretical value displayed in equation 2-23. In the end, the critical stress needed for crack propagation in a brittle material is given by

$$\boldsymbol{\sigma_c} = \sqrt{\frac{2E\gamma_s}{\pi a}} = \frac{K_{Ic}}{\sqrt{\pi a}} \qquad \text{(2-24)}$$

Where E is Young's modulus, γ_s is the specific surface energy and *a* is half the length of an internal crack. If the value of the stress at the tip of the defect becomes higher than the critical stress, crack formation and crack propagation occur.

Silicon possesses a brittle-to-ductile transition temperature. Fracture appearing over the brittle-to-ductile transition temperature range will present morphological features of both types of fractures – brittle and ductile.

2.5.1.1. The Brittle-to-Ductile Transition (BDT) Temperature in Silicon

At room temperature, silicon is brittle. Therefore, in terms of stress-strain behavior, it is elastic until its fracture point and fails without any plastic deformation. However, it becomes ductile above a certain temperature, called the brittle-to-ductile transition temperature. This temperature varies with the loading rate and the doping level of the material. It typically increases with increasing load rate. It characterizes itself by a sudden increase in fracture toughness from 3 to 8 times the value of the fracture toughness at room temperature on a very small range of temperatures (about 10°C) [80]. Figure 2-12 shows the fracture toughness increase of low doped silicon measured in function of temperature by Brede et al.[80]

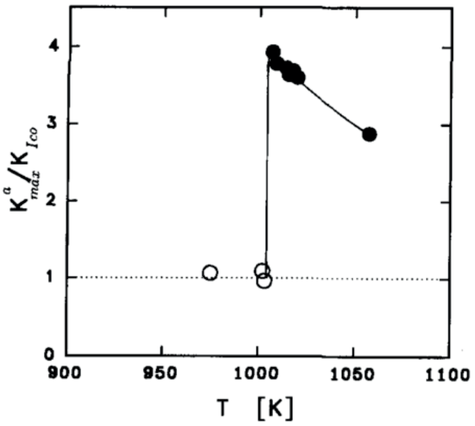

Figure 2-12. BDT of Silicon as function of temperature measured by Brede et al. on pure silicon doped with 5.2.10^4 boron atoms/cm^3 (Float zone process, < 10^{15} oxygen atoms/cm^3, loading rate 5.5 µm/min, K^a_{Ico} = 0.88 ± 0.07 MPa.m$^{1/2}$) [80]

Brittle-to-ductile transition temperatures as low as 550°C and as high as 1100°C[81] [82] [80] have been measured for monocrystalline silicon, depending on the loading rate and the doping level. Lower BDT have been determined by simulations[83]. BDT also experiences a size effect as it was found to decrease with the size of the sample (micron to nano scale)[84].

At the atomic level, the brittle-to-ductile transition is a result of a competition between cleavage fracture and dislocation nucleation motion at the crack tip. The stress is raised at the tip of the crack until a critical stress for which dislocations are able to nucleate is reached. Dislocation nucleation and motion along the slip planes allow stress release at the crack tip by shielding its propagation. Therefore, the BDT is a capability of the material to prevent the crack tip stress to reach fracture strength. The latter is governed by two parameters: dislocation number and mobility, and the number of slip systems at the front of the crack tip[83]. Well below the BDT, brittle fracture occurs. Well above the BDT, ductile failure prevails.

Wheeler et al.[76] measured the stress-strain curve of a Si monocrystalline wafer <100> by micropillar compression. The measured stress-strain curves are displayed on Figure 2-13. It can be observed that as the temperature increases, silicon adopts a more and more ductile behavior.

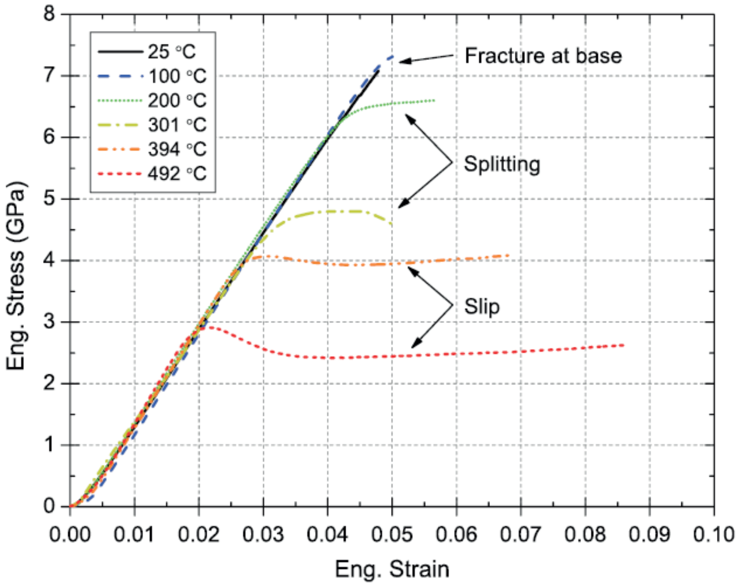

Figure 2-13. Stress-strain curves for Si <100> single crystal measured by micropillar compression at different temperatures[76]

The BDT is essential to understand the eventual cracking behavior of silicon at high temperature. Its existence indicates that careful process temperature should be selected to avoid brittle crack propagation in the silicon structures.

2.5.2. Silicon Thermal Properties

Silicon melts at 1414°C and evaporates at 3265°C. Solidification and evaporation occur at a constant temperature as silicon is a pure compound. The enthalpy of liquefaction and evaporation of silicon are respectively 50.21 and 383 kJ/mol. Its density in the solid phase at room temperature is generally taken as 2.33 g/cm^3, and its density in the liquid state as 2.57 g/cm^3. A graph showing silicon density as a function of temperature as measured and fitted by Ohsaka et al.[85] is given in Figure 2-14. Heat capacity and thermal conductivity of crystal and liquid silicon as a function of temperature are given in Figure 2-15. It is interesting to note the drastic change of properties upon the change of state.

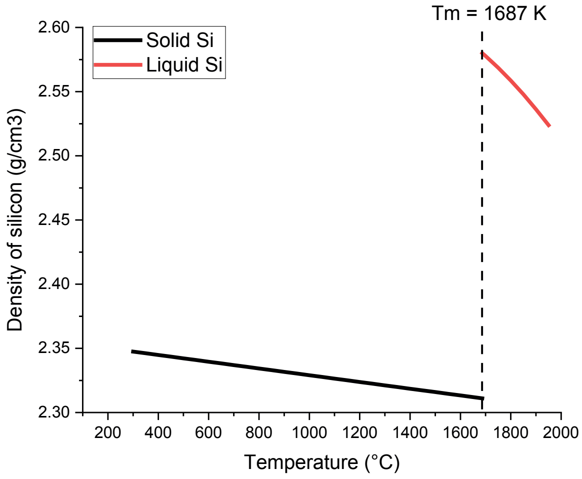

Figure 2-14. Density of solid and liquid silicon as a function of temperature as measured and fitted by Ohsaka et al.[85]

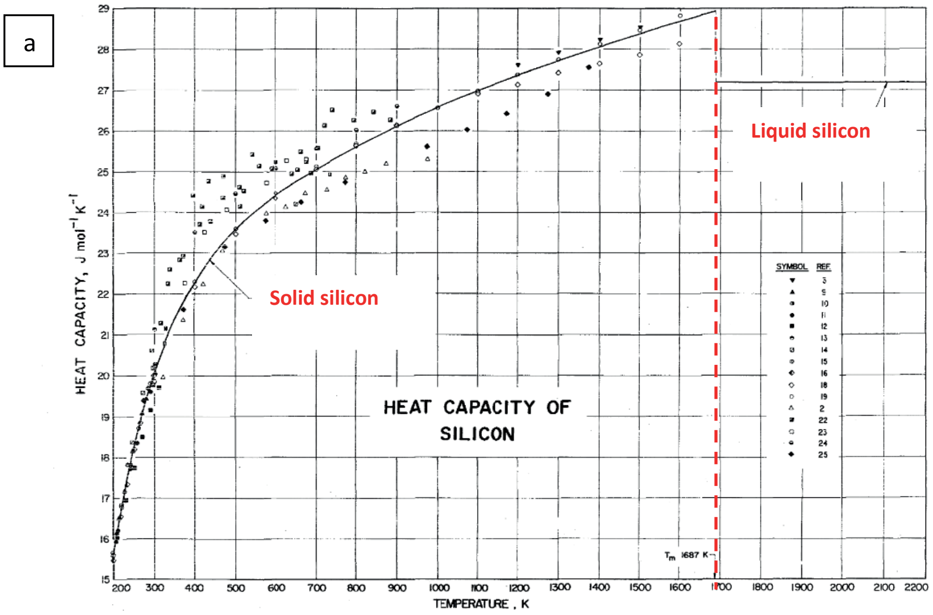

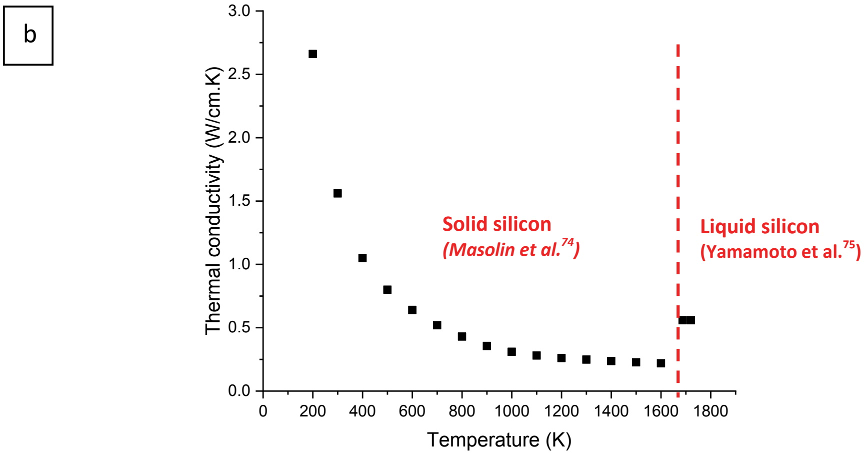

Figure 2-15. Thermal properties of crystalline and liquid silicon as a function of temperature: (a) thermal capacity[86], (b) thermal conductivity[87 88]

The thermal expansion coefficient α of solid silicon measured by Okada et al.[89] was

$$\alpha(T) = \left(3.725\left(1 - e^{-5.88.10^{-3}(T-124)}\right) + 5.548.10^{-4}T\right).10^{-6} \quad (K^{-1}) \qquad (2\text{-}25)$$

This equation is later used in the Finite Element Modeling simulations carried out in this PhD work.

2.5.3. Silicon Optical Properties

Optical properties of silicon are essential for fundamental understanding and modeling of laser coupling with the material. Bulk silicon properties are well-known in the literature. However, silicon powder optical properties have not been extensively investigated. As the wavelength of the laser used in this study is 1064 nm, the optical properties of silicon discussed in the next paragraph are focused around this wavelength. There exist discrepancies between optical properties of bulk and powder silicon, as well as between its solid and liquid states.

2.5.3.1. Absorptivity and Reflectivity of Bulk Silicon in the Solid and Liquid State at 1064 nm

Sin et al.[90] calculated absorption coefficients of Si as a function of temperature at 1064 nm and plotted them together with experimental data found in the literature. The results are shown in Figure 2-16. The absorption coefficient increases considerably with temperature. Those results were used in the approximation of the coefficient of absorption of silicon used in the FEM simulations presented in section 3.6.1.

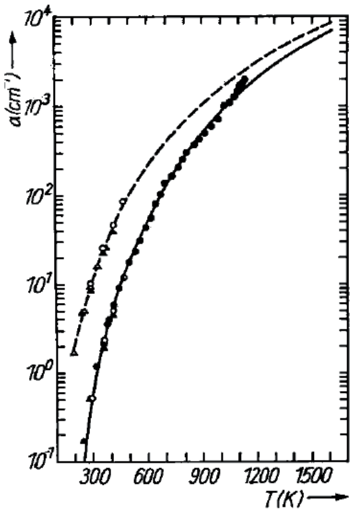

Figure 2-16. Absorption coefficient of silicon at λ=1152 nm (plain line) and λ=1064 nm (dotted line) calculated and fitted with experimental data[90].

Liu et al.[91] studied the change in reflectivity over time during heating and melting by illumination of a bulk silicon wafer with a 532 nm picosecond laser. The probe laser wavelength was 1064 nm and its fluence was kept below 1/30th of the 532 nm laser fluence (0.3 J/cm^2 above the melting threshold). They found that reflectivity of the solid phase was about 32% and the reflectivity of the liquid state was 76%, with decrease in reflectivity as the temperature increases. Such measurements are also consistent with a similar work conducted by von der Linde[92].

2.5.3.2. Absorptivity and Reflectivity of silicon powders in the solid state

For powders, light diffusion is expected to dominate. Therefore, the absorption coefficient and the reflectivity are expected to increase compared to the value of the bulk (at room temperature). Increase in absorption coefficient at 1064 nm has been shown by Kuz'min et al.[93] for nanopowders.

2.5.3.3. Emissivity

Emissivity of silicon over a broad range of wavelengths has been measured by Sato[94] and is displayed in Figure 2-17. In the visible range, the emissivity does not vary much with temperature, with values from 0.5 to 0.7.

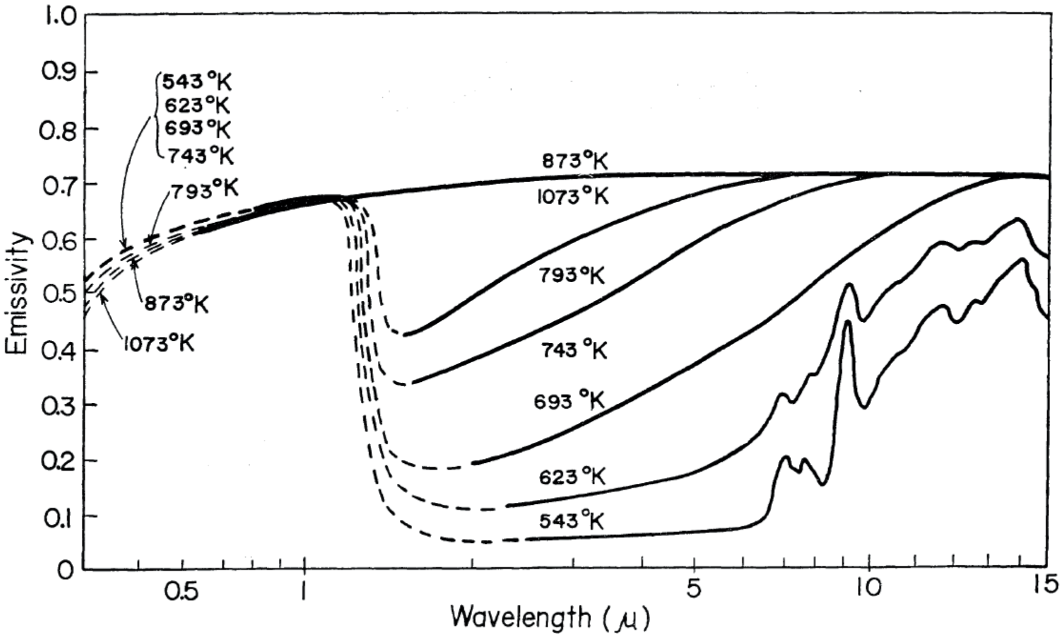

Figure 2-17. Spectral emissivity of bulk silicon by Sato[94]

However, liquid silicon has a much lower emissivity in the visible and near infrared range. Watanabe et al.[95] measured the emissivity of solid and liquid silicon at 1415°C. They found values of more than 0.35 for solid silicon and less than 0.3 for liquid silicon at the same temperature. They measured emissivity from 600 to 850 nm and from 1000 to 1200 nm and observed that emissivity of the solid phase decreased with increasing wavelength, whereas the emissivity of the liquid phase decreased with increasing wavelength. Takasura et al.[96] reported an emissivity of more than 0.47 for solid silicon (increasing emissivity with increasing wavelength) and about 0.27 for liquid silicon at the same temperature. They measured it in the range 400-800 nm. Knowledge of the emissivity of silicon as a function of temperature in the visible range allowed observations of the melt pool with a camera detecting in the visible range (cf. Chapter 3.3.1).

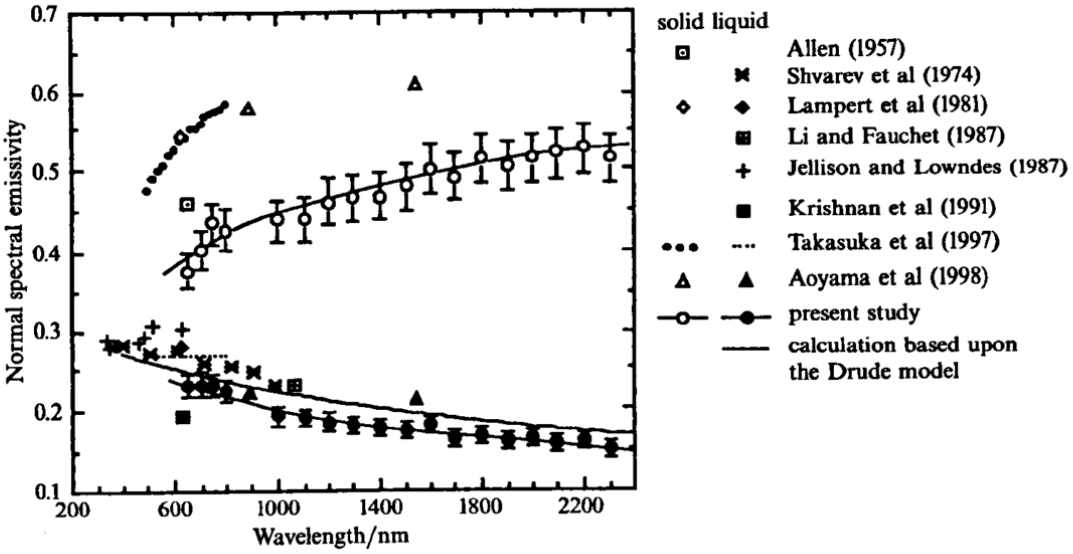

Figure 2-18. Emissivity of silicon in the solid and the liquid phase from 200 to 2600 nm measured by various authors

Chapter 3. Materials and Methods

In this Chapter, details concerning the experimental work carried out in this PhD study are presented: materials, processes, characterization techniques and methods.

3.1. Materials

3.1.1. Wafers

Wafers with two different orientations were used as substrates in this work. Their properties are listed in Table 3-1.

	Wafers <100>	Wafers <111>
Supplier	Center of Micronanotechnologies at EPFL, Lausanne, Switzerland	Si-MAT, Kaufering, Germany
Orientation	<100>	<111>
Thickness	525 ± 25 µm	525 ± 25 µm
Diameter	100 ± 0.5 mm	100 mm
Polishing	Single side	Single side
Doping	Boron or Phosphorus	p-doped with Boron
Resistivity	0.1-100 Ω.cm	1 to 10 Ω.cm

Table 3-1. List of properties of the wafers used as substrates in this study.

All the wafers were cleaved into pieces of typically dozens of mm in length and width for the experiments. The pillars were built on the polished wafer surface. The wafers were cleaned with ethanol before insertion into the chamber.

The resistivity of the wafers of the different batches were more precisely measured with a Single-Post Dielectric Resonator (Microwave Q-meter from Qwed, Poland). The principle is based on the measurement of the Q-factor and the resonant frequency of a TE_{01} microwave resonator, once empty and once loaded with the wafer sample. The non-contact measurement is carried out in transmission of the microwaves through the wafer. The difference of Q-factor and resonant frequency between the two measurements is directly linked to the complex dielectric properties of the sample that are directly linked to its resistivity.

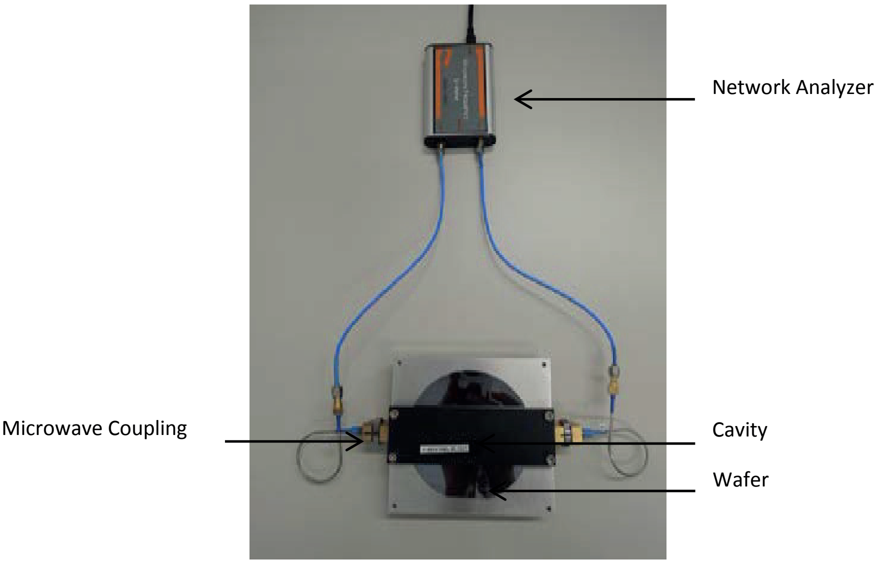

Figure 3-1. Photo of the resistivity measurement system

Similar resistivities were found for the batch of orientation <100> and the batch of orientation <111>. The measurements are also consistent with the values provided by the manufacturer. Therefore, the resistivity values for the wafers of the same batch do not differ considerably, and no influence is expected for different substrates.

Batch orientation	Resistivity
<100>	10 ± 2.1 Ω.cm
<111>	5.04 ± 0.12 Ω.cm

Table 3-2. Wafer resistivity measurement for the two batches used in this thesis

3.1.2. Powders

Two types of powders were used in this study, named Si_98% and Si_4N respectively. Their properties as given by the manufacturer are summarized in Table 3-3.

	Si_98%	**Si_4N**
Manufacturer	Keyvest, Belgium	Dalian King Choice Non-Ferrous Metals Products Co., Ltd**., China**
Purity	98 %	99.999 %
Particle size distribution	d_{50}=16.33 µm d_{10}=3.37 µm d_{90}=41.74 µm	less than 50 µm

Table 3-3. List of properties for the 2 types of powders used in this study.

The impurity content in Si_4N as given by the manufacturer is indicated in Table 3-4.

Fe	**Al**	**Ca**	**B**	**P**	**Cu**	**Na**	**K**
2.31	0.19	0.06	1	0.8	<1	<1	<1
Mg	**Hg**	**Pb**	**Cd**	**Ti**	**As**	**Cr**	**Ni**
<1	<1	<1	<1	<1	<1	<1	<1

Table 3-4. Amount of impurities contained in the powder Si_4N as given by the manufacturer in ppmw

When not used, the powders were always stored in an oven at 100°C under vacuum to avoid moisture and agglomeration. Powder morphology and impurity content have been measured and the results are respectively presented in Chapters 5.1.1 and 6.2.4.

3.2. Direct Laser Melting Process

3.2.1. Configuration

Direct Laser Melting (DLM) is part of the Direct Energy Deposition family of the additive manufacturing techniques. In this process, the powder is brought to the melt pool through a nozzle using a powder transportation channel. The laser beam and the center of the powder jet cross into a single point on top of the wafer substrate (Figure 3-2). The wafer is moved in the three directions by an actuated xyz stage on which a heating plate was mounted. The setup has been described in details elsewhere[97]. Therefore, a large part of the following description was directly taken from this paper.

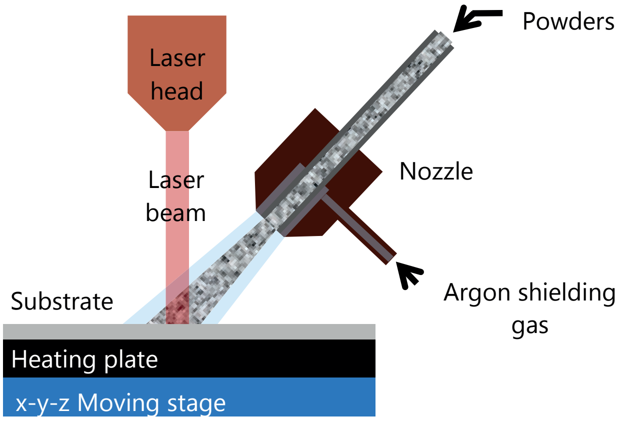
Powders
Laser head
Laser beam
Nozzle
Argon shielding gas
Substrate
Heating plate
x-y-z Moving stage

Figure 3-2. Schematic of the principle of DLM

3.2.2. Chamber

The set-up is a flexible research installation allowing for rapid modification or exchange of individual components. A large volume (550 mm height and 580 mm diameter) ultra-high vacuum (UHV) multi-flange reactor of more than 200 kg weight acts as chamber and mechanical base for the installation. A photo of the setup is shown in Figure 3-3. The flanges are used as feed-through for gases, powder supply, electric cables or as windows for the laser beam or optical observation purposes.

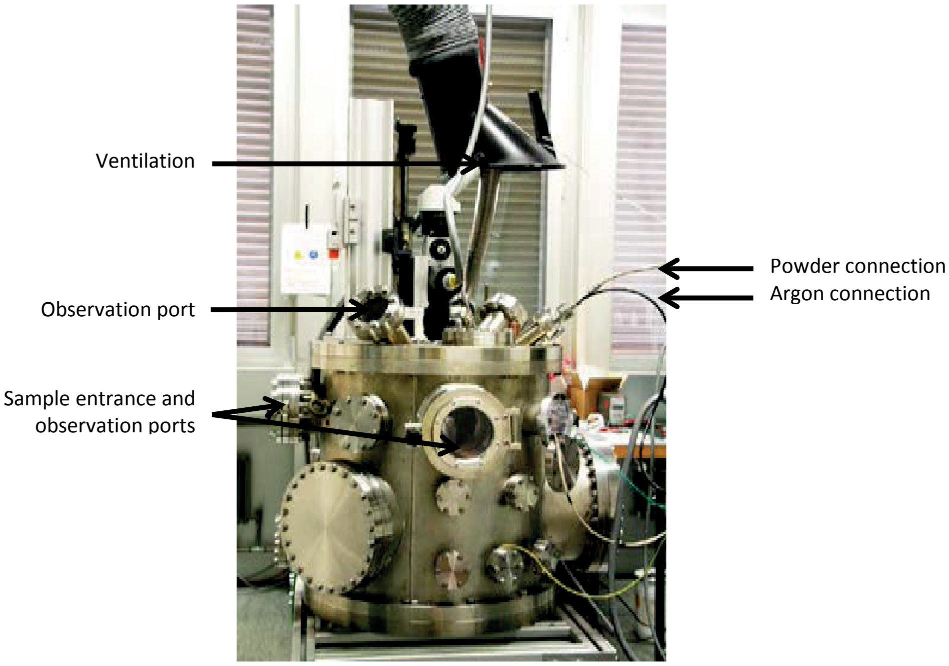
Ventilation
Observation port
Sample entrance and observation ports
Powder connection
Argon connection

Figure 3-3. Photo of the metallic chamber used for the DLM process

3.2.3. Laser

The illumination system used is a pulsed 1064 nm Nd:YAG solid state laser SLS 200 C60 (LASAG AG, Switzerland). The Nd:YAG is excited with a pulsed flash lamp under free-running pulse conditions. The pulse duration can be controlled in the range of 0.1-20 milliseconds and the energy limit per pulse is about 50 J. The laser beam is coupled into a 400 micrometer core diameter step index fiber LL422 (Rofin-LASAG, Switzerland) to deliver the beam to the laser beam head (LLBK45, Rofin-LASAG, Switzerland) fixed on a z-moving stage to adjust the image plane on the substrate surface. The fiber exit is magnified by 1.5, resulting in a focal spot of 600 micrometers on the substrate plate. Average peak intensities up to 177 MW/cm^2 can be delivered to the work-piece through the focal spot. The laser intensity is controlled through the flash lamp current, with a modulation frequency of 20 kHz. Due to the applied coupling into the multimode fiber a flat cone topped hat intensity profile is obtained (see Figure 3-4, top line in the focal plane (0 mm) with about 20% intensity maximum in the center as compared to the edge). The laser intensity had to be strongly reduced for measuring the beam profile by a beam splitter and neutral density filters. The very large depth of field of 2-4 mm deforms this intensity profile slightly by increasing the distance between the lens and the observation plane by 0.5 mm and 1 mm, at 2 mm out of focus. The intensity profile approaches a Gaussian-like intensity distribution that widens further away from the focal point (Figure 3-4).

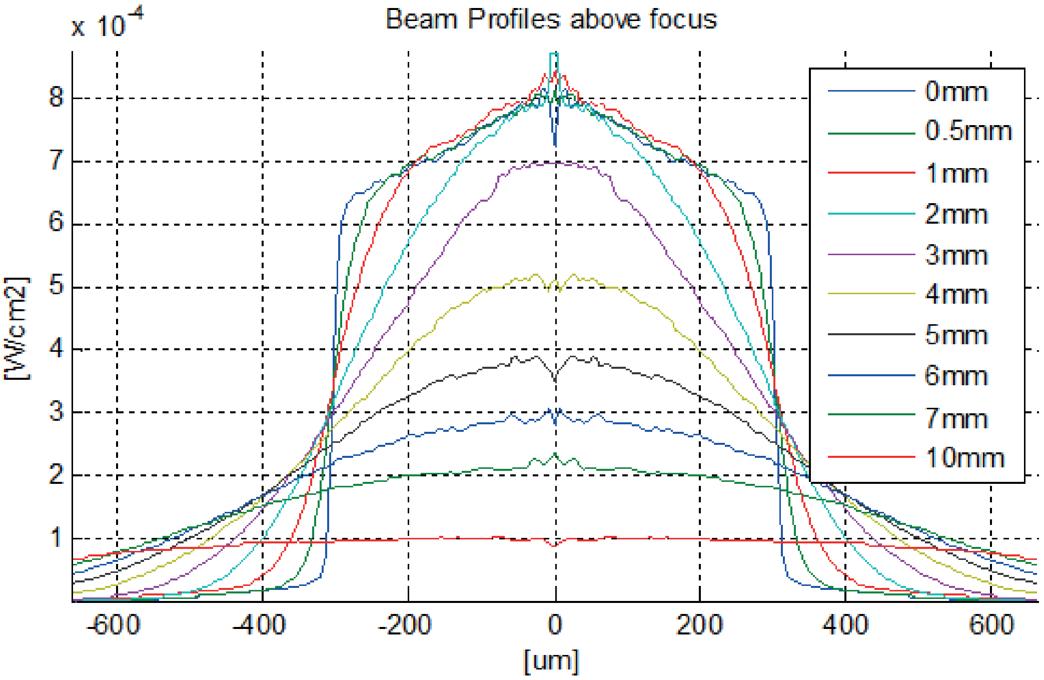

Figure 3-4. Reduced intensity beam profile in and out of focus for the pulsed 1064 nm Nd:YAG solid state laser (SLS 200 from LASAG AG, Switzerland)

An energymeter is included in the laser, and measures the energy per pulse delivered just before entering the laser fiber. However, due to loss of energy in the fiber and multiple reflections on the chamber glass window, the actual energy used in sample processing is much less than the one delivered by the laser. Therefore, the energy of the pulses arriving on the sample was measured with a powermeter Vega (Ophir, USA). The laser was always focused at the surface of the wafer at the beginning of each building process (house-like beam profile).

3.2.4. Moving Stages

Presently, three high precision linear motor driven stages are mounted to a x-y-z system (2 LINAX® Lxs 160F60 and 1 LINAX® Lxc 44F08 from Jenny Science, Switzerland), each with a resolution of 1 µm and an accuracy of ± 2 µm. Therefore, this system can achieve a precision of better than 5µm in the 3D space. The stroke in x and y directions is 160 mm and 44 mm in the z-direction. Very high maximum speeds of 3 m/s in the x and y direction and 2 m/s in the z direction can respectively be reached. The three stages (and further stages, if added) are controlled by a Beckhoff TwinCAT3 PLC system with feedback control and data I/O exchange up to 20 kHz (Beckhoff Automation AG, Switzerland). Furthermore, laser and powder trigger and power ramping can be controlled by this unit.

3.2.5. Nozzle

The powder nozzle consists of two coaxial tubes. The inner one, for powder transportation, has an inner diameter of 3 mm and an outer diameter of 6 mm. The outer tube used for the argon shield gas has an inner diameter of 7 mm. The argon supply is delivered through a tube placed perpendicularly to the powder tube (see Figure 3-2 and Figure 3-5). The argon shielding gas flow of about 14 L/min protects the powder from water or oxygen contaminations in the process chamber. The argon flow is controlled through a flowmeter, and forms a laminar flow at the exit of the tube, according to the calculated Reynold's number equal to 1500. The injection nozzle is positioned at an angle of 40°with respect to the laser beam, and the nozzle-to-substrate distance at the laser focus is 12 mm.

3.2.6. Heating Plate

A resistively heated silicon nitride hot plate (Bach Resistor Ceramics GmbH) was mounted on the moving stage to pre-heat the wafer substrates (Figure 3-5). Its temperature was controlled by a PID unit (LabHeat®, SAF Wärmetechnik GmbH) by recording the signal of a K-type thermocouple inserted under the hot plate. The thermocouple was inserted in a 1 mm hole drilled under the heating plate. The hot plate was thermally isolated from the motion stage platform with a 15 mm thick ceramic plate (Macor®MGC, Eperon Engineering, Switzerland). A wafer substrate can be clamped on top of the heating plate by two ceramic clamps (Macor®MGC, Eperon Engineering, Switzerland). The substrate was heated up in steps of 100°C every 2-5 min to avoid temperature overshooting.

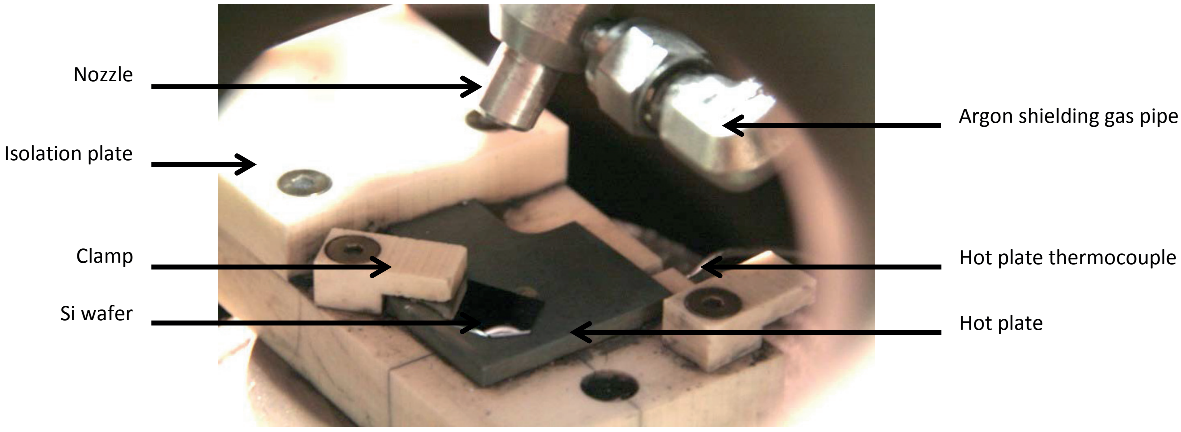

Figure 3-5. Photo of the DLM setup inside the chamber

3.2.7. Heat Controller and Temperature Measurements

Due to the high temperature rise of the plate and the slow actuator switching off time inside the temperature PID unit controller, the temperature of the heating plate was always fluctuating around the nominal temperature set on the controller. Therefore, we have measured the fluctuations of the plate and the wafer substrate around the nominal value with several K-thermocouples RS Pro (RS, Switzerland):

- One thermocouple was set under the heating plate to monitor its temperature with respect to the nominal value. This thermocouple constituted a feedback loop to the heat controller.
- One thermocouple was set on top of the wafer substrate by using the clamps. The thermocouple was bonded to the wafer with a ceramic paste Cerambond 671 (Aremco, USA). The temperature was measured without argon protective gas.
- The same thermocouple was used to monitor the temperature of the plate under a flow of 14 L/min of argon.

Figure 3-6 displays a typical temperature fluctuation of the heating plate in time measured by the thermocouple placed at the wafer surface for different sets of nominal values. No argon was flowing during these experiments. Figure 3-7 shows the average temperatures measured by the thermocouple placed on top of the wafer surface with and without argon shielding gas.

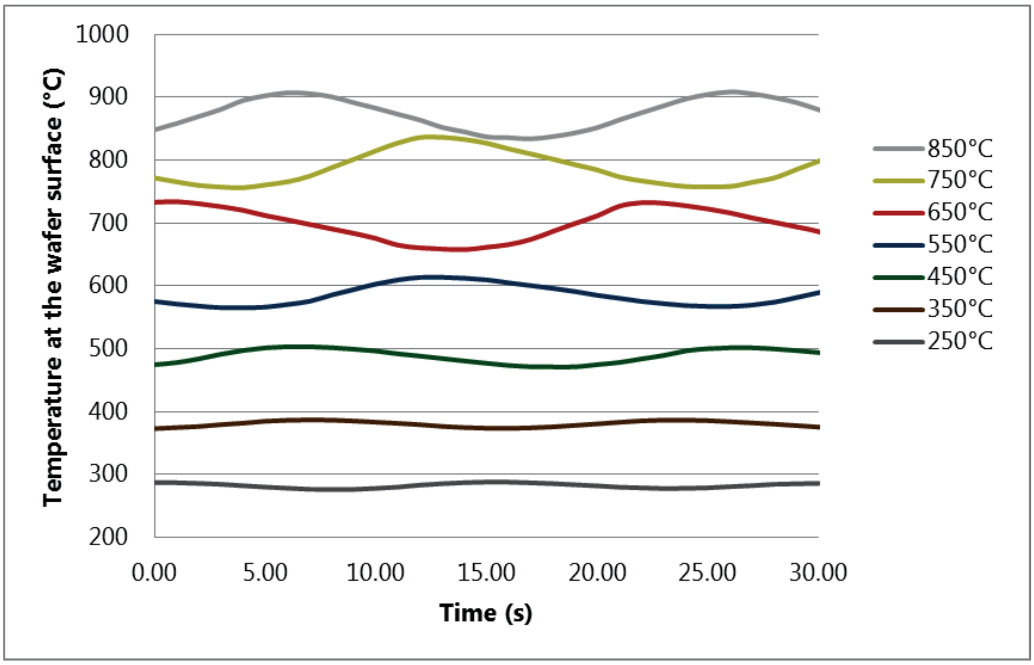

Figure 3-6. Temporal temperature fluctuations of the heating plate for several set temperature values when no protective gas is blowing

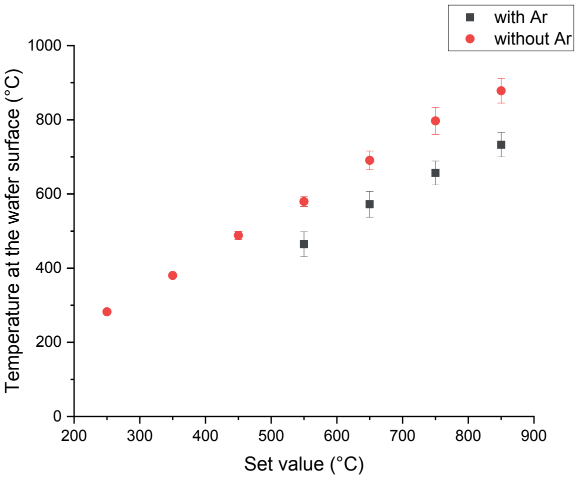

Figure 3-7. Average temperature measured by the thermocouples placed under the heating plate, on a wafer surface with and without the argon shielding gas of 14 L/min.

The substrate temperature displayed throughout the thesis refers to the average temperature of the wafer surface without any shielding gas.

3.2.8. Powder Feeding System

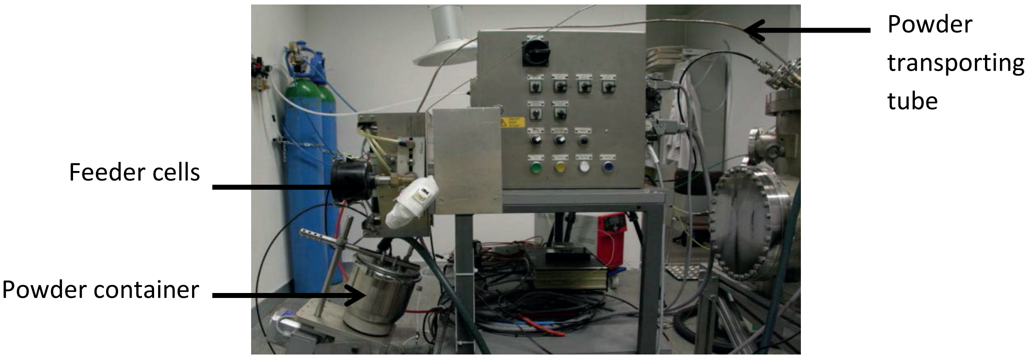

Figure 3-8. Photo of the powder feeding system

The powder injection takes place through a lateral injection nozzle (Figure 3-5) linked to a powder feeder (Figure 3-8). The powder jet center is aligned with the laser beam focus on the surface of the substrate (Figure 3-2). The powder feeder, ImpaktTM, was purchased from P&S Powder and Surface GmbH, Germany. The feeder consists of a powder container, a feeder chamber with two cells and a control unit. It is connected to a pressure bottle delivering the argon transport gas. The powder transport is based on the pressure difference between the feeder cells and the process chamber. In brief the functional principle is: first, the feeder cell is evacuated using a vacuum pump, then the powder is sucked into the cell due to the pressure difference between the powder container and the evacuated feeder cell. A filter membrane is retaining the powder in the cell. The argon is pressed into the powder containing feeder cell to increase the pressure and then the valve to the process chamber is opened leading to transport of the powder into the chamber. A schematic of the powder feeder principle is shown in Figure 3-10. Continuous repetition of this process results in a pulsed powder transport. In our case, only one cell was used, working at 5 Hz. Several chambers can run consecutively resulting in a pulsed quasi-continuous gas transported powder feed.

The powder is sucked into the feeder cell from a rotating container, inclined with an angle of about 30° with respect to a horizontal position, to keep powders moving. The container has a diameter of 20 cm and a height of 20 cm, and can contain up to 2 kg of powder. The sucking tube and the lid of the container are held in a fixed position. The container atmosphere is kept under a slight overpressure of Argon. A special stirring plate was mounted in the powder feeder container to keep the powder flowing during the feeding process. Two tubes are linking the cell and the nozzle: the first one made out of plastic, of inner diameter 4 mm and outer diameter 6 mm, followed by a stainless steel tube of inner diameter 3 mm and outer diameter 6 mm. The first tube is 105 cm long and the second one is 36.2 cm long.

The powder feed rate can be controlled by adapting the opening-closing time of the different valves governing the transport process. Smaller variations in the feed rate can then be controlled by selecting the vacuum (pressure) inside the cell. These two parameters control the quantity of powder delivered per powder burst.

In order to create a certain powder feeding pattern, the opening and closing time of the cell valves have to be programmed over one cycle. Different programs will lead to different types of feeding. Figure 3-9 shows the powder feeding program used in this study. As already mentioned earlier, the powders were delivered at a rate of 5 Hz. Thus, one cycle time lasts 200 ms. In this case, the vacuum was made inside the cell for 80 ms. During the last 30 ms of the vacuum, the powder was let in the cell. This valve opening time was varied from 8 to 30 ms to vary the feed rate. Then, for 20 ms, all valves were closed. In the last 100 ms of the cycle, both the gas pressure and the powder outlet valves were opened. The argon transporting gas was blowing with a flow of 20.2 L/min.

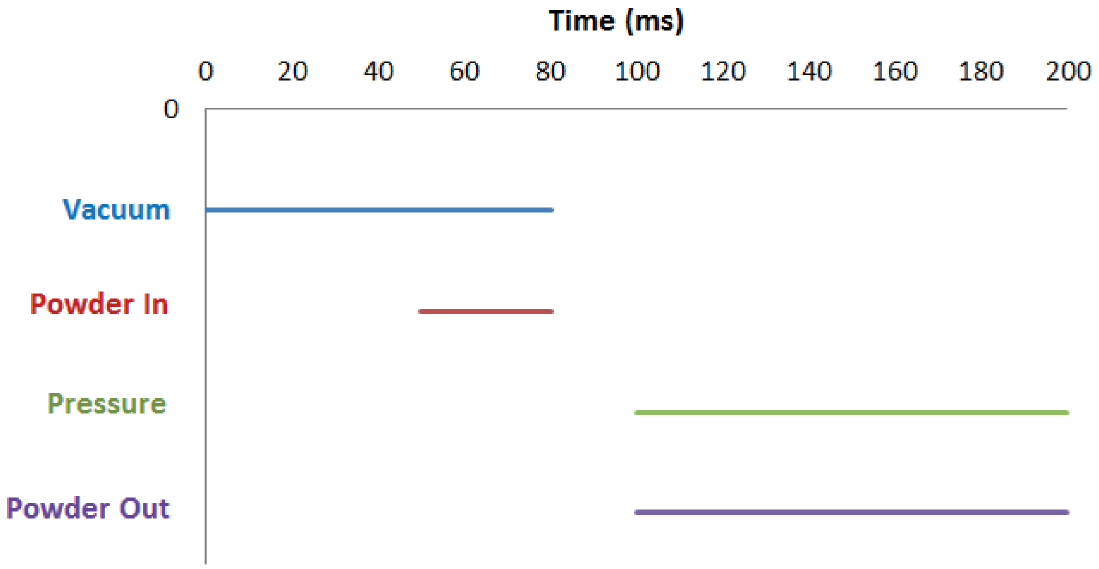

Figure 3-9. Powder feeder program in function of time over one cycle of 200 ms.

The feed rates were measured by collecting powders in a closed container for 3 min. The powder transport channel was disconnected from the nozzle and linked to the closed container. The collected powder was then weighted, and the feed rate was averaged on the 3 minute collection. Monitoring of the powder feed rate in time is presented in Chapter 5.1.1.

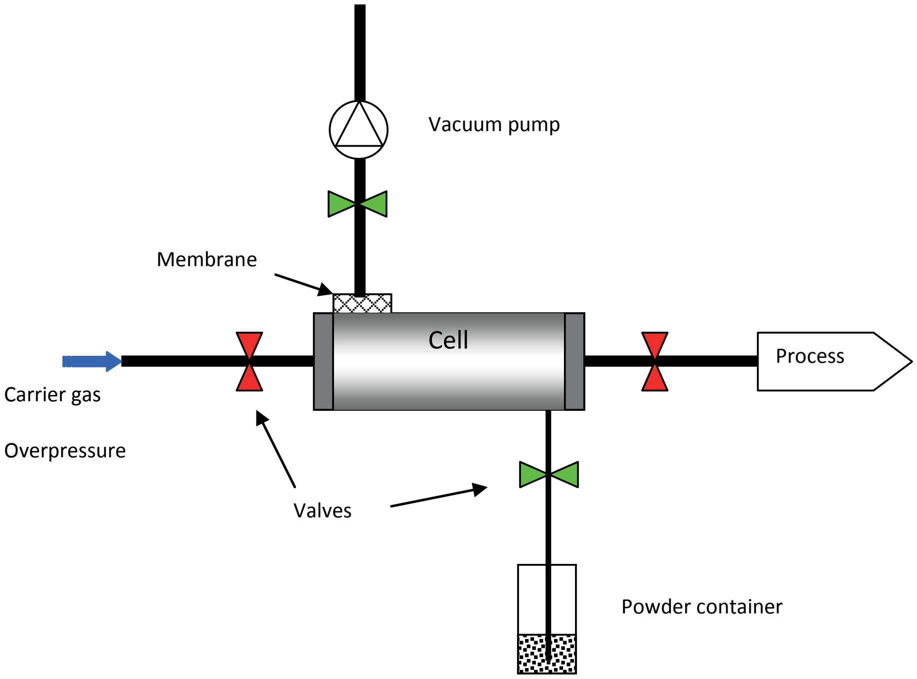

Figure 3-10. Schematic of the powder feeder system principle

3.2.9. Remote Control and Code

The pillars building stage parameters (start and final position, speed), ramping power trigger, laser and powder trigger could be programmed through the software TwinCAT via a coding interface. Programming especially ensured that triggering of events was coordinated in time. First, the laser was triggered, followed by the powder feeding. After powder feeding was triggered, the stage was programmed to move downwards at a constant speed. When the stage has completed its displacement, laser and powders were switched off. The position of the starting point of the laser was chosen beforehand.

The laser parameters such as power per pulse, pulse duration, repetition rate, ramping power, ramping pulse duration and ramping time were chosen on the laser interface.

3.2.10. Printed Structures

The laser started operation before the powders were injected to create a melt pool. The laser and the heating stage were switched off after growth of the Si-pillar, and the substrate was cooled down to room temperature.

We chose to focus on a simple geometry to be able to study the feasibility and understand the process parameters influence on DLM of silicon. Therefore, all printed samples were pillars of high aspect ratio and only the z axis of the stage was moved during pillar building.

3.3. In-Situ Observations

3.3.1. High-Speed Imaging

High-speed imaging was used to observe in situ parts of the DLM process.

The high-speed camera was a Videal Motion Pro Y4S3. The objective used for the observation was a Makro-Planar T* 2.0/100 mm f2 by Carl Zeiss, Germany. Its minimum focusing distance was 44 cm. The software used to record the data was Motion Studio 64 bit. The camera was triggered manually before the beginning of the observed process. The camera recorded light intensity mainly in the visible, but also in the near infrared region (Figure 3-11).

The high-speed camera was used in different configurations described in the following according to the different parts of the process observed in our study.

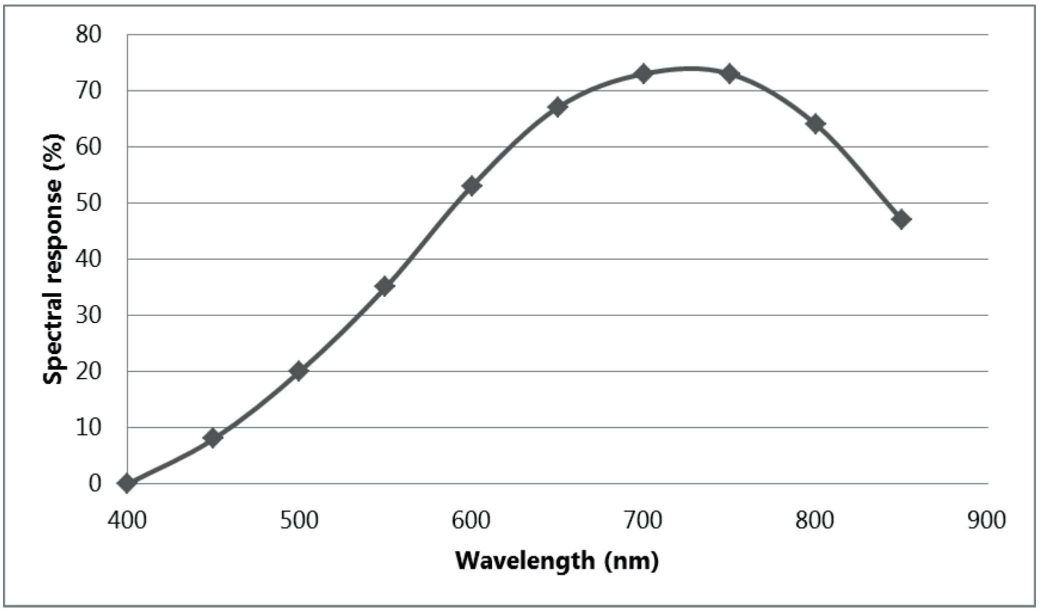

Figure 3-11. Spectral response of the camera sensor (copied from Videal (Motion Pro Y4 series)

3.3.1.1. High-speed imaging of the melt pool on a wafer during laser irradiation

Figure 3-12 describes the high-speed camera setup used to observe temperature variations of the melt pool during the laser irradiation on a Si-wafer.

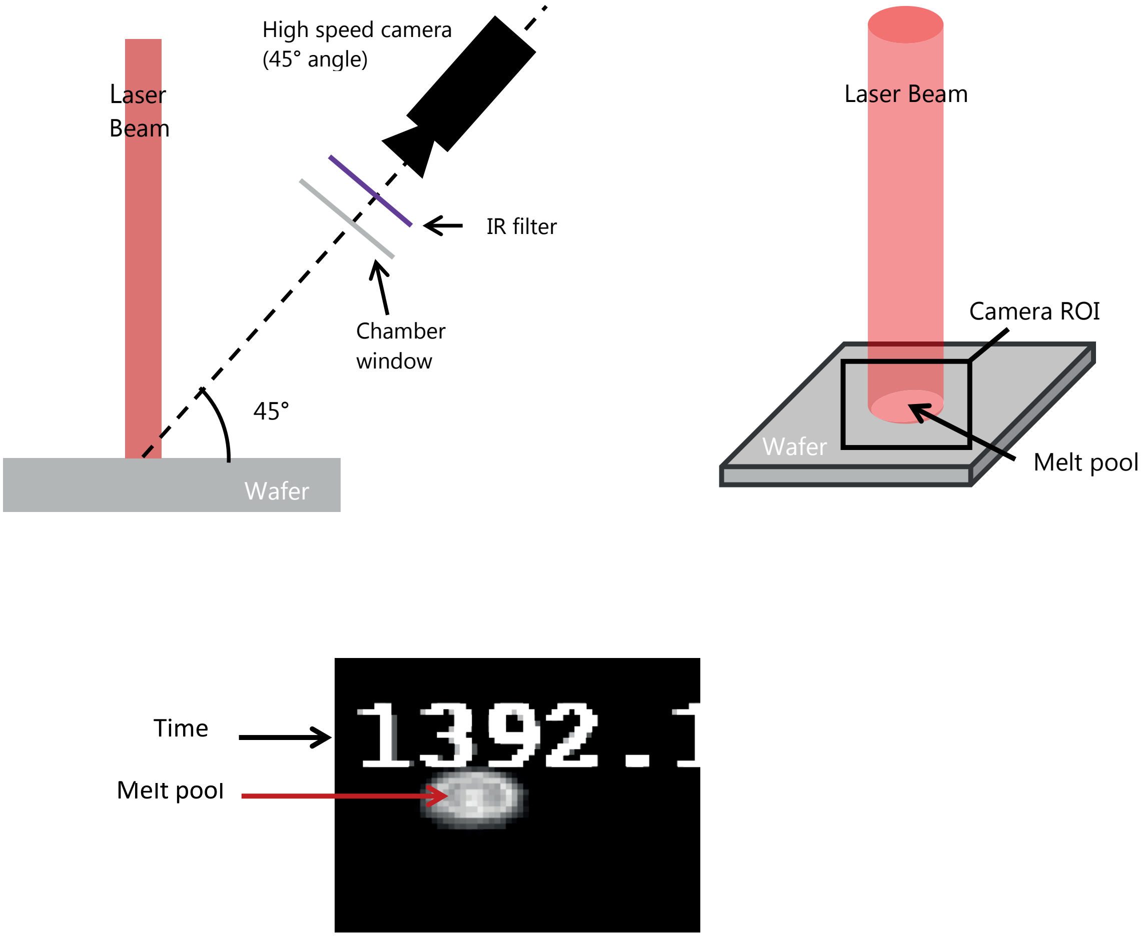

Figure 3-12. Schematic of the setup configuration for observation of the melt pool on a Si wafer during laser irradiation (a) side view and (b) region of interest recorded by the camera, from the point of view of the camera and (c) typical melt pool image, with indication of time (in ms).

The objective of the camera was set to an aperture f8 (focal length to aperture diameter ratio equal to 8). The camera was placed at the entrance port of the chamber at an angle of about 45° compared to the wafer substrate (Figure 3-12). Observations were carried out at the level of the melt pool formed on the wafer. The camera settings were fixed to an exposure time of 10 µs. The size of the region of interest (ROI) was 64x48 pixels, which enabled us to record images at a frequency of 70 kHz. The observable temperature window was a couple of hundred degrees as fixing the exposure time of the camera sensor results in capturing only a restricted window of light intensities.

A shortpass filter FESH1000 (Thor Labs, USA) was used to cut-off the wavelength of the laser reflected light and observe the melt pool. Its spectrum is shown on Figure 3-13. The filter was placed between the camera and the window of the chamber through which the observation was made.

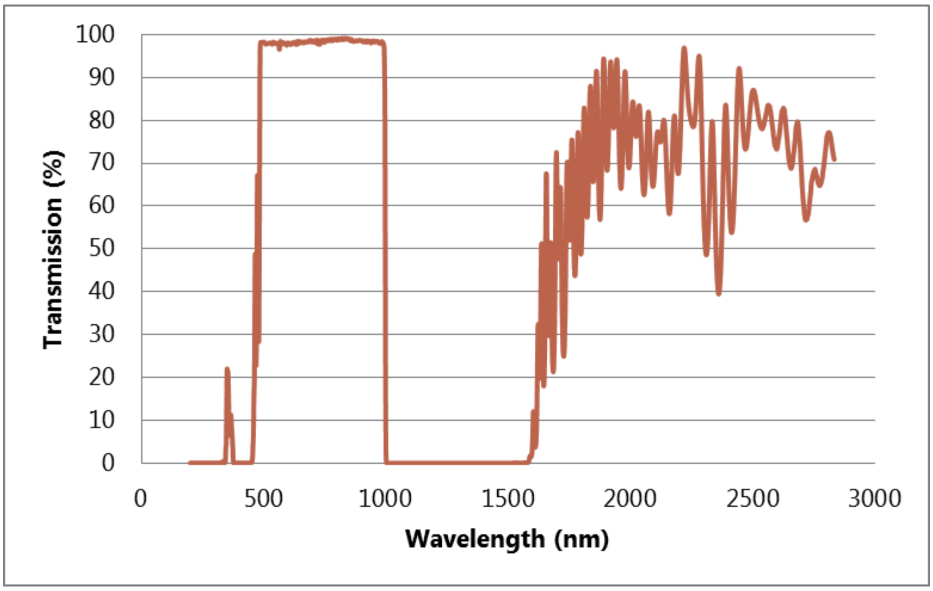

Figure 3-13. Transmission spectrum of the hard-coated shortpass filter FESH1000.

After recording, a set of 8-bits black and white images was obtained and they were analyzed with the software Image J. Black and white pictures were recorded, and the grey level of each pixel of the image was indicated by a number between 0 for black and 255 for white. For the analysis, the level of grey of one pixel of the melt pool was plotted as a function of time. The temperature increase is directly proportional to the brightness of the pixel. Thus, one can follow the temperature evolution during the illumination process.

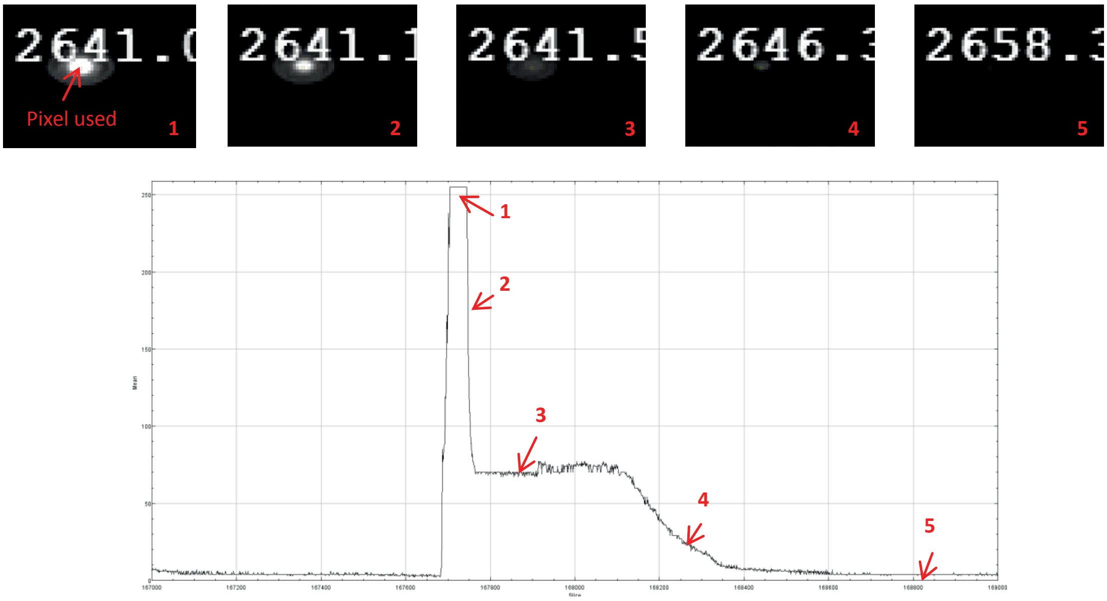

Figure 3-14. Schematic examples of a laser melt pool illuminated by the laser at different times. The pixel chosen for the analysis was located at the center of the melt pool. As temperature increases, the brightness of the pixel increases as well.

3.3.1.2. High-Speed Imaging of the Pillar during Pillar Building

Another setup configuration was used to observe pillars during the building process. In this configuration, the camera was set perpendicularly to the nozzle – pillar plane. In this way, the pillar building rate was observed as the stage was moving in the z direction. The same optical setup as previously discussed was used, with apertures varying from f8 to f11 to obtain a correct depth of field. The images were recorded with a frequency of 100-300 Hz. Small exposure times of 52 µs were used to observe building rate of the Si-pillars. Figure 3-15 shows the setup configuration, for which the main components are described in the figure. Figure 3-16 shows a typical image of a high-speed camera acquired during a pillar construction. The brightness of the pillar is a function of the camera exposure time. Each exposure time gives access to a certain range of temperatures that can be visualized within the window given by the pixel level of grey ranging from 0 to 255. In this case, the maximum level of grey 255 reaches a temperature smaller than the melting temperature. Therefore, saturation at 255 does not necessarily represent liquid state.

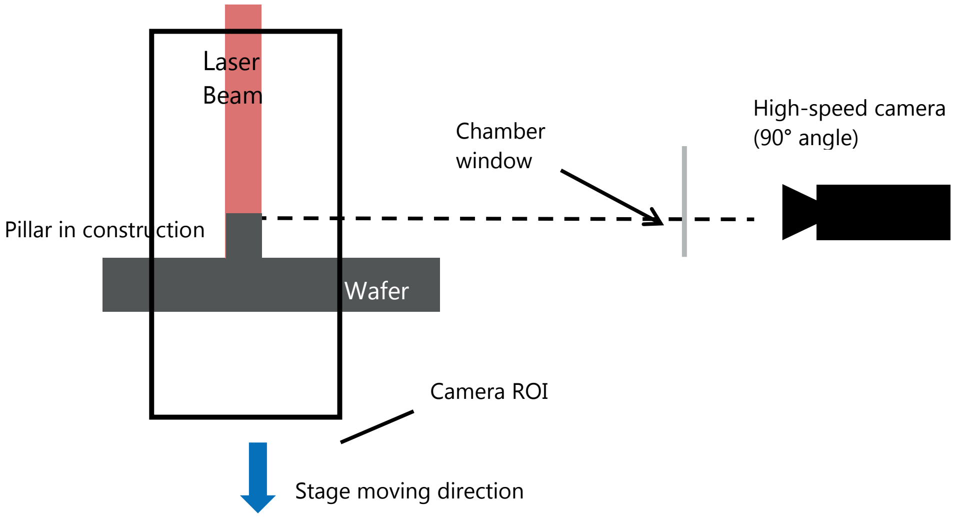

Figure 3-15. Schematic of the high speed camera configuration during pillar building observation.

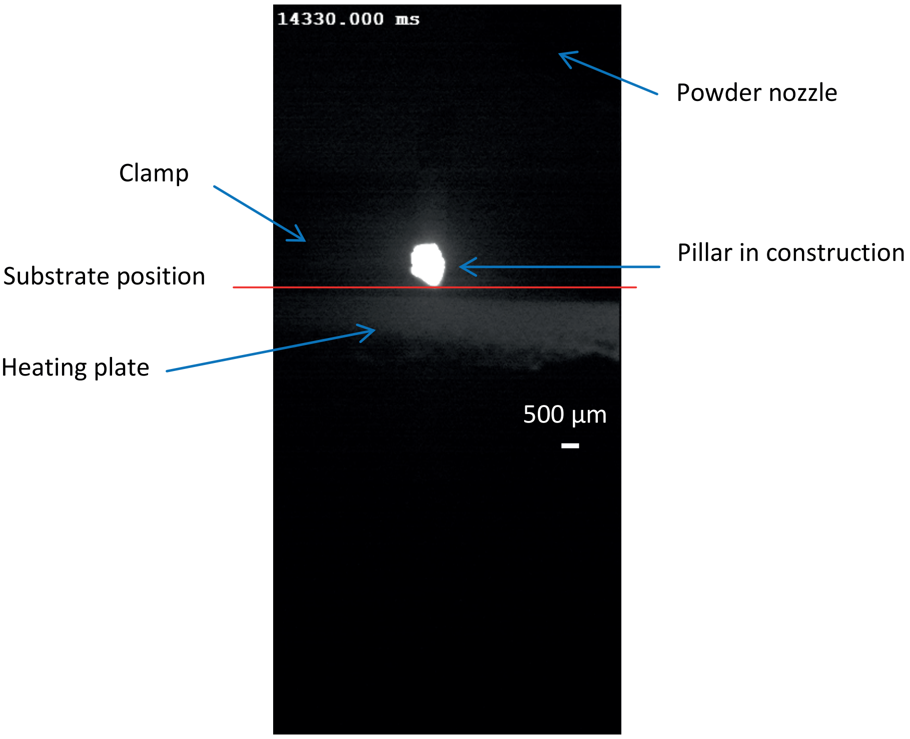

Figure 3-16. Typical high speed camera image taken during pillar building

To measure the building speed, we measured the height of the pillar for each selected frame using the software Image J. The height reference was the wafer thickness, which was 525 µm.

3.3.1.3. High-Speed Camera Recordings and Image analysis of the feed rate individual powder bursts

The high-speed camera was triggered manually before the starting the powder delivery. The aperture of the objective was set to f2. The high-speed camera recorded pictures at a rate of 200 Hz with an exposure of 3533.9 µs and total duration of 30 seconds for each measured feed rate.

The exact position of the high-speed camera is described in Figure 3-17. The high-speed camera was set at a 90° angle compared to the nozzle axis. The region of interest selected for the recordings is presented on Figure 3-18, as well as a typical picture recorded by the high-speed camera during the measurement. In order to make the powder bursts visible on the camera recordings we used the halogen lamp Intralux 4000 (Volpi, Switzerland) that emits in same spectral range as the sensitivity spectral range of the camera used in our recordings.

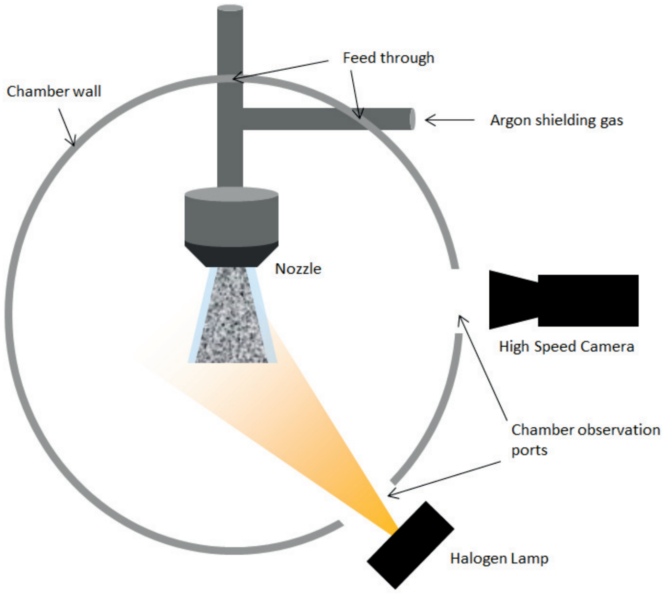
Feed through
Chamber wall
Argon shielding gas
Nozzle
High Speed Camera
Chamber observation ports
Halogen Lamp

Figure 3-17. Schematic top view of the experimental configuration inside and outside the chamber. The high speed camera was set at 90° angle compared to the nozzle axis. The lighting system was set up through another observation port of the chamber

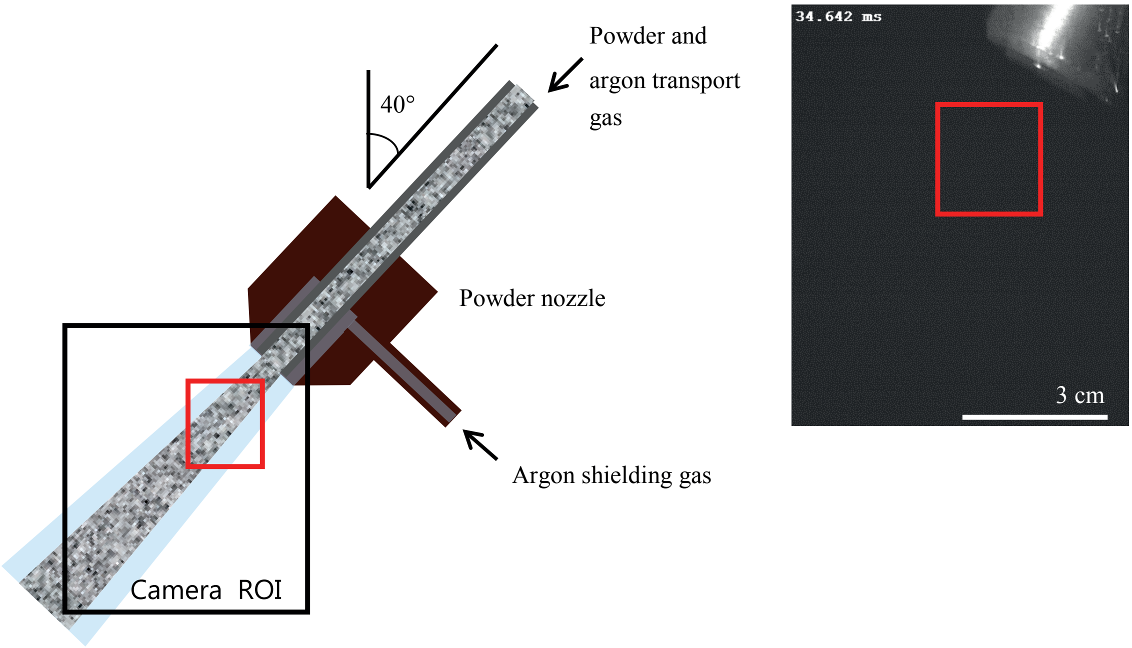
40°
Powder and argon transport gas
Powder nozzle
Argon shielding gas
Camera ROI
34.642 ms
3 cm

Figure 3-18. (a) Schematic of the region of interest (ROI) selected on the camera image to record the movies. (b) Typical picture obtained with the camera recording. The red box indicates the area for which the light intensity profile taken into account during the powder burst for image analysis

Additionally, bulk silicon reflects 30%-50% of the incident light in the visible spectral range[98]. This property was used to record the diffusion reflected light by the powder with the high speed camera.

To detect the reflected light from the powder bursts, the halogen light source was placed on the same side as the high speed camera as shown in Figure 3-17.

The powder feeder delivered powder in the form of pulsed bursts (see Chapter 3). Those bursts were observed during powder feeding with a high speed camera. Indeed, a burst that contains more powder appears brighter in the picture. This is due to less diffuse transmission and more diffuse reflection of the halogen lamp light by the powder burst. An in-house Matlab program was used to analyze the acquired images. The average pixel intensity in an area where powders appeared was compared to the average pixel intensity of a background area where no powders were present. The grey level of this area was plotted as a function of time (frame number, as presented in Figure 3-19). The integrated area below the curve corresponded to the measured mass of the powder bursts. Knowledge of the feed rate values allowed for the estimation of the individual powder burst weight. As the total mass m of the powder used during the measurement, the total area corresponding to all the powder bursts together *A* and the individual area below the curve corresponding to individual powder bursts A_i measured by image analysis were known, the weight of the burst m_i was the following:

$$m_i = \frac{A_i m}{A} \qquad (3\text{-}1)$$

The movie was recorded during 30 s of powder bursts for each feed rate condition. Even if the diffuse reflectance of the powder was enough to be able to measure the powder bursts volume, the collected light intensity was quite low and the measured intensity profiles were noisy (Figure 3-19).

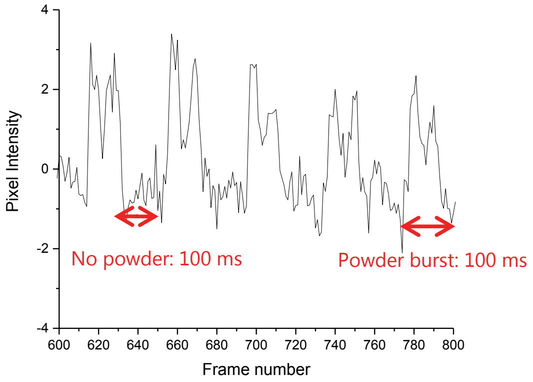

Figure 3-19. Typical plot of pixel intensity vs. frame number during image analysis. Areas with powder bursts were measured and individual powder burst weight was calculated.

3.4. Powder Characterization

3.4.1. Particle Size Analysis

The particle size distribution of Si_98% was analyzed by HELOS&RODOS Laser Diffraction Sensor of Sympatec GmbH. The shape factor was considered 1 during the measurements.

The particle size distributions of both Si_98% and Si_4N were analyzed using image analysis.

3.4.2. Particle Morphology

The morphology of the particles was observed by HR-SEM (Hitachi S-4800). A small quantity of powder was placed on a carbon tape. The acceleration voltage was 1.5 kV and the beam current was 10 µA.

3.4.3. Powder Flowability

The flowability of the powders was characterized by measuring their flow rate (g/s) through funnel orifices of different diameters, similarly to Hall flow testing[99]. The orifice diameters used were 2.5, 5, 8, 12 and 18 mm. About 30g of powder was weighted and placed into the funnel. A dry finger was blocking the orifice to prevent powder from discharging. A chronometer was triggered at the moment the finger was removed from the orifice and stopped when the last powder particles flows out of the orifice. The measurement was repeated three times, and the average flow rate was calculated.

3.4.4. Impurities

3.4.4.1. Metallic Impurities

The impurity contents in Si_98% and Si_4N powders were quantitatively analyzed by Glow Discharge Mass Spectroscopy (GDMS) by EAG Laboratories, France. Ultra-pure argon was introduced in the cell containing the sample. A voltage of 1 kV was applied between the sample (cathode) and the cells body (anode) to form an argon plasma. The Ar-ions were bombarding the surface of the sample. The sample material was then ionized to its atomic species and the latter were separated using their ratio between mass and charge in a magnetic field after acceleration by voltage difference. Two detectors were used: a Faraday detector for ionic currents above 5.10^{-13} A and a Daly detector for weak currents between 10^{-19} A and 5.10^{-13} A. The powder samples were pressed together with a binder (Indium) prior to the measurement. Impurities present in the binder were deducted from the total number of impurities measured in the sample.

3.4.4.2. Oxygen

The oxygen content in the powders was determined by combustion and infrared analysis using a LECO TC-500. Prior to the measurement, the powder was loaded in a tin capsule with nickel chips to lower its fusion temperature. The sample was then melted with an electrode in a graphite crucible. The oxygen level was detected as concentration of CO_2 after reaction with the graphite crucible by quantitative infrared analysis.

3.5. Pillar Characterization

3.5.1. Preparation for Observations of Pillar Cross-Section: Embedding

The pillars were embedded in a resin (7x SpeciFix Resin and 1x SpeciFix Curing Agent, Struers) for grinding and polishing. Flexible rubber molds with 3 cm diameter were used to facilitate demolding of the samples.

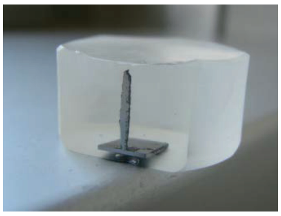

Figure 3-20. Photo of a pillar embedded in resin, grinded and polished to reveal its cross-section.

3.5.2. Preparation for Observations of Pillar Cross-Sections: Grinding and Polishing

Grinding was carried out manually using a grinding wheel and silicon carbide abrasive paper (WS FLEX 18 C, Hermes), using grids ranging from 180 to 4000. Then, final polishing was also done manually with slurry containing 1 µm diamond particles, following by a polishing emulsion containing 0.04 µm silicon dioxide particles. The samples were cleaned with water and ethanol and dried using a pressurized air stream. The aspect of the cross-section was checked between polishing steps to track the formation of polishing cracks. It is important to eliminate or reduce the surface roughness so that correct crystallographic and chemical information can be extracted using SEM, EDX and EBSD analysis.

3.5.3. Scanning Electron Microscope (SEM) Observations

All SEM observations were performed with a high resolution SEM Hitachi S-4800. The areas around the sample were painted with silver paint to avoid charging of the sample.

SEM observations of the pillar microstructure in cross-section were carried out with an acceleration voltage of 10-15 kV and a beam current of 10 µA. The observation was done in secondary electron mode.

SEM observation of the morphology of the pillar was carried out with an acceleration voltage of 1.5 kV and a beam current of 10 µA.

3.5.4. Energy Dispersive X-ray Spectroscopy (EDX)

The EDX analysis was performed using an EDX detector from EDAX, USA, mounted in the Hitachi S-4800 SEM chamber. The measurements were carried out with an acceleration voltage of 10-15 kV and a beam current of 10 µA.

3.5.5. Electron Back Scatter Diffraction (EBSD)

The samples were embedded in a resin and polished as described above. The areas around the samples were painted with silver paint to avoid electron charging during the measurement.

The microstructure of the pillars was probed with an EBSD detector (TSL, TexSEM Laboratories, Inc., USA) mounted in a SEM chamber (DSM 962, Zeiss, Germany). The EBSD maps were obtained with an acceleration voltage of 15-20 kV, a beam current of about 3 µA, at a working distance of 14-16 mm. The background was always recorded on the silver paint or the resin as close as possible from the sample. The EBSD maps were realized by measuring the Kikuchi patterns point by point with a 2-7 µm step size.

The obtained images are always presented with their crystallographic orientation oriented in the direction perpendicular to the wafer surface.

3.5.6. Stress Measurement: Raman Spectroscopy

Raman spectroscopy was used to measure the residual stresses in the Si wafers after laser illumination. Raman spectroscopy measurements were carried out using an upright ND-MDT NTEGRA Raman microscope. A 532 nm laser was used in combination with a microscope objective x100 and a numerical aperture of 0.95. The laser power was kept under 100 µW by using a neutral density filter placed below the microscope objective. The beam diameter was about 1 µm.

Raman spectra were extracted with a step size of about 4 µm along the predefined scan-line at surface of the sample.

The spectra were recorded at each point with 20 to 50 s acquisition time and a spectral resolution of 0.86 cm^{-1} in wavenumber. After the measurements, the obtained spectra were fitted using a lorentzian peak with the software MagicPlot (Magicplot Systems, LLC, Russia) to determine the Raman shift. Only the main silicon peak at around 520 cm^{-1} was considered in these measurements.

Prior to measurement, the samples were etched with a HNA reagent (20 mL HF 49%, 35 mL HNO_3 65% and 55 mL glacial acetic acid) for 5 min with an etching rate of 3-5 µm/min.

3.6. Modeling of the Laser Heating and Building process

Finite element modeling of the process was conducted using the commercially available finite element simulation software Abaqus 2017 (reference to Abaqus). Two models were realized:

- The first physical model simulated only the beginning of the process, when the wafer is only illuminated by the laser (no introduction of powders). The temperature and stress fields were calculated.
- The second model simulated the building of the pillar. The thermal field was calculated for different pillar heights.

3.6.1. Configuration 1: Si wafer Illuminated Perpendicularly with a Laser Beam

3.6.1.1. Geometry

The model used was an axisymmetrical 2D model, centered around the z axis. A schematic of the problem is given in Figure 3-21. The laser was illuminating the wafer substrate perpendicularly. The wafer was 525 µm thick and had a cylindrical area of 4 mm diameter and 1 mm thickness. The laser energy input on the Si-wafer was modeled using a surface heat source with a standard Gaussian profile:

$$S_l(r) = \frac{2P}{\pi r^2}\exp(-2\frac{r^2}{r_0^2}) \qquad (3\text{-}2)$$

Were P is the laser power and r_o is the radius of the laser beam (in this case 300 µm).

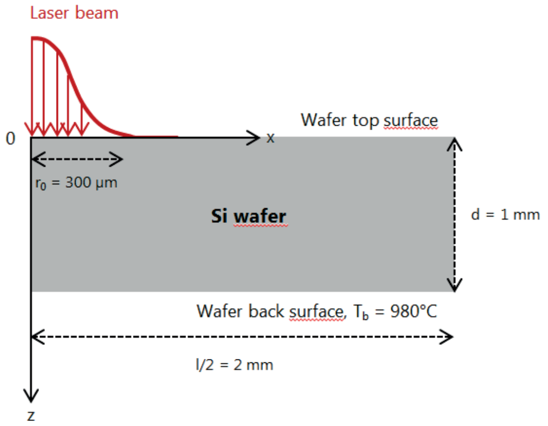

Figure 3-21. Schematic of the silicon wafer illuminated by the laser. r_0 is the laser beam radius, d is the thickness of the wafer, l is the total diameter of the wafer piece. The model is axisymmetrial around the z axis.

3.6.1.2. Assumptions

- The material was considered isotropic and homogenous
- The wafer dimensions are large enough that no border effect is expected
- The temperature at infinite distance z from the wafer surface is room temperature
- Convective flow effects due to temperature dependent surface tension in the liquid pool (Marangoni effect) were neglected because the beam was stationary.

3.6.1.3. Theory and Boundary Conditions

The temperature field T(r,θ,z,t) as a function of spatial coordinates and time satisfies the partial differential equation of heat:

$$\frac{1}{r}\frac{\partial}{\partial r}\left(rk_r(T)\frac{\partial T}{\partial r}\right)+\frac{1}{r^2}\frac{\partial}{\partial \theta}\left(k_\theta(T)\frac{\partial T}{\partial \theta}\right)+\frac{\partial}{\partial z}\left(k_z(T)\frac{\partial T}{\partial z}\right)+S(r,\theta,z,t)=\rho C_p(T)\frac{\partial T}{\partial t} \qquad (3\text{-}3)$$

Where $S(r,\theta,z,t)$ is a heat source or sink (W/m^3), $k(T)$ thermal conductivity of silicon (W/mK), $C_p(T)$ volumetric specific heat (J/m^{3}K), ρ is the density of silicon (kg/m^3). In our study, both $C_p(T)$ and $k(T)$ are function of temperature, and thus equation 1 is nonlinear. For simplification of the model, ρ only changes when a change of phase from solid to liquid is undergone.

A domain Ω was defined where the wafer was enclosed. The boundaries of the domain Ω satisfied Dirichlet or Neumann boundary conditions.The bottom of the wafer in contact with the hot plate was subjected to the following Dirichlet boundary condition:

$$T(x,y,z,t)=T_1(x,y,z,t) \qquad (3\text{-}4)$$

on the boundary at t > 0.

The bottom of the wafer was assumed to be in perfect contact with the hot plate.

The rest of the wafer surfaces were subjected to the following Neumann boundary condition:

$$Q(r,\theta,z,t)=Q_{cond}+Q_{conv}+Q_{rad}+Q_{laser} \qquad (3\text{-}5)$$

$$Q_{cond}=k_n\frac{\partial T}{\partial n} \qquad (3\text{-}6)$$

$$Q_{conv}=h(T-T_0) \qquad (3\text{-}7)$$

$$Q_{rad}=\sigma_{SB}\varepsilon(T^4-T_0^4) \qquad (3\text{-}8)$$

$$Q_{laser}=\begin{cases}\frac{P_\tau}{A_{laser}}\alpha_{abs}g(r)i(t) & during\ \tau\\ 0 & during\ \frac{1}{f}-\tau\end{cases} \qquad (3\text{-}9)$$

Q_{cond} are the thermal losses by conduction through the wafer substrate, k_n thermal conductivity normal to the boundary of Ω.The thermal conductivity of silicon as a function of temperature is given in Chapter 2.5.2.

Q_{conv} represents the thermal losses by forced convection of the argon protective gas on the wafer surface and h corresponding heat transfer coefficient (W/m^{2}K). The convection coefficient h of a round jet of argon impinging on a flat surface at 300 K was calculated with the following equations (Bergman et al.[100]):

$$\frac{Nu}{Pr^{0.42}} = G[2Re^{0.5}(1 + 0.005Re^{0.55})^{0.5}] \qquad (3\text{-}10)$$

$$G = \frac{D_h}{r_c} \frac{1 - \frac{1.1D_h}{r_c}}{1 + 0.1(\frac{H}{D_h} - 6)(\frac{D_h}{r_c})} \qquad (3\text{-}11)$$

$$Nu = \frac{hD_h}{k} \qquad (3\text{-}12)$$

$$Re = \frac{\rho D_h U_{jet}}{\mu} \qquad (3\text{-}13)$$

$$Pr = \frac{c_{P_{Ar}} \mu}{k} \qquad (3\text{-}14)$$

Nu, Re and Pr respectively correspond to the Nusselt, Reynolds and Prandtl numbers. Nu is the ratio between convective and conductive heat transfer at the interface between the fluid and the surface. Re is the ratio of inertial to viscous force within the gas. It gives an indication if the flow is laminar or turbulent. Pr is the ratio between the viscous diffusion rate and the thermal diffusion rate, The corresponding symbols and parameter values are given in Table 3-5 and Table 3-6. After calculation, $h = 134\ W/m^2K$. In the simulations, we used h values in the range of 30 to 173 W/m^{2}K, and did not obtain a noticeable influence of this coefficient, as pictured in Appendice B.

Hydraulic diameter D_h	1 mm
Distance argon jet – surface H	12 mm
Cooled region radius r_c	5 mm
Jet speed U_{jet}	24 m/s

Table 3-5. Geometrical considerations of the experimental configuration

Thermal conductivity k	0.016 W/mK
Dynamic viscosity μ	2.3 x 10^{-5} Pa.s
Density ρ (300 K)	1.45 kg/m^3
Specific heat $c_{P_{Ar}}$ (300K)	520 J/kgK

Table 3-6. Properties of the argon protective gas

Q_{rad} represents the thermal losses by radiation, σ_{SB} Stefan-Boltzmann constant (W/m^{2}K^4) and ε the emissivity of silicon. The emissivity ε of solid silicon was considered constant at 0.7 (Sato et al.[94]).

Q_{laser} is the surface heat source provided by the laser (W/m^2), P the laser peak power, τ the pulse duration, A_{laser} the surface of the laser beam and f the repetition rate, R is the reflectivity, g(r) and i(t) are the spatial and temporal distributions of the laser beam. α_{abs} is the absorption coefficient of silicon. It comprises the reflectivity and the absorption. It was first calculated in function of temperature for the wavelength 1064 nm[90] [91], and taken as a constant equal to 0.45 in the simulations, the average value between the solid and the liquid phase.

$$g(r) = \exp(-\frac{2r^2}{r_0^2}) \qquad (3\text{-}15)$$

$$i(t) = 1 \qquad (3\text{-}16)$$

In addition to the boundary conditions, the initial conditions should be specified for every point in Ω:

$$T(r,\theta,z,t)_{t=0} = T_0 \qquad (3\text{-}17)$$

Where T_0 is the ambient temperature far from the wafer surface (K).

3.6.1.4. The thermomechanical equation and the brittle-to ductile transition

The realistic simulation of the strain and stress distributions in the Si-wafer under melting conditions is a very complex problem. Therefore it is necessary to introduce simplifications of the real problem with the effort to keep the most prominent characteristics of the problem in the simplified model.

At temperatures ranging from 500 to 800°C, Si undergoes a brittle-to-ductile transition (BDT). In order to model the mechanical behavior and include the BDT in the simulations, a creep law has been used. The creep becomes much higher above the BDT as a characteristic of the ductile phase.

The total strain rate can be written as the sum of the individual components of the strain rates:

$$\dot{\varepsilon}_{ij} = \dot{\varepsilon}_{ij}^{E} + \dot{\varepsilon}_{ij}^{P} + \dot{\varepsilon}_{ij}^{T} + \dot{\varepsilon}_{ij}^{cr} \qquad (3\text{-}18)$$

Where i, j and k refer alternatively to x, y and z.

The different components of the total strain rate are due to the elastic ($\dot{\varepsilon}_{ij}^{E}$), plastic ($\dot{\varepsilon}_{ij}^{P}$), temperature ($\dot{\varepsilon}_{ij}^{T}$) and creep ($\dot{\varepsilon}_{ij}^{cr}$) loading contributions. The elastic and temperature contributions are typical of an elastic behavior whereas the plastic and creep contributions are typical of a plastic behavior.

The elastic strain is expressed as:

$$\varepsilon_{ij}^{E} = \frac{1+\upsilon}{E}\sigma_{ij} - \frac{\upsilon}{E}\sigma_{kk}\delta_{ij} \qquad (3\text{-}19)$$

Where υ is the Poisson's ratio of silicon, E is its elastic modulus and δ_{ij} is the Kronecker symbol:

$$\delta_{ij} = \begin{cases} 0\ when\ i \neq j \\ 1\ when\ i = j \end{cases} \qquad (3\text{-}20)$$

The temperature strain is given by:

$$\varepsilon_{ij}^{T} = \alpha(T - T_0)\delta_{ij} \qquad (3\text{-}21)$$

The creep strain rate is defined by a creep law of the following type:

$$\dot{\varepsilon}_{ij}^{cr} = A(T)\sigma_{ij}^{y} \qquad (3\text{-}22)$$

Where n is a function of the material, and more particularly of the creep mechanism, and $A(T)$ is a function of temperature of Arrhenius type:

$$A(T) = A_0 e^{-\frac{Q_c}{RT}} \qquad (3\text{-}23)$$

Where Q_c is the activation energy for creep mechanism to occur (atomic diffusion, dislocation generation…), A_0 is a constant and R is the gas constant.

In our study, we used a simple version of the above mentioned creep law of type

$$\dot{\varepsilon}^{cr} = A(T)\sigma^{y} f(\varepsilon^{cr}) \qquad (3\text{-}24)$$

Where σ is the uniaxial equivalent deviatoric stress, $f(\varepsilon^{cr}) = 1$, y is an exponent depending on the creep mechanism, and $\dot{\varepsilon}^{cr}$ is the uniaxial equivalent creep strain rate defined as the scalar product of the strain rate tensors:

$$\dot{\varepsilon}^{cr} = \sqrt{\frac{2}{3}\dot{\varepsilon}_{ij}^{cr} : \dot{\varepsilon}_{ij}^{cr}} \qquad (3\text{-}25)$$

3.6.1.5. Modeling of the liquid state

Si was considered to be liquid above 1687 K. The transition from solid to liquid silicon was modeled by integrating the effect of the latent heat of fusion to the heat capacity equation. The heat capacity is expressed by:

$$C_P(T) = \frac{\partial H(T)}{\partial T} \qquad (3\text{-}26)$$

$$C_P(T) = C_{P(sol)}(T) + C_{P(liq)}(T) + \frac{L_{fus}}{\Delta T} \qquad (3\text{-}27)$$

Where $C_{P(sol)}(T)$ and $C_{P(liq)(T)}$ are the temperature dependent heat capacity of the silicon solid and liquid phases respectively, L_{fus} is the latent heat of fusion and ΔT is the interval of temperature over which the change of phase occurs. In the case of a pure material like silicon, the liquefaction occurs at a constant temperature. However, for modeling purposes, in our model $\Delta T = 5K$. The heat capacity of silicon as a function of temperature is given in Chapter 2.5.2.

The stress in the liquid phase should be extremely small. Therefore, the temperature dependent yield strength of the material was artificially dropped to 10 MPa at 1687 K.

3.6.1.6. FEM Method

In the finite element method (FEM) a picewise linear function or polynomial is used to approximate the temperature field within each element:

$$T(x,y,z,t)=\sum_{i=1}^{nodes} N_i(x,y,z)T_i(t) \qquad \text{(3-28)}$$

Where N_i are basis functions dependent only on type of the element and it size. The nodal temperatures at time t are denoted by $T_i(t)$. The $T_i(t)$ are undetermined coefficients of the equation (3-28). By defining the mesh we define the basis functions Ni. Many different types of elements are possible, like four and eight node quads for 2D. The eight node and twenty node brick elements are used for 3D simulations.

In Abaqus simulation software we have a large library of the available elements. All elements in the Abaqus have a name that identifies the primary characteristic of the element as shown in Figure 3-22.

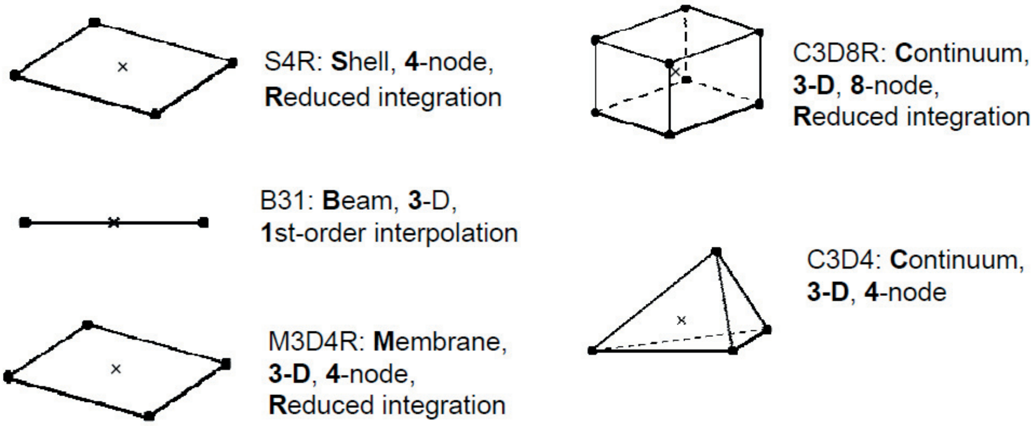
S4R: Shell, 4-node, Reduced integration
C3D8R: Continuum, 3-D, 8-node, Reduced integration
B31: Beam, 3-D, 1st-order interpolation
C3D4: Continuum, 3-D, 4-node
M3D4R: Membrane, 3-D, 4-node, Reduced integration

Figure 3-22. The element name identifies the primary element characteristics.

The evaluation of the $T_i(t)$ is done using the Galerkin FEM method[101]. If the approximation in equation (3-28) is substituted in the main heat equation a residual term should be added, otherwise the equation (3-28) would be exact solution of the heat problem. Thus the residual term should be zero as required by the Galerkin method:

$$\int \varepsilon N_i d\Omega = 0 \qquad \text{(3-29)}$$

Since there are i-nodes in the computational domain, equation (3-29) creates i ordinary differential equations which are integrated to form a set of nonlinear equations:

$$[K][T]=[R] \qquad \text{(3-30)}$$

where [K] is effective conductivity matrix and [R] is effective thermal load. The equation (3-30) is solved for the vector [T].

The FEM programs implement various forms of a Newton-Raphson solver, together with a direct matrix solver which are in more detail described in [101].

3.6.2. Configuration 2: Build-Up of Si Pillars

Experimentally, the laser was used as the heat source for melting the Si substrate and Si powder, which were supplied thanks to a delivery nozzle in the form of pulsed bursts while the stage was moving. In the case of our simulations, the feed rate of the Si powder was modeled as an ideal volume added to the pillar during the movement of the stage.

The geometry used was a 3D model of a cylindrical pillar with solid square wafer base, similar to the experimental setup. The laser beam was positioned vertically above the Si pillar. The silicon wafer was 1 mm thick and had an area of 8 x 4 mm. The laser energy input on the Si-wafer was modeled using a body heat source with a standard Goldak double ellipsoid heat source[102]:

$$S_c(x,y,z,t) = \frac{6\sqrt{3}Qf}{\pi\sqrt{\pi}abc}\exp\left[-3\frac{x^2}{a^2} - 3\frac{y^2}{b^2} - 3\frac{(z-vt)^2}{c^2}\right] \tag{3-31}$$

Were Q is a power of the laser, a, b, and c are respective radii of the ellipsoid, and f is a factor which describes how effective the heating process is. f takes into account absorption and reflection Similarly to the previous simulation of Si wafer heating, the above equation is implemented as function in DFLUX user-defined subroutine (Abaqus version 2017).

The Abaqus user-defined function UEPACTIVATIONVOL (Abaqus version 2017) is used to activate the elements of the pillar mesh, thus simulating constant feed rate of Si-powder supplied from the nozzle. We did not model the activation of the elements (adding volume) based on the experimentally measured value of the feed rate (Chapter 5.1.1), but rather on the stage speed. Activation of the elements is done using so called “birth element” method shown in Figure 3-23. We follow the study by Michaleris[103] where the elements are activated when the intensity of the laser beam absorbed in the element is equal to 5 % of the laser peak power.

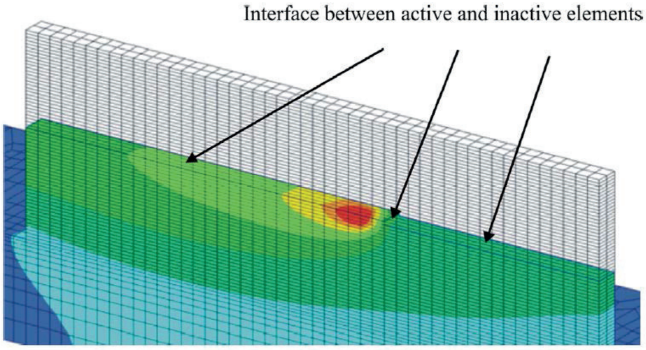

Figure 3-23. Schematic of the interface between active and inactive elements showing activation of elements using birth element method[103].

As shown in Figure 3-23, the internal interface between activated and inactive elements represents the radiation and surface convection boundary conditions. Of course, as the material is deposited, this internal surface continuously changes and correct surface and radiation boundary conditions should be applied on it. However, it was previously very difficult to implement these conditions using standard user defined routines in the Abaqus FEA code. The Abaqus version 2017 implements these boundary conditions currently only for 3D FEM mesh. Therefore, we used 3D mesh to model the build-up of the Si-pillars using the DLM.

Besides the characteristics stipulated above, the same modeling of silicon properties as for the simulations on the Si wafer was implemented, and the same equations were used.

Chapter 4. Crack Formation During Pillar Building

Before deposition of material for 3D growth, the cracking behavior of silicon has to be studied. Therefore, laser irradiation experiments and simulations were carried out on silicon wafers for understanding this behavior. Further on, by inserting silicon powder into the melt pool, parameters (substrate temperature, energy per pulse and repetition rate) were modified to establish a working window according to the cracking behavior. Crack-free samples were produced when the bottom of the substrate was preheated to more than 850°C, which corresponded to a wafer surface temperature of 730°C (included argon shielding gas) and sufficient high repetition rate of the laser pulses (> 100 Hz) was used in order to minimize the thermal gradients around the melt pool. The threshold repetition rate decreased with the feed rate.

The results presented in this chapter were all carried out on wafers of orientation <100>. Except when indicated, the wafer surface temperatures correspond to the temperature measured with argon shielding gas. Details of the simulation and experimental methods and the wafer heating characteristics are given in Chapter 3.6.1.

4.1. Results

4.1.1. Cracking Behavior on Silicon Wafers

4.1.1.1. Thermal behavior during laser illumination

First, the cracking behavior was studied exclusively on the wafer substrate, without powder deposition, which corresponds to the start of the process. Three different sets of laser conditions were mainly studied in this part: 50 Hz – 405 mJ (average power 20.2 mJ), 100 Hz – 285 mJ (average power 28.3 mJ) and 200 Hz – 160 mJ (average power 32.2 mJ). The pulse duration was 1 ms.

Figure 4-1 shows the cross-sections of wafers illuminated with two different sets of laser conditions and two different substrate temperatures. Figure 4-1 (a) and (c) refer to the conditions 50 Hz – 405 mJ with substrate surfaces set at room temperature and 730°C respectively. Figure 4-1 (b) and (d) refer to the conditions 200 Hz – 160 mJ with substrate surfaces set at room temperature and 730°C respectively. Intense brittle symmetrical cracking occurred, forming a hemisphere in the wafer for any laser condition when the substrate was kept at room temperature. Additional symmetrical cracks appeared closer to the surface in the case 50 Hz – 405 mJ for a substrate kept at room temperature, and another curved crack was observed next to the hemispheric first described crack. However, when the substrate surface was heated to 730°C, no cracks were observed for any of the two sets of laser parameters. The extent of the melt pool area could not be measured post-mortem, either by an optical microscope, SEM or EBSD. Subsequently, cross-sections of melt pools created with 200 Hz – 405 mJ were observed for different substrate temperatures ranging from room temperature to 730°C. No cracks were observed when the wafer substrate was at least preheated to 200°C.

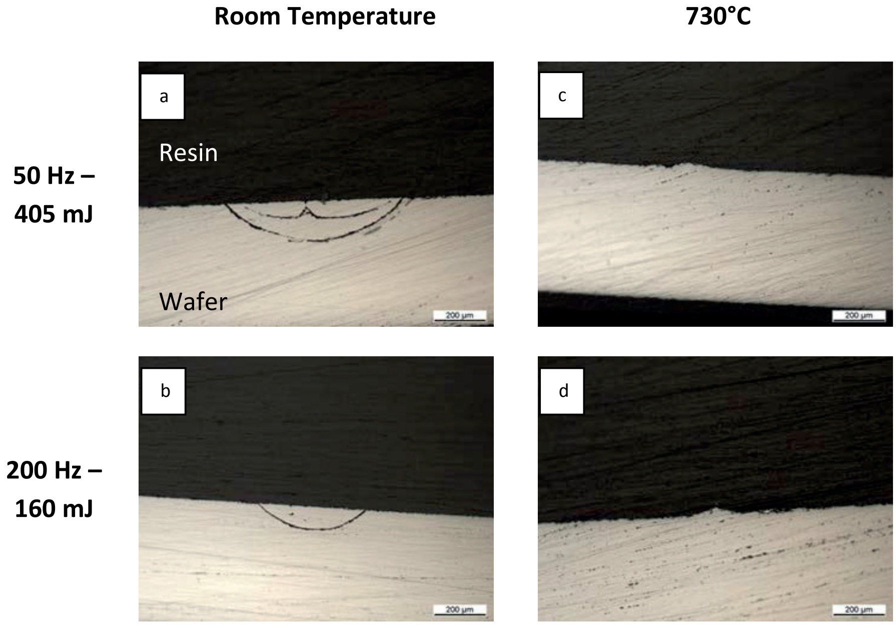

Figure 4-1. Optical microscope pictures showing cross-sections of wafers illuminated for 2s with the following laser conditions: (a) 50 Hz – 405 mJ – 1ms – substrate at ambient temperature, (b) 200 Hz – 160 mJ – 1 ms – substrate at ambient temperature (c) 50 Hz – 405 mJ – 1ms – substrate surface preheated to 730°C and (d) 200 Hz –160 mJ – 1ms – substrate surface preheated to 730°C.

The temperature variations in and out of the melt pool were resolved during laser illumination on a wafer using high-speed camera recordings. The temperature can be associated with the pixel grey level. A short-pass filter was used to cut the wavelength of the laser. Details about the experimental method are explained in Chapter 3. The results are displayed on Figure 4-2 and Figure 4-3.

Figure 4-2 shows the grey level of a pixel located at the center of the melt pool in function of time during 1.715 s of laser illumination on a wafer. The graphs displayed on the left side of the figure show a general aspect of the grey level signal in function of time for a time lapse of 1.715 s of laser illumination. The graphs displayed on the right side of the figure are a zoom on the time lapse 1.69-1.715 s. They enabled the material heating and cooling curves to be visualized over a cycle of laser processing. In all cases, rapid heating was observed at the beginning of the pulse. After pulse duration, rapid cooling occurred, followed by a solidification plateau. After solidification (in the cases where total solidification occurred), the solidified silicon cooled down. A slight increase in pixel intensity was seen at the end of each of the solidification plateau. This was due to the difference in emissivity between solid and liquid silicon, solid silicon having a much higher emissivity than liquid silicon at the melting point[95 96]. The solidification plateau increased in time with the number of laser pulses.

In the case of condition 50 Hz 405 mJ (presented in Figure 4-2(a)), a rapid temperature increase at the center of the melt pool was observed at the beginning of the illumination. About 100 ms after the first pulse, the signal saturated at 255. The melt pool solidified between each pulse, and cooled down to the zero level (dark image). A long solidification plateau of 4.5 ms was measured. Complete cooling could not be resolved due to the limited temperature window imposed by the high-speed camera parameters used.

In the conditions 100 Hz - 285 mJ (Figure 4-2 (b)) and 200 Hz 160 mJ (Figure 4-2(c)), a more progressive temperature increase at the center of the melt pool was observed, as it took more than 1.4 s for the intensity of the melt pool during the laser pulse to reach the saturation level of 255. In both cases, the minimum pixel intensity measured during the cooling phase between laser pulses increased with time and number of pulses. This minimum stabilized after about 1s of illumination, and reached 6 for 100 Hz – 285 mJ and 56 for 200 Hz – 405 mJ. In the latter case, no cooling of the solid phase was observed after 1.1 s of laser illumination (Figure 4-2(c)). The solidification plateau for the condition 100 Hz 285 mJ was 3.5 ms.

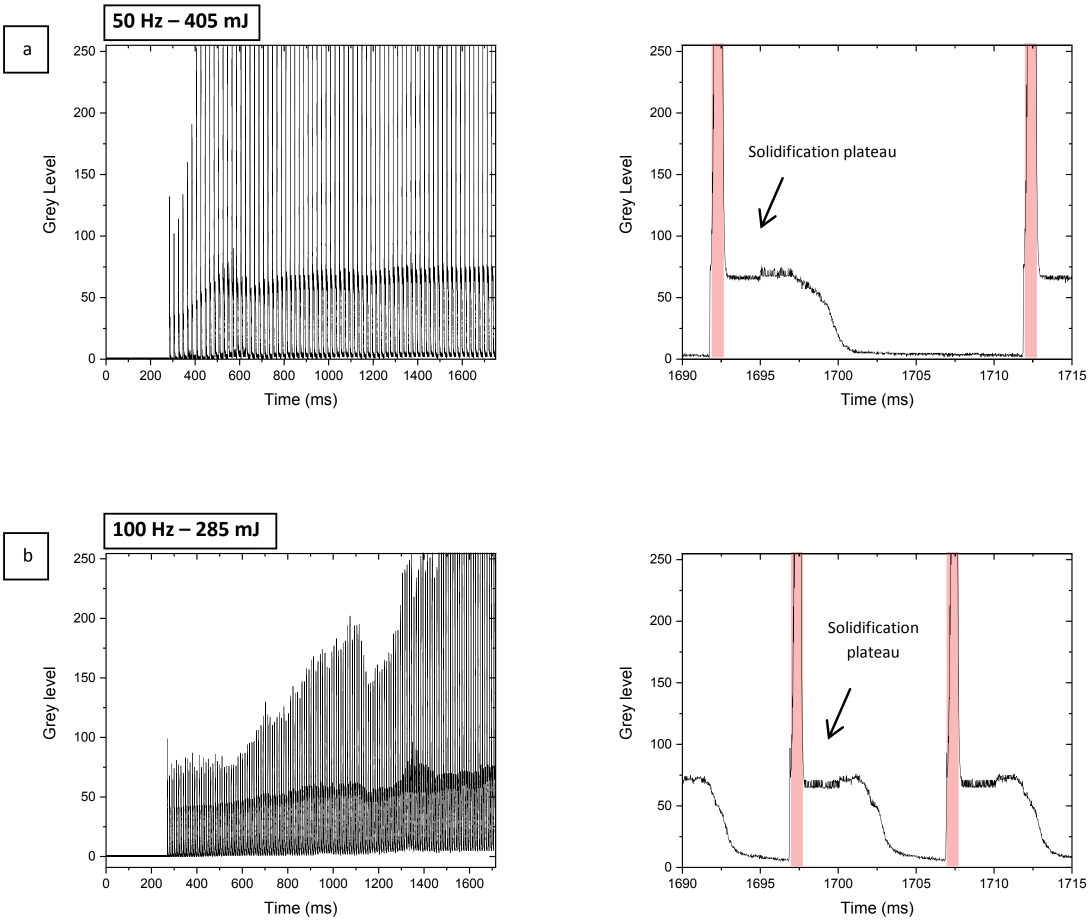

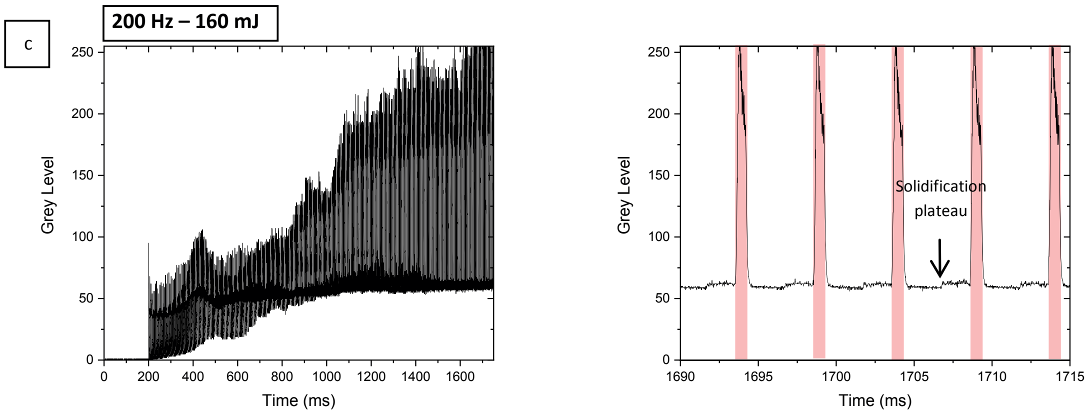

Figure 4-2. High-speed camera recordings of the signals showing the temperature variations in function of time at the center of the melt pool for a Si wafer illuminated by the laser at different conditions (a) 50 Hz and 405 mJ (b) 100 Hz and 285 mJ (c) 200 Hz and 160 mJ. The graphs on the right show a zoom on the more general graphs in order to see the shape of the emitted light intensity variations. The areas highlighted in red represent the time zones when the laser is illuminating the sample.

Figure 4-3 presents the same measurements as in Figure 4-2 for a pixel taken outside of the melt pool, at its border. The same observations as stated before were made. However, no melting occurred as the pixel chosen was located outside of the melt pool.

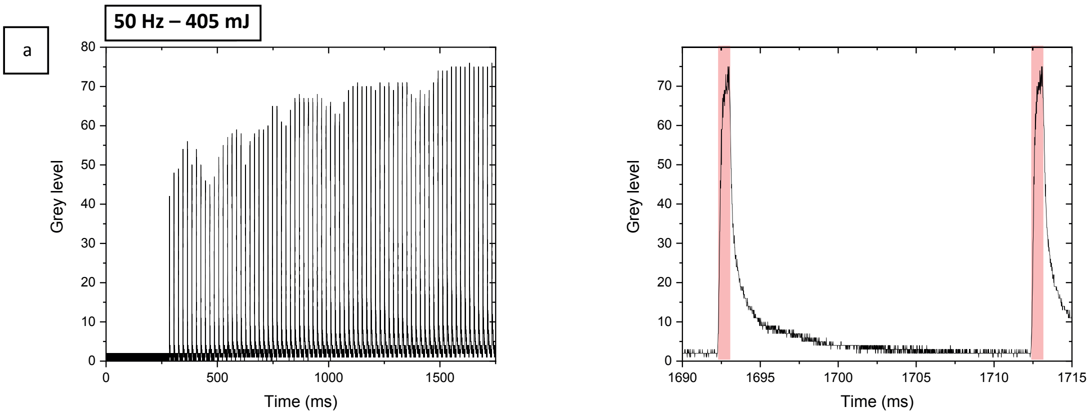

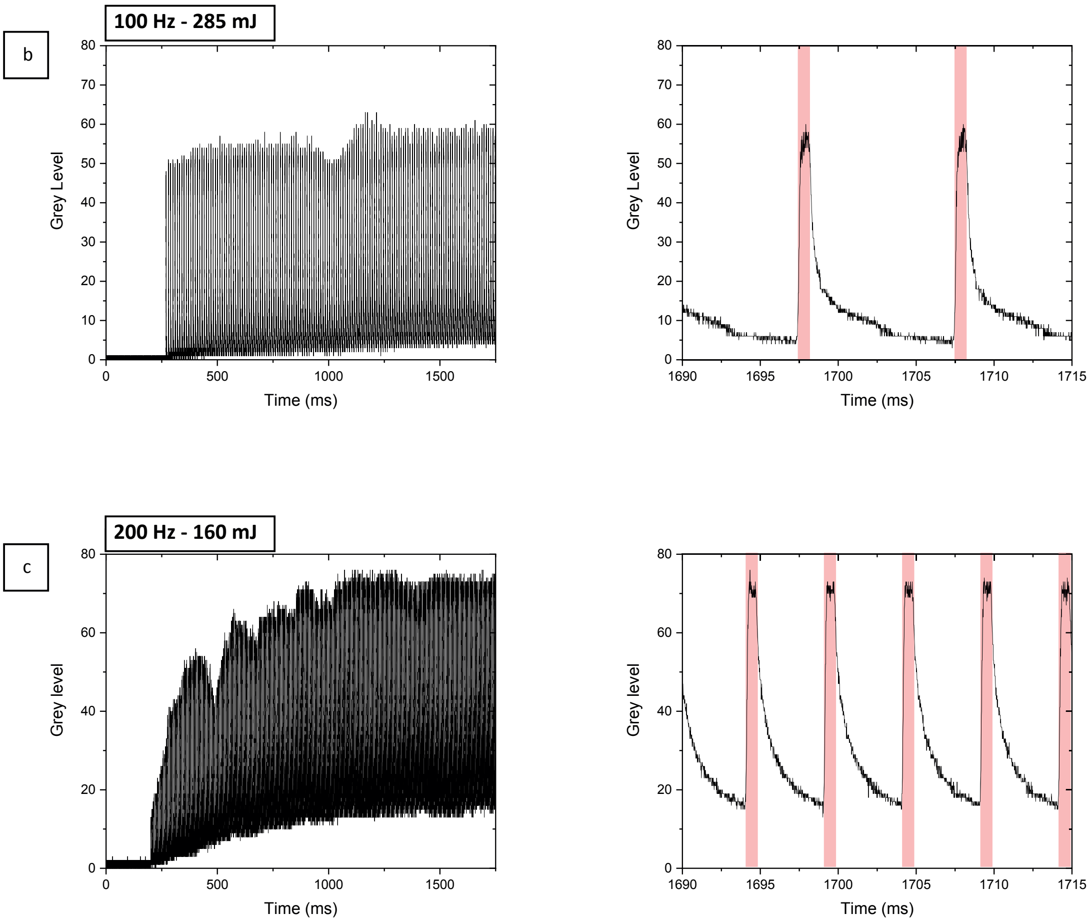

Figure 4-3. High-speed camera signals recorded for different conditions of illumination of the wafer substrate at the side of the melt pool. (a) 50 Hz - 405 mJ, (b) 100 Hz - 285 mJ and (c) 200 Hz - 160 mJ. The graphs displayed on the right show a zoom of the general graphs to be able to visualize the shape of the emitted light intensity variations. The areas highlighted in red represent the time zones when the laser is illuminating the sample.

For comparison, high-speed camera recordings of the melt pool formed on a wafer at room temperature were carried out as shown in Figure 4-4. The level of grey at the center of the melt pool was plotted as a function of time for two different conditions (50 Hz 405 mJ and 200 Hz 160 mJ). The red areas represent the time when the laser is ON. The fast temperature increase was observed at the beginning of the pulse. The short-pass filter was not used for this measurement, so the signal saturates at maximum grey level (255) during the laser pulse due to the laser intense light. The rapid cooling occurred during the time the laser was OFF until the signal reaches the zero saturation level. In both cases, the solidification plateau was hardly observed.

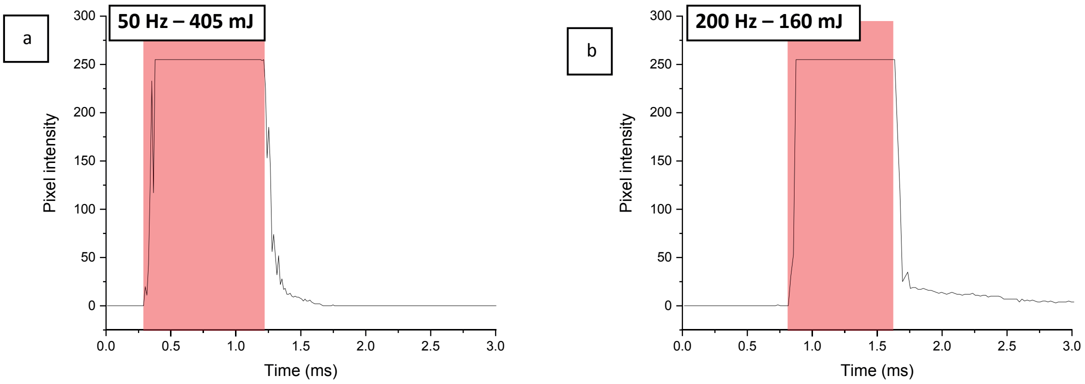

Figure 4-4. Grey level of a pixel taken in the center of the melt pool plotted in function of time for 2 different conditions (a) 50 Hz 405 mJ and (b) 200 Hz 160 mJ. In both cases, the substrate was at room temperature and the signal was recorded 1 to 2 s after the laser was on. The filter blocking the wavelength of the laser was not used in these measurements, therefore the signal always saturates at 255 when the laser is illuminating the wafer. The time zone when the laser is illuminating the wafer is indicated by the red areas.

The temporal development of the melt pool temperature was calculated by FEM simulations using Abaqus 2017 code[104]. In this model, a pulsed energy source representing the laser is brought perpendicularly to the surface of a silicon wafer. The laser beam is modeled with a Gaussian profile. Laser heating takes into account the absorption and reflection of silicon. Cooling by conduction, radiation and forced convection by the shielding gas are taken into account on the entire wafer surface. The temperature at the bottom of the substrate was set to 980°C, which corresponded to a surface temperature (with argon shielding gas) of about 900°C. This temperature was chosen because it allowed for a good agreement between the experimental and the modeled temporal temperature profiles. Details of the simulation models are given in chapter 3.

Figure 4-5 shows the temporal temperature variations in the center of the melt pool calculated by FEM for the laser conditions 50 Hz – 405 mJ (Figure 4-5(a)), 100 Hz-285 mJ (Figure 4-5(b)) and 200 Hz – 160 mJ (Figure 4-5(c)). The shapes of the temporal development of the temperature profiles are similar in the FEM calculations and in the experimental results. In each case, rapid heating occurs during the laser pulse, followed by rapid cooling of the melt pool, solidification and fast cooling of the solid. At the beginning of the illumination, the minimum temperature reached during the cooling phase rose. After 0.1 s for 50 Hz – 405 mJ, after about 0.15 s for 100 Hz – 285 mJ and after 0.25 s for 200 Hz – 160 mJ, a steady-state was reached. During this steady-state, complete solidification of the material between each pulse occurred in the case 50 Hz – 405 mJ, and the minimum temperature reached during the cooling phase was 1280 K, in the upper BDT range. The solidification duration of the melt pool was about 4 ms. In the case 100 Hz – 285 mJ, the minimum temperature reached between each pulse was 1350 K, and the solidification plateau also last 4 ms. The solidification plateau lengths are in good agreement with the experimental values of 3.5 and 4.5 ms found for the respective cases.

No cooling of the solid phase was observed in the case 200 Hz – 160 mJ. Therefore, the minimum temperature observed is 1687 K. The maximum temperature reached by the melt pool was 2500 K, well below the evaporation temperature of 3538 K. These calculations were in good agreement with the experimental results.

a

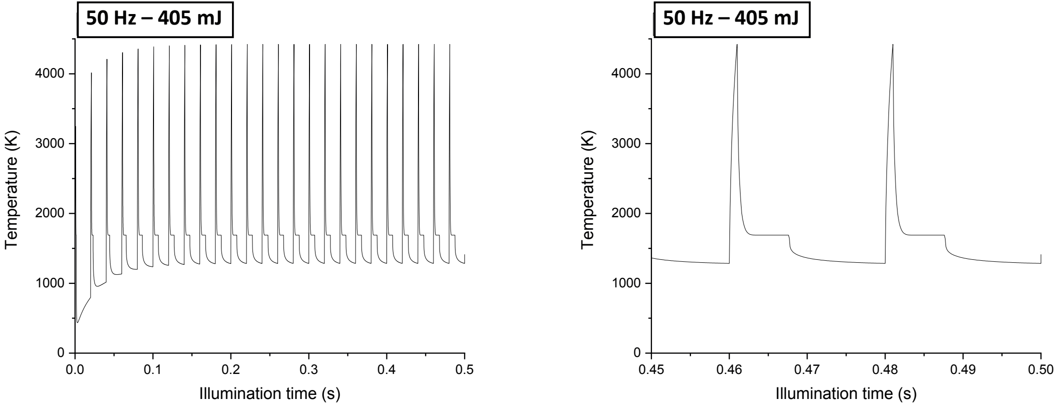

b

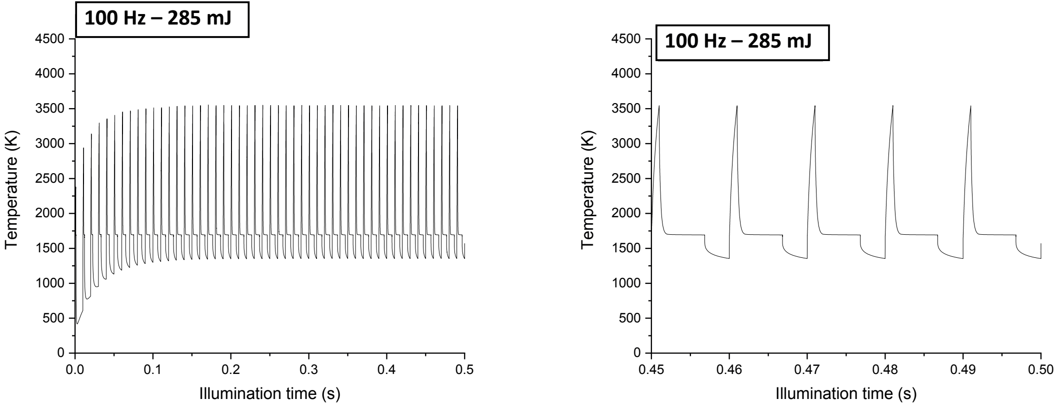

c

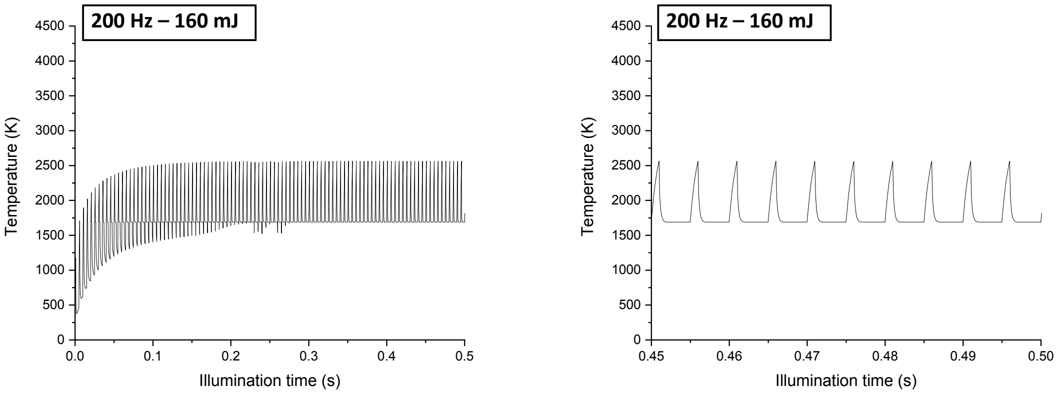

Figure 4-5. Simulation of temperature variations calculated by FEM during pulsing of the laser for 0.5 s using the conditions (a) 50 Hz – 405 mJ (b) 100 Hz – 285 mJ and (c) 200 Hz – 160 mJ. The substrate bottom temperature was 980°C.

Temporal developments of the temperature at the immediate vicinity of the melt pool (no melting) were also calculated by FEM, but are not shown here. The results were similar to those obtained experimentally. Minimum temperatures of 1280, 1330 and 1400 K were obtained between laser pulses.

The effect of substrate surface temperature on the temporal temperature profile was studied with FEM modeling. Figure 4-6 shows the temperature variations at the center of the laser beam after the steady-state is reached for the conditions 200 Hz – 160 mJ and substrate boundary conditions (bottom temperatures) of 920, 940, 960 and 980°C. The solidification plateau became longer as the substrate boundary temperature increased. As a result, the minimum temperature between pulses was reduced upon the solidification plateau increase in length. If a substrate bottom boundary condition is set to 980°C (surface temperature of 900°C), no cooling of the solid phase occurs.

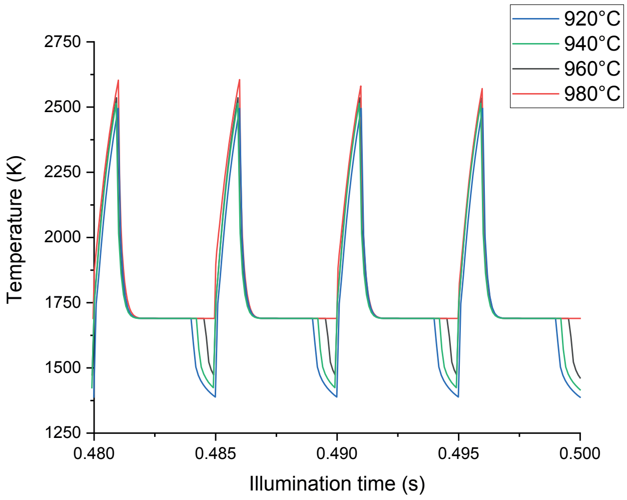

Figure 4-6. FEM calculation of the temperature profile as a function of time for the conditions 200 Hz – 160 mJ, with different substrate boundary conditions.

The temperature field across the heat affected zone (defined as the zone for which silicon underwent thermal modifications compared to the case when no laser is heating, HAZ) calculated using FEM modeling for a substrate surface temperature of 900°C and laser parameters 50 Hz – 405 mJ and 200 Hz – 160 mJ is shown in Fig.7. The frames presented in Fig 7. Are the temperature fields during the laser pulse after 0.5 s of laser illumination, during the steady-state. The grey color represents the liquid state.

For each condition, we found the highest thermal gradients were located in the solid phase, in the vicinity of the melt pool. For a substrate surface preheated to 900°C, the conditions 50 Hz – 405 mJ (Figure 4-7 (a)), 100 Hz – 285 mJ (Figure 4-7 (b)) and 200 Hz – 160 mJ (Figure 4-7 (c)) led to maximal thermal gradients of $-8.2.10^6$, $-6.2.10^6$ and $-4.2.10^6$ K/m respectively, located 300 µm away from the melt pool center (calculated from the temperature field but not shown in this Chapter). Maximum melt pool volumes of $1.1.10^{-2}$, $8.3.10^{-3}$ and $4.9.10^{-3}$ mm^3 were respectively calculated, which is in agreement with experimental and calculated solidification times decreasing with decreasing melt pool volumes.

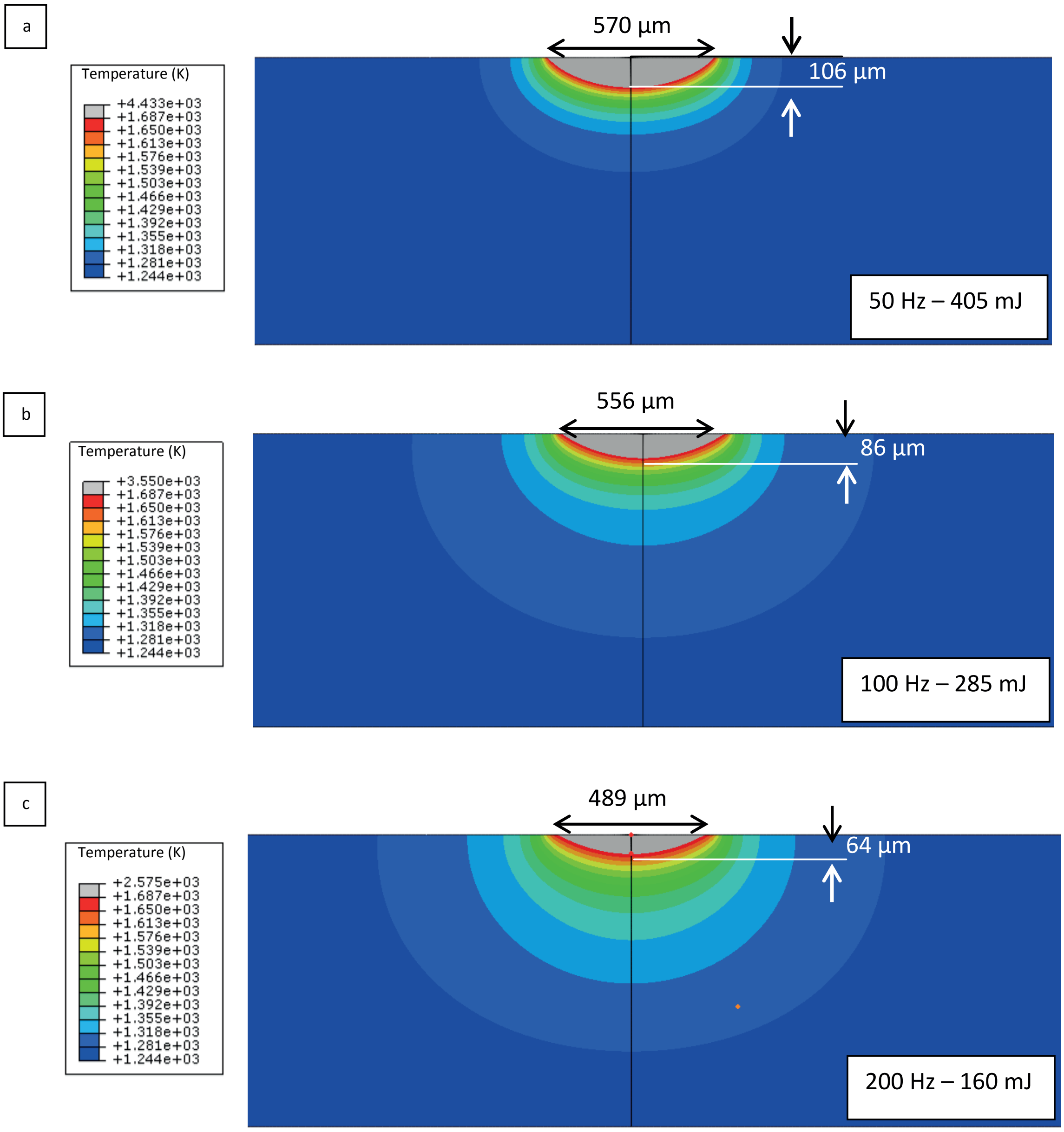

Figure 4-7. Maximum melt pool size and temperature field around the melt pool calculated after 0.5 s of laser illumination. The substrate bottom temperature was 980°C, corresponding to a surface temperature of 900°C. (a) 50 Hz – 405 mJ, (b) 100 Hz – 285 mJ (c) 200 Hz – 160 mJ. The grey area stands for temperatures higher than the melting point (liquid phase).

Then, a study of the residual stress in function of the laser illumination conditions was conducted, as we wanted to know the location of the maximum residual stresses. Therefore, the Raman shifts along the radii of the HAZ illuminated by the conditions 200 Hz – 160 mJ and 50 Hz – 405 mJ were measured.

In silicon, the central Raman peak of Si-I is located at around 520 cm^{-1} [105], and the second one, much weaker, at 300 cm^{-1}. The Raman shift of the central peak depends on all tensor components of stress. Assuming triaxial stress, (no shear stress components), the relationship between the Raman frequency shift $\Delta\omega$ and the stress contributions σ_{xx}, σ_{yy} and σ_{zz} (respectively in the x, y and z directions) as described by De Wolf[106] is:

$$\Delta\omega = -2.30 \times 10^{-9}(\sigma_{xx} + \sigma_{yy}) - 1.13 \times 10^{-9}\sigma_{zz}(Pa) \tag{4-1}$$

Figure 4-8 shows Raman spectra of a stress-free Si wafer, a Si wafer under compressive stress and a Si wafer under tensile stress. The peaks were fitted with a Lorentzian function. In silicon, a positive Raman shift indicates an overall compressive stress whereas a negative Raman shift indicates a tensile stress. For our measurements, the laser intensity was kept under 100 µW so that the Raman shift was not affected by any temperature rise caused by the heating of the laser beam[107]. However, the surface roughness and waviness of the sample were responsible for the noise in the measurement, as refocalization of the laser was necessary during the measurement. A HNA reagent was used to etch about 15-25 µm of the illuminated silicon surface to reduce the surface roughness. However, the waviness caused by the melt pool solidification, especially at the center of the melt pool (as seen in Figure 4-1) could not be avoided. Despite careful readjustment of the laser at each point, Raman shift measurements towards the center of the HAZ are error prone.

The predicted Raman shift was calculated by FEM simulations with Abaqus 2017. After 0.5s of laser illumination for each set of conditions at a boundary condition of 980°C (surface temperature of 900°C), rapid cooling from the molten state to substrate temperature was modeled, according to the cooling rates found in Figure 4-5. Then, slow cooling from substrate temperature to room temperature was performed. Calculation of the Raman shift was performed with equation (4-1) using the calculated radial, hoop and vertical stress contributions. The residual stresses used in the calculation of the Raman shift were extracted a few microns below the free surface of the Si-wafer. Details of the simulation method are given in Chapter 3.6.1.

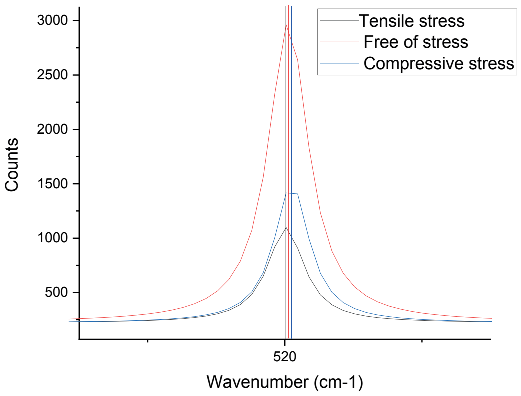

Figure 4-8. Typical Raman spectra for a stress-free Si wafer, silicon in compressive stress and silicon in tensile stress. The vertical lines correspond to the position of the maxima of the peaks: blue for compressive stress, red for free of stress and red for tensile stress.

After etching with HNA reagent, Figure 4-9 (a) and (c) show optical micrographs of the top of wafers illuminated with a laser using the conditions 200 Hz – 160 mJ and 50 Hz – 405 mJ, respectively. Raman measurements were performed on a line along the radius of the HAZ as denoted on the figures, from its center to approximately 480 µm. Figure 4-9 (c) and (d) display the experimental and FEM predicted Raman shift vs. radial position along these lines.

According to Figure 4-9 (b) overall compressive stress was observed at the center of the melt pool for the condition 50 Hz – 405 mJ, followed by tensile stress from 100 to 300 µm away from the center of the melt pool. The stress became slightly compressive again from 300 to 500 µm. Almost the same pattern was observed for 200 Hz – 160 mJ, with low stress from 0 to 50 µm, a tensile stress from 50 to 250 µm and a low overall compressive stress from 250 µm.

In both conditions, a minimum Raman shift corresponding to maximum tensile stress appeared 270 µm away from the center in the case 50 Hz – 405 mJ and 240 µm away from the center in the case 200 Hz – 160 mJ. The simulations results were in good agreement with the experimental observations, as the same trends were observed. The predicted maximum negative Raman shifts were larger in the simulation results, with -0.6 cm^{-1} for 50 Hz – 405 mJ and -0.45 cm^{-1} for 200 Hz – 160 mJ (0.3 and 0.25 cm^{-1} experimentally). Overall, the maximum negative Raman shift, which is associated with the maximum tensile stress, was higher for the condition 50 Hz – 405 mJ than for 200 Hz – 160 mJ.

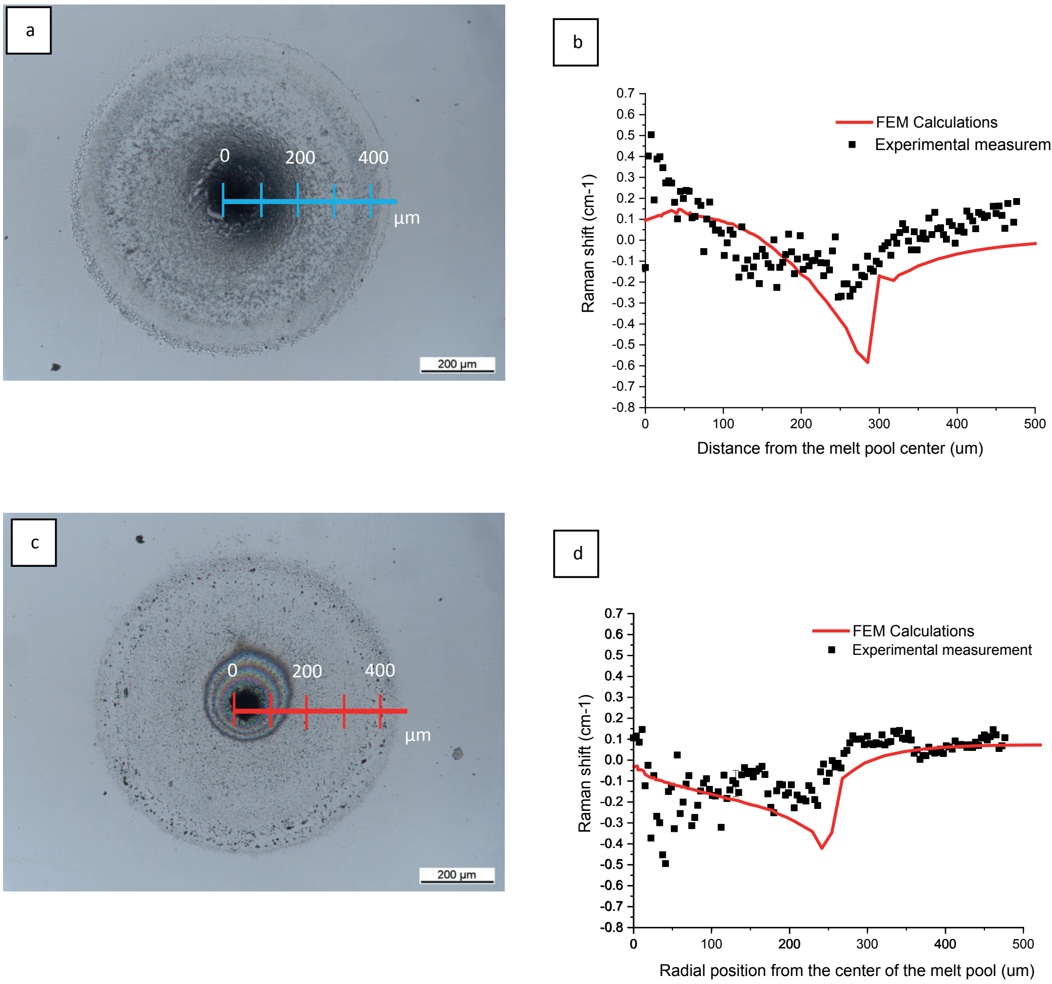

Figure 4-9. Optical images of the top view of a wafer surface after illumination for 1.5 s with (a) 200 Hz 160 mJ and (c) 50 Hz 405 mJ. The samples were etched with HNA reagent. (b) Raman shift measured and calculated by FEM along the HAZ radius presented in the optical microscopy pictures for the conditions 50 Hz – 405 mJ and (d) for the conditions 200 Hz – 160 mJ.

Figure 4-10(a) presents the results of stress FEM calculations in the radial and hoop directions in and around the melt pool at different processing times for the condition 50 Hz – 405 mJ and 200 Hz – 160 mJ and a substrate bottom temperature of 980°C (surface temperature 900°C). The results are presented in graphs showing the stress intensity as a function of the position on the HAZ radius, starting from the melt pool center.

Figure 4-10 (a) and (c) show the radial and hoop stresses during the laser heating phase (during the laser pulse), when the melt pool reaches its maximum size, for conditions 50 Hz – 405 mJ and 200 Hz – 160 mJ respectively. Figure 10 (b) and (d) show the radial and hoop stresses at the end of the melt pool cooling phase, for conditions 50 Hz – 405 mJ and 200 Hz – 160 mJ respectively.

During melt pool formation, the radial and hoop stresses around the melt pool were compressive in both cases (Figure 4-10 (a) and (c)). In the case, 50 Hz – 405 mJ, their maxima (-116 and -167 MPa) were located 360 and 300 µm from the melt pool center respectively. In the case 200 Hz – 160 mJ, their maxima were -115 and -178 MPa, located 210 µm from the center.

For all cases, after solidification occurred, both contributions became tensile within the solidified melt pool, and remained compressive outside (Figure 4-10 (b) and (d)). In the case 50 Hz – 405 mJ, the maximum tensile radial (150 MPa) and hoop (200 MPa) stresses were located 288 and 285 µm away from the melt pool center respectively. In the case 200 Hz – 160 mJ, their maxima were 101 and 132 MPa, located 180 µm from the center.

The maximum tensile stress values found in the case 50 Hz – 405 mJ were close to the 225-300 MPa necessary to reach the fracture strength of silicon at room temperature[78 77].

The stress pattern found by FEM during the cooling phase were in agreement with the Raman spectroscopy measurements and calculations, as the tensile stress peaks locations correspond to the tensile stress peaks found in the Raman measurements presented in Figure 4-9 (b) and (d).

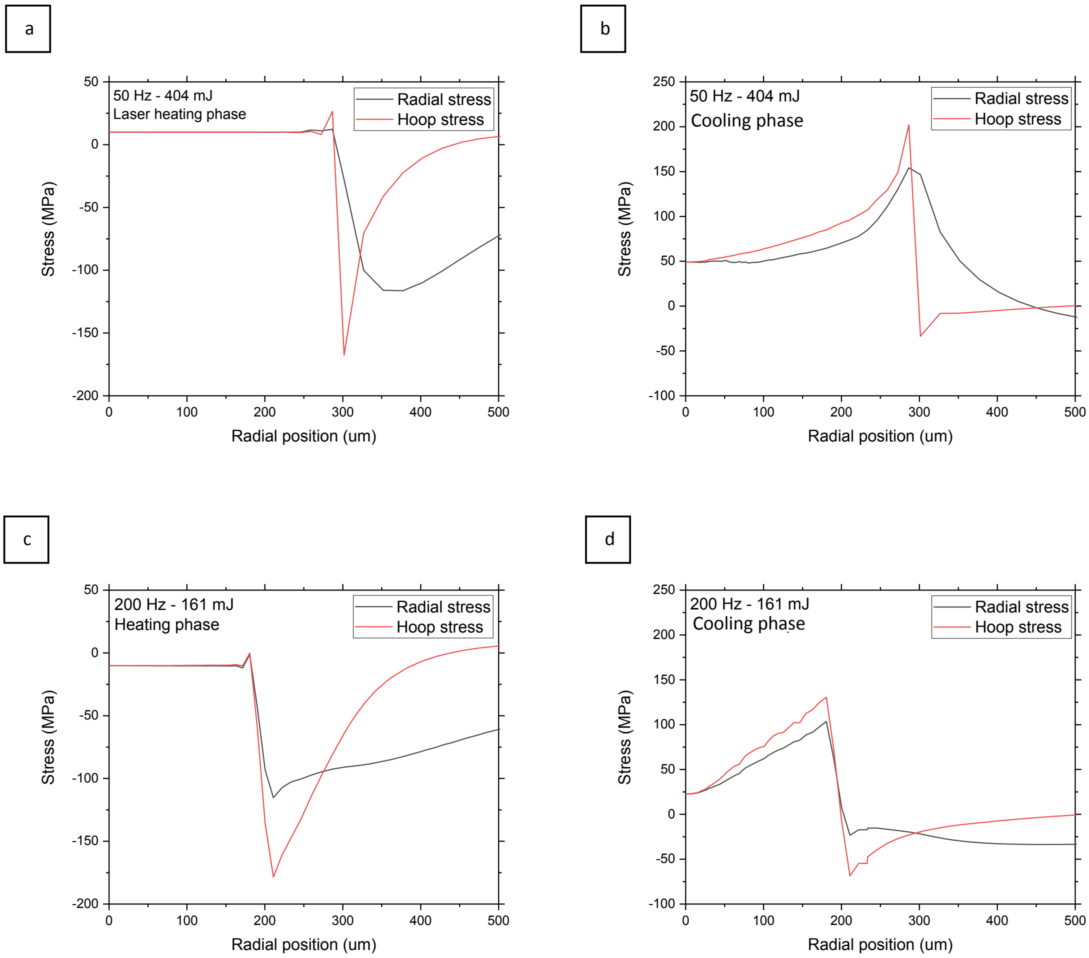

Figure 4-10. FEM stress calculations for 50 Hz – 405 mJ (a) radial stress during the laser heating phase (b) hoop stress during the laser heating phase (c) radial stress during the cooling phase and (d) hoop stress during the cooling phase

4.1.2. Working Conditions: Crack Formation and Propagation During Pillar Building

So far, only the cracking behavior without powders was studied. However, it is expected that the addition of “cold” powders to the melt pool induces changes the cracking behavior, especially with the addition of a transporting gas, which adds additional wafer/melt pool cooling.

In this section, crack formation and propagation was studied when powders were added to the melt pool. Optical micrographs of wafer surfaces after laser illumination with conditions 50 Hz – 405 mJ and 200 Hz – 160 mJ for 1.5 s are presented in Figure 4-11 (a) and (c) for a substrate temperature of 730°C. Figure 4-11 (b) and (d) display the same conditions, but several bursts of powders have been added to the melt pool before cooling down. For 200 Hz – 160 mJ, no cracks were found after addition of powders. For 50 Hz – 405 mJ, a crack formed at a 90° angle at the sides of the melt pool. The distance from the center of the melt pool to the crack was about 370 µm. This distance varied from sample to sample, but the average distance was 378 ± 17 µm. A few samples were found where this distance was a few dozens of microns larger.

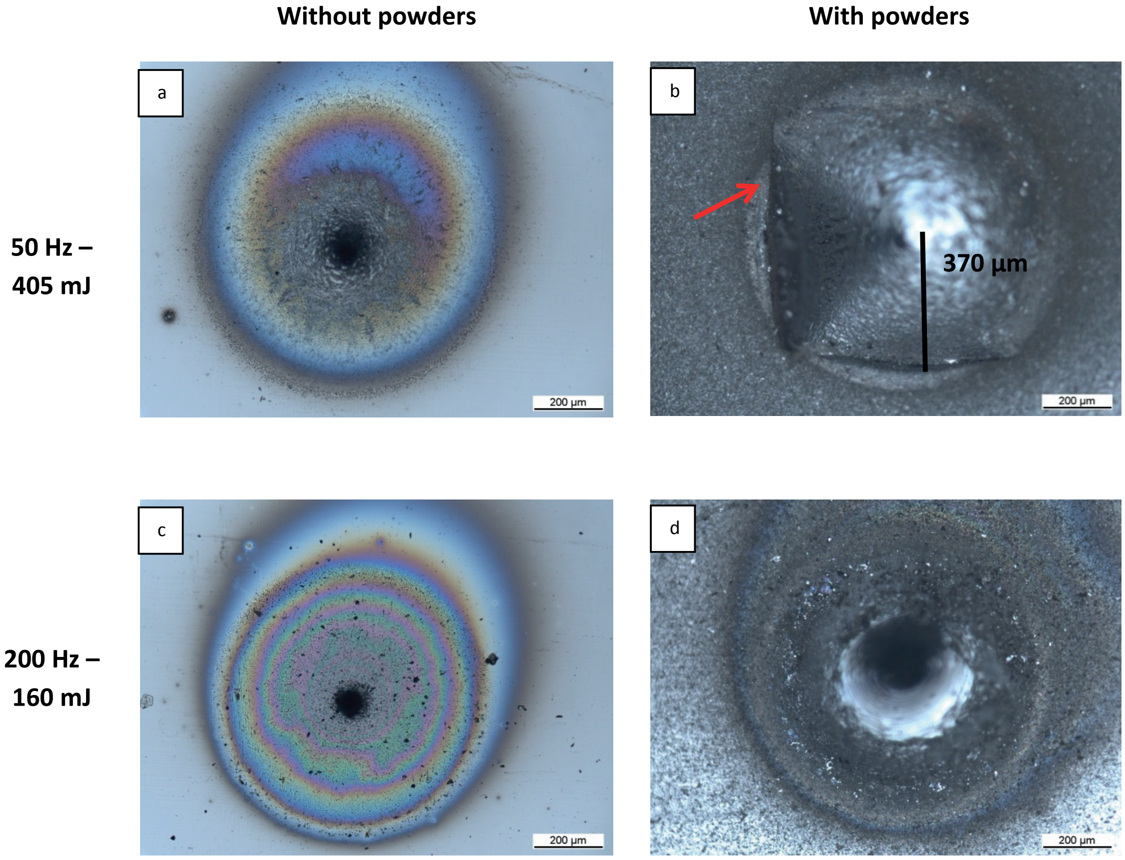

Figure 4-11. (a) Crack-free wafer after laser illumination at 50 Hz 405 mJ for 1.5 s. (b) Crack (indicated by a red arrow) induced by adding less than 1 second of powder to the melt pool formed by 50 Hz and 405 mJ laser illumination conditions, (c) Crack-free wafer after laser illumination at 200Hz – 160 mJ for 1.5 s. (d) crack-free wafer with addition of less than 1 s of powder to the melt pool formed with 200 Hz and 160 mJ. The feed rate was 15.0 g/min.

Figure 4-12 displays optical microscope observations of cross-sections of complete pillars built on a wafer with different substrate temperatures and laser parameters. The feed rate was set to 15.0 g/min. Figure 4-12 (a) and (b) show the cross-sections of pillars built at 50 Hz - 405 mJ and 200 Hz – 250 W respectively on substrates at room temperature. Figure 4-12 (c) and (d) show the same laser conditions for a substrate surface heated to 730°C. Pillars built on a non-preheated Si-substrate always cracked with brittle fracture at their base. Pillars built on a substrate with a surface temperature of 730°C cracked at the base of the pillar for the condition 50 Hz - 405 mJ. In the latter condition, the crack stopped about 200 µm below the wafer surface. Trenches were also often found (see example in Figure 4-15). When a complete pillar was built with 50 Hz – 405 mJ, the distance between the center of the melt pool and the crack increased in comparison with the case when only several powder bursts were added to the melt pool (Figure 4-11 (d)). This distance increased to 441 ± 44 µm.

However, crack-free pillars were successfully built with the conditions 200 Hz - 160 mJ.

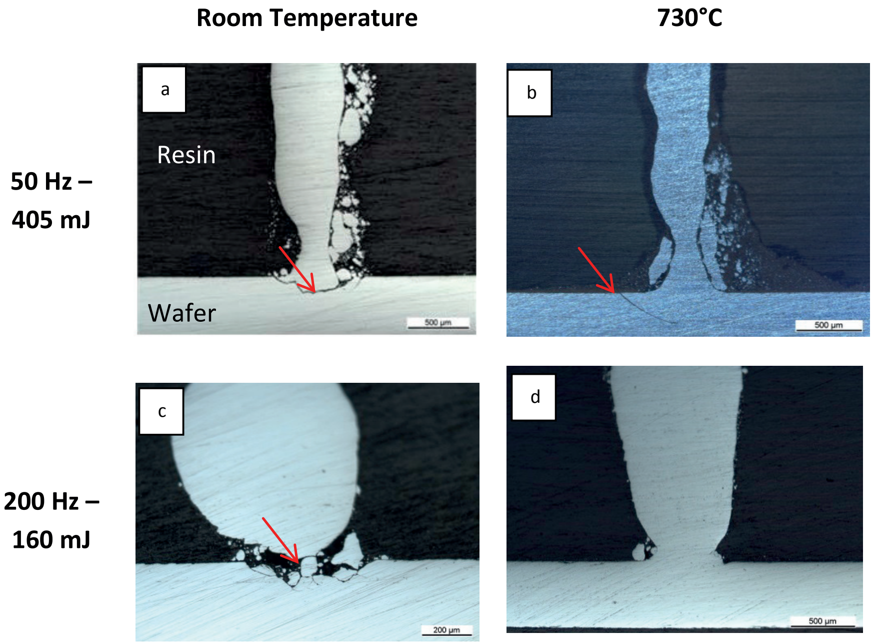

Figure 4-12. Optical microscope pictures of cross-section of pillars built on (a) Si wafers at 50 Hz – 405 mJ – 1ms – substrate at ambient temperature, (b) 50 Hz – 405 mJ – 1ms - substrate heated to 730°C (c) 200Hz – 160 mJ – 1 ms – substrate at ambient temperature (d) 200 Hz –160 mJ – 1ms – substrate heated to 730°C. The red arrows indicate the location of a crack on the picture. The feed rate was 15.0 g/min.

The crack-free conditions (200 Hz – 160 mJ) for a substrate heated at 730°C were taken as basis conditions to study the influence of the substrate temperature on cracking. Figure 4-13 shows optical microscope figures of cross-sections of pillars built with 200 Hz – 160 mJ with a feed rate of 15.0 g/min and a stage speed of 0.1 mm/s for different substrate temperatures. The temperatures presented are the wafer surface temperatures measured with a thermocouple when the argon shielding gas was flowing (see Chapter 3.2.6). Figure 4-13 shows that the substrate completely broke along the circumference of the melt pool for a temperature up to 300°C. For temperatures between 300 and

600°C, the pillar was attached to its substrate, but cracking was observed at the base of the pillar, starting a few dozens of microns away from the pillar base. At substrate temperatures above 650°C, crack-free structures could be built.

Most of the pillars built in these experiments presented necking and a protrusion. This phenomenon is further explained in Chapter 5. The presence of the protrusion, or the base of the pillar itself, can produce sharp angles (points of high stress concentration). For example, at 390°C, a crack appeared at sharp angle point additionally to the one found in the substrate.

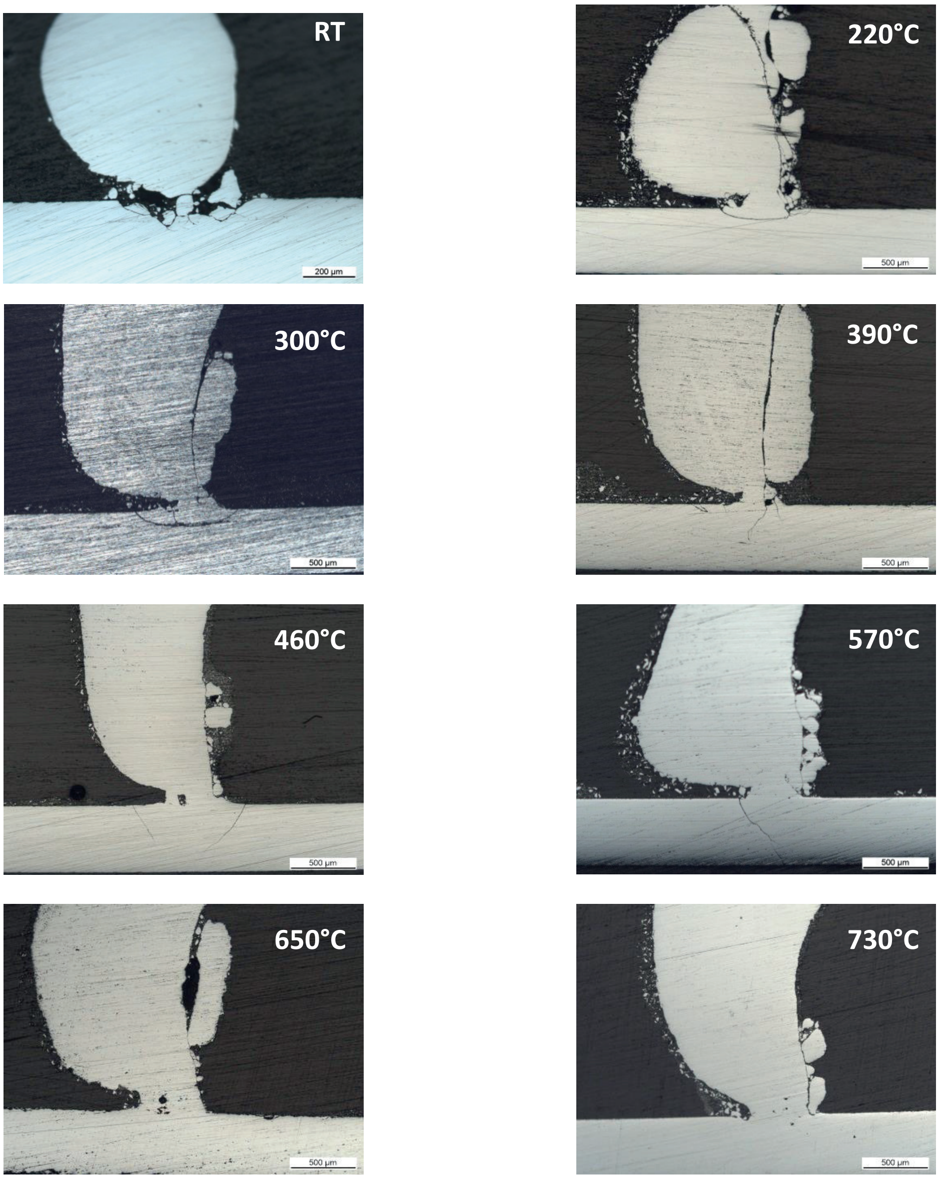

Figure 4-13. Optical microscope images of Si structures built on a Si wafer at different substrate temperature for the condition 200 Hz – 160 mJ. In all the temperature measurements, the argon shielding gas was ON. The temperature measurement does not take into account powder blowing.

Following observations presented in Figure 4-13, we studied the working conditions for which crack-free pillars can be built, for a substrate surface temperature of 730°C and a feed rate of 15.0 g/min. Figure 4-14 (a) shows the working conditions regarding the energy per pulse vs. repetition rate. Figure 4-14 (b) shows the working window in terms of average power vs. repetition rate. The green points and green area represent sets of conditions for which no cracking of the Si-pillars was observed. The red dots and red area represent sets of conditions for which cracking of the Si-pillars was always present. The orange dots represent conditions for which both configurations were found. The blue points and blue area stand for conditions for which pillars could not be properly built (bad powder coalescence or too thin pillar base leading to rupture). It was shown that crack-free pillars could be built when the laser pulse rate was set above 100 Hz. It was also observed that a certain amount of energy per pulse was necessary to be able to build a pillar depending on the repetition rate of the laser. This threshold energy per pulse diminished when the repetition rate decreased. Finally, a broad range of energy per pulse was allowed as long as the threshold was reached. Experimental observations as shown in Figure 4-14 (b), confirmed that the pillar cracking behavior did not depend on the average power but rather on the laser repetition rate as previously discussed. Diminishing the feed rate to 1.0 g/min led to a lower threshold value of 75 Hz. Micrographs of the pillars used to obtain this working conditions are presented in Appendix C.

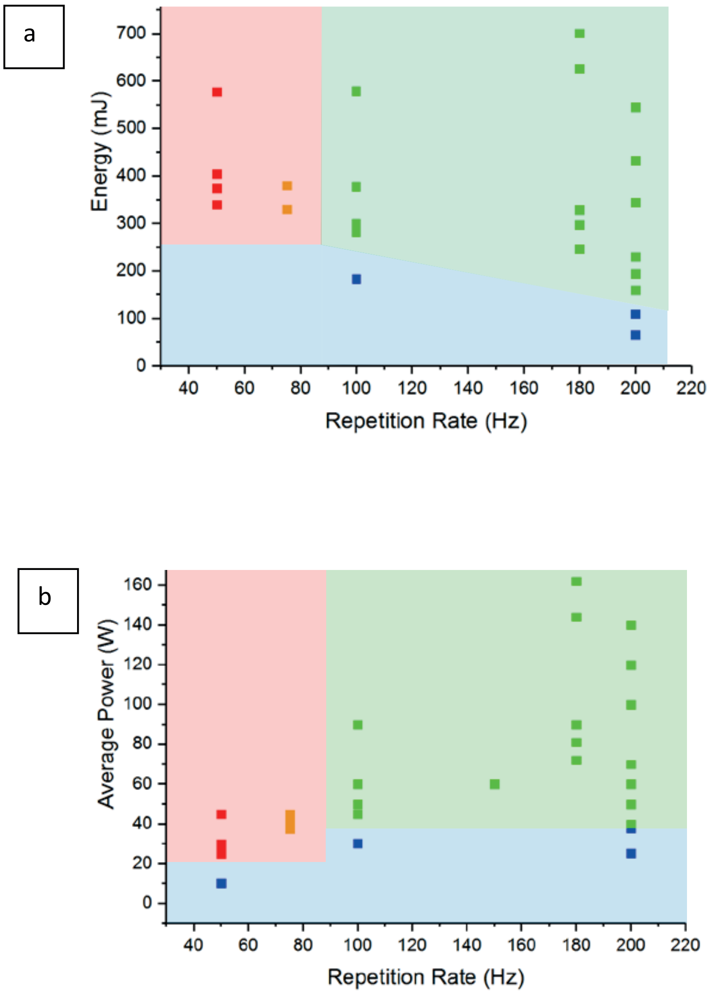

Figure 4-14. Working window for crack-free DLM processing of Si for a feed rate of 15.0 g/min, a stage speed of 0.1 mm/s and a substrate temperature of 730°C (a) Energy vs repetition rate (samples made with varying pulse duration and power) and (b) Average power vs. repetition rate. The green dots and the green area indicate conditions where the pillar could be built without cracks. The red dots and the red area indicate conditions where the pillars were built with cracking. The blue dots and the blue area stand for the conditions where no attachment to the wafer was possible.

The crack morphology obtained for a sample built with 50 Hz – 405 mJ and 15.0 g/min was observed to determine the type of fracture occurring during the low-frequency building of pillars. Figure 4-15 (a) displays an optical microscope image of a pillar built with 50 Hz – 405 mJ. Figure 4-15 (b) and Figure 4-15 (c) are close-up SEM pictures of the crack morphology close to the surface of the wafer and at the crack tip, respectively. Close to the wafer surface, the crack exhibits typical features of a brittle crack, with very smooth edges and visible cleavage. On the contrary, the crack tip exhibits the typical features of a ductile crack, with the formation of microvoids ahead of the crack tip, about 200 µm below the wafer surface.

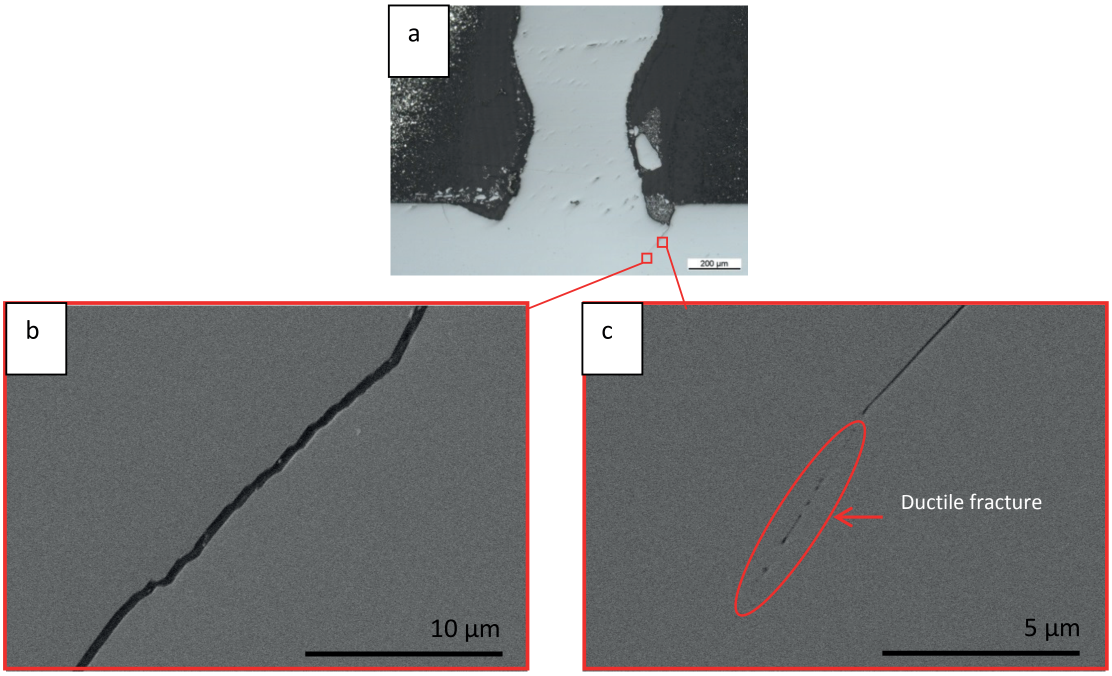

Figure 4-15. (a) Optical microscope image of a pillar built with 50 Hz – 405 mJ (b) SEM image of the crack close to the wafer surface (c) SEM image of the crack tip, about 200 µm under the wafer surface

4.1.3. Cracking in the Pillar Body

To study cracking in the pillar matrix, pillars built from two powders having different impurity content were compared. To begin with, impurity analysis was carried out on the two powders by GDMS. The results are presented in Table 4-1. As expected, Si_4N was purer than Si_98% by at least one order of magnitude. The main impurities in the two powders were Al and Fe for Si_98% and Al, Fe and Mo for Si_4N.

Si_4N				**Si_98%**			
Al	30	**Ca**	11	**Al**	1100	**Ca**	280
Fe	32	**K**	0.56	**Fe**	2600	**K**	1.5
Ni	5.3	**Na**	0.11	**Ni**	34	**Na**	10
Cu	6.2	**Mg**	0.17	**Cu**	32	**Mg**	16
Ti	1.7	**Cl**	9.5	**Ti**	160	**Cl**	7.7
Zn	2.5	**Co**	0.09	**Zn**	25	**Co**	7.1
P	18	**Ag**	2.0	**P**	36	**Ag**	8.7
B	77	**Pb**	0.26	**B**	26	**Pb**	310
As	15-130	**Li**	0.1	**As**	1.6	**Li**	0.11
Mo	160	**Pt**	< 0.5	**Mo**	52	**Pt**	<0.5
Cr	0.26	**Mn**	0.07	**Cr**	79	**Mn**	190

Table 4-1. Impurity content measured by GDMS in Si_4N and Si_98% in ppmw. The frames highlighted in red show the main metallic impurities. The frames highlighted in green show the dopants.

Figure 4-16 (a) shows a typical close-up SEM image in the cross-section of a pillar built with Si_4N or with Si_98% where no impurity inclusions were found. At these locations, no cracks were observed. Figure 4-16 (b) shows a SEM image of the cross-section of a pillar built with Si_98% or Si_4N, where impurity inclusions were found. The impurities were found mostly at the grain boundaries, but some were observed in grains too. In this case, micro-cracks were observed on the impurity precipitates, as indicated by the red arrows. EDX analysis (Figure 4-16 (c)) showed that the precipitates were mainly composed of Si, Al, and Fe, the latter being the main impurities found in the two powders (Table 4-1). Both pillars built with Si_4N and Si_98% presented impurity inclusions. However, their quantity and distribution were different. The distribution of impurities along the pillar height is discussed in more details in Chapter 6.2.4.

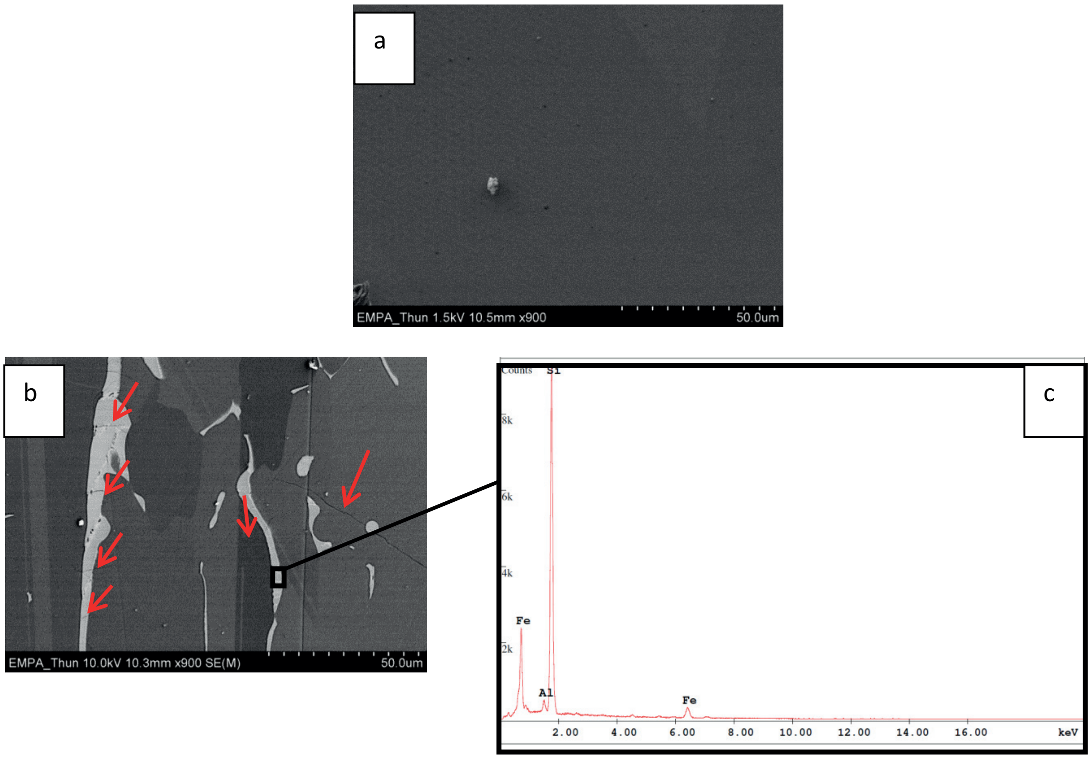

Figure 4-16. (a) SEM image of a typical surface of a cross-section of a pillar built with Si_4N. (b) SEM picture of the cross-section of a pillar built with Si_98%. Micro-cracks are indicated by red arrows on the picture. (c) EDX spectrum upon analysis of impurity precipitates.

Additionally, high-speed camera recordings of a laser illumination at the top of the pillar were carried out, but are not presented here. It was found that the solid phase did not cool down between the laser pulses, for any laser conditions.

4.2. Discussion

4.2.1. Wafer Surface Temperature

Even when the wafer bottom temperature was set to more than 850°C, a sharp temperature drop of about 100°C at the surface of the wafer was encountered due to forced convection cooling with the argon shielding gas (see Chapter 3.2.7), resulting in measuring a surface temperature of about 730°C. In the FEM simulations, the substrate bottom temperature was set at 980°C to obtain similar temporal temperature variations to in the experimental results. This resulted in a surface temperature of about 900°C. The discrepancy between the measured wafer surface temperature and the simulation substrate temperature necessary to achieve similar results suggests that the real wafer temperature was probably higher than the measured value. Indeed, contact between the thermocouple and the wafer was difficult to achieve, and the shielding argon gas was probably also cooling the thermocouple as well. In the end, the wafer real temperature was probably around 850°C. However, in this manuscript, we refer to the measured temperatures.

4.2.2. Cracking Behavior in a Monocrystalline Wafer Solely Illuminated by the Laser

The optical micrographs presented in Figure 4-1 show that Si wafers exhibited cracking if the substrate surface was not preheated, whereas heating the latter to more than 730°C avoided it, for every illumination conditions. Several reasons can explain this behavior.

Increasing the substrate overall and local surface temperature allows for the several following effects, all participating in diminishing the probability of crack propagation. First, it allows for an increase in the fracture toughness of silicon, of the order of 0.6 MPa.$m^{1/2}$ at room temperature. Then, it enables a decrease of the thermal stresses induced by strong thermal gradients present at the vicinity of the melt pool, and a decrease in the melt pool cooling rate.

Increase in the substrate overall and local surface temperature is implemented by playing on the following parameters: substrate temperature, repetition rate of the laser and energy per pulse. The natures of their contributions are developed in the next paragraphs.

The first important parameter to control is the substrate surface temperature. Simulations with Abaqus (Figure 4-6) showed that the solidification plateau became longer in time upon increasing the wafer preheating temperature. Making the solidification plateau longer enabled diminishing the solid cooling time between pulses and maintaining a high substrate temperature. High-speed camera measurements showing the temperature variations in time over several laser cycles also demonstrated that a larger solidification plateau (lower cooling rate) was obtained when the substrate was heated (more than 3 ms, Figure 4-2) compared to when it was kept at room temperature (less than 100 µs, Figure 4-4). This is due to higher heat flow by conduction through the colder Si-wafer, which reduces the solidification time.

The second important parameter that enables the local increase in temperature is the repetition rate of the laser. Increasing the repetition rate diminishes the cooling time between pulses (Figure 4-5). This way, the minimum temperature encountered in the vicinity of the melt pool can be maintained sufficiently high, as shown by the experimental temperature profile in Figure 4-2 and Figure 4-3, and the FEM temperature variation in Figure 4-5.

The third parameter that plays a role in maintaining a high local temperature is the energy per pulse. Using higher energy per pulse also enables obtaining longer solidification plateaus as it leads to the formation of higher melt pool volumes (Figure 4-7). This would also lead to shorter cooling times of the solid phase and help to maintain a high Si-wafer temperature. It was difficult to measure the melt pool volumes experimentally as it recrystallizes with the same orientation as the wafer, and therefore could not be observed either with optical microscopy, SEM or EBSD. However, it is expected that the experimental melt pool are larger than the calculated ones because melt pool dynamics such as the Marangoni effect which are not included in the FEM model. Simple calculations (Appendix B.1) showed that the recoil pressure was negligible in this case.

Cases of both low repetition rates and high energy per pulses result in higher thermal stress built during the process. Raman spectroscopy measurements confirmed this assessment, as the maximum overall residual tensile stress measured for the case 50 Hz – 405 mJ was found to be 50% higher than for the case 200 Hz – 160 mJ (Figure 4-9). Indeed, higher energy per pulse and the longer cooling time between pulses translate by higher thermal gradients and higher thermal dynamic range over one laser cycle, both resulting in higher stresses.

According to the FEM calculations of the temperature variations at the side of the melt pool (similar to Figure 4-5), the BDT of silicon was reached in each studied case when the bottom of the substrate was heated to 980°C. Indeed, the literature reports BDT values between 550 and 1100°C for silicon. Low BDT are usually found for low doped wafers and a small loading rate[108]. Considering the low conductivity of our wafer, it is reasonable to propose that the BDT of the silicon in the configuration we are using is closer to 550°C than to 1100°C. Therefore, in the experiments conducted at 730°C, it is assumed that the wafer surface is reaching a temperature higher than the BDT at the vicinity of the melt pool when only the argon shielding gas is blowing. The ductile nature of the material at this temperature prevents crack propagation.

When only the monocrystalline wafer is illuminated with 200 Hz – 160 mJ, heating the substrate to 200°C was sufficient to avoid crack propagation, because a silicon wafer is a perfect crystal without surface defects leading to no cracks. In case of cracking (substrate at room temperature), the crack follows the region of high stresses, located at the edge of the melt pool, as suggested by the FEM stress calculations shown in Figure 4-10.

4.2.3. Crack Formed During Pillar Building

Powder blowing induces additional constraints. First, defects can be formed at the surface of the wafer due to powder injection. Secondly, the powder transport gas is blown at a speed of about 47 m/s, which corresponds to a convection coefficient of about 150 W/m^{2}K, even higher than the convection coefficient found in the case when only the shielding gas is blowing. This leads to further cooling of the wafer surface, along with cooling by the “cold" powder added to the melt pool. All these phenomena favor crack initiation, compared to the previous case, because they lower the overall and local wafer surface temperature.

The critical stress necessary to induce cracking is especially diminished in this case. Equation (4-2) presented in Chapter 2 shows that the critical stress needed for crack propagation in a brittle material in the presence of defects is:

$$\boldsymbol{\sigma_c = \frac{K_{Ic}}{Y\sqrt{\pi a}}} \qquad (4\text{-}2)$$

Where K_{Ic} is the fracture toughness, Y is a parameter depending on crack and sample geometry, and a is half the length of an internal crack or the length of a surface crack. Therefore, the introduction of sharp powder indents, or any other defect due to powder feeding on the wafer, diminishes the critical stress. Moreover, cooling induced by the transport gas and the powders decreases the fracture toughness, which diminishes the critical stress as well.

Therefore, the overall and local increase in temperature should be even higher when powders are added to the melt pool. This assessment was verified as it was shown that a minimum substrate surface temperature of 730°C should be used (Figure 4-13), as well as a minimum repetition rate of 100 Hz (Figure 4-14) in order to build crack-free pillars for a feed rate of 15.0 g/min. The working window (Figure 4-14) also showed that the energy per pulse should be sufficiently high so that melting of the substrate as well as melting of the powders into the melt pool is ensured. However, above this threshold, a broad range of energy per pulse can be used.

The powder feed rate also has an influence on the wafer surface temperature. Decreasing the feed rate from 15.0 g/min to 1.0 g/min allowed shifting the threshold frequency (no crack) from 100 Hz to 75 Hz as mentioned earlier in the description of Figure 4-14. It was shown in Chapter 4 that for a feed rate of 15.0 g/min, the powder weight per burst was 15 times higher than for a feed rate of 1.0 g/min. Therefore, even if the transport gas velocity is the same in both cases, the cooling induced by the “cold” powder is more critical in the case of a high feed rate. This is an additional contribution to reducing the temperature at the wafer surface, which favored thermal shock and reduction of the surface temperature, leading to cracking. Similar results were found by Wilms et al.[19] during the growth of single crystal alumina by laser material deposition. They demonstrated that reducing the feed rate from continuous to pulsed allowed avoiding temperature differences caused by the “cold” powder and allowed the material to melt entirely between powder pulses. These modifications led to obtaining crack-free samples.

The fact that the condition 50 Hz – 405 mJ (along with all other conditions for which the repetition rate is smaller than 100 Hz) presented cracking is consistent with the higher residual tensile stress measured by Raman spectroscopy on this sample compared to 200 Hz – 160 mJ. The crack observed in Figure 4-11 was located further away from the melt pool center than the maximum tensile stress location measured by Raman spectroscopy. The discrepancy can come from the difference in melt pool size between the experiments and the calculation due to not taking the Marangoni effect into account. It can also come from the fact that the size of the defects created by powders can be bigger and sharper further from the melt pool, where the temperature is reduced. A crack would then initiate more efficiently at this location, and propagate around the melt pool.

Contrary to the case when the substrate is at room temperature, the crack present for 50 Hz – 405 mJ at 730°C was brittle at the wafer surface and became ductile and stopped a few hundred microns below the wafer surface (Figure 4-15). This confirms that the surface of the wafer is cooled down below the BDT for conditions where the repetition rate is below 100 Hz during pillar building. However, as the bottom of the wafer in contact with the hot plate reaches a temperature higher than the BDT, the crack stops when it reaches the ductile material.

These results of the two previous sections are consistent with the literature as most brittle materials had to be preheated before AM processing[19 20 21 22 23]. For some of them, the preheating temperature clearly had to reach the BDT[22] (see Chapter 2.3.1). The final surface temperature found by the simulation and the experiments lies in the preheating temperature range proposed by Zehavi et al.[35] (600 to 900°C) to successfully weld silicon. They are also consistent with literature as slow cooling of the part was generally preferred to avoid cracking[21] [20].

Even if it could not be measured, is it likely that cracking happens at the beginning of the process, and not during the final cooldown of the Si pillar. Indeed, the maximum stresses are located at the pillar base and are expected to reduce with time, as the high substrate temperature and the laser beam anneal the stress. This reasoning was approved by 3D simulations that were additionally conducted in the frame of this study, but were not presented here.

4.2.4. Mechanism of Crack Initiation and Propagation

As mentioned earlier, the defects produced by the powder blown onto the wafers are probably the starting point for crack initiation.

As the laser heats the wafer, compressive stress develops in the solid silicon, in the radial direction, due to thermal expansion of the material (Figure 4-10 (a) and (c)) and the high thermal gradients around the melt pool (Figure 4-7). Compressive stress exists in the hoop direction, due to Poisson's ratio. These results are consistent with the FEM calculations of stresses appearing during one pulse of a 1064 nm laser beam of 1 mm diameter on a silicon wafer at room temperature, conducted by Wang et al.[109], for a pulse of 2 ms and an energy per pulse of about 2 J. They also found that maxima of radial and hoop compressive stresses were located at the edges of the melt pool at the maximum melt pool size. For the fluence threshold above 254 J/cm^2, they observed radial cracks around the HAZ, and suggest that they were due to the high radial compressive stress existing at the edge of the melt pool during heating. However, we propose another mechanism, taking into account the cooling phase after solidification of the melted silicon.

When cooling occurs, the radial stress becomes tensile due to volume reduction of the silicon by cooling. The hoop stress then becomes tensile as well (Figure 4-10 (b) and (d)). Tensile stress occurs due to the shrinking of the solid phase upon cooling down (due to the thermal expansion coefficient). Therefore, according to our calculations, the most likely moment for a crack to initiate is during the cooling of the solid phase after solidification, in the region where both radial and hoop stresses have their maximum tensile stress. As the maximum tensile stresses found for 50 Hz – 405 mJ is close to 200 MPa, and the critical stress calculated for a defect of 10 µm at the surface of the wafer for a substrate temperature just below the BDT is about 280 MPa[108], this explanation is consistent with the results. This reasoning is consistent with the work of Gross et al.[110], who conducted experiments and calculations of residual stresses in silicon at room temperature. These authors used a Nd:YAG laser with energy per pulse ranging from 0.16 to 0.61 J. They claim that the residual tensile radial stress during the cooling phase was responsible for the formation of circumferential cracks during laser cutting.

After complete cooling down to room temperature, residual compressive stress exists at the center of the melt pool as shown by the Raman spectroscopy measurements in Figure 4-9. A compressive stress is found at the center of the HAZ, where the crystallization fronts reunite. As the melt pool has a free surface, the material forms an additional protuberance at the center of the melt pool during its solidification (Figure 4-1 (c) and (d)). A tensile residual stress region remained in most of the HAZ due to shrinking of the crystallized phase by cooling, with a maximum tensile stress at its border.

Compressive residual stress remained at the outside of the tensile zone due to thermal expansion during the heating phase.

Hence, from our experimental work and our FEM calculations, we can propose several mechanisms for crack formation and propagation in our process, depending on the experimental conditions.

- The wafer temperature is lower than 730°C
- The wafer temperature is higher than 730°C, and the repetition rate is lower than 100 Hz
- The wafer temperature is higher than 730°C, and the repetition rate is higher than 100 Hz

When the substrate surface temperature is lower than 730°C, the thermal gradients are the highest very close to the melt pool. The temperature reached around the melt pool is not high enough to overcome the BDT. As an extreme example, equation (4-2) can be adapted to the case of silicon at room temperature with K_{Ic}=0.6 MPa.$m^{1/2}$, Y=1.12 (case of a plate with an edge crack of length *a* under tensile stress)[111] and *a* typical crack length formed by the indentation of a powder particle of 10 µm diameter. In this case, $\sigma_C = 146$ MPa at room temperature. This value is probably largely overcome at room temperature, because the case where the substrate surface is preheated to 730°C already presents stresses of this order of magnitude (Figure 4-10). Therefore, cracks located at the circumference of the melt pool appear, along the regions of highest radial and hoop stresses (Figure 4-12). The result is a brittle crack propagating all around the pillar base (Figure 4-12 (a) and (c)).

When the wafer surface temperature is higher than 730°C, and the repetition rate is lower than 100 Hz, the temperature reached around the melt pool is not high enough to overcome the BDT, due to the substantial reduction in the surface temperature induced by the powder and its transport gas. Crack initiation can occur at the wafer surface by overcoming the critical stress, as suggested by the FEM calculations in Figure 4-10. The crack can be initiated further away from the melt pool due to colder temperatures and sharper indents. It is stopped in the wafer depth when the temperature is above the BDT temperature, as shown in Figure 4-15. The result is a brittle crack that turns into a ductile crack in the wafer depth following the regions of high-stress regions around the melt pool.

When the wafer surface temperature is higher than 730°C, and the repetition rate is higher than 100 Hz, the temperature reached around the melt pool is high enough to overcome the BDT. When the brittle-to-ductile transition temperature is reached, the fracture toughness increases by a factor 3 to 8, according to the study reported by Brede[80]. In this case, the stress induced by thermal stress is partially released by the creation of slips and dislocations around the crack tip, which prevents crack propagation. Stresses around the melt pool are also miminized thanks to lower thermal gradients (Figure 4-7 (c) and Figure 4-10 (d)). Therefore, no crack propagation occurs.

A summary schematic of the proposed mechanisms is displayed in Figure 4-17.

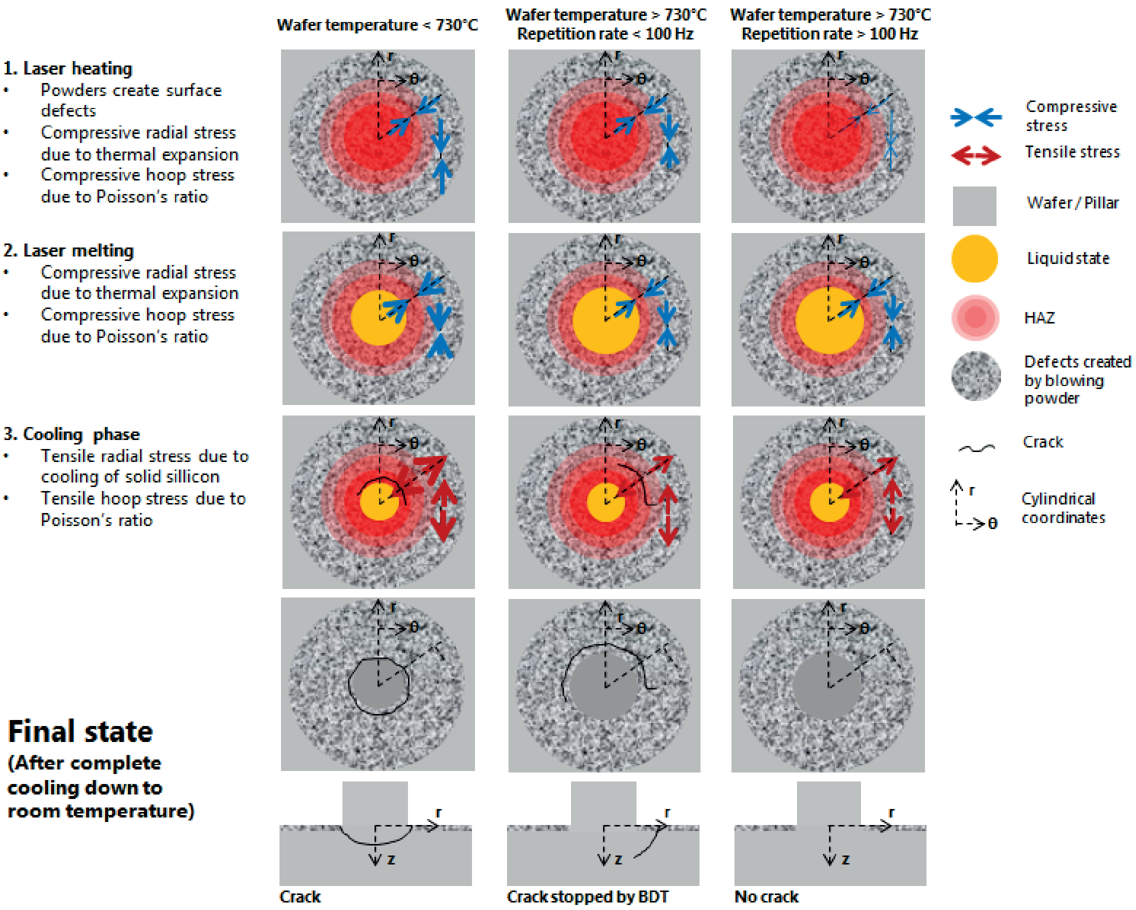
Wafer temperature < 730°C
Wafer temperature > 730°C
Repetition rate < 100 Hz
Wafer temperature > 730°C
Repetition rate > 100 Hz
1. Laser heating
• Powders create surface defects
• Compressive radial stress due to thermal expansion
• Compressive hoop stress due to Poisson's ratio
2. Laser melting
• Compressive radial stress due to thermal expansion
• Compressive hoop stress due to Poisson's ratio
3. Cooling phase
• Tensile radial stress due to cooling of solid sillicon
• Tensile hoop stress due to Poisson's ratio
Final state
(After complete cooling down to room temperature)
r
θ
z
Crack
Crack stopped by BDT
No crack
Compressive stress
Tensile stress
Wafer / Pillar
Liquid state
HAZ
Defects created by blowing powder
Crack
Cylindrical coordinates

Figure 4-17. Schematic of the proposed mechanism of crack formation in function of substrate temperature and laser conditions. The figures are represented in top view, except for the last row, represented in cross-section. These sequences represent the beginning of the pillar building process. The thickness of the arrows represents the relative stress intensity.

4.2.5. Cracking Due to Geometry

Cracks initiating at pillar inflection points also occasionally appear as illustrated by the sample built with a substrate surface preheated to 390°C in Figure 4-13. According to Equation (4-3):

$$\sigma_m = 2\,\sigma_0 \sqrt{\frac{a}{\rho_t}} \qquad (4\text{-}3)$$

Where σ_0 is the applied nominal stress, ρ_t is the radius of the curvature of the crack tip, a is the length of a surface crack or half the length of a crack if it is located in the bulk, the stress at the tip of a kink increases if its length increases and the radius of curvature at its tip decreases. In this case, the stress at the tip of the inflexion point overcame the stress created by thermal gradients. Therefore, the crack appeared at the kink location instead. Cracks due to geometry can be avoided by constructing straight pillars and avoiding that the melted material is blown away by the argon shielding and transport gases and the powder flow. Those improvements can be made by using a rotational stage, and decreasing the nozzle diameter.

4.2.6. Cracking in the Silicon Pillar Body

No cracks were observed in the silicon matrix composing the core of the pillar, except if impurity inclusions were present, as seen in Figure 4-16. In this case, microcracks appeared at the location of the impurity precipitates. This phenomenon is due to the difference of thermal expansion coefficient between silicon and the intermetallic impurities, that build high thermal stress around the impurity[112]. When no impurity inclusions were present, no cracks were detected in cross-section in the silicon matrix. Therefore, cracks can be avoided by using a pure powder.

Moreover, as the pillar grows higher, the heat losses by conduction decrease (see Chapter 5). Therefore, high temperatures can be maintained at the tip of the pillar, which limits cracking.

4.3. Conclusions and Summary

3D silicon structures have been successfully built on a silicon wafer with attachment to the wafer substrate without cracking, thanks to a controlled thermal management. The local increase in temperature above the brittle-to-ductile transition temperature was necessary to reach a good fracture toughness and plastic behavior of the material, along with diminishing thermal gradients at the side of the melt pool. These conditions enabled avoiding crack propagation induced by surface flaws already present on the wafer surface or created by the powder impact. Cracking probably appears at the beginning of the process, as the stress is expected to be relieved as the pillar grows. The exact moment of the crack initiation could not be determined. However, this exact time could be determined by acoustic emission, provided that the sound propagation of the crack has the different frequency as the intrinsic machine noise.

In order to build crack-free samples, the substrate should be preheated to more than 730°C, and the repetition rate should be set higher than 100 Hz. This threshold repetition rate can be decreased by decreasing the powder feed rate. Even if the energy per pulse had less influence on the cracking behavior, a minimum energy per pulse is required to be able to form a melt pool and attach new matter to the wafer. However, a too high energy per pulse can also lead to cracking and evaporation. The powder should preferentially be pure to avoid cracking because of the formation of intermetallic phases.

The heat losses by forced convection could be reduced in the future by decreasing the argon shielding gas debit or by working in a closed chamber under argon. However, a too small debit could lead to oxidation of the piece. In this study, working without protective gas under argon could not be realized experimentally due to the difficulty of making the chamber gas-tight.

Sharp angle kinks, especially created by the pillar necking and protrusion should be avoided as stress concentration at the kink tip can induce cracking. Better homogeneity in the pillar shape could be achieved by using a rotational stage.

A simple 2D axisymmetrical FEM model was implemented. Good agreement was observed with the experimental results, as the temporal profile of the temperature, as well as the Raman shift prediction, were consistent with the experimental observations. Therefore, this model represents well our process. Consequently, it was used as a tool to complement the experimental results and propose a mechanism for the propagation of the crack.

Chapter 5. Process Monitoring During Pillar Growth

Before being able to discuss the pillar microstructure as a function of experimental parameters, a good understanding of the process is required. First, the powders used in this study were characterized in terms of morphology, particle size and flowability. As poor powder flowability led to challenging powder transportation, the powder feed rate was monitored to understand the distribution of powder burst weight in time. Then, the pillar building rate was observed with a high-speed camera throughout the process. A correlation between feed rate, stage speed and pillar building rate was established. Pillar characteristics such as height, shape and building rate were also observed and discussed as a function of process parameters such as feed rate, stage speed and laser parameters. FEM simulations of the thermal history of the pillar during its building completed the experimental observations and the discussion.

5.1. Feed Rate and Pillar Building

5.1.1. Results

The two powders used in this PhD study were fully characterized in terms of particle size and particle morphology. Figure 5-1 (a) and (b) show the particle size distribution of Si_4N and Si_98% respectively measured by image analysis. The images used in the measurements are shown in Figure 5-1(a) and (b). The distribution is displayed in terms of probability vs. particle size in blue and the cumulative is shown in green. The particle size distribution for Si_4N was the following: d_{10}=13.0 µm, d_{50}=43.1 µm and d_{90}=93.4 µm. The distribution found for Si_98% was: d_{10}=10.6 µm, d_{50}=29.9 µm, d_{90}=75.3 µm. A broader particle size distribution was found for Si_98% than for Si_4N. However, Si_4N possessed bigger particles. These observations were confirmed by the SEM images shown in Figure 5-2 and Figure 5-3. Figure 5-2 shows SEM images of the powder Si_98% with x150 and x500 zooms. Figure 5-3 shows SEM images of Si_4N taken with x150 and x350 zooms. Si_4N contained particles close to 100 µm diameter and Si_98% contained finer particles. The morphologies of the two powders are similar, having sharp edges and facets.

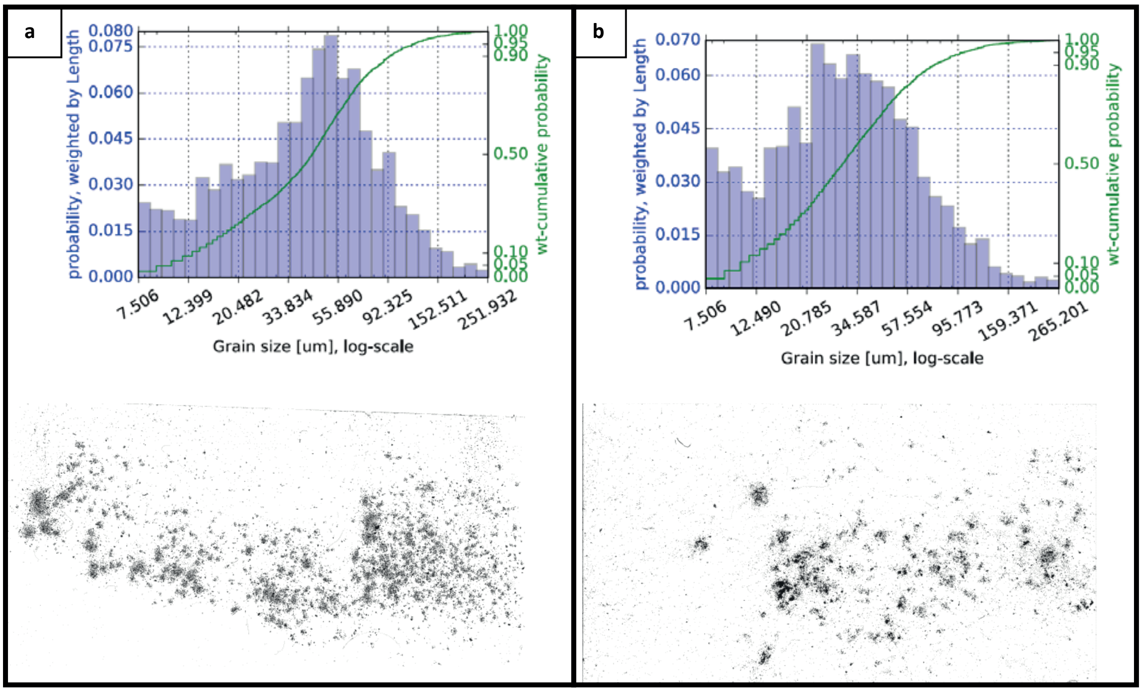

Figure 5-1. Particle size distribution and corresponding image used in image analysis of (a) Si-4N and (b) Si_98%

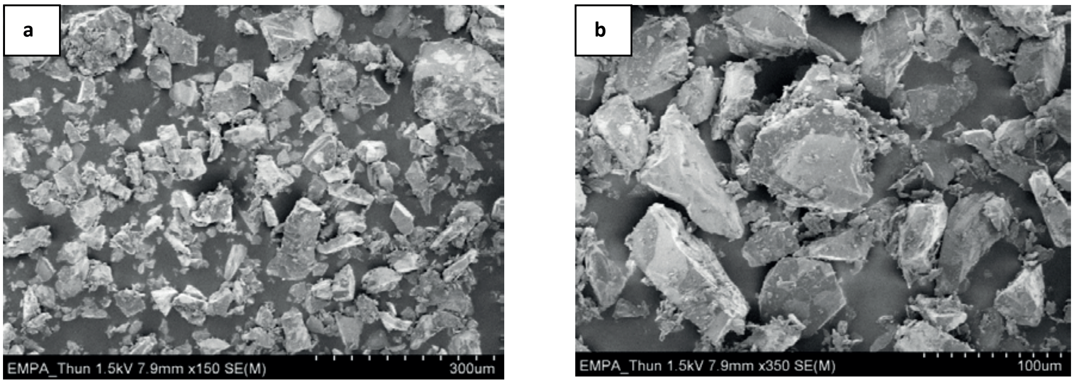
a
EMPA_Thun 1.5kV 7.9mm x150 SE(M)
300um
b
EMPA_Thun 1.5kV 7.9mm x350 SE(M)
100um

Figure 5-2. SEM image of Si_4N at different zoom magnitudes.

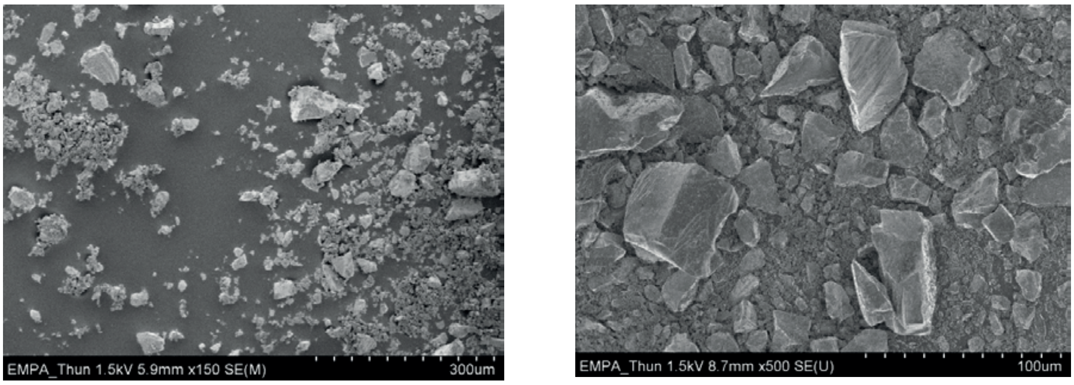
EMPA_Thun 1.5kV 5.9mm x150 SE(M)
300um
EMPA_Thun 1.5kV 8.7mm x500 SE(U)
100um

Figure 5-3. SEM image of Si_98% at different zoom magnitudes.

Powder flowability was estimated for both powders by measuring the weight per time flowing through orifices of different diameters, similarly to Hall flow testing (see Chapter 3.4.3). Si_98% could not flow even through the biggest orifice of 18 mm diameter. Si_4N could only flow through the biggest orifice, but not systematically, and by blocs of agglomerated powders. However, the powder could be transported to the melt pool thanks to the powder feeding system presented in Chapter 3.2.8. Si_4N was the powder used to study the process characteristics presented in this Chapter.

As seen in Chapter 3.2.8, the powder feeder delivered powder in pulsed bursts. Those powder bursts were observed during powder feeding with a high-speed camera, and the individual powder burst mass were evaluated for each feed rate. The procedure is detailed in Chapter 3.3.1.3.

Figure 5-4 presents the variations of powder burst weight during powder feeding as a function of time for feed rates: 15.0 ± 1.0, 3.4 ± 0.8 and 1.0 ± 0.3 g/min. Except for the two first ones at 22.4 and 14.6 mg, the powder burst weight for the feed rates 1.0 and 3.4 g/min were oscillating around a value of 11.3 ± 2.2 mg and 3.3 ± 1.8 mg respectively. However, the powder burst weight varied in time for the feed rate 15.0 g/min. It increased from 60 to about 65 mg from 0 to 7 s. Subsequently, it decreased constantly, but always remained at least three times higher than other feed rates. Its average value was 49.7 ± 11.5 mg per burst. The higher feed rates were steadier in time as the variation in burst mass for 15.0 g/min and 3.4 g/min was 23 % and 19 %, and the variation in burst mass for 1.0 g/min was 54 %.

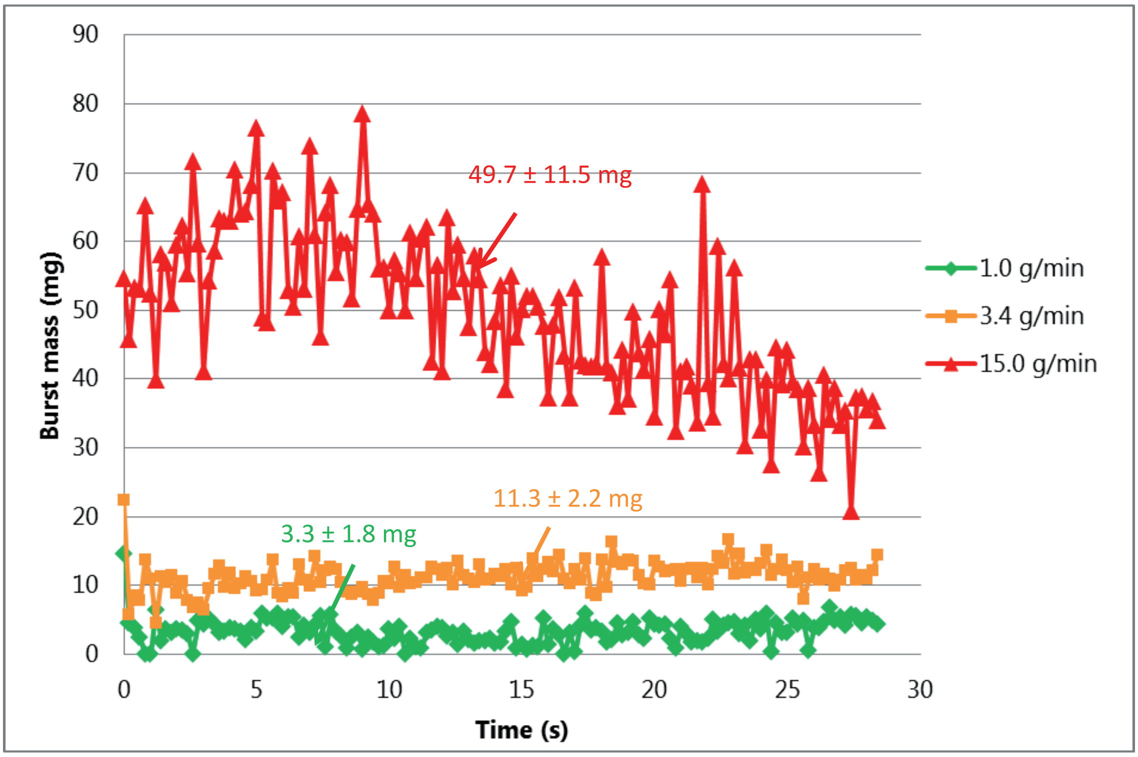

Figure 5-4. Mass per burst as a function of time for different feed rates monitored by different cell opening times during powder suction.

The reproducibility of the process has been checked for the investigated conditions. It was found that the height of the pillar was reproducible within an error margin of about 1 mm for the same process conditions.

Figure 5-5 presents an example of reproducibility for the pillar height as a function of time for a feed rate of 1.0 g/min and a stage speed of 0.1 mm/s. The pillar heights were measured on high speed camera sequences (details of the experimental procedure in chapter 3). The total pillar height was fairly reproducible, with a height of 5.1 ± 0.5 mm for a given processing time of 50 s. The 3 first seconds of the building were highly reproducible. However, fluctuations were encountered from 3s to the end of the process.

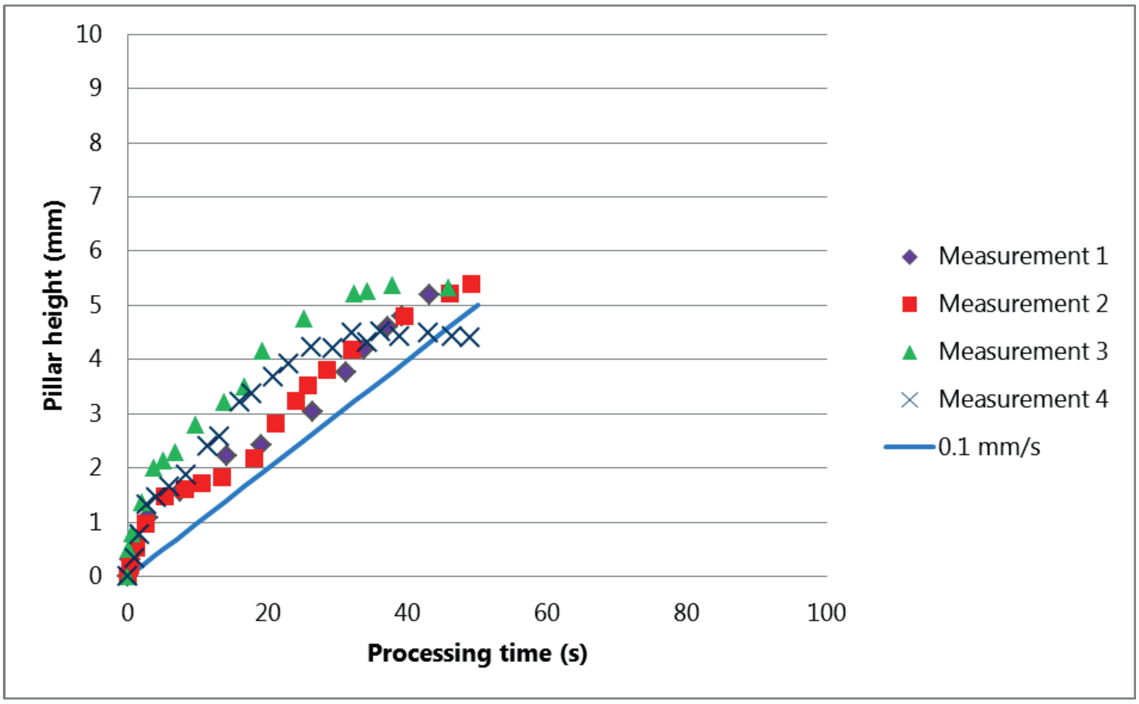

Figure 5-5. Reproducibility of the measurement of pillar height as a function of processing time for a feed rate of 1.0 g/min and a stage speed of 0.1 mm/s. The straight blue line would show the theoretical pillar height vs. processing time if the building rate was controlled by the stage speed of 0.1 mm/s.

Figure 5-6-Figure 5-9 show typical high-speed camera sequences of pillars building. The pillars appear in white and shades of grey in the image due to their emissivity in the visible wavelengths at high temperature. At the selected high-speed camera sensor exposure, it was not possible to distinguish the solid and the liquid phases, as the saturation level of the CCD sensor, marking the maximum pixel brightness to 255, corresponded to a temperature below the melting point. In the figures, the laser beam location is indicated by a red area, the powder feeding direction by a large grey arrow and the wafer surface by a grey horizontal straight line. Below the wafer, the heating plate is visible as it also emits in the visible light at a temperature of 850°C. The stage was programmed to move 5 mm in the z direction, indicated by a blue arrow. The yellow lines delimitate the area of the powder stream.

In Figure 5-6, the pillar was built at a stage speed of 0.3 mm/s and a feed rate of 15.0 g/min. First, the deposited silicon formed a viscous droplet at the top of the wafer surface, judging by its dynamics in the film recorded by the camera (the oscillations of the droplet were visible in the recorded movie). This droplet tipped slightly during the first three seconds and then stabilized. The pillar grew at a constant speed during the rest of the process. In this case, the center of the powder stream was always aligned with the tip of the pillar.

In Figure 5-7, the pillar was built at a stage speed of 0.1 mm/s and a feed rate of 1.0 g/min. As previously, the deposited silicon first formed a droplet at the top of the wafer surface at the laser beam location. This droplet enlarged and tilted on the side in the direction of the powder feed flow during the first 8 seconds and stabilized. Then, the pillar grew in the direction of the powder stream and the location of the laser beam.

In Figure 5-8, the pillar was built at a stage speed of 0.0167 mm/s and a feed rate of 15.0 g/min. As already previously observed, the deposited material formed a droplet at the wafer surface. Then, the pillar rapidly grew until its tip reached the edge of the powder stream. Afterward, its building rate decreased. Melt spattering was also observed at 3.850 s.

In Figure 5-9, the pillar was built at a stage speed of 0.3 mm/s and a feed rate of 1.0 g/min. As previously observed, the deposited silicon formed a viscous droplet at the top of the wafer surface. This droplet grew bigger and tilted on the side in the direction of the powder flow during the first 9 seconds and then stabilized. After 5 seconds, the pillar stopped growing. Melt spattering was observed at 7.740 s, most probably induced by the powder stream blowing off parts of the melt. Towards the end of the process (duration 20 s), the pillar stopped growing even if the powder was still arriving on the processing zone.As the pillar grew, the tip of the pillar became misaligned with the center of the powder stream.

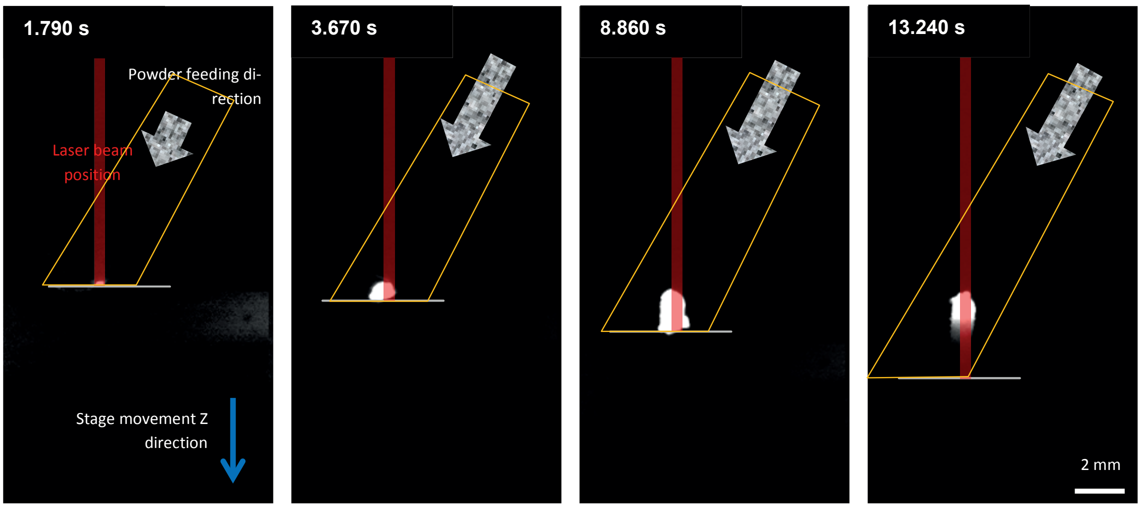

Figure 5-6. High-speed camera imaging of a pillar during its building at a stage speed of 0.3 mm/s and a feed rate of 15.0 g/min. The numbers in the top left corner indicate the recording time during the process. The yellow area indicates approximately the area of the powder stream.

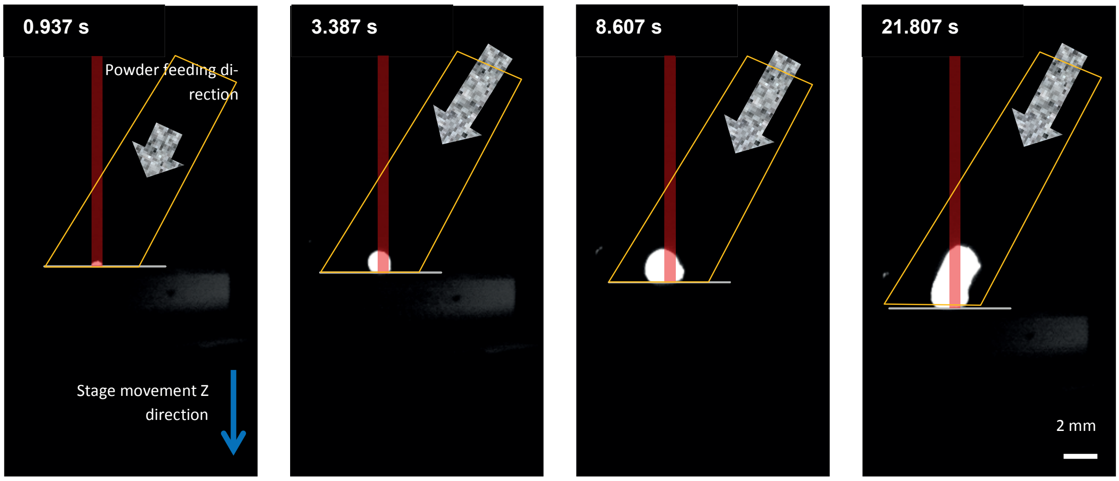
0.937 s
Powder feeding direction
Stage movement Z direction
3.387 s
8.607 s
21.807 s
2 mm

Figure 5-7. High-speed camera imaging of a pillar during its building at a stage speed of 0.1 mm/s and a feed rate of 1.0 g/min. The numbers in the top left corner indicate the recording time during the process. The yellow area indicates approximately the area of the powder stream.

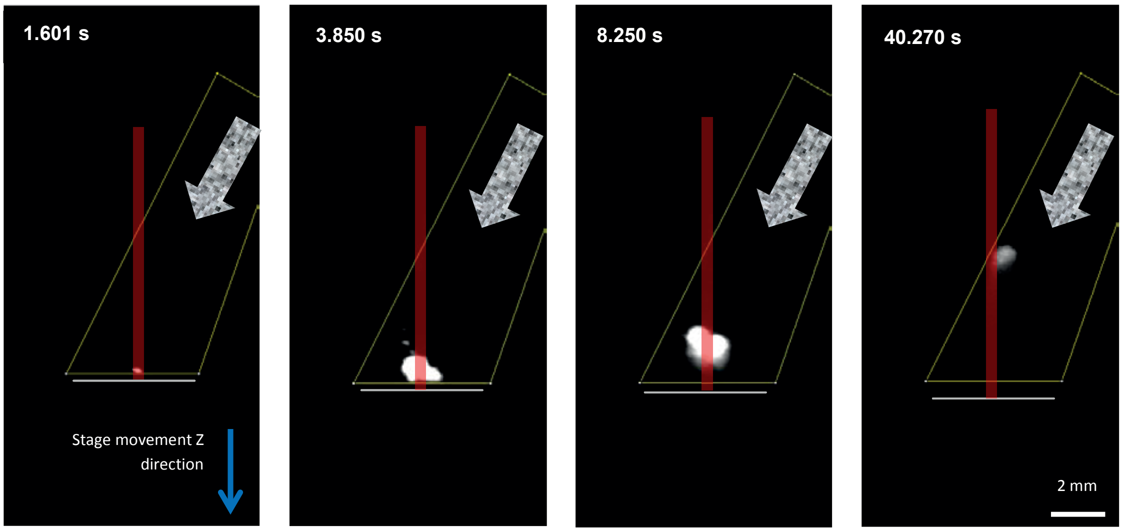
1.601 s
Stage movement Z direction
3.850 s
8.250 s
40.270 s
2 mm

Figure 5-8. High-speed camera imaging of a pillar during its building at a stage speed of 0.0167 mm/s and a feed rate of 15.0 g/min. The numbers in the top left corner indicate the recording time during the process. The yellow area indicates approximately the area of the powder stream.

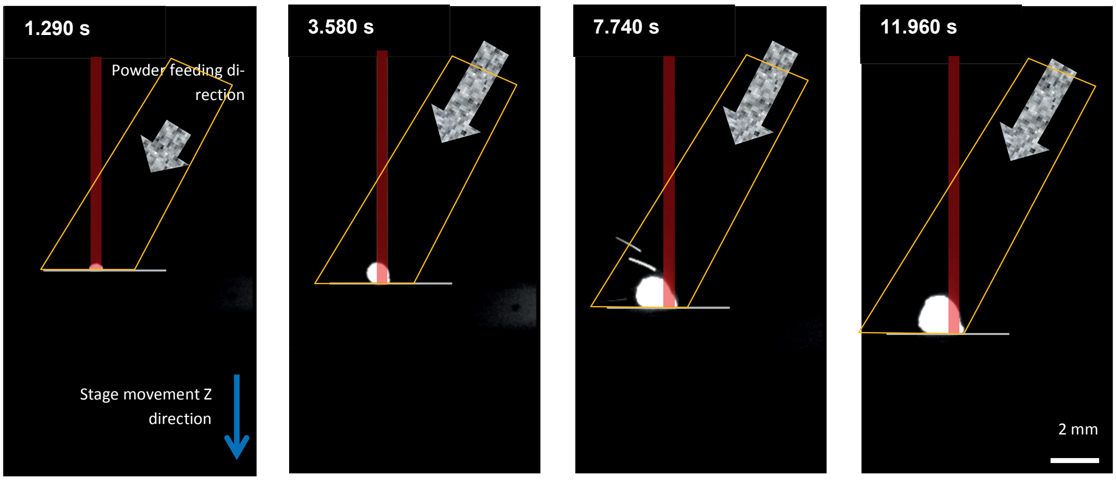

Figure 5-9. High-speed camera imaging of a pillar during its building at a stage speed of 0.3 mm/s and a feed rate of 1.0 g/min. The numbers in the top left corner indicate the recording time during the process. The yellow area indicates approximately the area of the powder stream.

Figure 5-10 (a) shows the pillar height as a function of processing time measured on the high-speed camera images for pillars built with a feed rate of 15.0 g/min at different stage speeds. For the three different stage speeds, the same steady speed of about 0.3 mm/s was observed from 0 to 20 seconds. After 20s, the pillar processed at 0.3 mm/s was completed. For a stage speed of 0.1 mm/s, the building rate decreased to 0.1 mm/s after about 25 s, and decreased to 0.023 mm/s for the stage speed 0.0167 mm/s. The expected pillar height of 5 mm was met only when the stage speed was adjusted to 0.3 mm/s. In this case, the average pillar building speed was 0.3 mm/s. Otherwise, the pillar grew taller.

Figure 5-10 (b) shows the pillar height as a function of processing time for different stage speeds at a feed rate of 1.0 g/min. The pillars heights were measured on the high-speed camera images. From 0 to 3 s, a high pillar building rate of about 0.3-0.5 mm/s was observed for all stage speeds. From then, for a stage speed of 0.3 mm/s (images are shown in Figure 5-9), the pillar stopped growing, whereas a relatively steady speed of 0.03 mm/s was observed in the case of 0.0167 mm/s and 0.1 mm/s. A higher speed of about 0.1 mm/s in average was recovered from the second 20 for the stage speed 0.1 mm/s (images shown in Figure 5-7). As a reminder, the stage was programmed to move 5 mm in the z direction at the chosen speed. Therefore, the expected pillar height of 5 mm was met only when the pillar was built at a stage speed of 0.1 mm/s. In this case, the average pillar building speed was 0.1-0.2 mm/s.

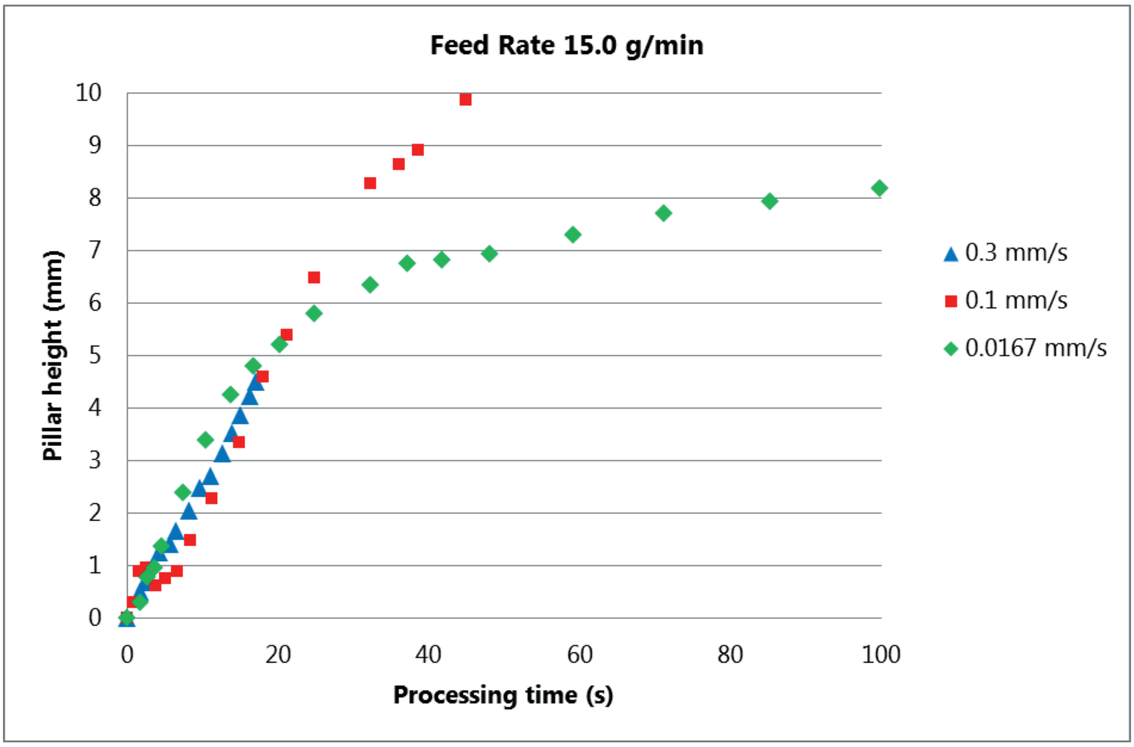

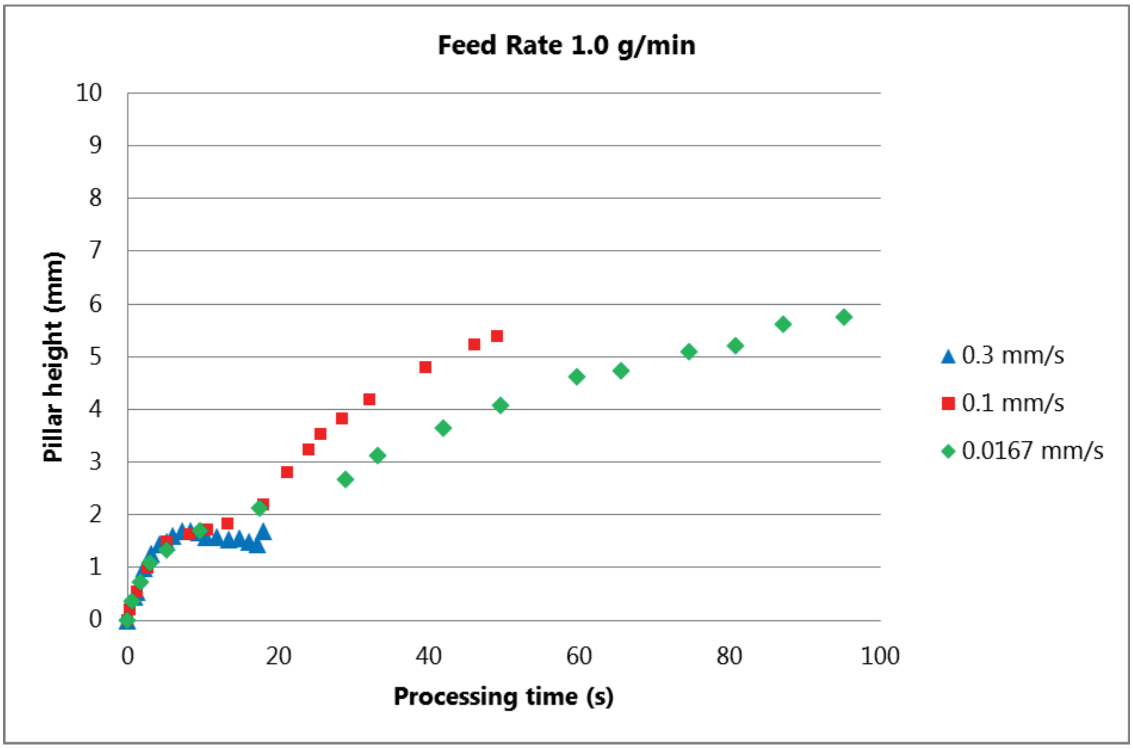

Figure 5-10. (a) Pillar height as a function of processing time for different stage speeds. The feed rate is 15.0 g/min. (b) Pillar height as a function of processing time for different stage speeds. The feed rate is 1.0 g/min. The dashed black line indicates the expected height of the pillar at the end of the process. For measurements at a stage speed of 0.0167 mm/s, only a third of the process is shown as the time was too long to be able to record it with the camera.

Figure 5-11 shows the pillar height as a function of processing time for a stage speed of 0.0167 mm/s and varying feed rates of 15.0 and 1.0 g/min. The blue linear curve shows the expected pillar height as a function of time if the pillar building rate was controlled by the stage speed.

In both cases, three building phases could be identified (marked 1, 2 and 3 in Figure 5-11). At 15.0 g/min, in the first phase, the pillar grew at the rate of 0.3 mm/s up to about 14 s. From 14 to 37 s, the building rate slowed down. Then, it approximately followed the stage speed after about 37s of building. A similar behavior was encountered for the feed rate 1.0 g/min. Phase 1 was shorter and last only 3 s at the same building rate of 0.3 mm/s. In phase 2, the rate slowed down up to about 60 s. In phase 3, the building rate followed the stage speed.

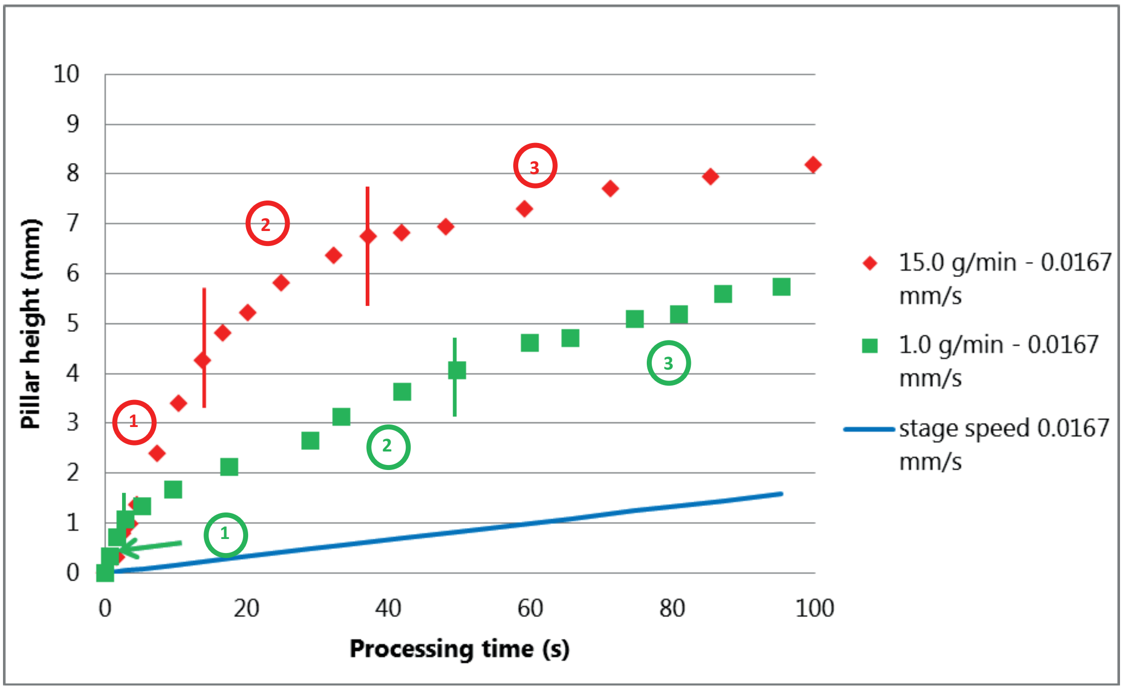

Figure 5-11. Pillar height as a function of processing time for a stage speed of 0.0167 mm/s for different feed rates. The plain blue lines would show the theoretical pillar height vs. processing time if the building rate was controlled by the stage speed indicated in the legend. The vertical lines delimitate the regions 1, 2 and 3 for each case.

5.1.2. Discussion

First, the two powders presented a large particle size distribution, with especially a large portion of small particles (Figure 5-1), and irregular particle morphologies (Figure 5-2 and Figure 5-3). These characteristics were consistent with their poor flowability. The poor flowability of the powder justified the use of a large nozzle diameter (3 mm) for the powder delivery. However, due to the wide nozzle diameter compared to the laser beam diameter, the yield of the building process was very poor. Indeed, in the current conditions, it varied from 0.08% for the highest feed rate used (15.0 g/min) to 2.5% for the lowest feed rate (1.0 g/min).

The values of mass per burst in time corresponding to the different feed rates were sufficiently separated from one another throughout the pillar building time, which allowed us to study the influence of the feed rate on the pillar build up. Indeed, image analysis of the powder stream revealed that the feed rate was homogeneous at low values. Figure 5-4 showed that only the 2 first powder bursts were higher by a factor 2 for the feed rate 3.4 g/min and by a factor 4 for the feed rate 1.0 g/min compared to the rest of the sequence. The subsequent burst masses had a constant value in time. For a feed rate of 15.0 g/min, the mass per burst increased during the first seconds and then decreased, but remained at least three times higher than the lower feed rates.

In the first three seconds of processing, the building rate was independent of the feed rate and the stage speed: it remained at about 0.3-0.5 mm/s for any tested experimental condition. However, it could be expected that the difference in burst size from one feed rate to another makes a difference during these first 3 seconds. In the case of low feed rate (1.0 g/min), it was described in Figure 5-4 that two high weight primary bursts were present at the beginning of the powder feeding. Nevertheless, these two bursts constituted only 400 ms of powder feeding, which is not enough time to cover the 3s of high building rate. Moreover, these two bursts were still significantly lower in weight than the bursts of the 15.0 g/min feed rate. The reason why the building rate is independent of the feed rate and the stage speed during the 3 first seconds of the process is still under investigation. However, one main scenario has been thought of. When the process begins, both feed rates could be too high for the primary size of the melt pool (diameter less than 600 µm, as seen in Chapter 4). In this case, the amount of powders that can be incorporated and melted by the melt pool would be limited by the amount of energy available to do so. The powders that could not be incorporated would be blown away by the transport and the shielding gases. After the melt pool has become larger and that its temperature has increased (see the second part of this chapter), more energy would be available to incorporate the powders, and the amount of powder incorporated would be now limited either by the powder burst size monitored by the feed rate or the amount of energy available in the melt pool, which also depends on the amount of laser light shielded by the powder and the process of powder incorporation into the melt pool, as discussed in Section 5.1.2.1 Moreover, the cooling of the melt pool is expected to be less efficient in case of low feed rates, as a smaller density of “cold” powders constitute the powder burst. Therefore, the melt pool size and temperature are likely to rise even more in this case.

Except for the three first seconds, the building patterns are different for high and low feed rates for the rest of the process. Within those two feed rate modes, three cases can occur: either the stage speed is optimized, too low, or too fast for the chosen feed rate. Those cases are explained in the next paragraphs.

5.1.2.1. The Case of Optimized Stage Speed

The high feed rate (15.0 g/min) helps the pillar cooling down due to the high amount of cold powder arriving on the melt pool, which results in only a small amount of tipping of the silicon droplet formed at the beginning of the pillar building, as shown by the high-speed images in Figure 5-6. This enables the pillar to be built with a relatively constant speed throughout the whole process as shown in Figure 5-10(a), as the center of the powder stream, is always aligned with the tip of the pillar, and there is no laser defocusing. In the case of 15.0 g/min, the optimized stage speed was 0.3 mm/s, leading to a pillar building speed of about 0.3 mm/s.

On the contrary, for low feed rates (1.0 g/min), the building rate can be divided into three stages, represented in Figure 5-12. The first stage is a high building rate of about 0.3 mm/s, explained earlier. In case of low feed rate, less cold powder hit the melt pool during the process due to the lower density of particles per burst. Subsequently, heat accumulates and keeps the droplet close to the liquid state longer than in the case of high feed rate. This results in strong tilting of the droplet, which slows down the building rate in stage 2. When the droplet is finally sufficiently cooled to stop being blown away by the powder stream, the pillar continues its building at an average speed of 0.1 mm/s until the end of the process, with a slight acceleration from 20s due to partial recovery of the laser focus (stage 3). This situation is schematized in Figure 5-12. The optimized stage speed for a feed rate of 1.0 g/min is 0.1 mm/s. In this case, the average pillar building speed was 0.1-0.2 mm/s.

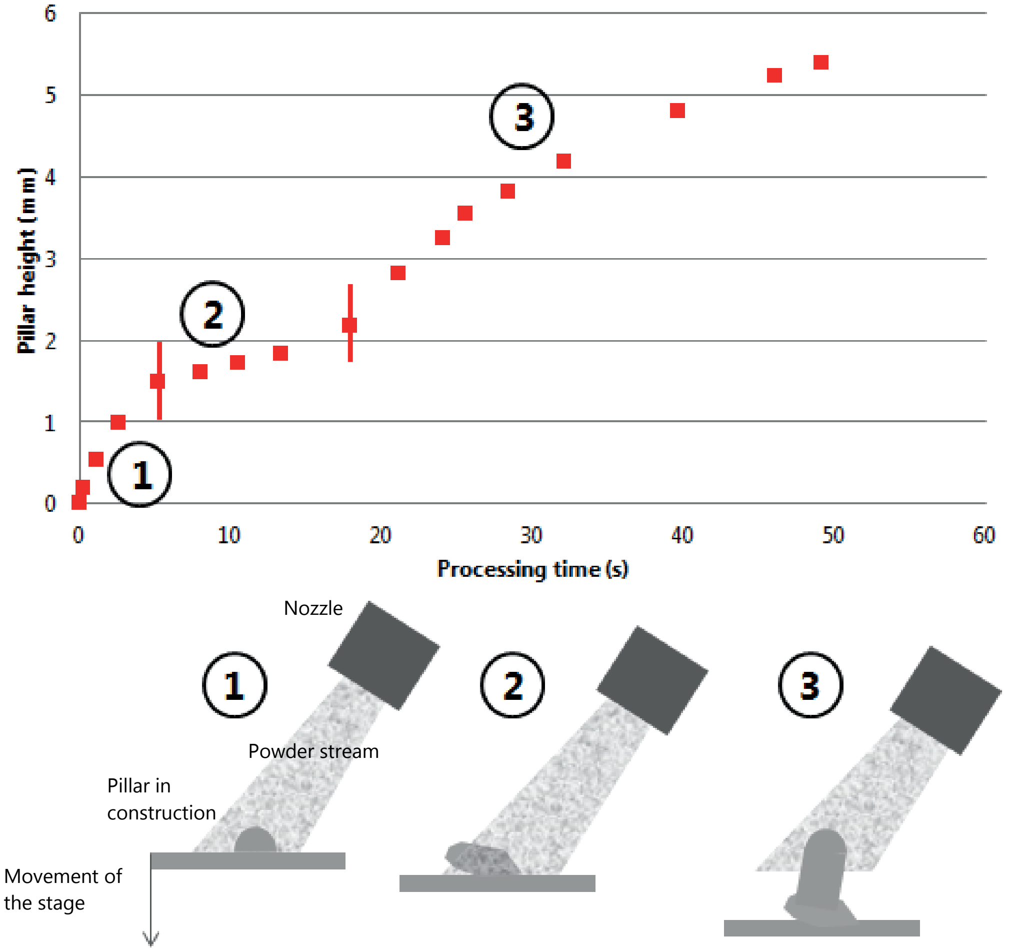

Figure 5-12. Schematic summarizing the building of a pillar built at low feed rate at an optimized stage speed. (1) Formation of a silicon droplet on top of the wafer (2) Tipping of the droplet due to powder and argon gas blowing (3) rapid building due to focused large powder stream. The vertical red lines delimitate the regions 1, 2 and 3.

Simple calculations allow the theoretical determination of the building rate for a feed rate of 15.0 g/min and 1.0 g/min, to be able to compare with the experimental results. A certain amount of hypotheses had to be considered to carry out these calculations:

- No laser shielding (light diffusion, scattering, absorption) by the powder is included
- We considered the values of melt pool temperature and volumes calculated by FEM and presented in Figure 4-7
- The heat capacity of liquid Si is constant with temperature

- We considered individual laser pulses and powder bursts
- The temperature increase with pillar height not taken into account
- The powders are at room temperature when they reach the melt pool
- The powder burst results in the deposition of a homogenous layer of powder over an area of 5 mm diameter around the melt pool (Figure 5-13 shows the trace left by a powder jet on a wafer).

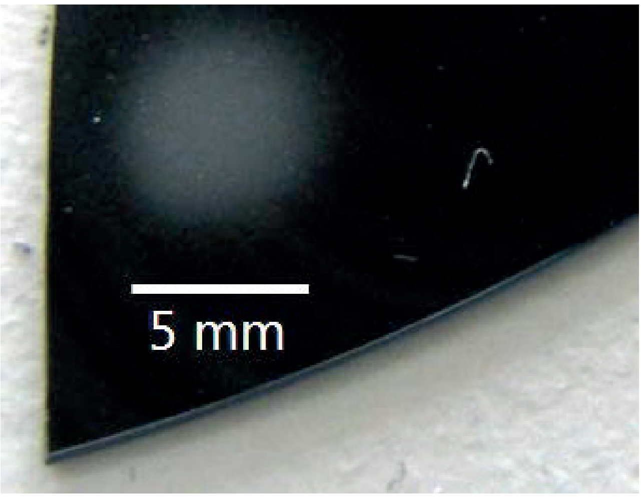

Figure 5-13. Photo of the trace left by the powder jet on a wafer.

First, one needs to calculate the theoretical thickness of silicon added to the melt pool for the different feed rates. In a first step, the flux of powder F per area during 1 burst is calculated:

$$\mathrm{F} = \frac{\mathrm{m}_i}{t_b A_n} \qquad (5\text{-}1)$$

Where m_i mass per burst, t_b burst duration (equal to 100 ms) and A_n nozzle cross-section area (here taken as 5 mm diameter from observations of the area affected by the powder burst on the wafer during the process).

From this data, the maximum mass per burst m_{max} reaching the melt pool is calculated:

$$m_{max} = F t_b A_{mp} \qquad (5\text{-}2)$$

Where A_{mp} is the melt pool area. The theoretical thickness per burst h obtained if it is considered that the powder is homogeneously distributed over the melt pool area is:

$$h = \frac{m_{max}}{d_{Si} A_{mp}} \qquad (5\text{-}3)$$

with d_{Si} is the silicon density.

The results of expected layer thicknesses are displayed in Table 5-1 for each feed rate.

Feed Rate (g/min)	Powder flow at the wafer level (g/cm^2s)	Maximum mass reaching the melt pool (µg)	Corresponding layer thickness (um)	Corresponding pillar growth rate (mm/s)
1.0	0.168	48	72	0.36
15.0	2.5	705	1000	5.4

Table 5-1. Theoretical bulk silicon layer thickness per burst calculated for the feed rates 1.0 and 15.0 g/min.

However, the melt pool can incorporate only a limited amount of powder corresponding to the energy contained in the latter. For the condition 200 Hz – 160 mJ, for which a maximum melt pool temperature of 2500 K was calculated (see Chapter 4, Figure 4-7), the energy contained in the melt pool volume of $4.5.10^{-6}$ cm^3 (calculated from the FEM model presented in Figure 4-7) is:

$$Q = mCp\Delta T = 0.014 \text{ J} \qquad (5\text{-}4)$$

As the energy necessary to melt one gram of silicon from room temperature is $Q_l = 986 J/g$, it is possible to melt 14 µg of powder per laser pulse, or 280 µg/powder burst maximum. 280 µg corresponds to a theoretical silicon thickness of 400 µm, according to equation 5-3.

Therefore, in case of low feed rate, the maximum mass of powder per burst reaching the melt pool being lower than the maximum mass that the melt pool is capable of melting suggests that the building rate of the pillar is limited by the amount of powder reaching the melt pool. On the contrary, at high feed rate, the building rate is in the ideal case limited by the amount of powder that the melt pool can incorporate.

It follows that the expected pillar building rate R is:

$$R = \frac{h}{2t_b} \qquad (5\text{-}5)$$

The above calculations have been carried out for feed rates of 1.0 and 15.0 g/min and the results are displayed in Table 5-1.

Feed Rate (g/min)	Powder flow at the wafer level (g/cm^2s)	Maximum mass reaching the melt pool (µg)	Corresponding layer thickness (um)	Expected building rate (mm/s)	Experimentally observed building rate (mm/s)
1.0	0.168	48	72	0.35	0.3-0.5 (5 first seconds) 0.1-0.2 (average)
15.0	2.5	705	400	2	0.3

Table 5-2. expected building rates calculated for the feed rates 1.0 and 15.0 g/min. The expected building rate for a feed rate of 1 g/min is limited by the amount of powder reaching the melt pool and the expected building rate for a feed rate of 15 g/min is limited by the amount of powder that can be incorporated into the melt pool (melt pool size and energy)

The expected building rate of 0.35 mm/s is in good agreement or lower than the experimentally observed growth speed for 1.0 g/min at the beginning of the building that is about 0.3-0.5 mm/s as shown in the last column of table 5-2 (and Figure 5-5). The estimated powder supply into the melt pool can therefore be higher than the estimated 48 µg per burst probably due to a higher particle density in the inner part of the powder burst as compared to the assumption of having a homogeneous powder distribution in the burst. With increasing deposition time and pillar growth, tilting of the “droplet” at the beginning of the process slows down considerably the building speed after 5 s, resulting in an average building rate of 0.1-0.2 mm/s by using the optimized stage speed of 0.1 mm/s (Figure 5-12). On the other hand this rough estimation shows that all the powder reaching the melted surface is caught and adds to the melt.

In the case of 15 g/min, the expected building rate found in the calculations (2 mm/s) is much higher than the optimized building speed found experimentally (0.3 mm/s using the optimized stage speed of 0.3 mm/s). However, several other contributions neglected in the model severely affect the building rate. First, during incorporation of the particles into the melt pool, the first particles to reach will be in contact with the liquid whereas the following particles may ripple on their predecessor and not be incorporated (see Figure 5-14). The efficiency of the powder incorporation also depends on the efficiency of the mass flows within the melt pool (Marangoni effect). Secondly, stronger shielding of the laser beam during the powder burst occurs. In this case, the laser radiations can be absorbed, scattered or diffusely reflected by the powders (Figure 5-14). In case of absorption, the powders can be heated by the laser beam before being incorporated into the melt pool. However, most of these heated powders are probably not incorporated into the melt pool as only the top of the powder burst absorbs the radiations. In this case, the energy available to form the melt pool is lower than the theoretical predictions.

The cooling of the melt pool created by the transport gas, and the poor thermal conductivity of the powders are also phenomena that can reduce the amount of energy present in the melt pool and slow down powder melting, which gives more time for the coming particles to ripple on the partially incorporated ones.

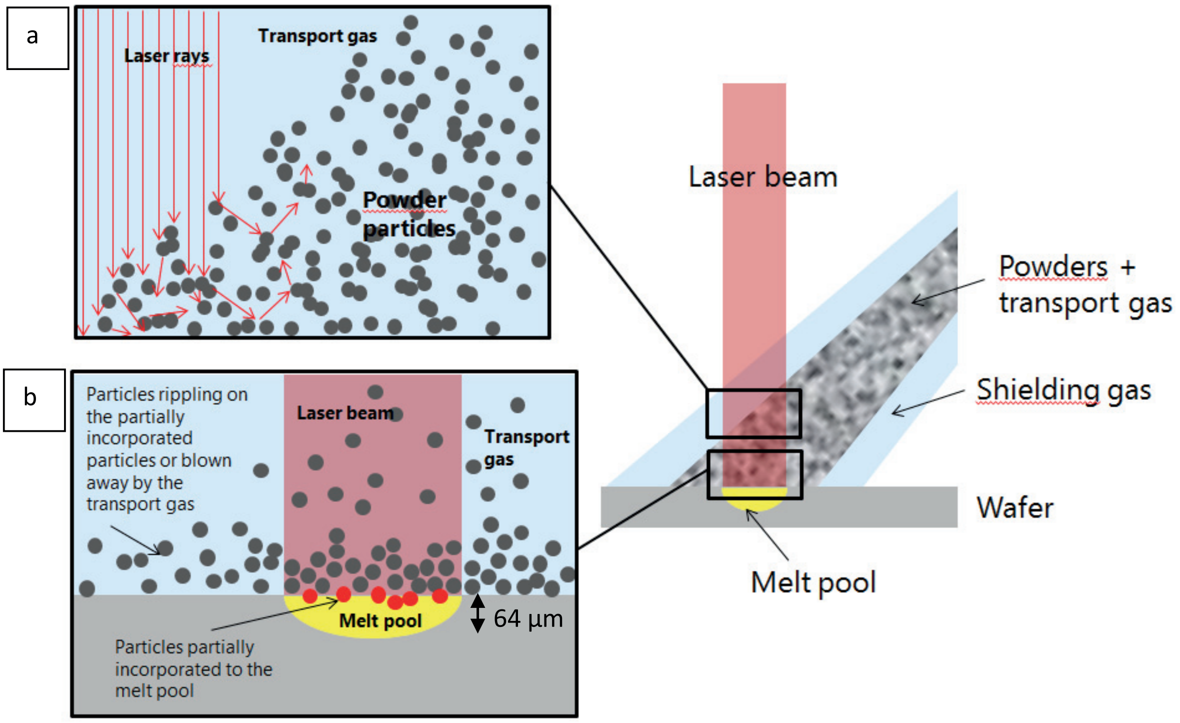
a
Laser rays
Transport gas
Powder particles
b
Particles rippling on the partially incorporated particles or blown away by the transport gas
Laser beam
Transport gas
Melt pool
64 µm
Particles partially incorporated to the melt pool
Laser beam
Powders + transport gas
Shielding gas
Wafer
Melt pool

Figure 5-14. Schematic of the two phenomena occurring during pillar building not taken into account in the theoretical calculations. (a) Laser shielding by light diffusion, scattering or absorption in the powder at the top of the powder burst. (b) The particles arriving at the melt pool can ripple on the partially incorporated particles.

Therefore, the amount of powder that the melt pool can incorporate is actually much lower than the calculated one. These phenomena can explain the high theoretical expected building rate comparedto the experimental findings However, as fluctuations on the building rate and the pillar height are encountered within the same set of experimental parameters during the process (due to powder fluctuation, nozzle alignment…), case by case the experimental results can deviate from these theoretical predictions.

5.1.2.2. The Case of Insufficient Stage Speeds

Let us assume that the particle density within the powder burst is Gaussian. Therefore, the powder density is high in the middle of the stream and decreasing at the edges. In both cases, three regions could be identified, as displayed in Figure 5-11.

For high feed rates (15.0 g/min), the angle formed by the powder stream is wide due to the high particle density per burst (Figure 5-4). Therefore, the melt pool is fed correctly up to a certain pillar height, as long as the tip of the pillar remains within the powder stream (up to about 20 s in Figure 5-11) (phase 1). After 20 s, the tip of the pillar meets the edge of the powder stream because the stage is not moving fast enough to compensate the high building rate of the pillar. At this point, the melt pool can only be fed at the speed of the stage. Moreover, strong defocusing of the laser (due to a pillar building speed almost 15 times higher than the stage speed), decreases the amount of energy available to melt the powders. These effects result in a slowdown of the building rate (phase 2) up to matching the stage speed (phase 3), as shown in Figure 5-11. Slight decrease in the weight per burst (Figure 5-4) can also contribute to the speed decrease.

For low feed rates (1.0 g/min), the area formed by the powder stream is smaller due to a lower powder density per burst (Figure 5-4). Tipping of the droplet (or dropping of liquid silicon) triggers speed decrease after the high building rate of phase 1 (explained earlier). Phase 2 is a similar effect as for the high feed rates but for a longer amount of time. In phase 3, the building rate matches the stage speed due to reaching the edge of the powder feed area.

5.1.2.3. The Case of too High Stage Speeds

As described in chapter 3, the powder stream is pulsed. The powder is fed to the melt pool for 100 ms and stops for 100 ms. Therefore, if during the 100 ms where no powder is added the stage covers more distance than the height of the previously added layer, laser defocusing occurs at the tip of the pillar (the stage speed being too fast compared to the building speed). The laser energy becomes insufficient to melt the supplied powder and to maintain the melt pool. Moreover, fewer amount of powder is available to be melted due to powder stream misalignment (Figure 5-9). This is the case presented in Figure 5-10 (b). Indeed, for a feed rate of 1.0 g/min, the optimized stage speed was 0.1 mm/s. Therefore, during a cycle of 200 ms, 0.02 mm is ideally added to the tip of the pillar to form a new layer. If now the stage speed is 0.3 mm/s, 0.02 mm is added during 100 ms of powder feeding, and the stage goes down 0.3 mm during the next 100 ms. Therefore, progressive laser and powder defocusing occurs, leading to decrease of the building rate.

As mentioned earlier in the case of low feed rates, the primary droplet formed on the wafer surface tilts significantly due to powder feed blowing. This effect slows down the building rate and finally prevents the pillar growth completely.

5.1.3. Conclusion

The feed rates are sufficiently stable that they can be considered homogenous through the process. Therefore, the effect of the variation in feed rate weight per burst within the same powder feeder parameters will be neglected, and the feed rate will be considered homogeneous for the rest of the study. The influence of feed rate individual burst variations on the pillar building can be studied in the future. More precise in-situ feed rate monitoring is under development using acoustic measurements.

To achieve the most stable pillar building rate, the stage speed should be adjusted to 0.3 mm/s for a feed rate of 15.0 g/min and 0.1 mm/s for a feed rate of 1.0 g/min. Otherwise, variations in pillar building rates are encountered when the stage speed is either too slow or too fast compared to the optimized speed. Those variations in pillar building rates could be avoided by using a more focused powder stream. However, the large opening employed for this study was justified by the poor flowability of the silicon powders. We believe that this problem can be solved in the future by spheroidizing the silicon powder, which would lead to better flowability and therefore the possibility to use a smaller nozzle diameter.

5.2. Thermal History of the Process and Pillar Shape

In this part, thermal characteristics throughout the pillar structure and resulting pillar shape will be discussed. Details of the simulation methods and hypotheses are given in Chapter 3.6.2.

5.2.1. Results

Temperature, thermal gradients (G) and heat flux direction during the pillar building were calculated using FEM simulation with Abaqus 2017[104] for different pillar heights by building a 3D pillar model. In this model, the pillar was built using "birth" element method[103] at a constant speed of 0.1 mm/s. The substrate temperature was 980°C. Heat conduction, radiation and forced convection due to argon cooling on the sides of the pillar were taken into account. The phase transition from solid to liquid was modeled. An energy source was set at the top of the pillar to model the average power of the laser. The diameter of the pillar was set to 600 µm. The temperature fields, thermal gradients, and heat flux directions were calculated at different processing times. The details of the simulation method are described in Chapter 3.6.2 and 3.6.1.

Figure 5-15(a) shows the quarter of the pillar used to model the pillar building. The temperature was measured along the path denoted by the red line in the center of the pillar, as represented in Figure 5-15(a). The results are shown in Figure 5-15(b) for building times of 1, 2, 3.3, 4 and 6s, which correspond to respective heights of 0.1, 0.2, 0.33, 0.4 and 0.6 mm. For each of the pillar heights, a plateau of temperature was observed in the liquid phase on a length of about 100 µm from the tip of the pillars. Then, the temperature decreased gradually. The liquid zone widened as the pillar grew, and the temperature of the melt pool increased as well. The thermal gradients remained very high throughout the building process, in the order of 10^6 K/m. The thermal gradients reduced from 2.10^6 to 10^6 K/m as the pillar grew from 0.1 to 0.6 mm. As the pillar diameter was fixed and set as a boundary condition, no expansion of the pillar diameter was allowed in the simulations.

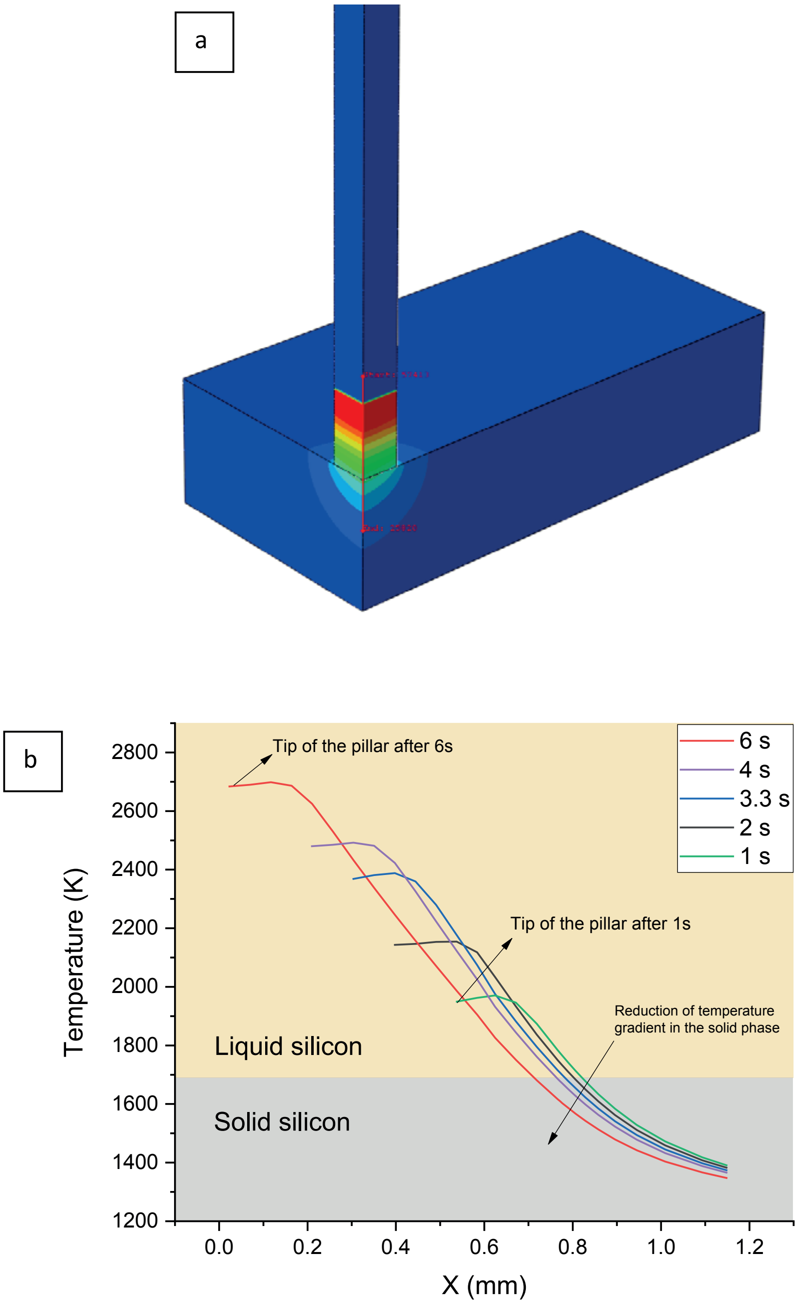

Figure 5-15. (a) Geometrical model of the pillar used to model the Si pillar building. The red line indicates the path used to plot thermal gradient. (b)Temperature along the path for different pillar heights (for building times ranging from 1 to 6 s). The building rate was 0.1 mm/s.

Figure 5-16 displays the results of the FEM calculations of the radial and vertical components of the heat flux during the building of the silicon pillar. Note that the vertical z-axis is oriented positively towards the bottom of the wafer. Each frame (a), (b) and (c) shows the radial contribution to the heat flux for pillar heights of 0.1, 0.3 and 0.6 mm. Frames (d), (e) and (f) show the vertical component to the heat flux for pillars of the same heights. At the beginning of the building, both radial and vertical heat flux contributions were high, of the order of 10^3-10^5 W/m^2. As the pillar builds up, the radial heat flow located a little bit below the pillar tip increased as the pillar height increased. On the contrary, the vertical heat flow component reduced as the pillar built up. These contrary trends led to more and more oblique heat flux stream lines at the sides of the building pillar. However, the vertical heat flux stayed one to two orders of magnitudes higher than the radial flux. The direction of the heat flux remained perpendicular to the wafer substrate at the center of the pillar as the pillar height increased as only a very weak (1-10^2 W/m^2) radial flux existed. A small vertical heat flux consistently exists at the top of the pillar throughout the process.

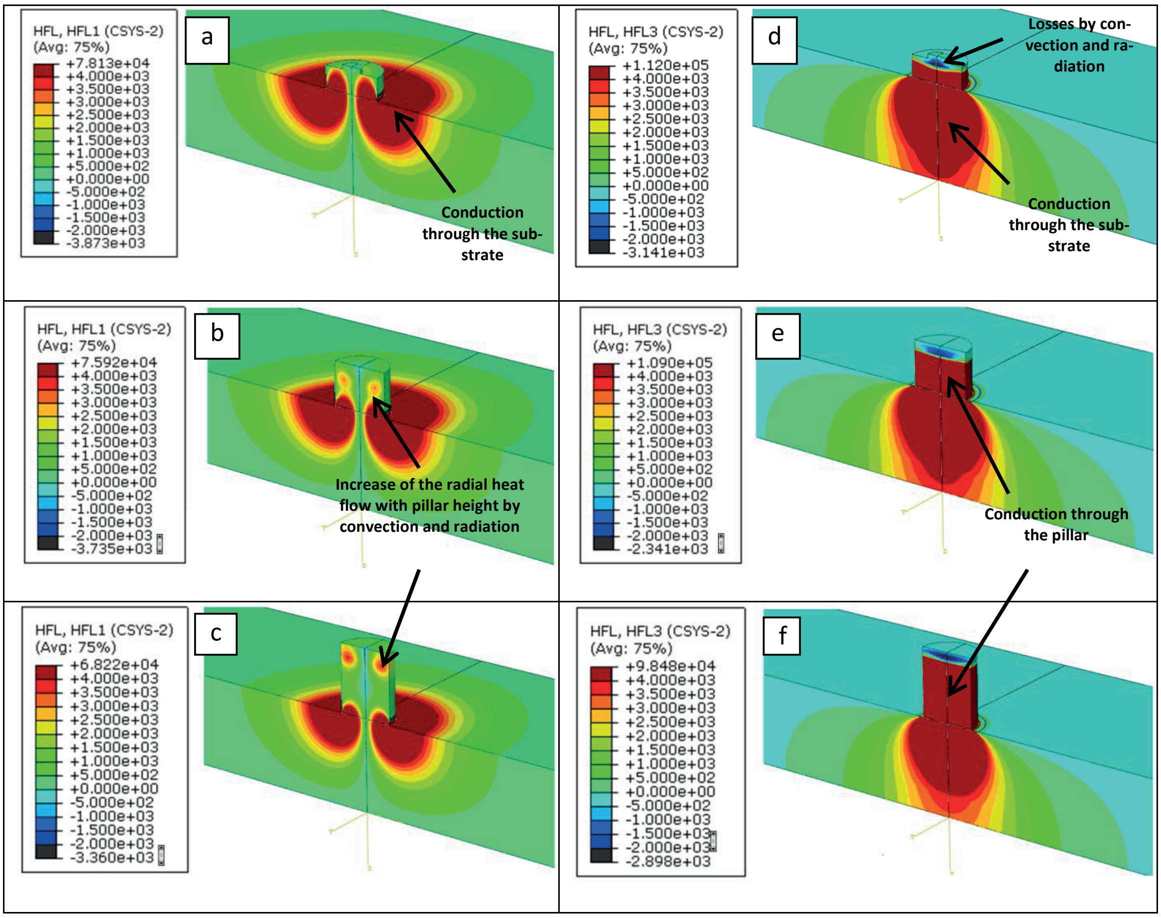
a
HFL, HFL1 (CSYS-2)
(Avg: 75%)
+7.813e+04
+4.000e+03
+3.500e+03
+3.000e+03
+2.500e+03
+2.000e+03
+1.500e+03
+1.000e+03
+5.000e+02
+0.000e+00
-5.000e+02
-1.000e+03
-1.500e+03
-2.000e+03
-3.873e+03
Conduction through the substrate
d
HFL, HFL3 (CSYS-2)
(Avg: 75%)
+1.120e+05
+4.000e+03
+3.500e+03
+3.000e+03
+2.500e+03
+2.000e+03
+1.500e+03
+1.000e+03
+5.000e+02
+0.000e+00
-5.000e+02
-1.000e+03
-1.500e+03
-2.000e+03
-3.141e+03
Losses by convection and radiation
Conduction through the substrate
b
HFL, HFL1 (CSYS-2)
(Avg: 75%)
+7.592e+04
+4.000e+03
+3.500e+03
+3.000e+03
+2.500e+03
+2.000e+03
+1.500e+03
+1.000e+03
+5.000e+02
+0.000e+00
-5.000e+02
-1.000e+03
-1.500e+03
-2.000e+03
-3.735e+03
Increase of the radial heat flow with pillar height by convection and radiation
e
HFL, HFL3 (CSYS-2)
(Avg: 75%)
+1.090e+05
+4.000e+03
+3.500e+03
+3.000e+03
+2.500e+03
+2.000e+03
+1.500e+03
+1.000e+03
+5.000e+02
+0.000e+00
-5.000e+02
-1.000e+03
-1.500e+03
-2.000e+03
-2.341e+03
Conduction through the pillar
c
HFL, HFL1 (CSYS-2)
(Avg: 75%)
+6.822e+04
+4.000e+03
+3.500e+03
+3.000e+03
+2.500e+03
+2.000e+03
+1.500e+03
+1.000e+03
+5.000e+02
+0.000e+00
-5.000e+02
-1.000e+03
-1.500e+03
-2.000e+03
-3.360e+03
f
HFL, HFL3 (CSYS-2)
(Avg: 75%)
+9.848e+04
+4.000e+03
+3.500e+03
+3.000e+03
+2.500e+03
+2.000e+03
+1.500e+03
+1.000e+03
+5.000e+02
+0.000e+00
-5.000e+02
-1.000e+03
-1.500e+03
-2.000e+03
-2.898e+03

Figure 5-16. Results of the simulation using FEM showing the radial (left side) component and vertical (right side) components (denoted by HFL1 and HFL3 of the heat flow throughout the pillar structure for different heights assuming a constant speed of 0.1 mm/s (a) (d) after 0.1 mm, (b) (e) after 0.3 mm and (c) (f) after 0.6 mm.

Figure 5-17 shows the picture of typical silicon pillars built on top of silicon wafers. Figure 5-17 (a) shows the photo of a pillar built with a feed rate of 15.0 g/min and a stage speed of 0.3 mm/s, laser parameters 200 Hz – 160 mJ. Figure 5-17 (b) shows a pillar built with a feed rate of 0.6 g/min and a stage speed of 0.1 mm/s, laser parameters 200 Hz – 160 mJ. Figure 5-17 (c) displays the cross-section of a pillar built with a feed rate of 1.0 g/min and a stage speed of 0.1 mm/s, laser parameters 50 Hz – 405 mJ. The pillar started building with a diameter of about 400 to 700 µm, depending on the size of the melt pool. At a feed rate of 15.0 g/min (stage speed 0.3 mm/s and laser parameters 200 Hz – 160 mJ), the pillar diameter increased from 0.58 to 1 mm after a height of 0.25 mm. At a feed rate of 1.0 g/min (stage speed 0.1 mm/s and laser parameters 200 Hz – 160 mJ), the pillar diameter increased rapidly at the pillar base. The diameter increase to 1.3 mm hid the necking. When the pillar was built with the same feed rate and stage speed conditions, but with laser parameters of 50 Hz -405 mJ, necking took place over 1 mm, and the diameter increased from 0.5 to 1 mm.

The pillars built with a low feed rate and laser conditions 200 Hz – 160 mJ also often presented a protuberance in the powder feeding direction. However, this characteristic was less prominent in the case of pillar built with a higher feed rate for the laser conditions 200 Hz – 160 mJ.

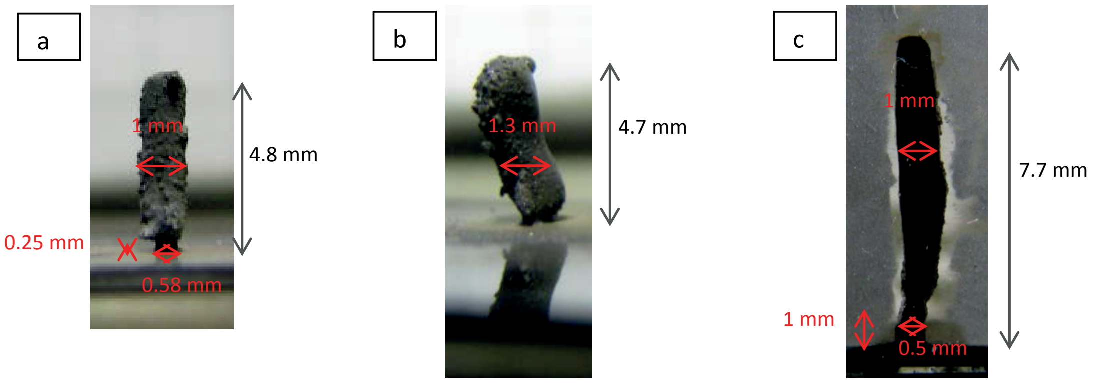

Figure 5-17. Typical shape of a silicon pillar built on a silicon wafer (a) built with a feed rate of 15.0 g/min and a stage speed of 0.3 mm/s, laser parameters 200 Hz – 160 mJ. (b) Pillar built with a feed rate of 1.0 g/min and a stage speed of 0.1 mm/s, laser parameters 200 Hz – 160 mJ. (c) Photo of a cross-section of a pillar built with a feed rate of 1.0 g/min and a stage speed of 0.1 mm/s, laser parameters 50 Hz – 405 mJ

5.2.2. Discussion

5.2.2.1. Thermal gradients and heat flux direction

The thermal gradients remain high through the building of the pillar due to the localized energy source provided by the laser. However, the gradients decrease once the pillar gets taller as revealed by the simulations results presented in Figure 5-15. For our system, the heat is lost mostly by conduction through the silicon wafer and pillar, hence the large (10^3-10^5 W/m^2) heat flow opposite to the build direction of the pillar present during the entire process. The thermal losses by convection (forced convection through the protective argon gas) and radiation (at high temperature) are contributing much less. Indeed, at the beginning of the process, the wafer acts as a heat sink. Therefore, thermal gradients are reaching values up to 10^6 K/m in the solid phase. As the pillar grows, losses by conduction are still dominating, but are lowered due to the pillar geometry. Indeed, the energy Q_{Cond} lost by conduction can be expressed as:

$$Q_{Cond} = \frac{kA(T-T_0)}{l} \qquad (5\text{-}6)$$

Where k is the thermal conductivity of silicon, A the cross-section of the pillar, $T - T_0$ the difference of temperature between the top and the bottom of the pillar and l the pillar length. Therefore, by having a small cross-section and an increasing length, thermal losses by conduction become smaller. This results in an increase in temperature in the melt pool, and particularly at the pillar tip. The temperature plateau (translated by low to negative thermal gradients) observed at the same location is due to the continuous energy input provided by the laser and the difficulty to evacuate it.

The thermal losses by convection and radiation increase as the pillar grow higher, as observed below the tip of the pillar in Figure 5-16. Thermal losses by conduction Q_R and convection Q_{Conv} are described by:

$$Q_{rad} = \varepsilon \sigma_{SB} A(T^4 - T_0^4) \qquad (5\text{-}7)$$

$$Q_{Conv} = hA(T - T_0) \qquad (5\text{-}8)$$

Where ε is the emissivity of silicon, σ_{SB} the Stefan-Boltzmann constant, h the convection coefficient, A the area of the pillar, T the temperature of the pillar and T_0 the temperature of the surrounding medium. According to equation 4-2, losses by radiation soar at high temperatures. Moreover, the pillar area increases as it grows. Therefore, as the pillar builds up, those two contributions become non negligible and so does the contribution of the radial component of the heat flow. The presence of a weak vertical heat flux at the tip of the pillar can also be explained by losses due to radiation and convection at the top of the melt pool.

5.2.2.2. Pillar shape

All pillars showed necking above about 0.3 mm from the base of the pillar, with a diameter of about 400-700 µm. After about 0.3 mm, the pillar diameter increased to about 1 mm, as illustrated in Figure 5-17. It was stated earlier, at the beginning of the process, heat losses by conduction are very efficient due to the heat sink formed by the wafer substrate. This phenomenon causes the melt pool to stay smaller or of the size of the laser beam up to a certain height. The efficiency of heat flow by conduction is reduced as the pillar grows higher. It leads to decrease of thermal gradients and an increase in temperature at the top of the pillar (Figure 5-15). As the heat cannot efficiently be released, the melt pool diameter increases and liquid silicon can run outside of the melt pool, sometimes causing droplets to run along the already solidified pillar. This statement is consistent with the results of the FEM calculations developed with Abaqus. Indeed, an increasing fraction of the pillar was in the liquid state as its height increases (Figure 5-15). However, in our model, no expansion of the pillar diameter was allowed to compensate for the amount of liquid produced by heat accumulation, even if it would be expected to expand already from a height of 0.2 mm (0.4 mm of liquid silicon). The laser depth of focus being quite large (over 1 mm, see chapter 3), it is believed that laser defocusing due to the speed fluctuations presented in the last section was not the primary reason for the increase in pillar diameter, even if it may contribute. Similar observations were found by Peyre et al.[17], who experimentally visualized and calculated the melt pool size at different layers of the DMD process. They found that the latter increased with increasing layer number, due to lower heat dissipation through the substrate.

The difference in height and diameter between a pillar grown with 200 Hz – 160 mJ and a pillar grown with 50 Hz- 405 mJ observed in Figure 5-17 can be explained by the difference in thermal management. Indeed, in the case of 50 Hz - 405 mJ, the energy per pulse is higher, but the time to cool down between the laser pulses is much longer (1 ms of laser pulse, 19 ms of cooling) than for the condition 200 Hz – 160 mJ (1 ms of laser pulse and 4 ms of cooling). Therefore, heat accumulation is higher in the latter case. This point is further discussed and demonstrated in Chapter 5. This phenomenon leads to a higher melt pool temperature, which leads to a larger melt pool diameter. Additionally, in the 50 Hz – 405 mJ case, larger cooling times between pulses (19 ms vs. 4 ms for the case 200 Hz – 160 mJ) enable the pillar to have time to solidify. Therefore, the droplet "tilt" observed with the high-speed camera in the case 200 Hz – 160 mJ (Figure 5-7) does not happen in the case 50 Hz – 405 mJ. This enables faster continuous building, close to the mechanism explained in the previous section for the pillars built with a feed rate of 15.0 g/min and stage speed of 0.3 mm/s, laser parameters 20 Hz – 160 mJ (Figure 5-6).

Pillars built with a low feed rate additionally present a protrusion in the direction of the powder feeding flow. This protrusion is consistent with the results presented in Figure 5-7, where it was found that a liquid droplet was formed at the beginning of the process. As a low feed rate leads to reduced laser shielding and lower melt pool cooling (see the previous section), the droplet is pushed to the side by the powder feeding flow. Subsequently, at the position where the melt pool is formed, i.e. at the laser position, the pillar is built.

The pillar diameter increase can also lead to further increase in contribution of the radial heat flow. Indeed, if the laser diameter is smaller than the pillar diameter, the heat flows along the melt pool radius, as illustrated in Figure 5-18.

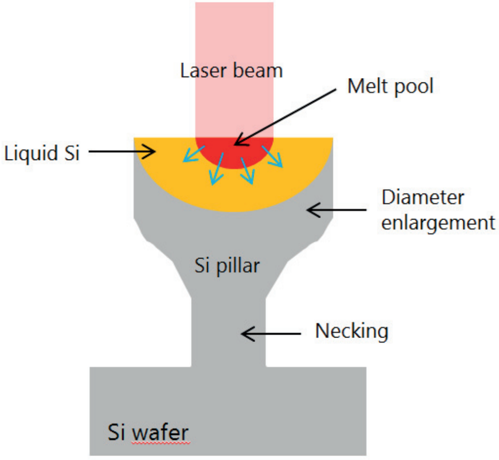

Figure 5-18. Schematic of the growing pillar showing the pillar diameter broadening. The blue arrows indicate the radial heat flux induced by the diameter broadening around the melt pool.

5.3. Remarks on the Relevance of the Native Oxide for DLM Processing

To complete the impurity analysis, the oxygen contents measured by combustion and infrared analysis for SP_98% and SP_4N are given in Table 5-3. Both powders exhibit a similar relatively low oxygen content. SP_4N contains slightly less oxygen (0.5 wt%) than SP_98% (0.78 wt%). This is probably linked to the lower surface-to-volume ratio of SP_4N compared to SP_98% due to larger particle size.

Powder name	Oxygen content
SP_98%	0.78 ± 0.03 wt%
SP_4N	0.5 ± 0.2 wt%

Table 5-3. Oxygen measurements by combustion and infrared analysis for Si_4N and Si_98%.

The powder native oxide did not prevent the building of pillars. No SiO_x inclusions have been observed in the pillar cross-section matrix. As the particles are incorporated into the melt pool, the native oxide presumably dissolves into the melt. Silicon monoxide (SiO), a product of the reaction between SiO_x and Si, has time to evaporate and leave the melt pool. If the temperature reaches more than 1000°C, the SiO_x can also decompose into SiO gas during transport as the laser beam hits the powder. Therefore, the native oxide was not detrimental to the process. The oxygen can be incorporated as interstitial oxygen impurities in Si crystal. However, we studied the influence of powder oxygen content on laser processing of silicon powder pellets, and we showed that the powder should be deoxidized to less than 0.1 wt% to obtain smooth laser tracks. These results suggested that deoxidation was necessary for silicon powder bed laser processing. The study is presented in Appendix D.

5.4. Conclusions and Perspectives

Despite the poor flowability of the powder used, the latter were successfully transported by using the powder feeder described in Chapter 3, and pillars were successfully built on silicon wafers.

The fluctuations in the building rate are avoided at maximum when the feed rate and the stage speed match (0.3 mm/s for 15 g/min and 0.1 mm/s for 1.0 g/min). The building rate was the most constant for large feed rates due to the reduction of heat accumulation. However, pillar diameter enlargement and eventual liquid drop were unavoidable due to difficulties in cooling the heat accumulated due to the increase in pillar height and decrease in heat sink cross-section. These problems must be tackled by diminishing the laser energy and/or frequency during pillar building. Adding a rotational stage could also help avoiding the formation of “bellies” due to the unidirectional powder feeding.

The thermal gradients stayed high throughout the process, of the order of 10^6 K/m. The vertical contribution to the heat flux was dominating, but the radial heat flux contribution also increased as the pillar grew. This phenomenon leads to offset of the heat flow from the build direction to close to the boundaries of the pillar and particularly near the top of the melt pool. This phenomenon could affect the pillar microstructure, as discussed in Chapter 6.2.3.

The native oxide present in the as-received powders did not hinder the pillar construction. However, the quantity of oxygen present in the powder can influence the silicon electrical and mechanical properties if it is incorporated in the material. This study was not the objective of the present dissertation, but can be explored in the future.

Chapter 6. Pillars Microstructure and Epitaxial Growth

As seen in Chapter 2.4.2, the quality and the capacity to maintain epitaxial growth through a crystal growth process (directional growth or laser cladding) depends on two main process characteristics: thermal gradients (G) and growth rate (V). These parameters should be carefully adjusted so that the growth mode stays columnar. Process parameters such as feed rate and substrate temperature, and laser parameters such as power and repetition rate have an influence on G and V.

As a reminder of the discussion in Chapter 2.4.2, Figure 6-1 displays the schematic of a microstructure map of silicon as a function of growth rate and thermal gradients. It allows the reader to visualize where the DLM process stands compared to standard growth techniques. The red zone corresponds to equiaxed dendritic growth mode, the blue zone corresponds to columnar faceted growth and the white zone is an intermediate zone. The blue and red lines delimitate the Columnar-to-equiaxed transition (CET) and equiaxed zone as calculated by Mangelinck et al.[51] The dotted white line represents the shift of CET at higher impurity concentrations. Delimitation of the zones above 10^3 K/m are only trend lines extrapolated from the CET calculated by Mangelinck-Noël et al. for Si and by Kurz et al.[48] for E-LMF of nickel-based superalloy and are only represented to give an idea of the microstructure map at high thermal gradients. The uniqueness of the DLM process consists in combining high thermal gradients and relatively high speeds (see Chapter 5). Czochralski and directional solidification growth combine low gradients[113] and low speeds[61]. These techniques can achieve epitaxial growth and quasi-mono silicon growth. Ribbon growth combines intermediate thermal gradients[114] and very high speeds[61] and produces polycrystalline samples either in the columnar or dendritic growth regions.

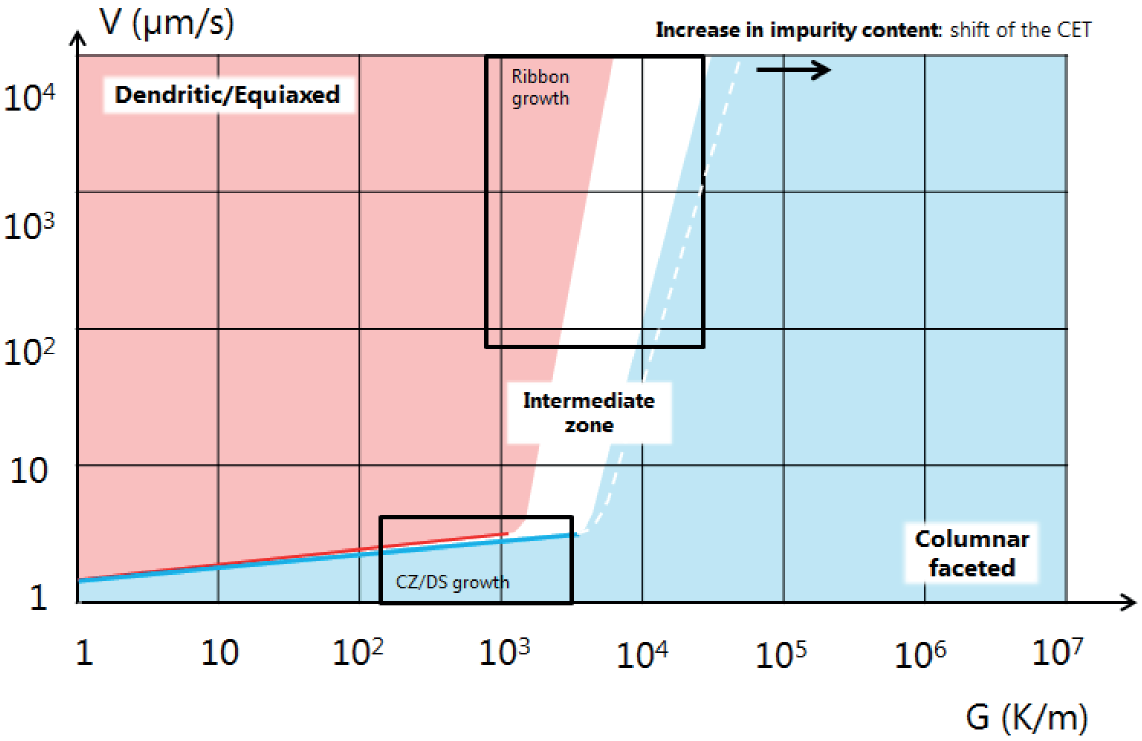

Figure 6-1. Schematic of microstructure map for Si as a function of growth rate and thermal gradients. The red zone corresponds to equiaxed dendritic growth mode, the blue zone corresponds to columnar faceted growth and the white zone is an intermediate zone. The blue and red lines delimitate the CET and equiaxed zone as calculated by Mangelinck et al.[51] The dotted white line represents the shift of CET at higher impurity concentrations. Delimitation of the zones above 10^3 K/m are only extrapolations of the CET calculated by Mangelinck-Noël et al. for Si and by Kurz et al.[48] for E-LMF of nickel-based superalloy and are only represented to give an idea of the process map at high thermal gradients. DS: directional solidification, CZ: Czochralski.

Chapter 4 showed that a substrate preheated to 730°C and a repetition rate above 100 Hz allowed the building of crack-free silicon pillars. The results presented in this section are within this working window so that pillar attachment to the substrate was ensured.

This chapter discusses the influence of process parameters such as feed rate, stage speed and thermal gradients on the microstructure. The process of epitaxial growth of silicon by DLM is compared to existing techniques and models. The influences of raw materials properties such as amount of impurities and crystallinity of the substrate on the microstructure are also presented.

Unless specified, all the pillars presented in this study were built with the powder Si_4N (99.999% purity, announced by the manufacturer) and a substrate wafer with orientation <100>.

6.1. Results

6.1.1. Influence of Feed Rate and Stage Speed

In our process, the growth rate (V) of the pillar is mainly controlled by the powder feed rate at the beginning of the building and by the stage speed in a second step, as illustrated in Chapter 4. Therefore, we first studied the influence of the feed rate on the pillar microstructures.

Figure 6-2 shows EBSD maps of cross-sections of pillars built on a <100> wafer with varying feed rates, at a speed of 0.1 mm/s. The nature of the grain boundaries found in each of the EBSD maps is displayed in Figure **6-3**. Figure 6-2 (a), (b) an (c) show the microstructure of a pillar built on a <100> oriented Si substrate for feed rates of 47.5, 3.4 and 1.0 g/min respectively. All of them presented columnar grains oriented in the direction of the pillar building direction. The grain growth always started epitaxially to the substrate, and became polycrystalline after a certain height. For a feed rate of 47.5 g/min, the microstructure consisted of a polycrystalline structure with numerous high aspect ratio grains of several hundreds of microns in length. Epitaxial growth was observed only on maximum 200 µm. If lots of grain boundaries are random, lots of them are also twins. The microstructure presented the smallest grain size of all three feed rates and the highest amount of crystallographic defects such as incoherent twins and random grain boundaries. The microstructure obtained with the intermediate feed rate (3.4 g/min) presented longer grains and a lower amount of random grain boundaries, as well as more coherent twins. It was also textured in the orientation of the wafer substrate and its twin orientations. For a feed rate of 1.0 g/min, much larger grains were obtained, and almost all of the grains presented a twin relationship. The sample is strongly textured in the same orientation as the substrate or in its twin orientation over more than 1 mm.

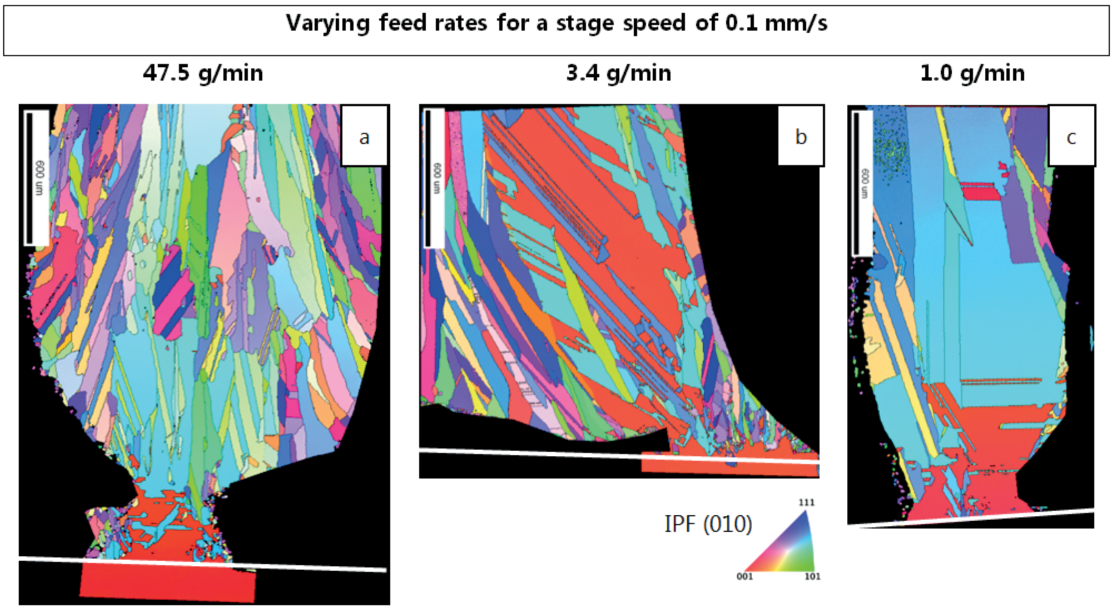

Figure 6-2. EBSD crystal orientation mapping of pillar cross-sections built with the powder Si_4N, with the following conditions: frequency 200Hz, 160 mJ, pulse duration 1 ms, stage speed 0.1 mm/s, (a) feed rate 47.5 g/min, (b) feed rate 2.4 g/min and (c) feed rate 1.0 g/min. The pillars were built on a <100> wafer. The grains appearing in the black zone are artefacts measured on the silver paste and the resin used in the experiments. The white line indicates the wafer upper surface. The IPF color scale shows the crystal orientations in the pillar growth direction.

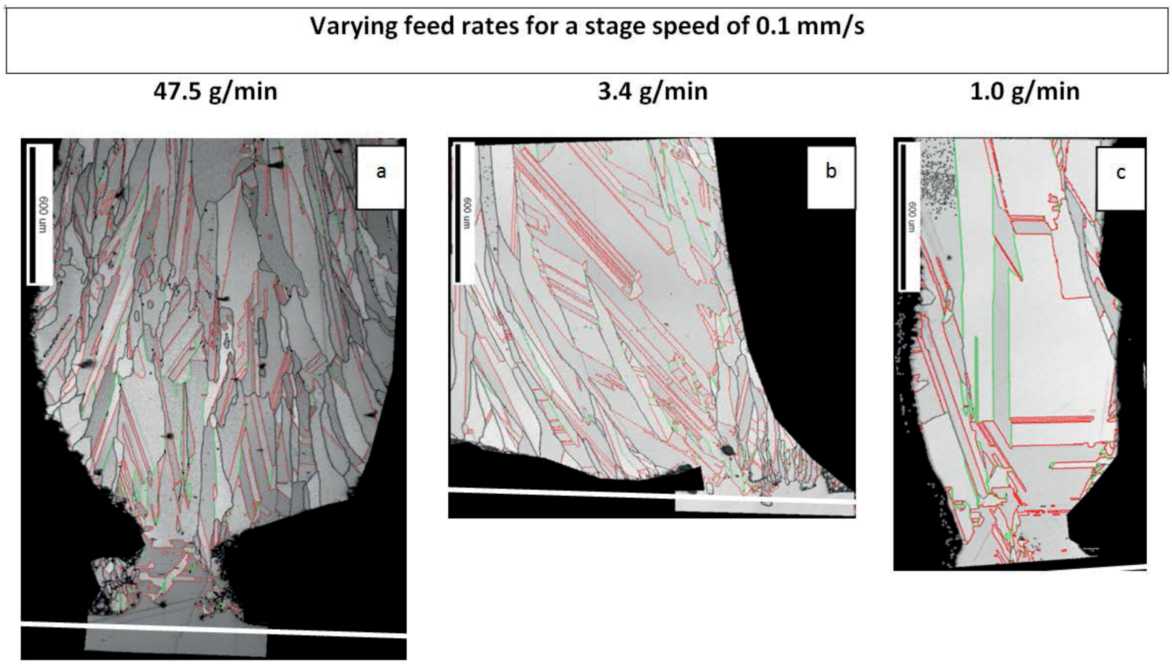

Figure 6-3. EBSD pattern quality and grain boundaries maps showing the nature of the grain boundaries in the pillar cross-sections built with the powder Si_4N, with the following conditions: frequency 200Hz, 160 mJ, pulse duration 1 ms, stage speed 0.1 mm/s, (a) feed rate 47.5 g/min, (b) feed rate 2.4 g/min and (c) feed rate 1.0 g/min. The pillars were built on a <100> wafer. The crack appearing at the base of the pillar in (a) appeared during the polishing step. The colored lines represent the different coincident lattice sites (CSL): red for twin boundaries (∑3), green for ∑9 boundaries and black for random grain boundaries. The crack appearing at the base of the pillar in (a) appeared during the polishing step. The grains

appearing in the black zone are artefacts measured on the silver paste and the resin used in the experiments. The white line indicates the wafer upper surface.

As seen in Chapter 5, 0.1 mm/s was the optimized stage speed for the feed rate 1.0 g/min. The optimized stage speed is defined as the stage speed required in order to obtain the most constant growth rate during the process. Different EBSD maps of pillars built with varying stage speeds at a constant feed rate of 1.0 g/min are presented in

Figure 6-4. At lower stage speeds (0.0083 and 0.0167 mm/s), twinning occurred mostly parallel to the building direction, and slightly smaller grains can be seen as well as random grain boundaries. Higher stage speeds (0.05 and 0.1 mm/s) led to twins boundaries perpendicular to the building direction and bigger grains. Similar observations were made for pillars built at a feed rate of 15.0 g/min with a stage speed of 0.1 mm/s and 0.3 mm/s (Figure 6-5(a) and(b) respectively). For the optimized stage speed of 0.3 g/min (see Chapter 5), bigger grains and better epitaxy was achieved, as the microstructure was more strongly textured in the substrate orientation and its twin.

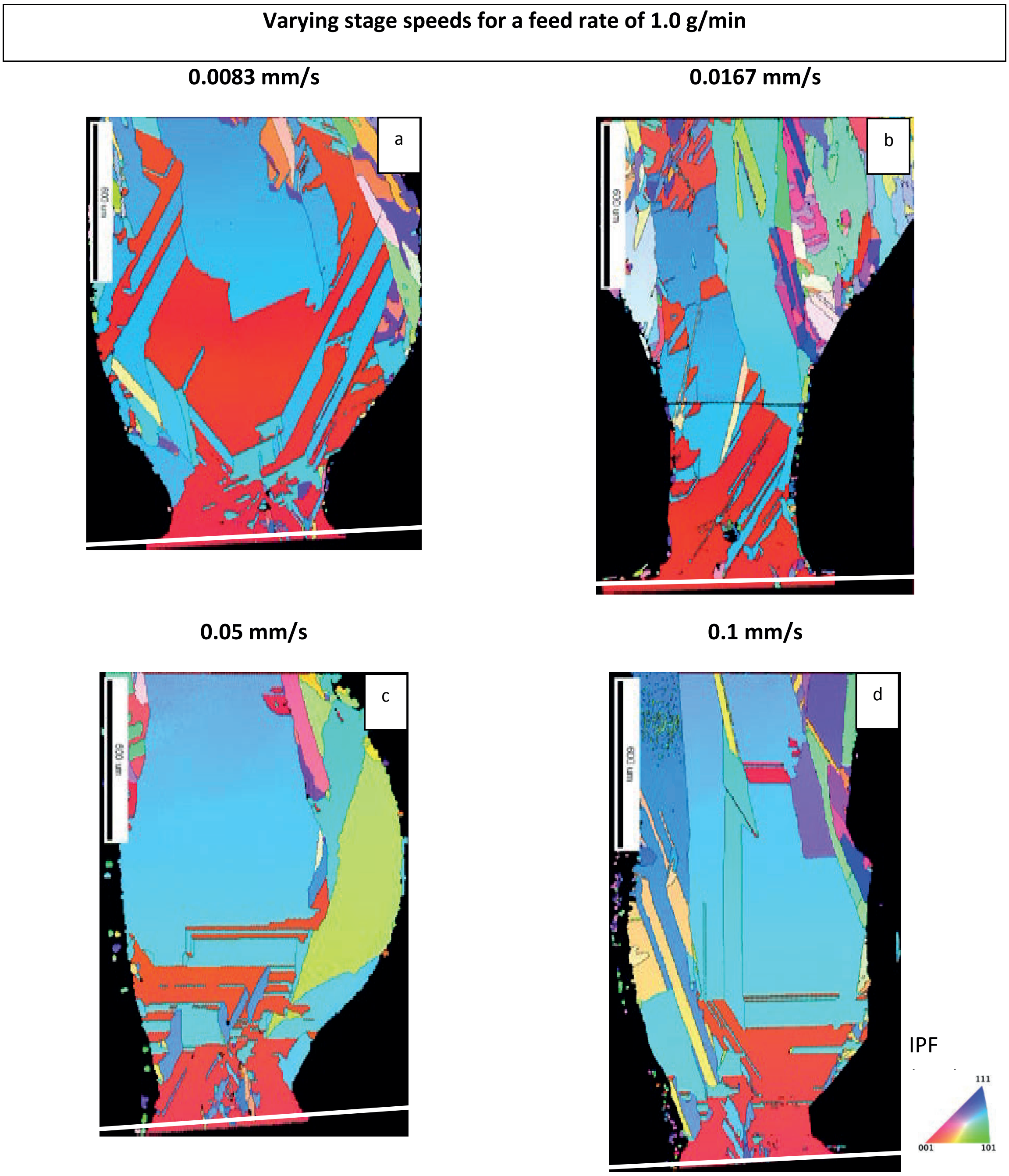
Varying stage speeds for a feed rate of 1.0 g/min
0.0083 mm/s
0.0167 mm/s
a
b
600 um
0.05 mm/s
0.1 mm/s
c
d
IPF
111
001
101

Figure 6-4. EBSD mapping of the cross-sections of pillars built with the powder Si_4N with the following conditions: frequency 200 Hz, 160 mJ, pulse duration 1 ms, feed rate 1.0 g/min, built on a <100> wafer substrate, stage speed (a) 0.0083 mm/s (b) 0.0167 mm/s, (c) 0.05 mm/s and (d) 0.1 mm/s. The grains appearing in the black zone are artefacts measured on the silver paste and the resin used in the experiments. The white line indicates the wafer upper surface. The IPF color scale shows the crystal orientations in the pillar growth direction.

Varying stage speeds for a feed rate of 15.0 g/min

0.1 mm/s **0.3 mm/s**

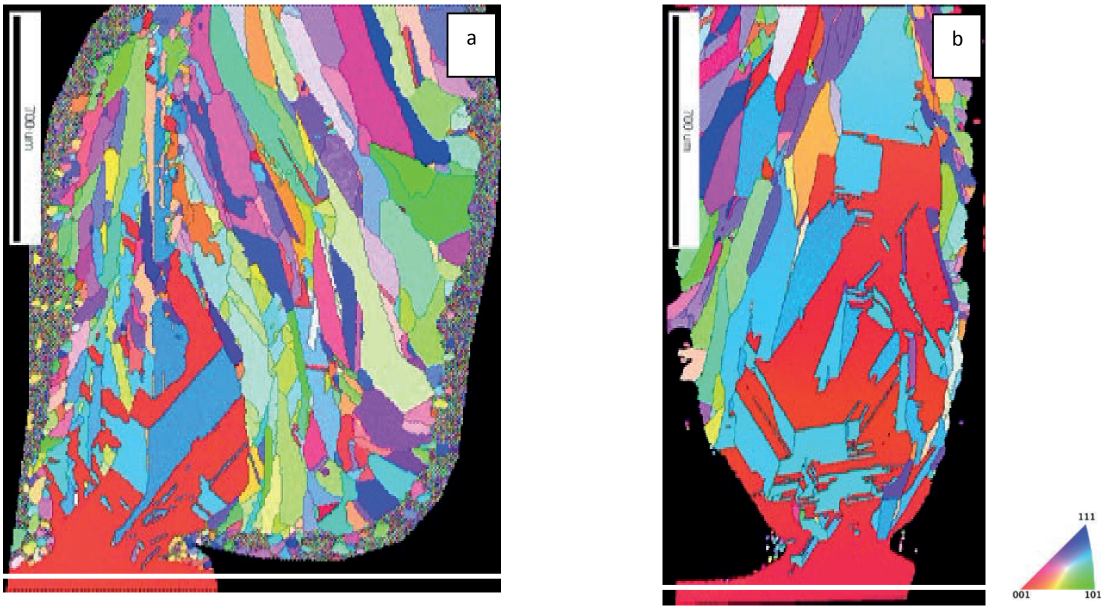

Figure 6-5. EBSD mapping of the cross-sections of pillars built with the powder Si_4N with the following conditions: frequency 200 Hz, 160 mJ, pulse duration 1 ms, feed rate 15.0 g/min, built on a <100> wafer substrate, stage speed (a) 0.1 mm/s and (b) 0.3 mm/s. The grains appearing in the black zone are artefacts measured on the silver paste and the resin used in the experiments. The white line indicates the wafer upper surface. The IPF color scale shows the crystal orientations in the pillar growth direction.

Figure 6-6 shows the EBSD map of a cross-section of a pillar built with a feed rate of 1.0 g/min, stage speed of 0.05 mm/s and laser parameters 200 Hz – 160 mJ. As for all the pillars presented in this chapter, necking appears at the base of the pillar on about 0.3 mm height, after which the pillar diameter widens to about 1 mm. The epitaxial growth was maintained over more than 4 mm (excluding twin boundaries). However, after 1.5 mm of height, the grains started to grow from the pillar surface to its center in an oblique direction, indicated by the black arrows in Figure 6-6. Consequently, the main epitaxial grain was gradually overcome by smaller randomly oriented grains as the pillar builds up.

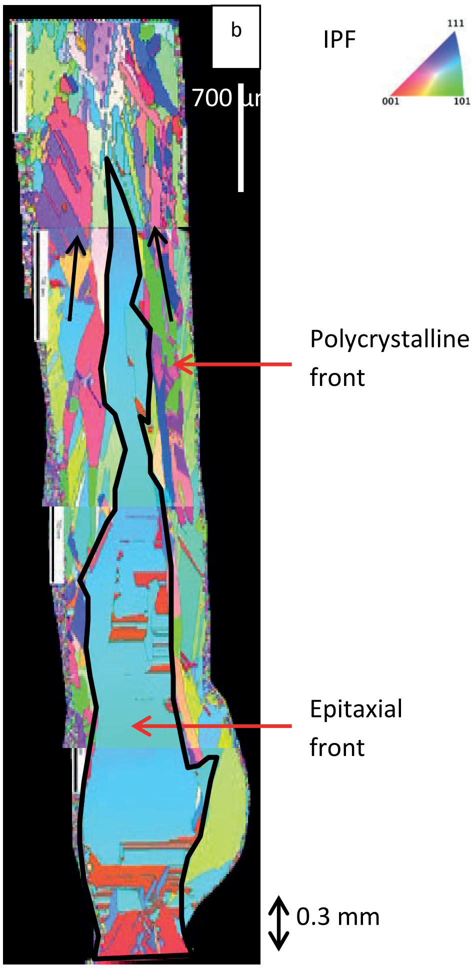

Figure 6-6. EBSD map showing the microstructure of a pillar built with a feed rate of 1.0 g/min, stage speed of 0.05 mm/s and laser parameters 200 Hz – 160 mJ. The epitaxial front is circled in black. The black arrows indicate the growth direction of the polycrystalline grains. The white line indicates the wafer upper surface. The IPF color scale shows the crystal orientations in the pillar growth direction.

6.1.2. Influence of Impurities

Then, the influence of impurities on the pillar microstructure has been studied. In this aim, two silicon powders of different impurity content were used: Si_4N (99.999% purity announced by the manufacturer) and Si_98% (98% purity, announced by the manufacturer). Their impurity content was measured by GDMS (cf. Chapter 4.1.3). The content of the main impurities Al and Fe of Si_98% was 2 orders of magnitude above that of Si_4N.

The microstructures of the pillars built successively with the powder Si_98% and Si_4N are compared in Figure 6-7 for a feed rate of 1.0 g/min. The two samples were built with 100 Hz, 285 mJ and 0.13 mm/s. In this case, important differences in the pillar microstructures were noticed. Even if the quality of the epitaxial growth is largely improved in both cases thanks to the low feed rate, the samples containing more impurities present a columnar structure with more grain boundaries than the one built with the purer powder.

The same study was conducted with a feed rate of 47.5 g/min. In this case, the microstructures of the pillars built successively with the powder Si_4N and Si_98% are compared in Figure **6-8**. The microstructure obtained was completely polycrystalline. The grains were elongated in the direction of growth, similar to what has been previously shown on Figure 6-2. No significant difference between the two powders was found in terms of pillar microstructure. They both contained numerous small high aspect ratio grains with random orientation, crystallographic defects and incoherent twin boundaries.

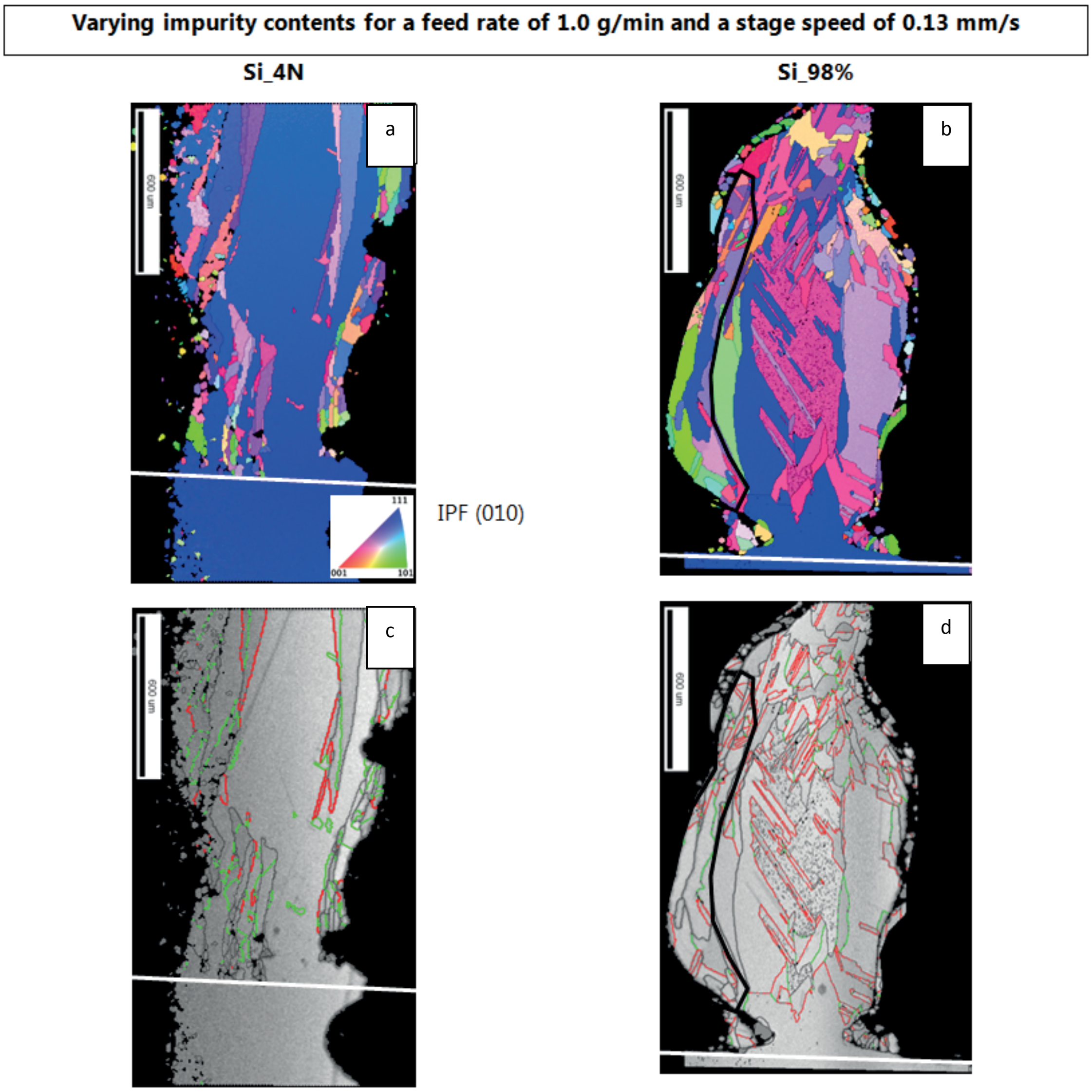
Varying impurity contents for a feed rate of 1.0 g/min and a stage speed of 0.13 mm/s
Si_4N
Si_98%
a
b
600 um
IPF (010)
111
001
101
c
d

Figure 6-7. EBSD mapping of cross-sections of pillars built with 100 Hz, 285 mJ, stage speed 0.13 mm/s, feed rate 1.0 g/min for two different powder purities: (a) Si_4N and (b) Si_98%. The area circled in black corresponds to an area where liquid silicon probably dropped off the melt pool along the side of the pillar. (c) and (d) are the IQ map of (a) and (b) showing the different boundary types across the EBSD map. Red lines indicate twin boundaries. Green lines indicate Σ9 boundaries. Black lines indicate random boundaries. The grains appearing in the black zone are artefacts measured on the silver paste and the resin used in the experiments. The white line indicates the wafer upper surface.

Varying impurity content for a feed rate of 47.5 g/min and a stage speed of 0.1 mm/s

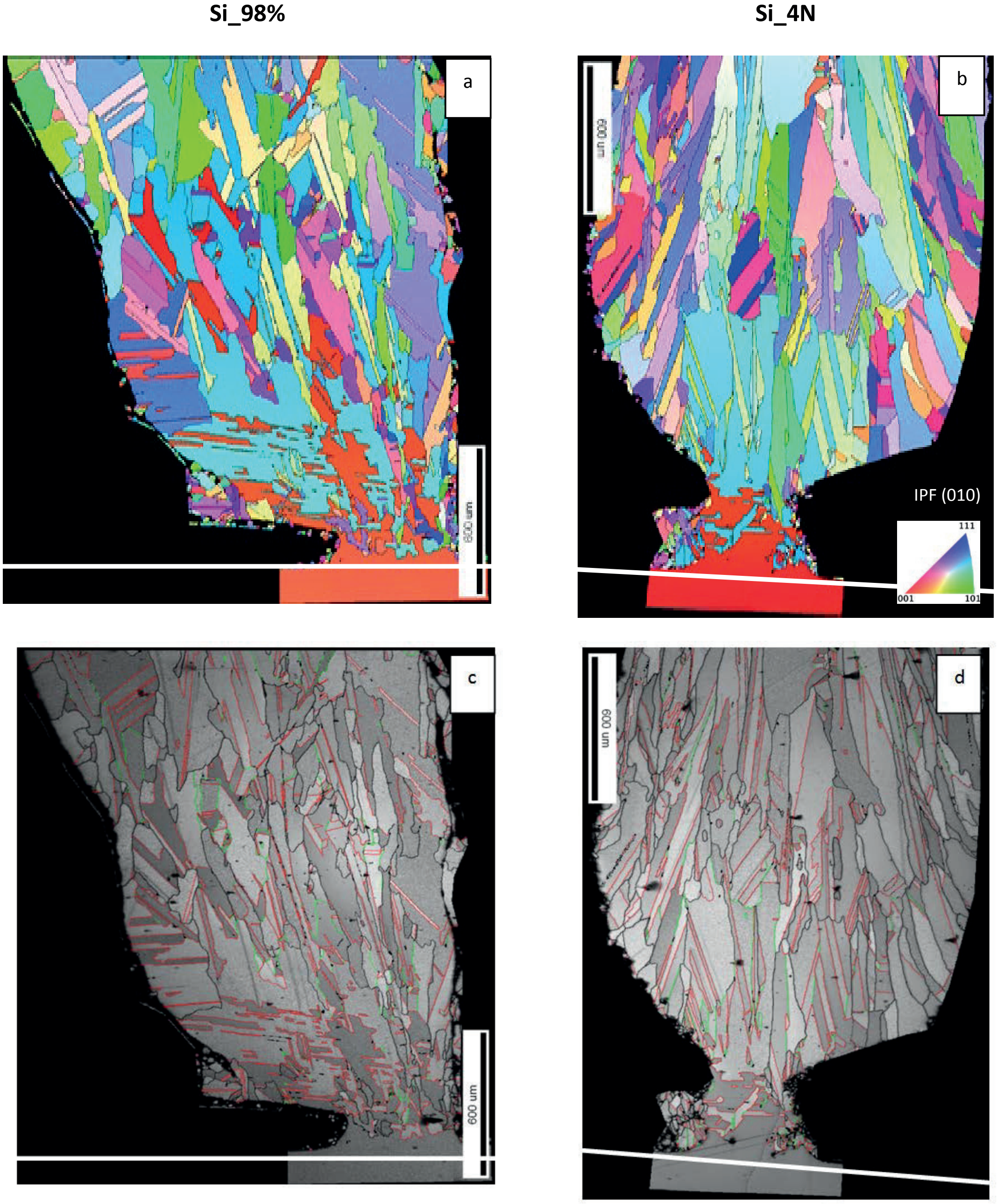

Figure 6-8. EBSD mapping of the cross-section of pillars built with the following conditions: frequency 200Hz, 160 mJ, pulse duration 1 ms, stage speed 0.1 mm/s and feed rate 47.5 g/min (a) pillar built with the powder Si_98% and (b) pillar built with the powder Si_4N. Smaller grains can be observed in the microstructure of the pillar built with the metallurgical grade powder. Randomly oriented grains are also more present. Red lines represent twin boundaries, green lines represent Σ9 boundaries and black lines stand for randomly oriented grains. The grains appearing in the black zone are artefacts measured on the silver paste and the resin used in the experiments. The white line indicates the wafer upper surface.

Figure 6-9 shows an optical microscope picture of the cross-section of a pillar built with Si_98% and Si_4N with a feed rate of 1.0 g/min (laser parameters 100 Hz – 285 mJ). The picture is centered close to the base of the pillar. Only a few precipitates can be spotted by optical microscopy, compared with the pillar built with a feed rate of 47.5 g/min (Figure 6-10), which correlates with the better quality of epitaxy found in Figure 6-7 (a) and the lower feed rate used. More and more precipitates were observed as the pillar height increased.

Varying impurity content for a feed rate of 1.0 g/min and a stage speed of 0.13 mm/s

Si_98% **Si_4N**

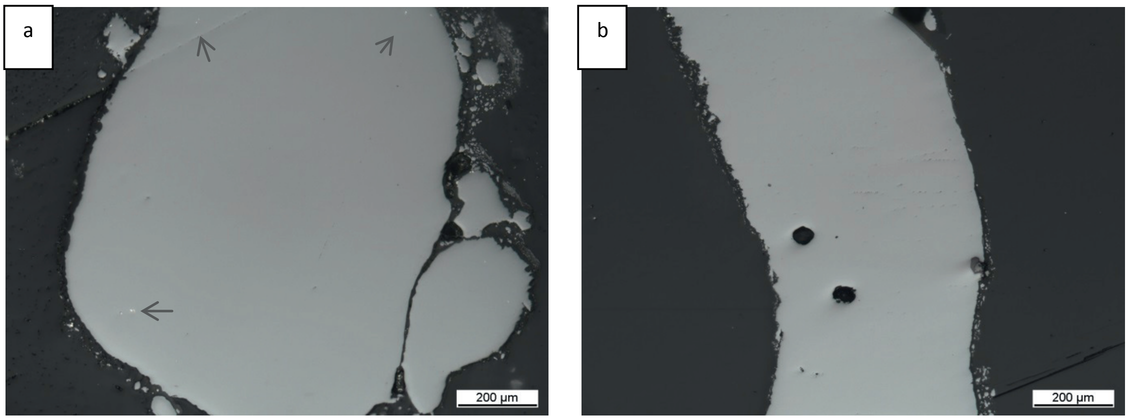

Figure 6-9. Optical microscope pictures of cross-sections of pillars built with 100 Hz, 285 mJ, stage speed 0.13 mm/s, feed rate 1.0 g/min (a) with Si_98% and (b) Si_4N. Some of the visible impurity precipitates are shown with arrows.

Figure 6-10 displays optical microscope pictures of cross-sections of pillars built with Si_98% and Si_4N. The sample built with Si_98% showed numerous precipitates homogenously distributed along the pillar height. They became more and more numerous as the height increases. The precipitates were mostly located at the grain boundaries, as illustrated in the SEM picture of Figure 6-11. However, some were also found inside the grains. EDX analysis of the precipitates shown in Figure 6-11 (b) revealed that the latter were mainly composed of Si, Fe and Al, the two main sources of metallic impurities found in the raw material (Chapter 4.1.3). On the contrary, the pillar built with the purer powder showed only a few visible macroscopic precipitates along the ingot (indicated by arrows in Figure 6-10), except at the top of the pillar.

Varying impurity content for a feed rate of 47.5 g/min and a stage speed of 0.1 mm/s

Si_98% **Si_4N**

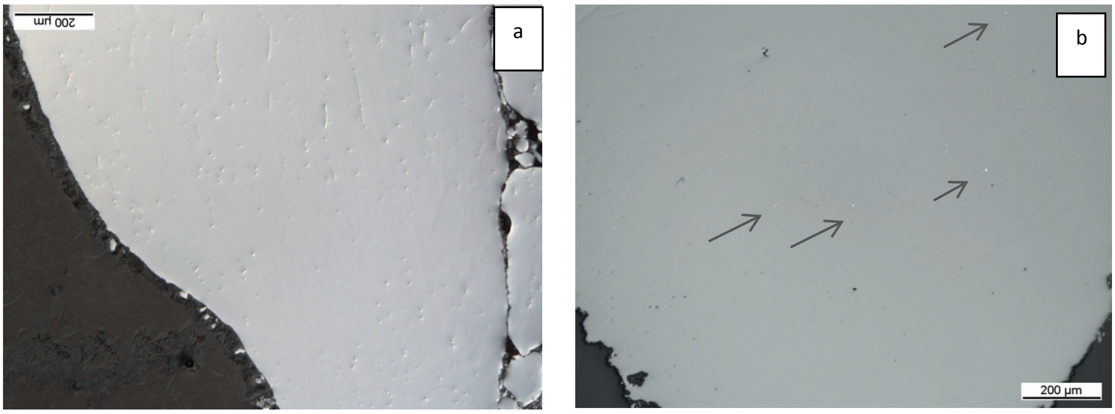

Figure 6-10. Optical microscope picture of pillar cross-sections polished. The pillars were built with the following conditions: feed rate 47.5 g/min, stage speed 0.1 mm/s, repetition rate 200 Hz, energy per pulse 160 mJ. (a) Pillar built with the powder Si_98% and (b) pillar built with the powder Si_4N. Some of the visible impurity precipitates are shown with arrows.

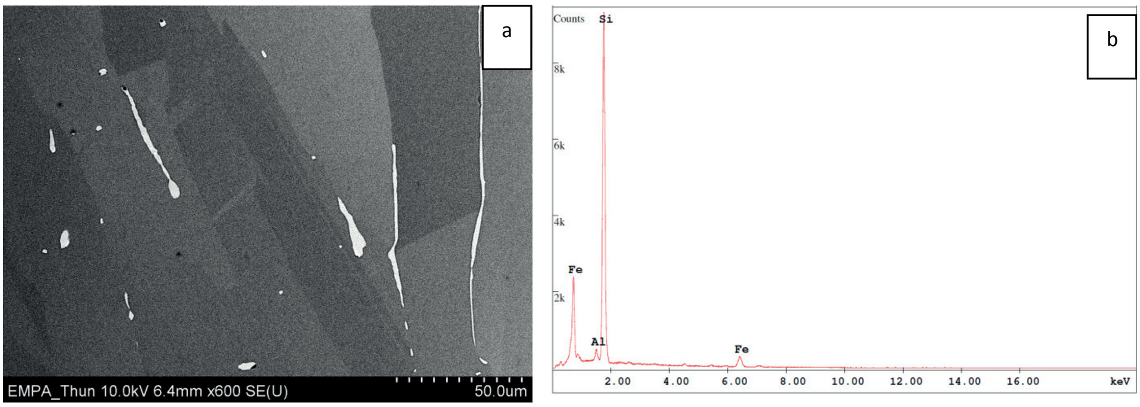

Figure 6-11. (a) SEM picture of the cross-section of a silicon pillar Si_98% and showing impurity inclusions (b) EDX analysis of the impurity inclusions. EDX analysis shows that the inclusions are due to Fe and Al metallic impurities, mixed with Si. The inclusions tend to segregate at the grain boundaries.

6.1.3. Influence of the Wafer Substrate Crystallographic Orientation

Finally, we studied the influence of the substrate orientation on the microstructure of the built pillar. In this aim, two different batches of substrates were used: one with the orientation <100> and the other one with the orientation <111>.

Figure 6-12 shows EBSD maps of cross-sections of pillars built from <100> and <111> substrate orientations. The pillars have both been built with the lowest feed rate (1.0 g/min) with the laser parameters 200 Hz – 160 mJ. Fewer twinning occurred in the epitaxy of the pillar grown on <111> wafer compared to the one grown on <100> wafer. About 1 mm of twin-free epitaxial growth was achieved from the <111> oriented wafer. The pillar built from the <111> oriented wafer in Figure 6-12 (a) presented a polycrystalline part on the right side (indicated by the area circled in black), which probably corresponds to liquid silicon dropping from the top of the pillar during building.

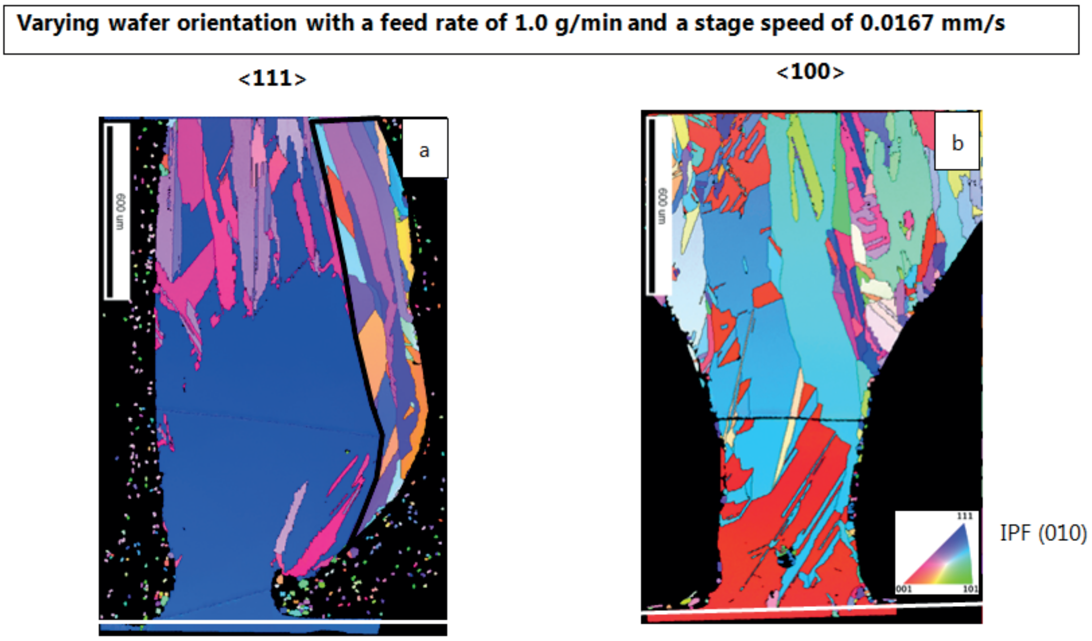
Varying wafer orientation with a feed rate of 1.0 g/min and a stage speed of 0.0167 mm/s
<111>
<100>
a
b
600 um
600 um
IPF (010)
111
001
101

Figure 6-12. EBSD mapping of pillars built with the powder Si_4N with the following conditions: pulse duration 1 ms, feed rate 1.0 g/min, stage speed 0.0167 mm/s, frequency 200 Hz, power 160 mJ, (a) substrate orientation <111> (b) <100>. The area circled in black corresponds to liquid silicon that dropped off the melt pool along the pillar side during the process. The grains appearing in the black zone are artefacts measured on the silver paste and the resin used in the experiments. The white line indicates the wafer upper surface. The IPF color scale shows the crystal orientations in the pillar growth direction.

6.2. Discussion

6.2.1. On the Shape of the Pillars

All pillars introduced in this chapter presented necking at the base of the pillar. The explanation for that is the following: as the pillar builds up, heat accumulates due to the geometrically higher aspect ratio (increase in length and decrease in cross-section compared to the wafer heat sink). Therefore, the pillar diameter widened. Heat accumulation increases the risk of silicon melt dropping out of the melt pool. This phenomenon was clearly encountered in some of the cases such as in Figure 6-7 (a) and Figure 6-12 (a), where the EBSD maps show some polycrystalline silicon droplet which flew off the melt pool and solidified along the already solid pillar side. It is particularly encountered in the cases of low feed rates, for which fewer “cold” particles per burst are brought to the melt pool, and less laser beam shielding occurs. This should be avoided because those droplets form polycrystalline zones in the pillar microstructure. Improvement could be implemented by carefully diminishing the energy per pulse during pillar building, and using a rotating stage or a coaxial nozzle so that powder can be evenly distributed. These observations are in accordance with the thermal gradients decrease and temperature increase calculated as a function of pillar height, and the high speed camera observations conducted in Chapter 5.

Despite these phenomena, epitaxial growth could still be studied. Indeed, the center of the pillar was little affected by the droplet formation. Moreover, the heat flow direction remains perpendicular to the substrate in the center of the pillar.

6.2.2. Achievement of Epitaxial Growth: Growth Velocity, Thermal gradients and Feed Rate

All the microstructures obtained in the experiments showed a columnar growth, with a zone of epitaxial growth followed by a zone of polycrystalline grains elongated in the direction of building. This is consistent with a high G/V ratio. Indeed, the thermal gradients at the liquid/solid interface remained of the order of 10^6 K/m (calculated in Chapter 5.2) throughout the process. The pillar building speeds varied between 0.0083 and 0.5 mm/s. However, the liquid/solid interface velocities are not equal to the pillar building speeds, and were not measured in this study. The interface velocities fluctuate throughout the process due to the pulsed nature of the laser illumination and the powder feed, and can be slower or faster than the building speed depending on the efficiency of evacuation of heat. However, the building speed is an average value for the liquid/solid interface velocity through the entire pillar building process. For comparison, the thermal gradients and growth rates used in the Czochralski process are of the order of less than 1K/m and some µm/s respectively. Especially, it was shown in Chapter 5 that during the first 3s of pillar building, the growth rate was independent of the feed rate and the stage speed and was about 0.3 mm/s. It was also shown that the thermal gradients were the highest at the very beginning of the process. Therefore, the presence of high gradients enabled the use of high speed while staying in columnar growth mode and favor epitaxial growth.

In all samples, twin boundaries are the boundary types that mostly form in the microstructures of the pillar grown by DLM, according to Figure 6-3 and Figure 6-7. Twin boundary is the stacking fault that takes up the least amount of energy to form, demanding about 5 times less energy than a random grain boundary [115]. Similarly, twin boundaries Σ3 and higher orders (Σ9, Σ27…) are the boundary type that is the most found in the classical silicon crystal growth processes. For example, Voigt et al. [116] studied the grain orientation of cast silicon wafers, and found that about 42% of the grain boundaries were twin boundaries or twin boundaries of higher order. Oliveira et al. [117] observed twin formation on <111> seeded directional growth of silicon with a pulling rate of 3.3 µm/s and a thermal gradient of 25 K/m. They found that formation of a twin defect was at the origin of multiple twinning, which takes place between the newly formed twin and the matrix. According to the same authors, impurities and particles can also promote the formation of twin boundaries by lowering the grain boundary energy. This correlates with the high amount of twin boundaries found in the DLM process, where powder particles are introduced into the melt, and metallic impurities are present in higher quantities in the powder raw material, which is not of solar grade.

Using the same feed rate, noticeable differences in the microstructures were found for the pillars built with a stage speed lower or equal to the optimized stage speed. Figure 6-2 and Figure 6-5 showed that larger grains and stronger texture in the substrate orientation and its twin were observed if the pillar was built with an optimized stage speed-feed rate match. This effect is attributed to the significant laser beam defocus when the stage speed is lower than the optimized stage speed. Therefore, less energy is available to maintain proper melting of the powders in the melt pool, which results in the formation of equiaxed grains. However, pillars built with the lowest feed rate (1.0 g/min) presented the best epitaxial growth (Figure 6-4 compared to Figure 6-5), with less amount of twinning and bigger grains compared to pillars built at 15.0 g/min. Indeed, higher burst particle density due to higher feed rates results in more “cold” powder hitting the melt pool. Therefore, some particles may only partially dissolve into the melt pool before the latter cools down. Higher powder density also shield parts of the laser light, which results in less energy available to properly melt the particles. Those particles induce new grain growth with a new orientation and disrupt epitaxial growth. Then, the density of liquid silicon is higher (2.57 g/cm^3) than that of solid silicon (2.33 g/cm^3). Added to the surface tension effect, a higher melt density could encourage the particles to float on top of the melt pool instead of sinking in.

On the contrary, if the pillars are built with a low feed rate (1.0 g/min), the particles have time to dissolve into the melt. The melt pool is also not cooled down as much because the density of particles per burst is lower. Therefore, nucleation of new grains from the feeding powder is less likely to happen, and epitaxial growth is promoted. Similar results were obtained by Wang et al.[118] during the Laser Melting Deposition of a titanium alloy. They studied the influence of the feed rate from 6 to 59 g/min on the microstructure of tracks formed with a laser beam of 6 mm diameter and a speed of 16.6 mm/s. They found that increasing the powder feed rate favored the apparition of equiaxed grains due to insufficient powder melting and lower melting penetration in the underlying layer due to low melt superheating. On the contrary, lower feed rates promoted epitaxial growth from the previous layer.

Careful feed rate control is also necessary as fluctuations in growth rate were found to favor the formation of twin boundaries, which are always present in the growth of pillars on <100> wafers. Kutsukake et al. observed twin formation during silicon casting experiments. By varying the cooling rate of the ingot from 3 to 50 K/s, they experimentally demonstrated that twin formation is more likely to be triggered with a drastic change in the growth rate than with a steady high growth rate[115]. They also showed that twin boundaries were more likely to appear at fast growth rates. Su et al.[119] studied directional solidification of metallurgical grade silicon with a thermal gradient of 2.10^4 K/m. They also found that increasing the growth rate from 5 to 60 µm/s led to a decrease in grain sizes, while maintaining columnar growth thanks to the high thermal gradients.

It is believed that further decrease of the feed rate could lead to even better epitaxial growth. However, in this study, the feed rate decrease was limited by the flowability of the powder, which became more difficult to transport in our powder feeding system.

As demonstrated by Gäumann et al. in their study of processing-microstructure maps of laser metal forming of a Ni-base superalloy [50], other parameters such as laser power, beam diameter and substrate temperature can influence the CET. Diminishing the power, beam diameter and substrate temperature is beneficial to obtain higher thermal gradients. The beam diameter was chosen to be fixed. The minimum power to be used was determined by the ability to melt the wafer surface and establishing crack-free pillar building conditions. Last, the substrate temperature range allowed was small: it could not be raised because of risks of damaging the hot plate and could not be significantly diminished because of silicon cracking (see Chapter 4).

6.2.3. Loss of Epitaxial Growth

As the pillar grows higher, the probability of producing a defect increases. Indeed, the apparition of a randomly oriented grain due to nucleation on an impurity precipitate, a particle or a grain boundary is an unavoidable, even in the best conditions. Apparition of a new grain can be influenced by many events due to melt pool instability coming for example from powder injection and powder flow, laser focusing and defocusing or splashes. The pillar then becomes polycrystalline by multiplication of grain nucleation on the defects already formed.

Then, maintaining epitaxial growth also requires that the heat flow stays perpendicular to the substrate throughout the process. At the beginning of the pillar building, cooling is dominated by conduction through the wafer substrate, which acts as a heat sink. Therefore, the heat flow is mainly directed in the direction perpendicular to the wafer surface, which favors epitaxy and columnar growth.

However, as the pillar builds up, the radial component of the heat flow becomes more important. Indeed, temperature increase in the melt pool enhances the heat losses by radiation (chapter 4) from the pillar surface close to the melt pool. Pillar diameter enlargement also favors the increase of the contribution of the radial heat flow. Indeed, the heat input of the laser beam becomes confined to an area smaller than the cross-section of the pillar. Therefore, instead of remaining perpendicular to the growth direction, the heat flux direction around the melt pool changes for a more radial direction.

The increase in radial heat flow promotes grain growth from partially molten powder particles stuck at the side of the pillar. This phenomenon is well illustrated by the pillar cross-section presented in Figure 6-6 where the main epitaxial grain is taken over by grains growing from the surface of the pillar to the inside in an oblique direction. It also promotes the growth of more equiaxed grains.

6.2.4. Effect of Powder Impurities

Segregation of metallic impurities at the top of the pillar and their precipitation at the grain boundaries is a common phenomenon in directional crystal growth of silicon. The segregation coefficients (defined as the ratio between the concentration of impurity atoms in the growing crystal and that of the melt) for Fe and Al are respectively $6.4.10^{-6}$ and 0.002 [120], which explains their higher concentrations at the top of the pillar as they will rather stay in the melt than being incorporated into the crystal.

Most of the metallic impurities seen in the pillars are present at the grain boundaries. Indeed, gettering of metallic impurities at the crystal defects and grain boundaries takes place during directional growth, especially for fast diffusers such as Fe. However, many inclusions can also be observed within grains. Indeed, precipitation of metallic impurities because of supersaturation of the melt can also occur, as well as direct incorporation of incompletely dissolved metallic particles[121] as they are incorporated into the melt pool. Moreover, the high growth rate of the pillars can also prevent the impurities to have time to diffuse to the grain boundaries, as their diffusion coefficient diminishes exponentially with temperature. Then, natural segregation and segregation towards gettering sites compete during crystal growth. This competition results in much higher contamination through the ingot height than if only natural segregation is taken into account[61].

Pillars built with a feed rate of 1.0 g/min with the purest powder led to maintenance of epitaxial growth over more than 1.3 mm (excluding twin boundaries) whereas the powder containing more impurities led to a more polycrystalline material.

These observations are attributed to the fact that metallic precipitates act as nucleation sites for the growth of new silicon grains. Mangelinck-Noël et al.[51] calculated processing-microstructures maps of silicon as a function of G (10^3-10^5 K/m), V (1-4 µm/s), and potential grain nucleation site number, created by impurities present in the melt. They found that for 4 orders of magnitudes more impurities, the thermal gradients necessary to stay in the columnar growth would have to be multiplied by 1 to 2 orders of magnitude as the CET is shifted towards higher thermal gradients. In our case, the microstructure obtained still shows columnar growth as the thermal gradients stay high. However, epitaxial growth is more easily disrupted when a high amount of impurities are present (Figure 6-7). Moreover, when a high amount of impurities are present in the raw material, constitutional undercooling is not negligible anymore, and enhances impurity precipitation ahead of the solidification front. However, epitaxial growth is improved even using a powder with high impurity content at low feed rate because segregation of metallic impurities is more efficient at low velocities. Therefore, less precipitates were present in the length of the pillar (Figure 6-9), which leads to less potential nucleation sites for new grains. This behavior is similar to observations made in silicon growth methods. Sun et al. studied the effect of pulling rate (2 to 3.8 µm/s) on the microstructure of directionally solidified silicon ingots. They showed that a higher pulling rate made the distribution of impurities along the ingot height more homogenous, which led to smaller grains[122]. Huang et al. studied the resistivity of metallurgical grade silicon ingots grown with the cold crucible directional solidification process at a pulling rate of 25 µm/s. They reported that regions of the ingot with higher impurity concentration (in the case of silicon of metallurgical grade) presented smaller more randomly oriented grains, as well as higher density of crystal defects[123] .

At high feed rate, no significant difference could be found in the microstructure of the pillar built with the 2 powders of different impurity contents. Indeed, as discussed earlier, high feed rates already imply a higher amount of nucleation sites in the melt pool due to powder incorporation. Therefore, as the powder nucleation effect and the laser defocusing are stronger than the impurity nucleation effect, no significant improvement in epitaxial growth was observed when the purest powder was used.

6.2.5. Effect of Substrate Orientation

In our observations, less twinning occurred for epitaxial growth from <111> oriented substrates (Figure 6-12). This is in agreement with literature. Indeed, the {111} plane is the plane with the lowest energy because it has the lowest amount of dangling bonds. It is also the only plane for which the interface solid/liquid is atomically smooth (Jackson's criterion, ref. chapter 2)[124]. It has been observed by optical microscopy observation during crystal growth that a faceted interface composed of {111} planes forms during the growth of {100} planes during crystal growth at high growth velocities (superior to 0.147 mm/s, for a thermal gradient of 8K/mm). However, they can be maintained planar if the growth velocity is sufficiently low[46], or the thermal gradients sufficiently high. On the contrary, the solid/liquid interface for the growth of a {111} plane can be maintained planar even at high growth velocities[124] . It has also been shown that twinning is more likely to occur at faceted interfaces, at grain boundaries[125 126]. Twin boundaries are not detrimental to the electrical properties of the material as no dangling bond is formed in the process. They can even increase the yield strength by preventing dislocation motion, and increase the fracture toughness by avoiding crack propagation[127]. Therefore, depending on the application, twin boundaries can even be beneficial. However, multiple twinning during directional growth can finally lead to randomly oriented grains and polycrystallinity, as demonstrated by Voigt et al in their study of cast multicrystalline silicon wafers. [116]

However, if starting with a <111> oriented substrate helps reducing the amount of twinning, pillars built with a <100> oriented wafer displays a higher epitaxial zone (if twins are not taken into account). As {111} is the only atomically smooth plane of Si, it also has the lowest growth velocity. Therefore, if other grains nucleate on the sides of the pillar or in the melt pool during powder feeding, those grains could take over the <111> oriented grains by growing faster.

6.3. Conclusions and Perspectives

Epitaxial growth of silicon on a monocrystalline silicon wafer was successfully achieved on at least 1 mm of the height of the pillar. This achievement could be reached by carefully choosing the materials used and identifying the main influential parameters. It was found that the high thermal gradients induced by laser processing due to a highly localized point source allowed relatively high growth rates while remaining in a columnar growth mode. However, parameters adjustment was necessary to ensure proper epitaxial growth.

The combination of stage speed and powder feed rate was identified as the critical control parameter to ensure maintenance of the epitaxial grain growth in this study. Within the crack-free working window (see Chapter 4.1.2), a feed rate of 1.0 g/min coupled with its optimized stage speed (about 0.1 mm/s) gave the best epitaxial results. The powder used as starting material should be the purest possible (99.99% in our study). It was also found that twins can be best avoided by using a substrate with crystalline orientation <111>. Despite this achievement, loss of epitaxial growth along the pillar building direction could not be avoided.

Many similarities were found between conventional directional Si crystal growth processes and DLM of silicon. However, the main difference lies in two main characteristics: high thermal gradients and powder feeding.

In a future work, improvements on the DLM machine can be implemented to obtain a more focused powder stream (coaxial nozzle, nozzle diameter decrease) to avoid growth rate variations, and to improve the pillar shape (rotating stage). Improvements on the raw material consequently have to be implemented (spheroidization) to obtain more flowable powders, and be able to further lower the feed rate. Studies on the effect of laser energy per pulse decrease as a function of pillar height could be implemented. Research on the influence of energy per pulse, repetition rate, beam diameter and substrate temperature on the quality of epitaxial growth could also be conducted.

Chapter 7. Conclusions and Outlooks

This manuscript presents the feasibility of building silicon 3D structures on a monocrystalline silicon wafer from silicon powders by DLM, an additive manufacturing technique. As this work represents the first steps into this field, we chose to carry out this study on pillar structures because of their simple geometry.

This chapter summarizes the main results of this thesis and gives recommendations for future work.

7.1. Summary

First, the influence of process parameters on the cracking behavior of the base of silicon pillars was established, as well as a process working window. A mechanism for crack initiation and propagation was proposed, based on experimental and FEM calculation results. The main results can be summarized as follows.

- Even with poor flowability, silicon powders could be transported to the melt pool by a special powder feeder whose principle is based on pressure difference between a powder container and a vacuum cell, and then between an overpressurized cell and a transport channel.
- Silicon pillars could successfully be built on a wafer without cracking, thanks to a good thermal management. A minimum substrate temperature of 730°C and a minimum repetition rate of 100 Hz were necessary to ensure temperature rise close enough to the brittle-to-ductile transition temperature. Therefore, increase of fracture toughness and decrease of thermal gradients led to decrease of thermal stresses around the melt pool. These conditions were necessary to avoid crack propagation induced by powder at the beginning of the pillar building.
- Diminishing the feed rate from 15.0 g/min to 1.0 g/min led to a shift of the threshold repetition rate necessary to ensure the production of crack-free samples from 100 Hz to 75 Hz.
- In the case where the substrate temperature was less than 730°C and/or the repetition rate was less than 100 Hz, crack propagation was most probably triggered by the tensile radial

and hoop stress present during the cooling phase of the melt pool. The location of the tensile stress maxima during cooling of the solid phase was responsible for the crack propagation around the melt pool.

- Pure powder should be used to avoid cracking due to impurity precipitation in the pillar matrix.

- A simple 2D axisymmetrical FEM model was built and was in good agreement with the experimental results. This model enabled us to propose the above mentioned mechanism for crack propagation at the base of silicon pillars.

Then, process monitoring was carried out, and building rates were discussed as a function of process parameters such as feed rate and stage speed. The pillar shape was discussed as a function of laser parameters with the help of FEM simulations. The main results can be summarized as follows.

- A steady pillar building rate was achieved when the feed rate and the stage speed were adjusted to each other. In this case, the pillar building speed was equal to the chosen stage speed. For a feed rate of 15.0 g/min, the optimized stage speed was 0.3 mm/s. For a feed rate of 1.0 g/min, the optimized stage speed was 0.1 mm/s. A too fast stage speed for a given feed rate led to a building rate smaller than the stage speed. A too low stage speed resulted in a faster building rate than the stage speed. In both the latter cases, important fluctuations in the building speed were encountered.

- Pillar built by DLM presented necking due to expansion of the pillar diameter after about 0.3 mm. The diameter widening was mostly due to reduction of the cross-section of the heat flux and increase in length of the pillar. Both these phenomena decreased the efficiency of the heat evacuation by conduction, which led to an increase in temperature which causes the melt to flow and the pillar diameter to widen.

- FEM 3D axisymmetrical model conducted with Abaqus 2017 showed that high thermal gradients of the order of 10^6 K/m were present through the pillar building.

Finally, the possibility of producing pillars presenting epitaxial growth from their wafer substrate was demonstrated. Pillar microstructure control was discussed as a function of feed rate, stage speed, impurity content and wafer orientation. The results can be summarized as follows.

- The microstructure of the pillar was columnar for the experimental parameters used in the frame of this study. The high thermal gradients present during the process (10^6 K/m) allowed for the use of relatively high building speeds (0.0167-0.3 mm/s) while still remaining in the columnar growth mode.

- Epitaxial growth of silicon on a monocrystalline silicon wafer was achieved without winning, on more than 1 mm height by using a feed rate of 1.0 g/min, a stage speed of 0.0167-0.1 mm/s, laser parameters 100 Hz – 285 mJ and 200 Hz – 160 mJ, a powder 4N pure and a wafer of crystallographic orientation <100> or <111>.

- The main parameter influencing epitaxial growth was found to be the feed rate, A smaller feed rate was preferable as it introduced less nucleation sites due to less cooling from introducing cold powders to the melt pool. Moreover, better epitaxy was achieved if the optimized stage speed was used with the appropriate feed rate.

- Increase in powder purity led to better epitaxial growth.

- Changing the substrate orientation from <100> to <111> avoided twinning during epitaxial growth, most probably due to the energetic and geometric stability of the {111} plane.

- Loss of epitaxial growth always occurred after 1-2 mm of pillar height, due to crystal defect accumulation, increase of the radial contribution of the heat flow and multiple twinning.

In the end, a trade-off between the process time consumption, pillar cylindrical shape, crack free sample production and epitaxial growth achievement was found in the frame of this work. The process parameters should be adjusted carefully to lie in the working window for which all the previous mentioned characteristics are achieved.

7.2. Outlooks

Considering the previous section, the feasibility of additive production of silicon structures on silicon was proven. However, this study is only a beginning and many more steps are necessary to be able to get more fundamental understanding of the process and be able to push it to commercialization. Among them, the following points could be tackled in a future work.

Improvements of the raw powder material will be necessary to achieve finer structures and better control of the feed rate and building speed. The influence of the powder shape and particle distribution on pillar growth and building speed control can be studied.

- Spheroidization of the powder particles, either by plasma processing or by atomization, to achieve better flowability. Developing these processes on silicon could also allow for a direct reuse of silicon powders that are products of the wastes generating during wafer production. For example, powders recycled from diamond sawing waste could be used directly for 3D printing.
- Sieving can narrow the particle size distribution and also lead to better flowability.

Along with improvements of the powder material, improvements of the DLM machine will be necessary to achieve better precision, better building control and achieve better controlled pillar shapes.

- The powder delivery angle could be reduced.
- Smaller laser diameter could be used
- The nozzle diameter could be smaller (inducing a good powder flowability)
- A rotating stage could be installed in order to have more homogenous powder delivery
- Making the chamber gas-tight and conducting the process under 1 bar argon would avoid the cooling of the wafer substrate by the current shielding gas.
- In-situ observation techniques could be improved, especially to be able to observe and differentiate the melt pool from the solid phase during pillar building. More accurate temperature measurement could be developed.
- The temperature of the hot plate should be more finely tuned by carefully choosing the heat controller.

Building of more complex structures could be tackled. In this aim, making lines instead of pillars should be explored. Indeed, clads are the fundamental starting point to be able to make complicated 3D structures. Many difficulties will have to be tackled. Among them, the cooling of the silicon structures as they are getting bigger in height. The structure will have to be locally or entirely pre-heated above the brittle-to-ductile temperature transition and on a large area as the laser scans the structure. The building direction will have to be considered to avoid agglomeration of powders on the line. A new working window will have to be established as at least one new parameter will be introduced: the scan speed. The microstructure of the clads could be analyzed as a function of process parameters.

Fundamental knowledge about the process is still lacking.

- Crack initiation and propagation has not been observed in-situ, either in time or in space. Acoustic detection could be a good mean to locate the apparition of the crack in time.
- Influence of the laser pulse duration on the cracking working windows could be explored.
- Formation of pores present at the pillar base was not discussed in this work. However, learning how they form and how to avoid them is essential to bring the process forward.

- Microstructure control could be finely tuned by specifically focusing on the influence of parameters evoked in Chapter 6 (feed rate, stage speed, impurities, and crystallographic orientation) and their influence on the G/V ratio.
- Other parameters having influence on the microstructure control have not been yet tackled, such as energy per pulse, beam size and substrate temperature.
- Differences between a pulsed and a continuous beam influence on the microstructure could be studied.
- Fundamental reasons for the loss of epitaxial growth during the process could be explored.
- Can epitaxial growth be maintained if the pillar is not built perpendicular to the substrate anymore (e.g. coil)?
- The shape of the pillars should be optimized by carefully controlling the input laser average power (peak power per pulse, pulse duration, repetition rate) in time during the pillar building process. For example, decreasing the energy per pulse or the repetition rate as the pillar grows higher helps regulating the heat input and avoid diameter expansion.

SLM of silicon powders could be explored as an alternative additive manufacturing process for silicon powders. SLM has especially the advantage of better precision and resolution, particularly appreciated in the watch and MEMS industry, for example. However, many challenges will have to be overcome, such as:

- Powder flowability (powder spheroidization)
- Careful substrate heating
- Powder oxidation state.

  Indeed, the powder native oxide did not hinder the construction of silicon pillars by DLM. However, a protective gas was necessary to avoid formation of silicon dioxide on the pillar surface. On the contrary, in a powder bed process, it was found that the powders should be deoxidized to less than 0.1 wt% to be able to make a smooth track when illuminated with a laser beam. This difference was due to powder handling during processing. In a powder bed, SiO gas is released as the laser beam melts the powders, leading to spattering. In DLM, the powders are partially heated in flight, and their native oxide is dissolved in the melt pool or evaporates thanks to the formation of SiO gas. The results of this study can be found in Appendice.

It would also be interesting to extent the process to other brittle and semiconducting materials, and compare the results to the conclusions drawn in this PhD work.

Appendix A – Coding Interface used to Build a Pillar

As explained in chapter 3, the stage, laser and powder feeder were piloted from the Beckhoff controller via a coding interface. Figure A-1 shows a typical example of the code used to build a pillar. First, the laser is triggered, followed by the powder feeding. After powder feeding is triggered, the stage moves down at constant speed. When the stage has completed its displacement, laser and powders are switched off. The meanings of the commands are displayed in green.

```
M51; - Opens the laser shutter

M60; - Triggers Powders

G01 G17 G90 X83 Y83 Z35 F6; - Displacement of the stage to the coordinates x=83 mm, y=83 mm and z=35mm at the speed F6=0.1 mm/s

M52; - Closes the laser shutter

M63; - Powder feeding off
```

Figure A-1. Typical code to build a pillar. The sentences in green are comments on the command.

Appendix B – Simulation Hypotheses

B.1. Recoil Pressure and Evaporation Cooling

The recoil pressure is given by the following equation [128]:

$$\mathrm{P(T)} = 0.54\ \mathrm{P_a} \exp\left(-\frac{\lambda}{K_B}\left(\frac{1}{T} - \frac{1}{T_b}\right)\right)$$

Where Pa is the ambient pressure, λ is the evaporation energy per particle (enthalpy of vaporization by N_A), K_B the Boltzmann constant and T_b Si boiling temperature = 3548 K.

The net material evaporation flux is gven by the Hertz-Knudsen equation[128]:

$$J_v = 0.82\ A \frac{P(T)}{\sqrt{2\pi MRT}}$$

Where P(T) is the recoil pressure, M the molar mass of silicon, R the gas constant and T the temperature. This equation was adapted to the case of silicon and plotted in function of temperature as shown in Figure B-1.

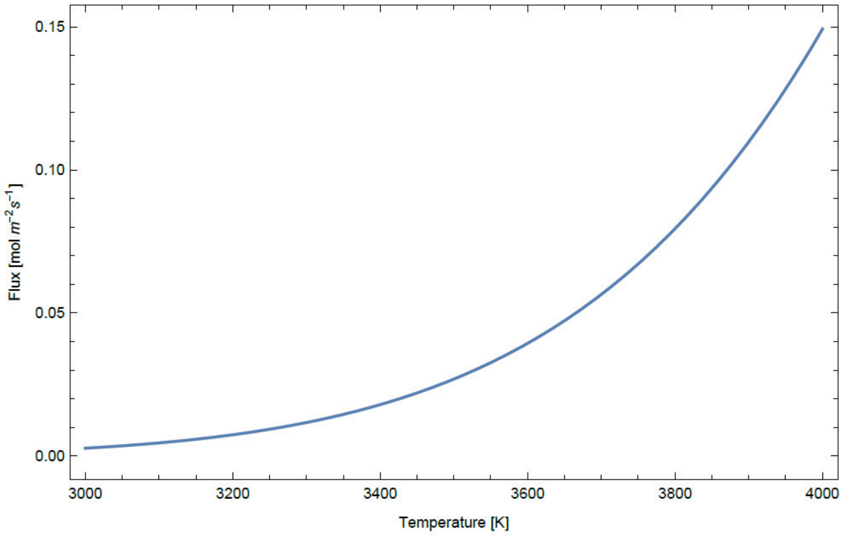

Figure B-1. Net material evaporation flux as function of temperature, calculated for silicon

After integration over 40 s and over the laser bea area, the energy E_{lost} lost during silicon evaporation is calculated as:

- At 3000 K: E_{lost} = 0.012 J over 40 s
- At 4000 K: E_{lost} = 0.65 J over 40 s

As comparison, the laser energy ranges between 0.2 and 0.6 J per pulse. Therefore, on 40 s, the energy lost during material evaporation is negligible compared to the energy provided by the laser during this period of time.

B.2. Influence of the convection cooling coefficient

Temporal temperature profiles of the melt pool for the conditions 200 Hz – 160 mJ were calculated for different convection coefficients corresponding to the argon shielding gas cooling. The results of the FEM simulations for those profiles are shown in Figure B-2. No relevant differences could be observed between the coefficients h at 30 W/m^{2}K and 173 W/m^{2}K.

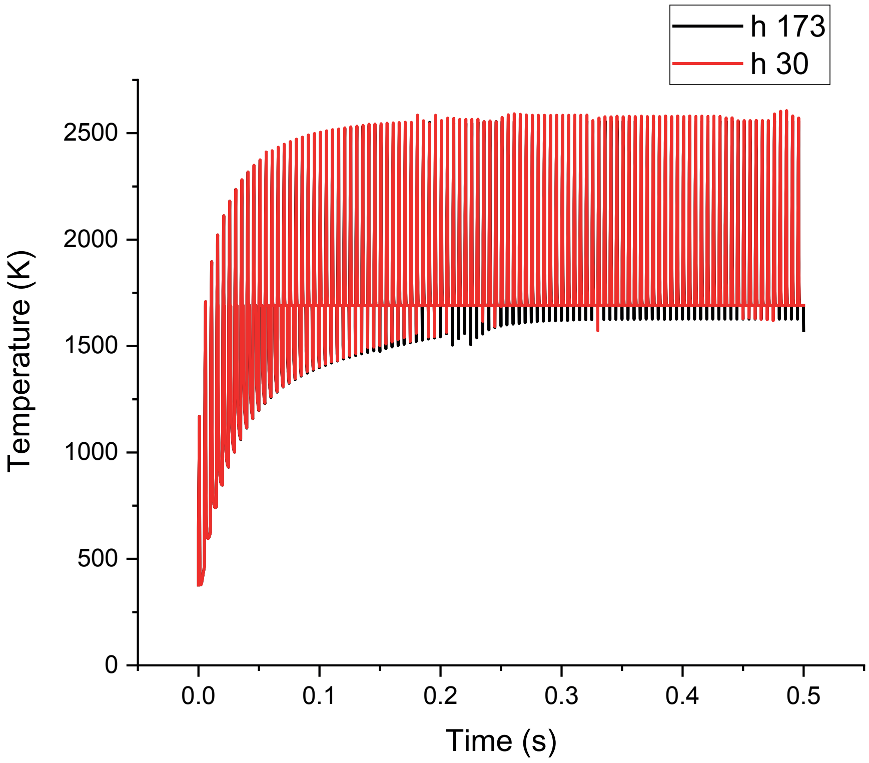

Figure B-2. Temporal temperature profile of the center of the melt pool calculated for different convection coefficients h corresponding to the argon shielding gas.

Appendix C – Limit of Detection of the Optical Method of Powder Burst Weight Quantification

As described earlier, the powder feed rate can be controlled by changing the cell opening time and the pressure inside the cell during the opening time. These parameters are used to control the feed rate values. In order to assess the sensitivity of the measurement, image analysis described in Chapter 3 was carried out on powder feed rates monitored either by the cell opening time or by the vacuum intensity.

Figure C-1(a) displays the burst size distribution for a sample of 25 bursts for different cell opening times but the same pressure in the cell. It was observed that for different cell opening times, the feed rate individual powder burst weight distributions were well separated. A cell opening time of 40 ms (corresponding to a feed rate of 1.0 g/min) has a maximum of distribution around 0. A cell opening time of 50 ms (corresponding to a feed rate of 3.4 g/min) has a maximum of distribution around 8000. A cell opening time of 80 ms (corresponding to a feed rate of 15.0 g/min) has a maximum of distribution around 13000. The areas for the feed rate 1.0 g/min were difficult to determine because of the light noise on the pictures.

Figure C-1(b) displays the burst size distribution for a sample of 25 bursts for different cell pressures but the same cell opening time. It was observed that the method did not enable a good separation of the individual powder burst weights when different cell pressures were applied.

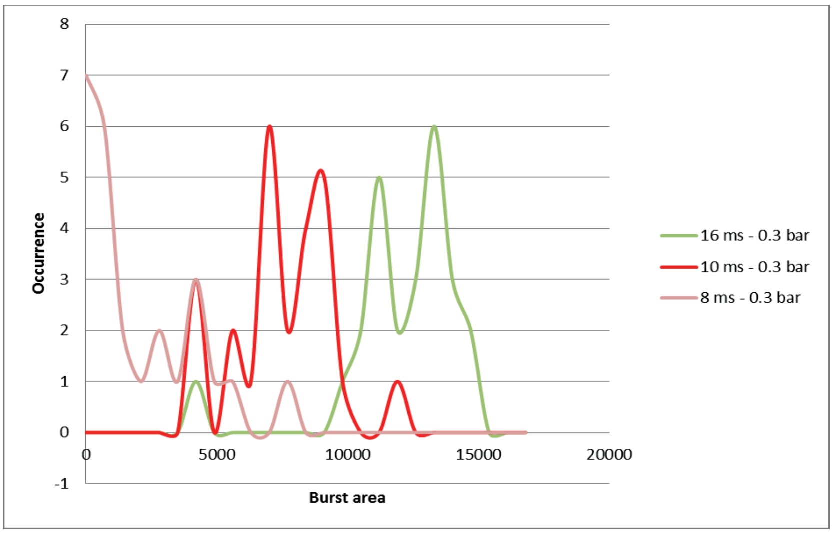

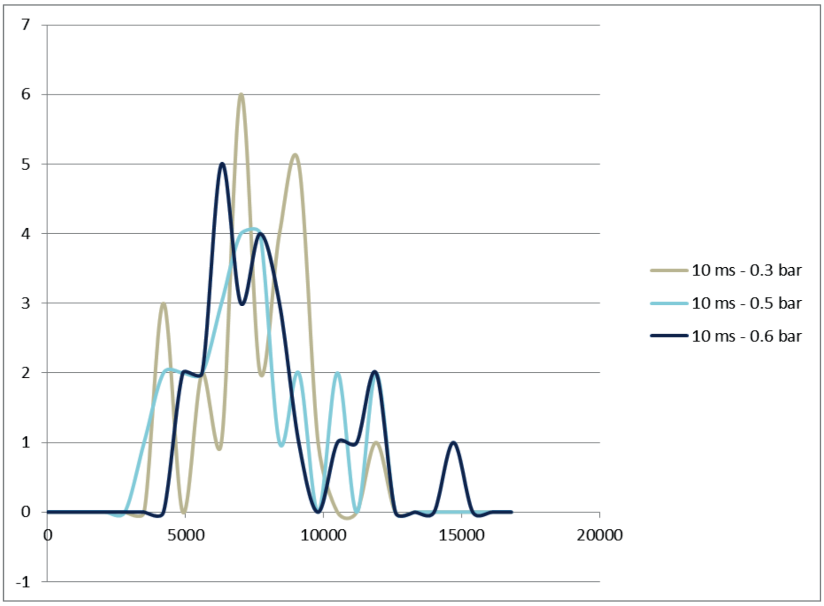

Figure C-1. Mass per burst in function of time (a) for different cell opening times and the same cell pressure, (b) for the same cell opening time but different cell pressures.

Therefore, when the feed rate needed to be varied, modifying the cells opening times was preferred to modifying the pressure inside the cell.

Appendix D – Microscope Images Used to Plot the Working Window to Build Crack-Free Pillars

The pictures of the pillars used in Figure 4-14 are displayed in this section. Cracks that appeared during the polishing step are indicated with a red arrow.

D.1. Feed rate 15.0 g/min

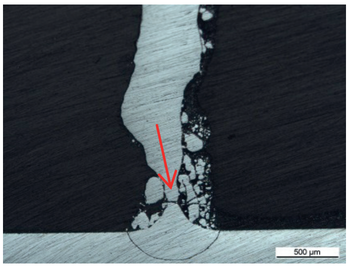

50 Hz – 350 W – 1 ms

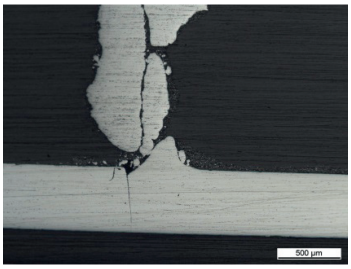

50 Hz – 500 W – 1 ms

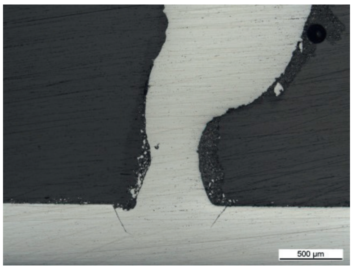

50 Hz – 600 W – 1 ms

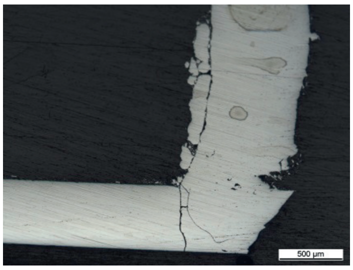

50 Hz – 900 W – 1 ms

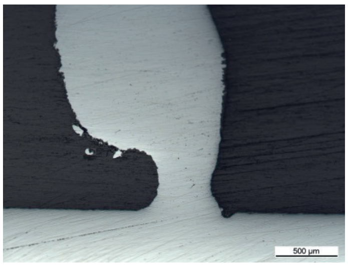

75 Hz – 500 W – 1 ms

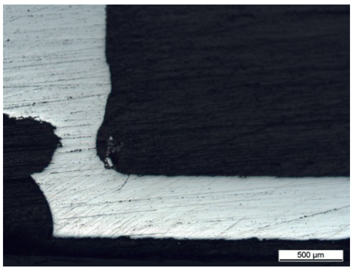

75 Hz – 600 W – 1 ms

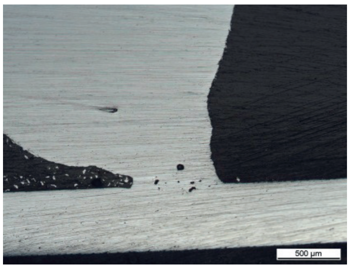

75 Hz – 700 W – 1 ms

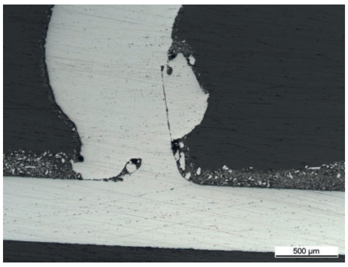

100 Hz – 450 W – 1 ms

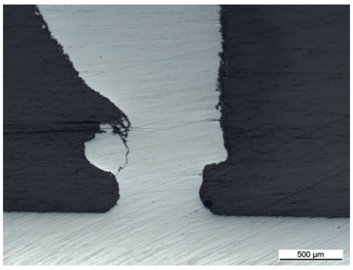

100 Hz – 500 W – 1 ms

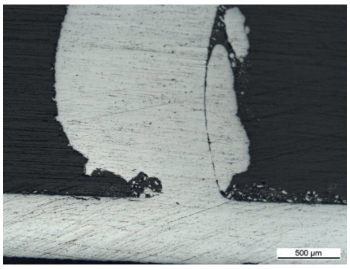

100 Hz – 600 W – 1 ms

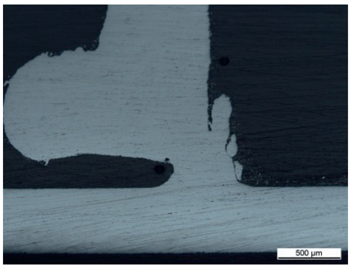

150 Hz – 300 W – 1 ms

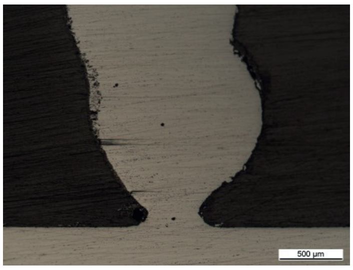

150 Hz – 400 W – 1 ms

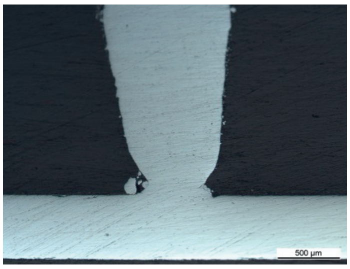

200 Hz – 250 W – 1 ms

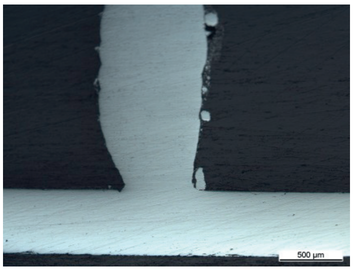

200 Hz – 300 W – 1 ms

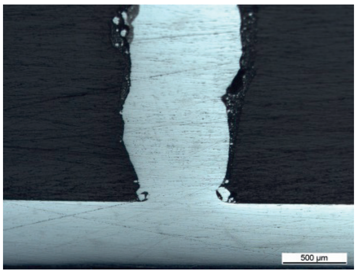

180 Hz – 400 W – 1 ms

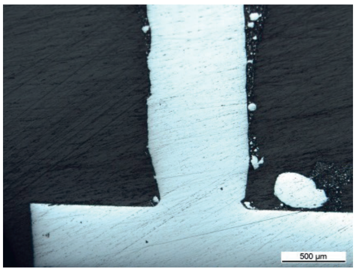

180 Hz – 450 W – 1 ms

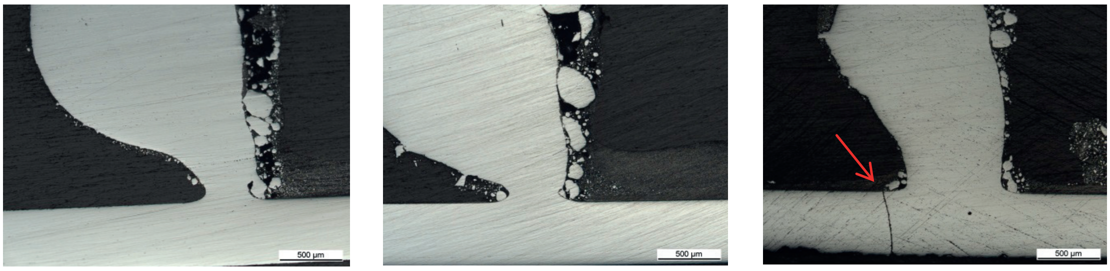
500 µm
500 µm
500 µm

200 Hz – 250 W – 2 ms   200 Hz – 250 W – 4 ms   200 Hz – 300 W – 4 ms

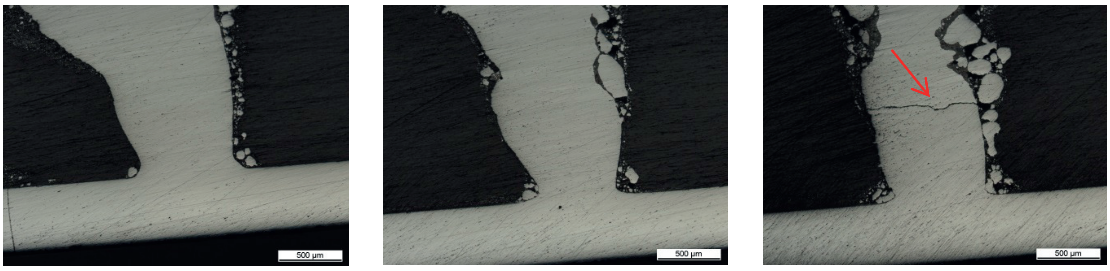
500 µm
500 µm
500 µm

200 Hz – 350 W – 4 ms   180 Hz – 400 W – 4 ms   180 Hz – 450 W – 4 ms

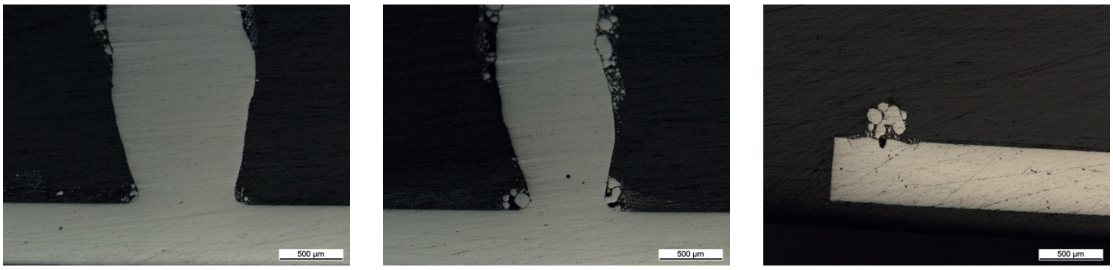
500 µm
500 µm
500 µm

180 Hz – 550 W – 4 ms   180 Hz – 600 W – 4 ms   200 Hz – 250 W – 0.5 ms

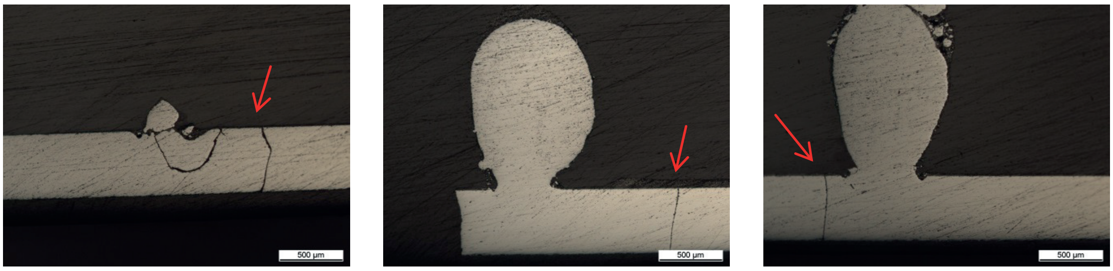
500 µm
500 µm
500 µm

200 Hz –250 W – 0.75 ms   200 Hz – 250 W – 1.25 ms   200 Hz – 250 W – 1.5 ms

Figure D-1. Optical microscope images of pillars built at different laser conditions, for a substrate surface temperature of 730°C. These images were used to establish the working window presented in Chapter 4.1.2.

D.2. Feed rate 1.0 g/min

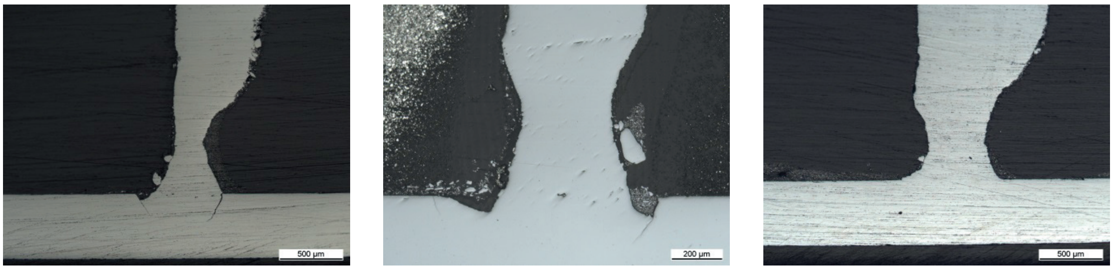
500 µm
200 µm
500 µm

50 Hz – 500 W – 1 ms   50 Hz – 600 W – 1 ms   50 Hz – 900 W – 1 ms

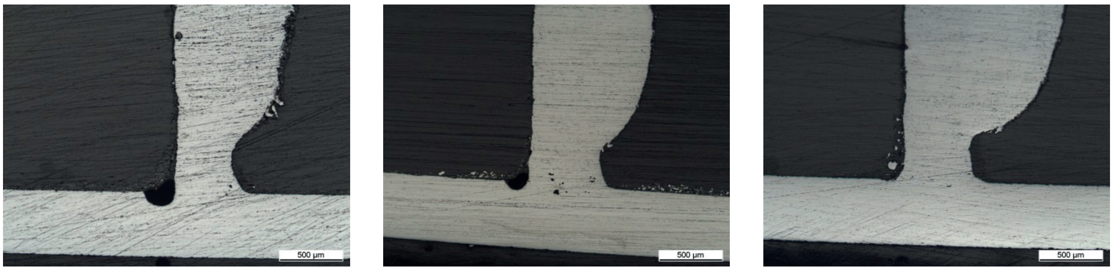
500 µm
500 µm
500 µm

75 Hz – 500 W – 1 ms   75 Hz – 600 W – 1 ms   75 Hz – 700 W – 1 ms

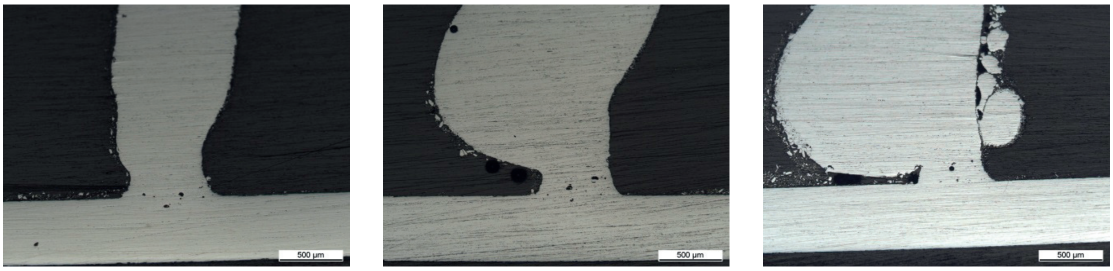
500 µm
500 µm
500 µm

100 Hz – 500 W – 1 ms   100 Hz – 600 W – 1 ms   150 Hz – 300 W – 1 ms

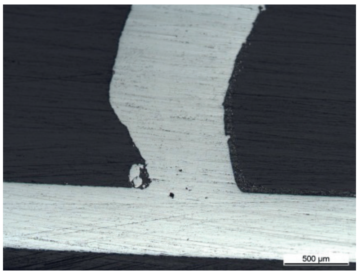

150 Hz – 500 W – 1 ms

Figure D-2. Optical microscope images of pillars built at different laser conditions, for a substrate surface temperature of 730°C. These images were used to establish the working window presented in Chapter 4.1.2.

Appendix E – On the importance of the oxygen content of the powder raw material in case of powder bed processing – Paper draft

Production of free standing silicon tracks by laser melting of compacted micron-sized powders in preparation for additive manufacturing of silicon I: influence of oxygen content and pellet density on track morphology

Marie Le Dantec[1], Matthias Leistner[1], Renato Figi[2], Marc Leparoux[1], Patrik Hoffmann[1]

[1] Empa (Swiss Federal Laboratories for Materials Science and Technology), Feuerwerkerstrasse, 39, CH-3602 Thun, Switzerland

[2] Empa (Swiss Federal Laboratories for Materials Science and Technology), Überlandstrasse, 129, CH-8600 Dübendorf, Switzerland

Abstract

Additive manufacturing (AM) is currently limited to only 3 classes of materials: ceramics, polymers and metals. There is a need to extend the process to new materials, in order to expand the possibilities and solve common issues. We propose a preliminary study on the interactions between silicon fine powder pellets and a pulsed Nd:YAG 1064 nm laser, in the scope of preparing AM of semiconductors such as silicon.

In this paper, we investigate the influence of oxygen concentration contained in the initial silicon powders on the morphology of the tracks produced by a pulsed Nd:YAG 1064 nm laser during laser melting of silicon powder pellets. We subsequently studied the influence of pellet density on the morphology of the molten tracks.

The oxygen content in the powder was measured by combustion and infrared analysis. To understand the final morphology of the track in function of oxygen content, additional in-situ measurements were performed. A high speed camera was used to observe the formation of the plume in the different cases. The thermal and optical properties of the pellets were also investigated. The pellets were pressed with different loads to obtain different densities. Morphology observations were carried out by optical microscopy and SEM.

It was found that the initial oxygen content of the processed powders should be less than 0.1 wt% to produce a smooth silicon melted track. This result is most probably due to formation of gaseous SiO by reaction between silicon and its native oxide during the process. It was also demonstrated that lower densities simply lead to deeper melted tracks due to less material present in the same volume. The obtained results were successfully used in Selective Laser Melting (SLM) of a silicon track on a wafer, with epitaxial growth.

Keywords

Laser melting, fine silicon powders, silicon oxide, oxygen, density, track morphology, additive manufacturing

Introduction

Additive manufacturing (AM) has been the center of attention during the past few years. It is especially popular in the fields of aerospace and defense, medical applications and automotive industries, since it provides numerous advantages over conventional manufacturing, such as a high degree of customization, material saving, design of complex parts and creation of lightweight pieces.

Currently, three categories of materials have mostly been studied for AM: ceramics, polymers and metals. Into these categories, only a limited amount of materials are available. Concerning AM of metals, the most popular ones are steels, aluminium and its alloys, titanium and its alloys, and Ni-based superalloys[18]. There is a need to extend AM to new materials because "improvements to feedstock materials or development of new materials could have a direct impact on facilitating more widespread use of AM"[129].

Semiconductors have not yet been (extensively) studied as potential materials for AM in a powder-bed approach. The semiconductor industry is currently able to make 2.5D structures, mostly through a "top-down approach" usually involving photolithography and etching. However, the third dimension is missing to reach total freedom in design. However, semiconductor nanoparticles have been used in AM materials as additives to improve their mechanical properties[130]. Eventually, only one paper was found to have tried SLM of semiconductor: El-Desouky et al.[25] put their interest in Bismuth

Telluride for its thermoelectric properties, and managed to melt Bi_2Te_3 powders by SLM, opening novel routes to a new class of materials.

Silicon bulk interaction with lasers has been widely studied. Deposited layers of amorphous silicon are recrystallized by laser[131, 132]. In stealth dicing[133], the laser is used to create micro defects that ease silicon cutting. However, only a few papers have studied laser sintering/melting of silicon powders. Iwabuchi et al.[134] have laser sintered recycled silicon powders mixed with carbon nanofibers to create anodes for lithium-ion batteries. Straboni et al.[135] developed a process based on hot pressing and zone melting recrystallization to sinter silicon powders as substrates for thin-film solar cells. Ai et al.[136] also developed substrates for solar cells, using spark plasma sintering. Free form patterning of Si has been performed[4], by means of layers of chemical vapor deposition of silicon followed by Ga ion implantation by FIB and etching. The features obtained had dimensions of dozens of nanometers to micrometers. However, to the best of our knowledge, no literature reports powder-based AM of silicon (neither powder bed fusion nor direct energy deposition).

Silicon is brittle at room temperature and the cleanroom processes are already well established and competitive. However, it would be interesting to have an alternative solution in case of small number of tall structures to be build on a wafer. In this case, one could avoid material wasting caused by extensive etching. Another advantage of 3D printing of silicon would be additional freedom in design of mechanical parts, e. g. MEMS or watch parts. Moreover, starting with an elemental semiconductor like Si prevents stoichiometric problems from arising. Therefore, it is a good starting point to study the feasibility of processing semiconductors by AM.

Currently, powder-based AM can only produce parts down to several mm. There is a need to fabricate 3D parts at the micrometer scale, especially if one wants to combine it to the semiconductor industry, where Moore's law governs. In laser AM, resolution is driven by several parameters, mainly laser beam size and powder particle size (and layer thickness for SLM). Higher resolution means finer powders (< 5um) and smaller laser beam diameter. Therefore, in this study, we use silicon powders that are <3 µm in size. Selective laser micro sintering is already trying to satisfy these requirements, as it can produce parts with a precision < 30 µm and a roughness of about 3 µm. This process is based on the same principle as Selective Laser Sintering (SLS), but is using finer powders (< 10 µm), a q-switched laser of pulse duration in the range of 100 ns and a spot diameter of a few dozens of microns[137].

In this paper, we study the laser-silicon powder interactions to prepare AM of silicon, mainly in a powder bed fashion. Pellets of silicon powders were pressed and molten tracks were produced with a pulsed Nd:YAG 1064 nm laser under N_2 and O_2 free controlled atmosphere. A very fine powder was used (< 3 µm) to anticipate the use of this powder in AM. The goal was to understand which parameter(s) have the most influence on silicon powder processing. In this scope, the oxygen content in the initial powder was varied. Its influence on the morphology of the final track was observed.

Oxygen is known to influence the melt pool and the final AM parts through diverse mechanisms. Oxides were mostly found to disturb the wetting of the molten metal on the solid part, which leads to the so-called balling effect. They can also change the melt pool dynamics and the laser absorptivity. They also trigger the formation of oxide inclusions and impurities in the final parts. Louvis et al. [138] demonstrated that oxide was main responsible for material defect after SLM of aluminium. Indeed, the oxide formed on top of the melt pool is vaporized by the laser, and the oxide at the bottom of the melt pool is broken by the Marangoni effect. However, the oxide formed on the sides remains, because the melt pool could not wet the surrounding material. This led to porosity and defects. Oxygen has a huge influence on titanium mechanical properties[139]. Dubenskaia et al. demonstrated that oxygen had an impact on the melt pool temperature in stainless steel SLM[140].

Silicon powder native oxide is well-known for hindering its melting properties. Seo et al.[141] have attempted melting Si powders recycled from kerf loss in a graphite crucible. They observed the formation of a slag composed of Si, oxygen and carbon, with porosity. Success was reached when they attempted the melting in a reducing atmosphere (H_2 + Ar) and opted for directional solidification to push the gas bubble upwards. Eyer at al.[142] tried to melt Si powder layer by Zone Melting Process (ZMR) and noticed that uniform melting was prevented by SiO evaporation. Cramer et al.[143] worked on Si kerf recycling and melting. They assess that dedicated stirring is necessary to allow SiO evaporation from the melt and prevent inclusions.

In this paper, we show that oxidation has to be avoided in order to obtain smooth silicon tracks. In this aim, powder with different starting oxygen content will be used. We also discuss the results to explain why oxygen is detrimental to the process. We study the influence of pellet density on the molten tracks. We used these results to successfully make a silicon track on a wafer by SLM.

Experimental

Material. Samples used in this study were prepared from commercial silicon powders bought from Dalian King Choice Non-Ferrous Metals Products Co., Ltd. It has 99.99% purity. The supplier gave the following information: D_{10}=1.535 um, D_{50}=2.966 um, D_{90}=4.817 um. To check its particle size, we used the laser diffraction method with a CILAS 1090. The powder was preliminary dispersed in water. Particle morphology was observed by SEM Hitachi S-4800.

Sample preparation.

Press. The silicon powder were pressed into pellets (**Figure E-3**) of 10 mm diameter and about 920 µm height with 140 bar held for 45 s by hydraulic pressing in a stainless steel die. This process led to pellets of density 60%, compared to the density of monocrystalline silicon (2.33 g/cm^3).

For the density experiment, the silicon powders were pressed into pellets of 10 mm diameter with 40, 60, 100, 120 and 140 bar held for 45 s by hydraulic pressing in a stainless steel die.

Deoxidation. The deoxidation was made according to the following procedure. The powders are first crushed with a spatula. A suspension is then made with about 100 mL of water per gram of powder. This suspension is agitated by ultrasound for 30 min to deagglomerate. 20 mL of 49%HF is added to the suspension, in order to get a 1%HF solution. 30 min of ultrasound is again applied to the solution. The suspension is then vacuum filtered through a paper filter (pore size < 2µm) to recover the deoxidized powder as wet filter cake. The wet filter cake is placed in a beaker and the beaker in a desiccator and dried under vacuum at 50°C over night at 15 mbar pressure. After deoxidation, the powders are thermosealed in aluminium polyethylene bags under argon, and placed into a desiccator to avoid moisture uptake.

Thermal oxidation. The thermally oxidized samples were placed in a resistance furnace under air. The powder was heated up to 900°C at 15K/min and maintained at this temperature for 1h. Then, the sample slowly cooled down in the furnace.

Laser, chamber and in-situ measurements. We used a chamber dedicated to laser-material interactions (Figure E-1). All experiments were performed with a pulsed Nd:YAG 1064 nm fiber laser. The beam profile was top hat and the beam diameter is 600 µm. The laser head position was fixed on a vertical position above one of the window ports of the chamber. The sample was mounted on an XYZ moving stage inside the chamber. The chamber was filled with 1 bar Ar. Its atmosphere was monitored with a mass spectrometer, and the humidity was kept under 40 ppm of oxygen. All melted tracks presented in this article were performed at a laser power of 333 W, pulse duration of 1 ms and scanning speed of 1 mm/s.

In-situ observations of the plume created during laser processing of silicon powder pellet were carried out with a high speed camera Videal MotionPro at 20000 frames/s and 0.1 µs exposure. The camera was placed at 70° angle with respect to the laser beam in order to observe the plume from the side (Figure E-2).

Sample analysis.

Oxygen measurements. The oxygen measurements were performed by combustion and infrared analysis with a LECO TC-500. The powder was placed in a tin capsule with nickel chips. The sample was then melted in a graphite crucible in an electrode furnace at about 3000°C. The oxygen was detected as CO_2 after reaction with the graphite crucible by infrared quantitative analysis.

Thermal diffusivity measurements. Thermal diffusivity of the powder pellets were determined by laser flash technique. The sample was heated at the desired measurement temperature in a furnace, under argon. The pellets edges were impregnated with resin (SpeciFix-20) on about 1 mm to consolidate the edges and avoid fracture during the measurement. The pellet was spray coated with carbon before measurement. The measurement was carried out according to the decomposition temperature of the resin. The latter was measured by TGA and was found to start at around 300°C. Therefore, the temperature range was set between 25 and 280°C. We have measured thermal diffusivity for silicon powder pellets of 60% density, with oxygen contents ranging from 0.07 to 14.3 wt%. There are 2 measurements for each of the sample, one performed during heating, and one during cooling down of the sample under test.

Sample observation. Sample track morphology was observed by optical microscopy, and SEM Hitachi S-4800. EDX analysis has been performed with an EDAX detector mounted on the same SEM chamber.

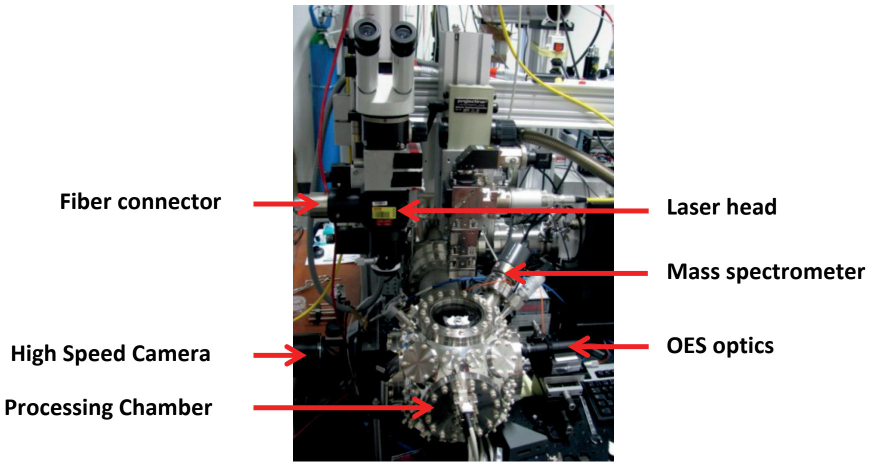

Figure E-1. Dedicated setup for laser-material interactions. The chamber is equipped with a 1064 nm pulsed Nd:YAG laser and several ports to observe laser-material interactions in-situ. Among them, a mass spectrometer is controlling the atmosphere inside the chamber, a spectrometer records the optical emission of the plume, and a high speed camera allows observing spattering and plume formation.

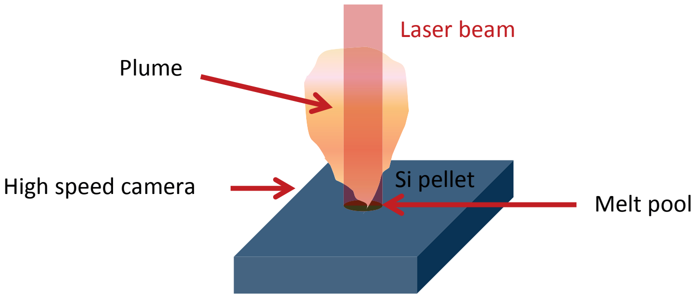

Figure E-2. Schematic of the in-situ observation of the plume with a high speed camera. The plume is observed on the side at a 90° angle with respect to the laser beam.

SLM

SLM of the fine Si powders was performed with a M2 cusing (Concept Laser GmbH, Germany). The powder layer was deposited manually. The laser had a diameter of 90 µm and a wavelength of 1064 nm. The process was carried out under 1 bar argon and less than 0.3 % oxygen in the atmosphere. The thickness of the powder was about 90 µm.

Results

Powder analysis.

Figure E-4 shows the particle size measurement performed on the silicon powders used in this study. It shows a broad particle size range, centered around 3 um, and a broad sub-micron tail. After measurement, we found the following distribution: D_{10}=0.53 µm, D_{50}=3.09 µm and D_{90}=10.58 µm. This analysis was confirmed by the SEM picture on Figure E-3. We observe irregular silicon chunks up to sizes such as 5 µm, surrounded by micron to sub-micron particle size particles. The broad particle size distribution facilitates having pellets of high density because the small particles can occupy voids between larger ones.

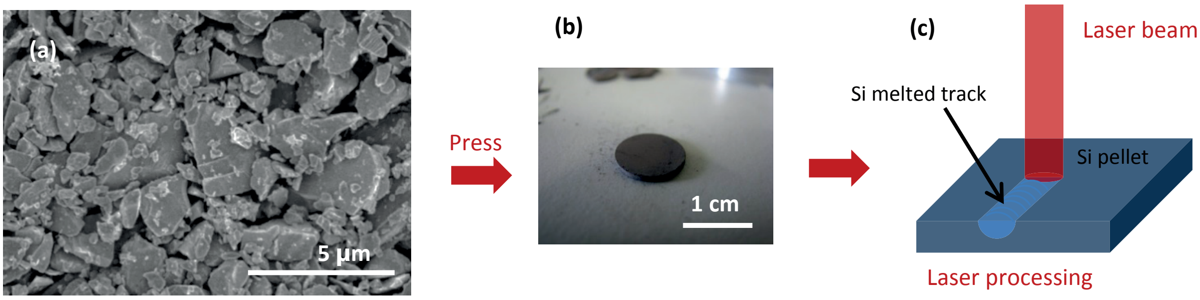

Figure E-3. (a) Observation of silicon powders by SEM, as-received from the manufacturer, (b) Silicon powder pellet of diameter 10 mm, thickness 950 µm and density 60% obtained by hydraulic pressing of the initial powders, and (c) schematic of the process under investigation: a laser beam is moved on a straight line across the pellet to form a Si molten track.

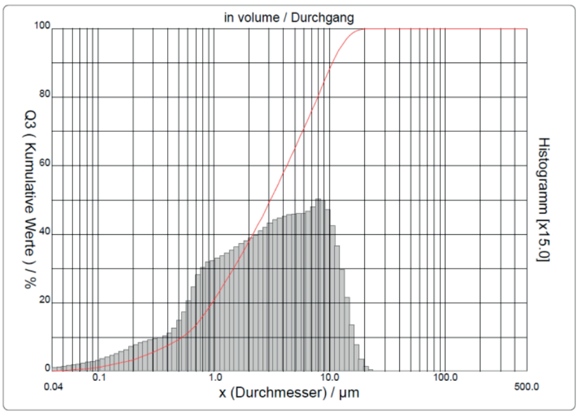

Figure E-4. Particle size measurement in volume of the silicon powder used in the process. We found D10=0.53 µm, D50=3.09 µm and D90=10.58 µm.

Track morphology. The results of silicon pellet processing by laser with respect to the oxygen content of the initial powder is shown on Figure E-5. We found out that the track morphology was very dependent on the initial powder oxygen content. The as-received powder supplied directly from the manufacturer contained 2.6 wt% oxygen. Laser processing of pellets made from such powders resulted in balling, spattering, loss of material and oxidation traces (Figure E-5, a). EDX analysis of the oxidation trace revealed that it is composed of Si and O in similar atomic quantity (Figure E-5). After deoxidation up to 0.4 wt% of oxygen, no oxidation traces are observed, and only few spattering (Figure E-5, b). Only when the powder were deoxidized to less than 0.1 wt%, a smooth shiny track was obtained (Figure E-5, c), without any of the 4 undesirable effects mentioned earlier. The irregularities in the tracks can be due to cracks already present in the pellet after pressing, as it is challenging to take out the pellets out of the die without breaking it.

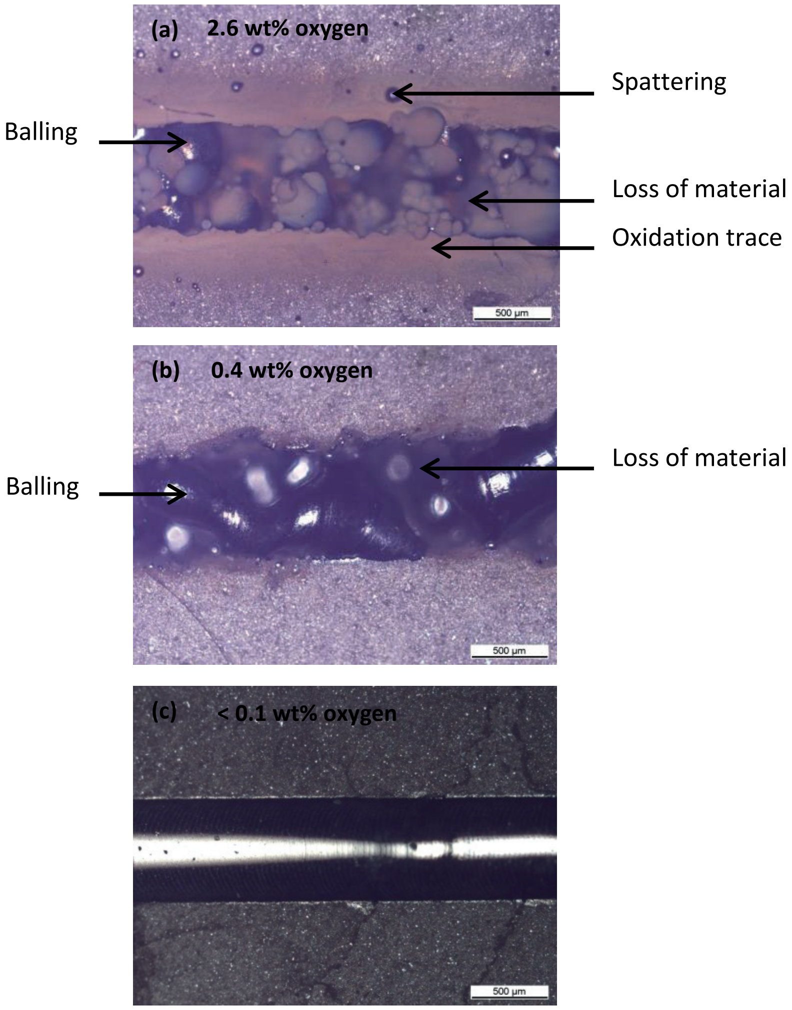
(a) 2.6 wt% oxygen
Spattering
Balling
Loss of material
Oxidation trace
500 µm
(b) 0.4 wt% oxygen
Loss of material
Balling
500 µm
(c) < 0.1 wt% oxygen
500 µm

Figure E-5. Track morphology for different oxygen contents in initial silicon powders after laser processing with power 333W, pulse duration 1 ms and scanning speed 1 mm/s (a) 2.6 wt% (b) 0.4 wt% (c) less than 0.1 wt%. Higher oxide concentration in the initial powder lead to balling, spattering, material loss and oxidation traces

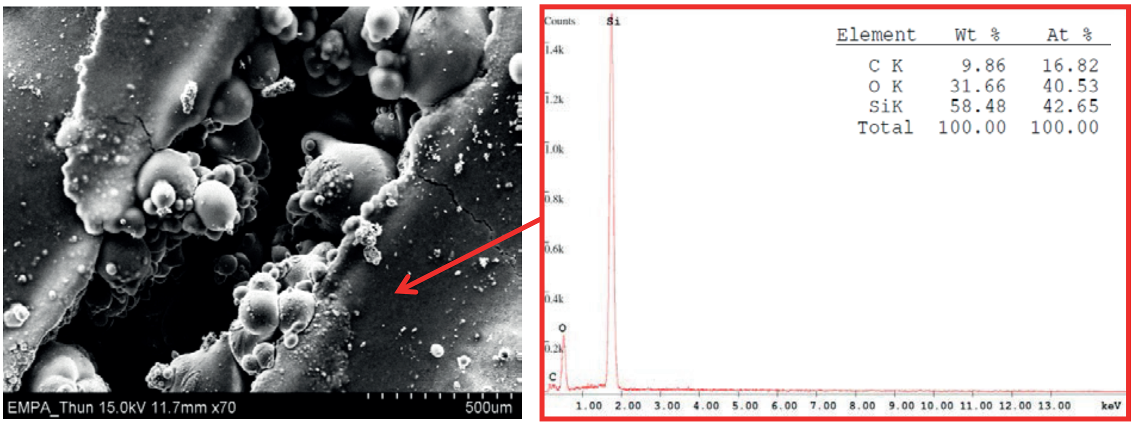

Figure E-5. (a) SEM picture of the track made from powder containing 2.6 wt% oxygen. (b) EDX spectrum of the oxidation trace. The trace is composed of Si and O in similar atomic quantity.

Microstructure of the silicon track. In SLM, the thickness of the powder layer should be between 20 and 150 µm. Therefore, it is of interest to know the thickness and depth of the molten silicon track. Thus, the cross-section and the microstructure of a silicon track have been observed. Figure E-6 displays the optical microscope observation of the track cross-section. The thickness of the molten track is about 70 µm. The microstructure, observed by SEM, comprises two regions: one with small equiaxed grains at the bottom of the track, and one with columnar larger grains, at the top of the track. Nucleation occurs first at the bottom of the track due to smaller temperature. Larger columnar grains form on top of the equiaxed grains due to the upwards movement of the solidification front.

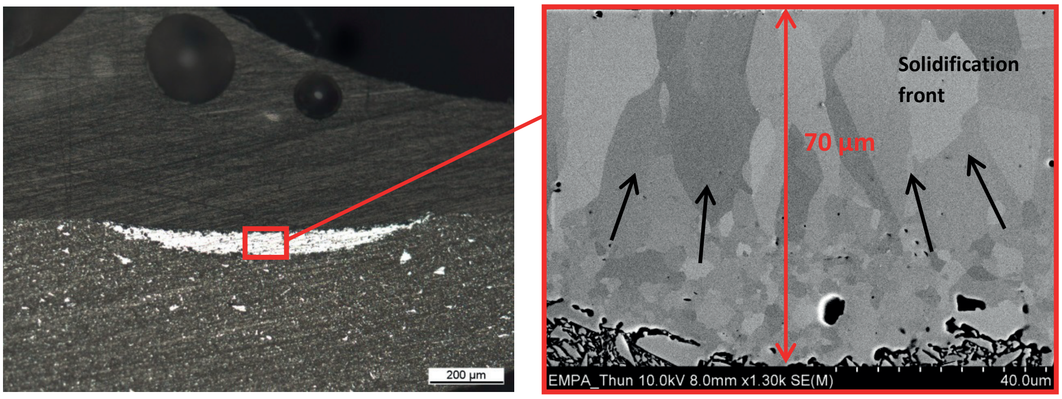

Figure E-6. (a) Optical microscope picture of the cross-section of a melted silicon track processed with powders containing 0.1 wt% oxygen. (b) Detail of the track observed by SEM, enhancing the grain contrast. Smaller equiaxed grains can be observed at the bottom of the track due to nucleation and larger elongated grains can be observed at the top of the track due to the upwards movement of the solidification front.

Plume analysis. In-situ observations with a high speed camera on a single laser shot of 333 W and 1 ms are reported on Figure E-7 for silicon powder pellets of different oxygen content. The plume formed during laser processing of oxidized silicon powder pellets expands as the material evaporates. Numerous droplets of liquid are spattered out of the melt pool. On the contrary, in the case of powder deoxidized to less than 0.1 wt% oxygen, the plume is much smaller and disappears quickly after the end of the pulse duration.

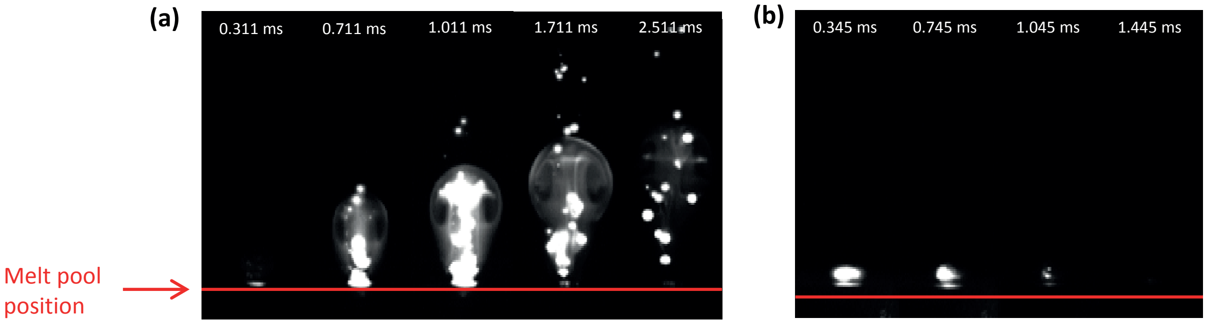

Figure E-7. In-situ high speed camera observations of a single laser shot on silicon powder pellets of different oxygen contents: (a) 2.6 wt% and (b) less than 0.1 wt%. The shot was made with a power of 333 W and a pulse duration of 1 ms. The pellet containing 2.6 wt% oxygen exhibits strong evaporation and spattering during laser processing, whereas the pellet containing less than 0.1 wt% exhibits no spattering and very little evaporation.

Pellets thermal properties. On Figure E-8 (a), thermal diffusivity of silicon powder pellets with different oxide contents are presented, as well as thermal diffusivity measurements for bulk silicon (Shanks et al.[144]) and silicon powder sintered by spark plasma sintering (SPS, Ashby et al.[145]). It was found that thermal diffusivity decreases for increasing oxygen content. It is reduced by 20% if silicon powder contained 2.58 wt% oxygen and by half if silicon powder were thermally oxidized to 14.3 wt% oxygen. Moreover, the thermal diffusivity of 60% density silicon powder is more than 3 orders of magnitude lower than the one of bulk silicon and about 2 orders of magnitude lower than the one of SPS consolidated silicon powders. This measurement explains why we need much less fluence to melt silicon powders with respect to a silicon wafer. The silicon powders used in the measurements of Ashby et al. was comparable to ours in size as they were > 1 um. They were prepared from bulk silicon of 10 Ω.cm resistivity, similar to our powder which contained around 1 ppmw of B and P and 20 ppmw of As (given by the supplier and measured by ICP-OES), which corresponds to about 15 Ω.cm . After SPS treatment, they obtained silicon pellets of density similar to ours (1.4-2 g/cm^3). The SPS treatment enhances considerably the thermal diffusivity as particles are bound together. In our case, the powders are only pressed against each other without further treatment.

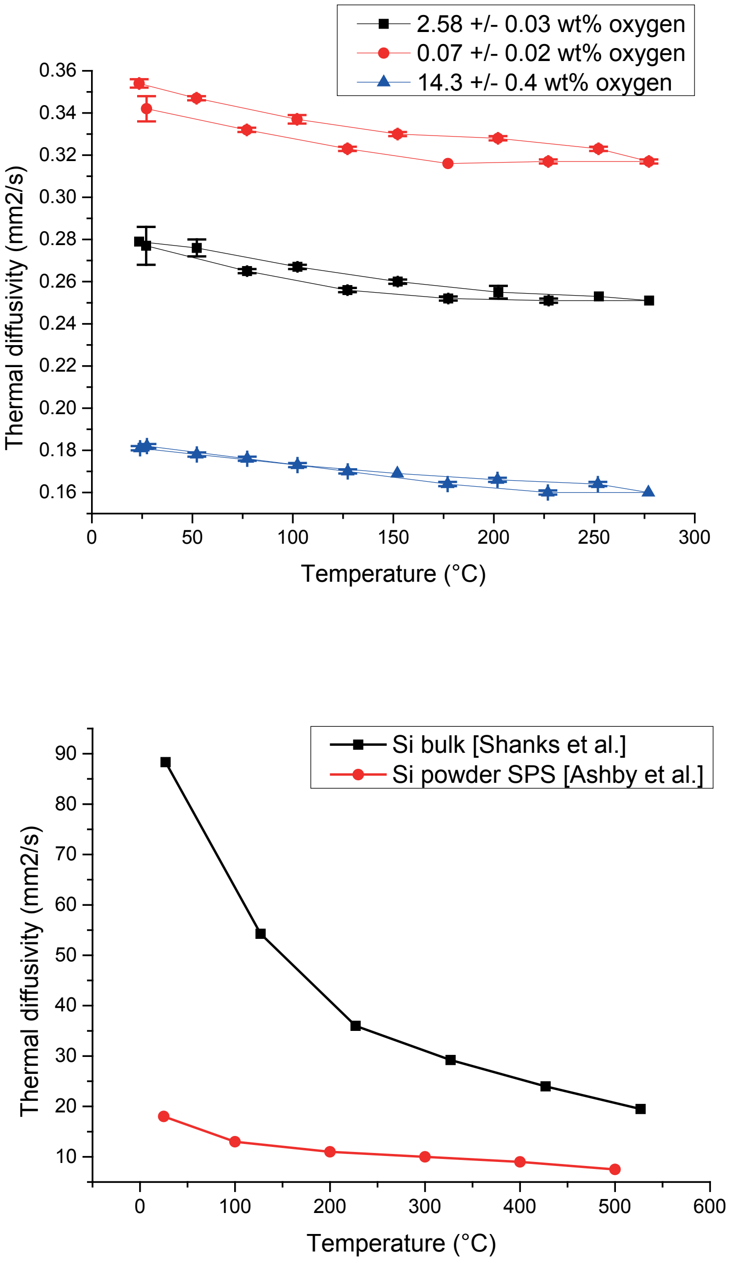

Figure E-8. (a)Thermal diffusivity measurements for silicon powder pellets of different oxygen content. The measurement has been done by laser flash analysis. Thermal diffusivity of deoxidized silicon powders are 3 orders of magnitude below the one of a monocrystalline silicon wafer. The more oxidized the powders, the lower the thermal diffusivity. (b) Thermal diffusivity measurements for bulk silicon (calculated from the data of Shanks et al.[144]) and silicon powder consolidated by SPS (Ashby et al.[145]).

Influence of pellet density on track morphology. To determine the applicability of these results to an SLM process, the correlation between powder density and track quality was investigated. The optical microscopy observations of the molten track, for densities varying from 51 to 61%, are shown on Figure E-9. Typical layer densities in SLM are around 60-65%, depending on the particle size distribution and shape. Jacob and al. measured the powder bed density of S17-4 PH stainless steel (spherical shape, D_{92}=53 µm, nominal layer thickness 20 µm) and found it to be around 60%[146]. The molten track sinks down into the pellet for decreasing densities. Figure E-10 displays a graph showing the area of a melted track and the total area affected by the laser. Here again, the total area affected by the laser is higher and higher as the density decreases. This can be attributed to the fact that a decreasing density means less material per unit of volume. Therefore, when silicon melts and recrystallizes, it occupies less and less space as it consolidates into fully dense material. This observation was confirmed by calculation in which we found that the amount of material at the beginning of the process is approximately the same at the end of the process. Therefore, we also learn that there is only little evaporation of the material. Additionnally, it is observed on figure E-11 that when the density decreases, the melted area slightly increases: it could be due to a lower thermal conductivity due to lower particle percolation, which finally leads to temperature rise.

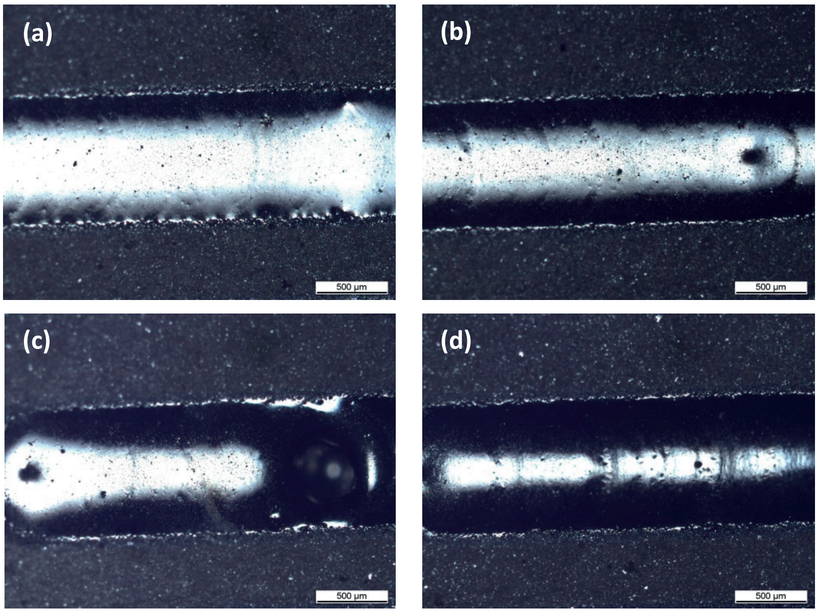

Figure E-9. Molten silicon track on pellets of decreasing densities. (a) 61% (b) 58% (c) 54% (d) 51%. The molten track sinks down into the pellet.

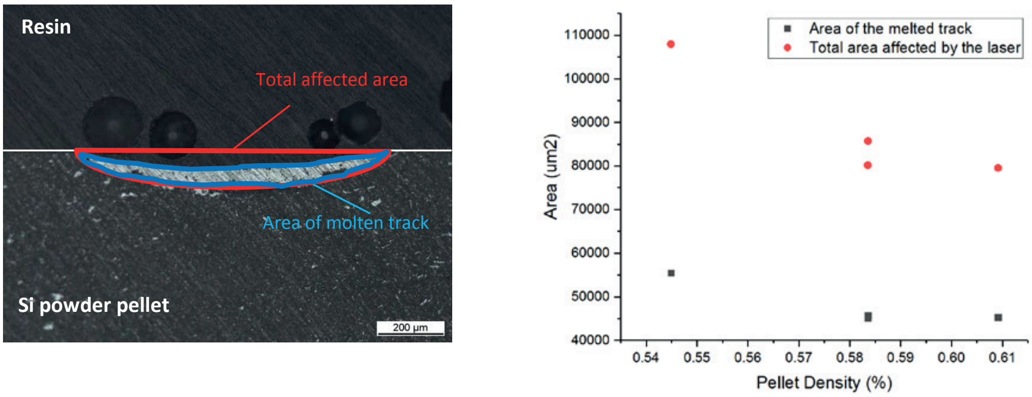

Figure E-10. (a) Optical microscopy photo of the cross-section of a track and (b) area of the melted track and total area affected by the laser for pellets of different densities. The less dense the pellet, the deeper the molten track.

Discussion

Oxidation traces and spattering effect. Oxidation traces observed on the sides of the tracks on figure 5(a) were found to be deposits of SiO (Figure E-5). The spattering observed during laser processing of the oxidized powder shown on Figure E-5 suggests that a gas is formed during the process and ejects molten silicon particles from the melt pool. These observations can be attributed to the condensation of SiO gas released during laser irradiation as a result of temperature rise, and recondensed during the cooling down. As the temperature reached during laser processing is at least equal to the melting temperature of silicon (1414°C), this gas is certainly released. This gas is released from underneath the surface of the melt pool and ejects molten droplets as spatter due to overpressure after heating. Additionally, a recoil pressure due to Si and SiO evaporation could be formed and enhance spattering.

These observations are in agreements with the conditions of formation of SiO found in the literature. Each powder particle is formed of a pure Si core and a SiO_2 shell. The formation of SiO gas from liquid silicon and its oxide at high temperatures has been well-established, according to the following equation[147]:

$Si(l) + SiO_2(s) \rightarrow 2\ SiO(g)$

This reaction start to release significant amounts of products at about 1000°C[148], and its evaporation rate increases with temperature[149]. In past investigations of the liquid silicon – solid SiO_2 systems, it was observed that the droplet of Si vibrated on its substrate due to the SiO gas formation[147 150].

It is very unlikely that adsoption of water on the oxidized silicon particles is the cause of gas release and spattering during laser processing. Indeed, additional experiments were made with silicon powder containing 2.6 wt% oxygen, where the powder was dried in a furnace for several hours before being pressed. The morphology of the track did not show any improvement. The decrease in surface tension due to increase in local oxygen partial pressure[151] could also enhance the spattering effect (Marangoni effect).

Additionally, thermal diffusivity α decreased when oxygen content increased (Figure E-8). Thermal diffusivity is linked to thermal conductivity with the following equation:

$$\alpha = \frac{k}{\rho C_P}$$

With ρ density of the material and C_P its thermal capacity. Therefore, in first approximation (keeping ρ and C_P constant in temperature), lower thermal diffusivity means lower thermal conductivity. Lower thermal conductivity leads to higher local temperature rise which enhances the reaction between SiOx and Si occuring from temperatures around 1100-1400°C[148 152]. The higher temperatures also encourages evaporation of the material.

Balling effect. After processing, we observed oxidation traces at the bottom of the track as shown in figure 11. As the wetting angle of molten Si on SiO_2 at 1693 K has been reported to be between 85 and 90° [153 154 155 156], liquid silicon is expected not to wet its oxide very well, leading to balling. Our material has also a rough surface as a powder, which enhances the phenomenon. Moreover, the important loss of material as spattering (Figure E-5, a) prevents the rest of the material to percolate. Therefore, it tends to ball under the effect of surface tension.

In this study, the oxygen partial pressure in the chamber was kept constant at a low level of less than 40 ppm, but the local oxygen pressure can be higher due to SiO gas formation. It has been proved in the literature for diverse materials that an increasing oxygen partial pressure in the atmosphere led to the so called balling effect. Li et al.[157] showed that an increase in the oxygen partial pressure from 0.1% to 1% in the atmosphere in the chamber led to balling for stainless steel and nickel powders. They attributed this effect to oxidation of the molten pool and consequently a dewetting of the molten material on the oxidized substrate.

SLM of fine silicon powders.

We successfully managed to produce molten silicon tracks on a wafer substrate by SLM by using the powder containing 0.1 wt% oxygen (figure E-12). The laser powder was 200W and the scan speed was 200 mm/s. The thickness of the layer was measured by confocal microscopy and was found to be 98 ± 13 µm.

Figure E-11 displays an optical microscope top view of the obtained molten tracks. Figure E-12 shows the SEM image of a cross-section of the track. The solidified melt pool is marked out by a rounded crack, and porosity can be seen. The liquid state having a higher density, pores are formed during the melting process and could not be eliminated due to fast cooling.

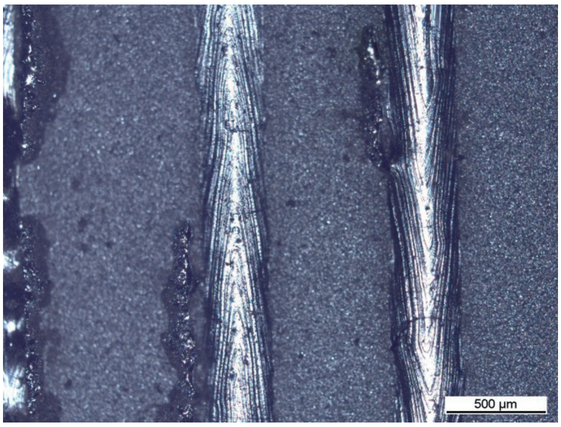

Figure E-11. Optical microscope picture of silicon tracks produced by SLM (top view). The thickness of the powder bed was 90 µm. The laser powder was 200W at 200 mm/s.

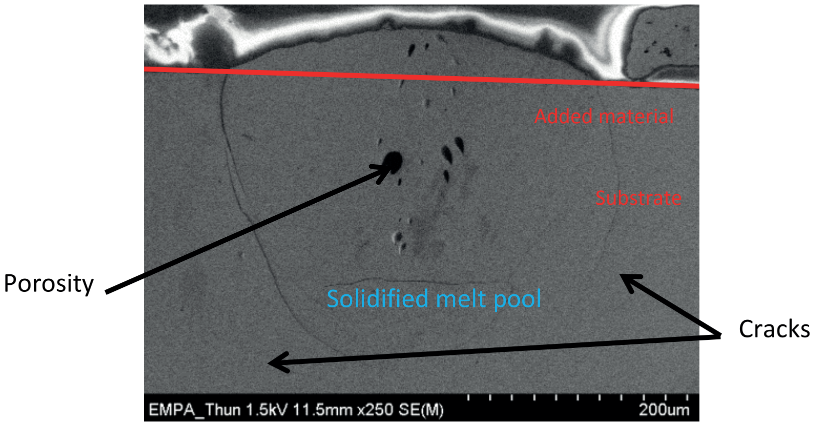
Added material
Substrate
Porosity
Solidified melt pool
Cracks
EMPA_Thun 1.5kV 11.5mm x250 SE(M)
200um

Figure E-12. SEM picture of the cross-section of the produced tracks. The heat affected zone can be pictured by a round crack. Pore formation is most likely due to the fact that the melt has a higher density than the bulk material, creating voids during cooling.

We carried out an EBSD map of the cross-section of the molten track (**Figure E-13**). We showed that the molten track had completely recrystallized epitaxially on the wafer. Only a grain at the top of the track has a different orientation, but this would not be a problem for further processing because the track would be partially remelted. The middle of the track exhibits a lattice defect with about 2° misorientation, as if two crystallization fronts had occurred and met in the middle. Most of the melt is formed within the substrate.

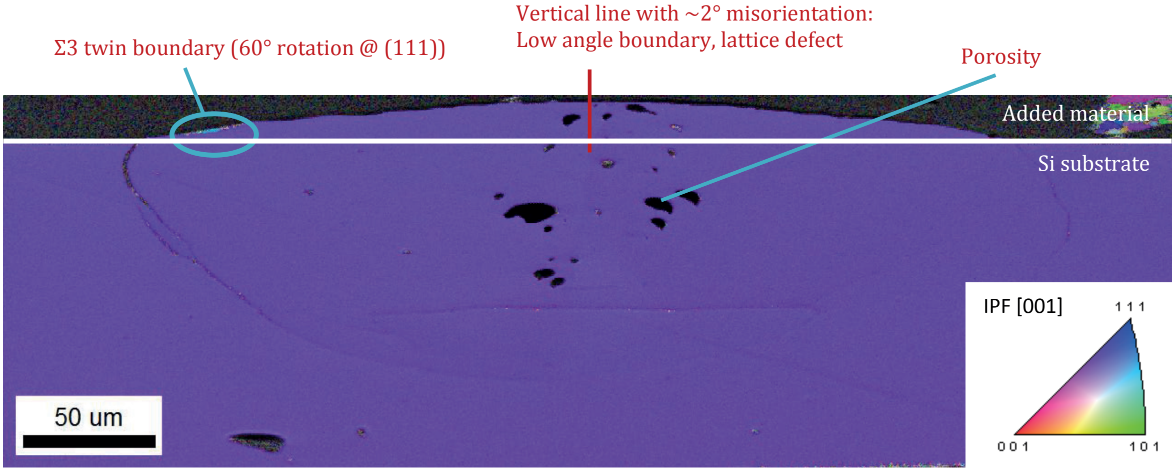
Σ3 twin boundary (60° rotation @ (111))
Vertical line with ~2° misorientation:
Low angle boundary, lattice defect
Porosity
Added material
Si substrate
IPF [001]
1 1 1
0 0 1
1 0 1
50 um

Figure E-13. EBSD mapping of the cross-section of the track. Silicon recrystallized epitaxially in the same orientation as the wafer. The sample is tilted at 70° angle, hence the distorted view.

Therefore, we successfully were able to produce a silicon track by SLM, by using fine powders that contained less than 0.1 wt% oxygen.

Conclusions

We have pressed pellets out of fine (< 5 µm) silicon powder with various oxygen contents. Then, we have made molten Si tracks with a pulsed Nd:YAG 1064 nm laser and observed the track morphology, in a chamber with controlled inert atmosphere. We have shown that the initial powder should contain less than 0.1 wt% of oxygen to produce smooth tracks. In-situ observations of the plume allowed us to conclude that the presence of oxide led to a reaction between Si and SiOx giving SiO gas that is the main responsible for material depletion and oxidation traces due to gas release and condensation. This reaction is enhanced by the fact that oxide leads to worse thermal conduction, so rising temperatures, even if less optical absorption occurs during the process.

Lowering the density of the pellets leads to deeper tracks due to shrinkage of the material after melting and recrystallization from powder to bulk.

These results were successfully used during a first trial of SLM of silicon fine powders. Several tracks could be produced on a silicon wafer without preheating, exhibiting epitaxial growth. The laser parameters, as well as a proper raking system still need to be adjusted to obtain optimized laser tracks and ensure repeatability. Thermal gradients should be reduced during the process to avoid cracking.

Acknowledgments

The authors would like to thank Lucas Güniat, Peter Ramseier, Hans-Rudolf Sieber and Oliver Nagel for their help and participation to the project.

References

1. Zaugg, A., Bifrare, C., Vorpe, S., Thiebaud, J. & Lippuner, M. Breguet Overcoil Balance Spring Made of Silicon-based Material. **1,** (2010).

2. Lin, S. Y. *et al.* A three-dimensional photonic crystal operating at infraredwavelengths. *Nature* **394,** 251–253 (1998).

3. Sheng Xu, Zheng Yan, Kyung-In Jang, Wen Huang, Haoran Fu, Jeonghyun Kim, Zijun Wei, Matthew Flavin, Joselle McCracken, Renhan Wang, Adina Badea, Yuhao Liu, Dongqing Xiao, Guoyan Zhou, Jungwoo Lee, Ha Uk Chung, Huanyu Cheng, Wen Ren, Anthony Banks, Xiuling, Y. Z. and J. A. R. Assembly of micro/nanomaterials into complex, three-dime sional architectures by compressive buckling. *Science (80-.).* **347,** 154–159 (2015).

4. Fischer, A. C. *et al.* 3D Free-form patterning of silicon by ion implantation, silicon deposition, and selective silicon etching. *Adv. Funct. Mater.* **22,** 4004–4008 (2012).

5. D. Bäuerle, G. Leyendecker, D. W. Laser grown single crystals of silicon. *Appl. Phys. A Solids Surfaces* **30,** 147–149 (1983).

6. Westberg, H. *et al.* Free-standing silicon microstructures fabricated by laser chemical processing Free-standing processing silicon microstructures fabricated by laser chemical. *Joural Apllied Phys.* **73,** (1993).

7. Takahashi, F., Miyamoto, K., Hidai, H. & Morita, R. Picosecond optical vortex pulse illumination forms a monocrystalline silicon needle. *Sci. Rep.* **6,** (2016).

8. *ISO/ASTM, 17296 Standard on Additive Manufacturing (AM) Technologies*. (2014).

9. Deckers, J., Vleugels, J., Kruth, J. & Introduction, I. Additive Manufacturing of Ceramics : A Review. **260,** 245–260 (2014).

10. W. J. Sames, F.A. List, S. Pannala, R.R. Dehoff, S. S. B. The Metallurgy and Processing Science of Metal Additive Manufacturing. *Int. Mater. Rev.* **61,** 315–360 (2016).

11. V.M. Weerasinghe, W. M. S. Laser Cladding with Pneumatic Powder Delivery. in *Applied Laser Tooling* (ed. Perez-Amor, O. D. . S. / M.) 183–211 (Martinus Nijhoff, 1983).

12. index @ www.pomgroup.com. Available at: http://www.pomgroup.com/.

13. Palaniswamy, S., Choi, J., Song, L. J., Mazumder, J. & Arbor, A. Additive Manufacturing by Direct Metal Deposition. *Adv. Mater. Process.* 33–36 (2011).

14. Sandia National Laboratories. *Laser Engineered Net Shaping.*

15. Saboori, Abdollah, Donato Gallo, Sara Biamino, Paolo Fino, M. L. An Overview of Additive Manufacturing of Titanium Components by Directed Energy Deposition : Microstructure and

Mechanical Properties. *Appl. Sci.* (2017). doi:10.3390/app7090883

16. Herderick, E. Additive Manufacturing of Metals: a Review. *Mater. Sci. Technol.* (2011).

17. Peyre, P., Aubry, P., Fabbro, R., Neveu, R. & Longuet, A. Analytical and numerical modelling of the Direct Metal Deposition Laser Process. *J. Phys. D. Appl. Phys.* **41,** (2008).

18. Herzog, D., Seyda, V., Wycisk, E. & Emmelmann, C. Additive manufacturing of metals. *Acta Mater.* **117,** 371–392 (2016).

19. Wilms, M. B., Biermann, T., Rolink, G., Weisheit, A. & Poprawe, R. Growing of bulk sapphire single crystals using laser material deposition. *J. Laser Appl.* **29,** 22013 (2017).

20. Luo, J., Pan, H. & Kinzel, E. C. Additive Manufacturing of Glass. *J. Manuf. Sci. Eng.* **136,** 61024 (2014).

21. Rittinghaus, S.-K., Weisheit, A., Mathes, M. & Vargas, W. G. Laser Metal Deposition of Titanium Aluminides – A Future Repair Technology for Jet Engine Blades? in *Proceedings of the 13th World Conference on Titanium* 1205–1210 (John Wiley & Sons, Inc., 2016). doi:10.1002/9781119296126.ch205

22. Rolink, G. *et al.* Laser metal deposition and selective laser melting of Fe-28 at.% Al. *J. Mater. Res.* **29,** 2036–2043 (2014).

23. Yves-Christian, H., Jan, W., Wilhelm, M., Konrad, W. & Reinhart, P. Net shaped high performance oxide ceramic parts by Selective Laser Melting. *Phys. Procedia* **5,** 587–594 (2010).

24. Li, X. P., Kang, C. W., Huang, H. & Sercombe, T. B. The role of a low-energy-density re-scan in fabricating crack-free Al85Ni5Y6Co2Fe2 bulk metallic glass composites via selective laser melting. *Mater. Des.* **63,** 407–411 (2014).

25. El-Desouky, A., Read, A., Bardet, P., Andre, M. & LeBlanc, S. Selective Laser Melting of a Bismuth Telluride Thermoelectric Material. *Proc. Solid Free. Symp.* 1043–1050 (2015).

26. El-Desouky, Ahmed, Carter, Michael, Mahmoudi, Mohamad, Elwany, Alaa, LeBlanc, S. Influences of energy density on microst ructure and consolidation of selective laser melted bismuth telluride thermoelectric powder. *J. Manuf. Process.* **25,** 411–417 (2017).

27. www.hitachi.com. *3D printing technology for semiconductors developed reducing MEMS sensor manufacturing time* (2017). Available at: http://www.hitachi.com/New/cnews/month/2017/02/170215.html.

28. Dongjo Kim, Sunho Jeong, Seong Hui Lee, Jooho Moon, J. K. S. Ink jet printing of organic semiconductor for fabricating organic thin film transistors.pdf. *Synth. Met.* **159,** 1381–1385 (2009).

29. Tran, Van-Thai, Yang, Hongyi, Wei, Yuefan, Du, H. Additive Manufacturing of ZnO Thin Film for Micro Size UV Photodetector. in *Proceedings of the 2nd International Conference on Progress in Additive Manufacturing (Pro- AM 2016)* 336–341 (2016).

30. Salea, A., Prathumwan, R., Junpha, J. & Subannajui, K. Metal oxide semiconductor 3D printing : preparation of copper (II) oxide by fused deposition modelling for multi- functional semiconducting. *J. Mater. Chem. C* **5,** 4614–4620 (2017).

31. Halevi, O., Jiang, H., Kloc, C. & Magdassi, S. Additive manufacturing of micrometric

crystallization vessels and single crystals. *Sci. Rep.* **6,** 1–8 (2016).

32. Tamaki, T., Watanabe, W. & Itoh, K. Laser micro-welding of silicon and borosilicate glass using nonlinear absorption effect induced by 1558-nm femtsecond fiber laser pulses. in *SPIE 6460, Commercial and Biomedical Applications of Ultrafast Lasers VII* **646018,** (2007).

33. Shu, K. M. & Shih, H. R. Ultrasonic Welding of Aluminum and Silicon Wafer. *Mater. Sci. Forum* **505–507,** 841–846 (2006).

34. Dolzhnikov, D. S. *et al.* Composition-matched molecular 'solders' for semiconductors. *Science (80-.).* **347,** 425 LP-428 (2015).

35. Raanan Y. Zehavi, Robert L. Davis, David B. Ackard, J. W. G. Crack free welding of silicon. **1,** (2001).

36. Raanan Y. Zehavi, Robert L. Davis, David B. Ackard, J. W. G. Method for welding silicon workpieces. (2002).

37. Raanan Y. Zehavi, Robert L. Davis, David B. Ackard, J. W. G. Two heat sources for welding. (2005).

38. Porter, D. A. & K.E.Easterling. *Phase Transformations in Metals and Alloys*. (Chapman & Hall, 1992).

39. Das, S. Physical Aspects of Process Control in Selective Laser Sintering of Metals. *Adv. Eng. Mater.* **2125,** 701–711 (2003).

40. Stefanescu, D. M. Thermodynamic Concepts—Equilibrium and Nonequilibrium During Solidification. in *Science and Engineering of Casting Solidification: Third Edition* 7–27 (2015). doi:10.1007/978-3-319-15693-4

41. Jackson, K. A. The Interface Kinetics of Crystal Growth Processes. *Interface Sci.* **10,** 159–169 (2002).

42. Jackson, K. A. The present state of the theory of crystal growth from the melt. *J. Cryst. Growth* **24–25,** 130–136 (1974).

43. Dantzig, J. A. & Rappaz, M. Departure from Equilibrium. in *Solidification* 50–64 (2009).

44. Beatty, K. M. & Jackson, K. A. Monte Carlo modeling of silicon crystal growth. **211,** 13–17 (2000).

45. Fujiwara, K. Crystal growth behaviors of silicon during melt growth processes. *Int. J. Photoenergy* **2012,** (2012).

46. Tokairin, M., Fujiwara, K., Kutsukake, K., Usami, N. & Nakajima, K. Formation mechanism of a faceted interface: In situ observation of the Si(100) crystal-melt interface during crystal growth. *Phys. Rev. B - Condens. Matter Mater. Phys.* **80,** 2–5 (2009).

47. Hunt, J. D. Steady State Columnar and Equiaxed Growth of Dendrites and Eutectic. *Mater. Sci. Eng.* **65,** 75–83 (1984).

48. Kurz, W., Bezençon, C. & Gäumann, M. Columnar to equiaxed transition in solidification processing. *Sci. Technol. Adv. Mater.* **2:1,** 185–191 (2001).

49. Basak, A. & Das, S. Epitaxy and Microstructure Evolution in Metal Additive Manufacturing. *Annu. Rev. Mater. Res.* **46,** 125–149 (2016).

50. Gäumann, M., Bezençon, C., Canalis, P. & Kurz, W. Single Crytal Laser Deposition of Superalloys: Processing-Microstructure Maps. *Acta Mater.* **49,** 1051–1062 (2001).

51. Mangelinck-Noël, N. & Duffar, T. Modelling of the transition from a planar faceted front to equiaxed growth : Application to photovoltaic polycrystalline silicon. *J. Cryst. Growth* **311,** 20–25 (2008).

52. Brynjulfsen, I., Arnberg, L. & Autruffe, A. Nucleation in small scale multicrystalline silicon ingots. *J. Cryst. Growth* **361,** 206–211 (2012).

53. Verneuil, A. V. . Process of Producing Synthetic Sapphires. (1911).

54. Ueltzen, M. The Verneuil flame fusion process: substances. *J. Cryst. Growth* **132,** 315–328 (1993).

55. Janaki Ram, G. D., Esplin, C. K. & Stucker, B. E. Microstructure and wear properties of LENS deposited medical grade CoCrMo. *J. Mater. Sci. Mater. Med.* **19,** 2105–2111 (2008).

56. Gäumann, M., Henry, S., Cléton, F., Wagnière, J.-D. & Kurz, W. Epitaxial laser metal forming: analysis of microstructure formation. *Mater. Sci. Eng. A* **271,** 232–241 (1999).

57. Bhattacharya, S. *et al.* Microstructural evolution and mechanical , and corrosion property evaluation of Cu – 30Ni alloy formed by Direct Metal Deposition process. *J. Alloys Compd.* **509,** 6364–6373 (2011).

58. Bezençon, C., Schnell, A. & Kurz, W. Epitaxial deposition of MCrAlY coatings on a Ni-base superalloy by laser cladding. *Scr. Mater.* **49,** 705–709 (2003).

59. Santos, E. C., Kida, K., Carroll, P. & Vilar, R. Optimization of laser deposited Ni-based single crystal superalloys microstructure. *Adv. Mater. Res.* **154–155,** 1405–1414 (2011).

60. Vilar, R., Santos, E. C., Ferreira, P. N., Franco, N. & Silva, R. C. Structure of NiCrAlY coatings deposited on single-crystal alloy turbine blade material by laser cladding. *Acta Mater.* **57,** 5292–5302 (2009).

61. Koch, W. *et al.* Bulk Crystal Growth and Wafering for PV. in *Handbook of Photovoltaic Science and Engineering* 205–254 (John Wiley & Sons, Ltd, 2005). doi:10.1002/0470014008.ch6

62. Kutsukake, K., Usami, N., Ohno, Y., Tokumoto, Y. & Yonenaga, I. Mono-like silicon growth using functional grain boundaries to limit area of multicrystalline grains. *IEEE J. Photovoltaics* **4,** 84–87 (2014).

63. Keck, P. H., Levin, S. B., Broder, J. & Lieberman, R. Crystal Growth by the Tip Fusion Method. *Rev. Sci. Instrum.* **25,** 298–299 (1954).

64. Lemiti, M. Vapor Phase Epitaxy. in *Crystal Growth of Si for Solar Cells* (ed. Nakajima K., U. N.) 159–175 (Springer, Berlin, Heidelberg, 2009). doi:https://doi.org/10.1007/978-3-642-02044-5_10

65. Jayant Baliga, B. Silicon Liquid Phase Epitaxy. *Jounal Electrochem. Soc.* **133,** 5–14 (1986).

66. Johnson, B. C., Mccallum, J. C. & Aziz, M. J. Solid-Phase Epitaxy. in *Handbook of Crystal Growth* (ed. Kuech, T. F.) **III,** 317–363 (Elsevier B.V., 2015).

67. D. Hoonhout, C.B. Kerkdijk, F. W. S. Silicon epitaxy by pulsed laser annealing of evaporated amorphous films. *Phys. Lett.* **66A,** 145–146 (1978).

68. Ota, Y. Silicon Molecular Beam Epitaxy. *Thin Sloid Film.* **106,** 3–136 (1983).

69. Ishihara, R., Tajari Mofrad, M. R., He, M. & Beenakker, C. I. M. Pulsed-Laser-Induced Epitaxial Growth of Silicon for Three-Dimensional Integrated Circuits. in *Subsecond Annealing of Advanced Materials* (ed. Skorupa W., S. H.) 123–138 (Springer, Cham, 2014). doi:10.1007/978-3-319-03131-6

70. O.P. Pchelyakov, Lovyagin, R. N., Krivorotov, E. A., Toropov, A. I., Aleksandrov, L. N. & Stenin, S. I. Silicon Homoepitaxy with Ion Sputtering. *Phys. Status Solidi Appl. Mater. Sci.* **17,** (1973).

71. Schwebel, C. Growth of silicon homoepitaxial thin films by ultrahigh vacuum ion beam sputter deposition. *J. Vac. Sci. Technol. B Microelectron. Nanom. Struct.* **4,** 1153 (1986).

72. Orrman-Rossiter, K. G., Al-Bayati, A. H., Armour, D. G., Donnelly, S. E. & van den Berg, J. A. Ion beam deposited epitaxial thin silicon films. *Nucl. Instruments Methods Phys. Res. Sect. B Beam Interact. with Mater. Atoms* **59,** 197–202 (1991).

73. sili2 @ hyperphysics.phy-astr.gsu.edu. Available at: http://hyperphysics.phy-astr.gsu.edu/hbase/Solids/sili2.html.

74. William D. Callister, J. *Materials Science and Engineering - An Introduction*. (2003).

75. Masolin, A., Bouchard, P.-O., Martini, R. & Bernacki, M. Thermo-mechanical and fracture properties in single-crystal silicon. *J. Mater. Sci.* **48,** 979–988 (2012).

76. Wheeler, J. M. & Michler, J. Elevated temperature , nano-mechanical testing in situ in the scanning electron microscope. *Rev. Sci. Instrum.* **84,** (2013).

77. Wu, J. D., Huang, C. Y. & Liao, C. C. Fracture strength characterization and failure analysis of silicon dies. *Microelectron. Reliab.* **43,** 269–277 (2003).

78. Barredo, J., Parra, V., Guerrero, I., Fraile, A. & Hermanns, L. On the mechanical strength of monocrystalline , multicrystalline and quasi-monocrystalline silicon wafers : a four-line bending test study. 1204–1212 (2014). doi:10.1002/pip

79. Petersen, K. E. Silicon as a Mechanical Material. in *Proceedings of the IEEE* **70,** 420–457 (1982).

80. Brede, M. The brittle-to-ductile transition in silicon. *Acta Metall. Mater.* **41,** 211–228 (1993).

81. St. John, C. The brittle-to-ductile transition in pre-cleaved silicon single crystals. *Philos. Mag.* **32,** 1193–1212 (1975).

82. Samuels, J., Roberts, S. . & Hirsch, P. . The brittle-to-ductile transition in silicon. *Mater. Sci. Eng. A* **105–106,** 39–46 (1988).

83. Xin, Y.-B. & Hsia, K. J. Simulation of the Brittle-Ductile Transition Silicon Single Crystals Using Dislocation Mechanics. *Acta Mater.* **45,** 1747–1759 (1997).

84. Jaya, B. N. *et al.* Microscale Fracture Behavior of Single Crystal Silicon Beams at Elevated Temperatures. *Nano Lett.* **16,** 7597–7603 (2016).

85. Ohsaka, K., Chung, S. K., Rhim, W. K. & Holzer, J. C. Densities of Si determined by an image digitizing technique in combination with an electrostatic levitator. *Appl. Phys. Lett.* **70,** 423–425 (1997).

86. Desai, P. D. Thermodynamic Properties of Iron and Silicon. *J. Phys. Chem. Ref. Data* **15,** 967–

983 (1986).

87. Masolin, A., Bouchard, P.-O., Martini, R. & Bernacki, M. Thermo-mechanical and fracture properties in single-crystal silicon. *J. Mater. Sci.* **48,** 979–988 (2012).

88. Yamamoto, K., Abe, T. & Takasu, S. I. Thermal diffusivity of crystalline and liquid silicon and an anomaly at melting. *Jpn. J. Appl. Phys.* **30,** 2423–2426 (1991).

89. Okada, Y. & Tokumaru, Y. Precise Determination of Lattice-Parameter and Thermal-Expansion Coefficient of Silicon between 300 K and 1500 K. *J. Appl. Phys.* **56,** 314–320 (1984).

90. Sin, E. H., Ong, C. K. & Tan, H. S. Temperature Dependence of Interband Optical Absorption. *Phys. Status Solidi Appl. Mater. Sci.* **85,** 199–204 (1984).

91. Liu, J. M., Kurz, H. & Bloembergen, N. Picosecond time-resolved plasma and temperature-induced changes of reflectivity and transmission in silicon. *Appl. Phys. Lett.* **41,** (1982).

92. D. von der Linde. Ultrashort Interactions in Solids - Surface Melting. in *Topics in Applied Physics* 164–168 (1988).

93. Kuz'min, G. P. *et al.* Nanosize Silicon Powders : The Structure and Optical Properties. *Laser Phys.* **10,** 939–945 (2000).

94. Sato, T. Spectral Emissivity of Silicon. *Jpn. J. Appl. Phys.* **6,** 339–347 (1967).

95. Watanabe, H., Susa, M., Fukuyama, H. & Nagata, K. Emissivities of liquid and solid silicon at the melting point. *High Temp. - High Press.* **31,** 587–593 (1999).

96. Takasuka, E., Tokizaki, E., Terashima, K. & Kimura, S. Emissivity of liquid silicon in visible and infrared regions. *J. Appl. Phys.* **81,** 6384–6389 (1997).

97. Le Dantec, M., Abdulstaar, M., Leistner, M., Leparoux, M. & Hoffmann, P. Additive Manufacturing of Semiconductor Silicon on Silicon Using Direct Laser Melting. in *International Conference on Additive Manufacturing in Products and Applications* (ed. Mirko Meboldt, Christoph K.) (Springer International Publishing, 2017). doi:10.1007/978-3-319-66866-6_10

98. Honsberg, C. & Bowden, S. Optical Properties of Silicon.

99. ASTM B 213. Standard test methods for flow rate of metal powders using the hall flowmeter. *ASTM Int.* 49–52 (2017). doi:10.1520/B0213-17.2

100. Bergman, T. L., Lavine, A. S., Incropera, F. P. & Dewitt, D. P. Chapter 7: External Flow. in *Fundamentals of Heat and Mass Transfer - 7th Edition* (2011).

101. Zienkiewicz, O. & Taylor, R. *The Finite Element Method.* (2013).

102. Goldak, J., Bibby, M., Moore, J., House, R. & Patel, B. Computer Modeling of Heat Flow in Welds. **17,** (1986).

103. Michaleris, P. Modeling metal deposition in heat transfer analyses of additive manufacturing processes. *Finite Elem. Anal. Des.* **86,** 51–60 (2014).

104. Dassault Systèmes. Abaqus Unified FEA. (2017).

105. Parker Jr., J. H., Feldman, D. W. & Ashkin, M. Raman scattering by silicon and germanium. *Phys. Rev.* **155,** 712 (1967).

106. De Wolf, I. Relation between Raman frequency and triaxial stress in Si for surface and cross-sectional experiments in microelectronics components. *J. Appl. Phys.* **118,** (2015).

107. Wu, X., Yu, J., Ren, T. & Liu, L. Micro-Raman spectroscopy measurement of stress in silicon. *Microelectronics J.* **38,** 87–90 (2007).

108. Brede, M. The brittle-to-ductile transition in silicon. *Acta Metall. Mater.* **41,** 211–228 (1992).

109. Wang, X. *et al.* Numerical and experimental study of the thermal stress of silicon induced by a millisecond laser. *Appl. Opt.* **50,** 3725 (2011).

110. Gross, T. S., Hening, S. D. & Watt, D. W. Crack formation during laser cutting of silicon. *J. Appl. Phys.* **69,** 983–989 (1991).

111. Tanner, B. K. *et al.* The geometry of catastrophic fracture during high temperature processing of silicon. *Int. J. Fract.* **195,** 79–85 (2015).

112. Orellana, T. *et al.* How do Impurity Inclusions Influence the Mechanical Properties of Multicrystalline Silicon ? *Int. J. Metall. Mater. Eng.* **1,** 1–11 (2015).

113. Huang, X., Taishi, T., Wang, T. & Hoshikawa, K. Measurement of temperature gradient in Czochralski silicon crystal growth. *J. Cryst. Growth* **229,** 6–10 (2001).

114. Hanoka, J. I. Overview of silicon ribbon growth technology. *Sol. Energy Mater. Sol. Cells* **65,** 231–237 (2001).

115. Kutsukake, K. *et al.* Formation mechanism of twin boundaries during crystal growth of silicon. *Scr. Mater.* **65,** 556–559 (2011).

116. Voigt, A., Wolf, E. & Strunk, H. P. Grain orientation and grain boundaries in cast multicrystalline silicon. *Mater. Sci. Eng. B* **54,** 202–206 (1998).

117. Oliveira, V. A. *et al.* Formation mechanism and properties of twinned structures in (111) seeded directionally solidified solar grade silicon. *Acta Mater.* **121,** 24–36 (2016).

118. Wang, T., Zhu, Y. Y., Zhang, S. Q., Tang, H. B. & Wang, H. M. Grain morphology evolution behavior of titanium alloy components during laser melting deposition additive manufacturing. *J. Alloys Compd.* **632,** 505–513 (2015).

119. Su, H., Zhang, J., Liu, L. & Fu, H. Preparation, microstructure and dislocation of solar-grade multicrystalline silicon by directional solidification from metallurgical-grade silicon. *Trans. Nonferrous Met. Soc. China* **22,** 2548–2553 (2012).

120. Coletti, G., Macdonald, D., Yang, D. Role of impurities in Solar Silicon. in *Advanced Silicon Materials for Photovoltaic Applications* (ed. Pizzini, S.) (John Wiley & Sons, Inc., 2012).

121. Buonassisi, T. *et al.* Synchrotron-based investigations of the nature and impact of iron contamination in multicrystalline silicon solar cells. *J. Appl. Phys.* **97,** (2005).

122. Sun, S. H. *et al.* Effect of Pulling Rate on Multicrystalline Silicon Ingot during Directional Solidification. *Mater. Sci. Forum* **675–677,** 53–56 (2011).

123. Huang, F. *et al.* Electrical resistivity distribution of silicon ingot grown by cold crucible continuous melting and directional solidification. *Mater. Sci. Semicond. Process.* **23,** 14–19 (2014).

124. Fujiwara, K. *et al.* Morphological transformation of a crystal-melt interface during

unidirectional growth of silicon. *Acta Mater.* **59,** 4700–4708 (2011).

125. Fujiwara, K. *et al.* Formation mechanism of parallel twins related to Si-facetted dendrite growth. *Scr. Mater.* **57,** 81–84 (2007).

126. Pohl, J., Müller, M., Seidl, A. & Albe, K. Formation of parallel (1 1 1) twin boundaries in silicon growth from the melt explained by molecular dynamics simulations. *J. Cryst. Growth* **312,** 1411–1415 (2010).

127. Chen, J., Lu, W. & Qiao, Y. Cleavage cracking across twin boundaries in free-standing silicon thin films. *Appl. Phys. A Mater. Sci. Process.* **91,** 663–666 (2008).

128. Khairallah, S. A., Anderson, A. T., Rubenchik, A. & King, W. E. Acta Materialia Laser powder-bed fusion additive manufacturing : Physics of complex melt fl ow and formation mechanisms of pores , spatter , and denudation zones. *Acta Mater.* **108,** 36–45 (2016).

129. Jurrens, K. & Energetics Incorporated. Measurement Science Roadmap for Metal-Based Additive Manufacturing. *Addit. Manuf.* 86 (2013). doi:10.1007/s13398-014-0173-7.2

130. Ivanova, O., Williams, C. & Campbell, T. Rapid Prototyping Journal Additive manufacturing (AM) and nanotechnology: promises and challenges. *Rapid Prototyp. J. Rapid Prototyp. J. Iss Rapid Prototyp. J. Iss Rapid Prototyp. J.* **19,** 353–364 (2013).

131. Hwang, D. J. Ultrafast laser-induced crystallization of amorphous silicon films. *Opt. Eng.* **42,** 3383 (2003).

132. Kim, E. S. & Kim, K.-B. Excimer Laser Crystallization of Amorphous Silicon Film with Artificially Designed Spatial Intensity Beam Profile. *J. Electrochem. Soc.* **154,** J295 (2007).

133. Kumagai, M. *et al.* Advanced dicing technology for semiconductor wafer - Stealth Dicing. *IEEE Int. Symp. Semicond. Manuf. Conf. Proc.* **20,** 215–218 (2006).

134. Iwabuchi, Y. & Yan, J. Laser sintering of silicon powder and carbon nano fi bers for porous composite thick fi lms. **26501,** 7–9 (2015).

135. Sow, A. *et al.* Characterization of recrystallized sintered silicon substrates for photovoltaic's solar cells. *Energy Procedia* **27,** 13–20 (2012).

136. Ai, B. *et al.* Preparation and characterization of Si sheets by renewed SSP technique. *J. Cryst. Growth* **270,** 446–454 (2004).

137. Streek, A. & Exner, H. Laser micro melting. *Proc. of ICALEO* 895–900 (2014).

138. Louvis, E., Fox, P. & Sutcliffe, C. J. Journal of Materials Processing Technology Selective laser melting of aluminium components. *J. Mater. Process. Tech.* **211,** 275–284 (2011).

139. Yan, M. *et al.* Review of effect of oxygen on room temperature ductility of titanium and titanium alloys. *Powder Metall.* **57,** 251–257 (2014).

140. Doubenskaia, M., Kotoban, D. & Zhirnov, I. M echanics I ndustry Study of oxygen effect on the melting pool temperature during. **707,** 1–11 (2016).

141. Seo, K. H., Kang, B. H. & Kim, K. Y. Fast Melting and Refining of Recycled Silicon Powders from the Wafer Back Grinding Process for Solar Cell Feedstock. *Mater. Sci. Forum* **706–709,** 859–864 (2012).

142. Eyer, A., Schillinger, N., Schelb, S., Räuber, A. & Grabmaier, J. G. Silicon sheets grown from

powder layers by a zone melting process. *J. Cryst. Growth* **82,** 151–154 (1987).

143. Cramer, A. *et al.* SIKELOR - Silicon kerf loss recycling. **20,** 2156 (2015).

144. Shanks, H. R., Maycock, P. D., Sidles, P. H. & Danielson, G. C. Thermal conductivity of silicon from 300 to 1400 K. *Phys. Rev.* **130,** 1743–1748 (1963).

145. Ashby, S. P., Bian, T., Ning, H., Reece, M. J. & Chao, Y. Thermal Diffusivity of SPS Pressed Silicon Powders and the Potential for Using Bottom???Up Silicon Quantum Dots as a Starting Material. *J. Electron. Mater.* **44,** 1931–1935 (2015).

146. Jacob, G., Donmez, A., Slotwinski, J. & Moylan, S. Measurement of powder bed density in powder bed fusion additive manufacturing processes. *Meas. Sci. Technol.* **27,** 115601 (2016).

147. Fujii, H., Yamamoto, M., Hara, S. & Nogi, K. Effect of gas evolution at solid-liquid interface on contact angle between liquid Si and SiO2. *J. Mater. Sci.* **34,** 3165–3168 (1999).

148. Hass, G. Properties, oxidation, decomposition, and applications of silicon monoxide. (1950).

149. Wetzel, S., Pucci, A. & Gail, H. P. Vapor pressure and evaporation coefficient measurements at elevated temperatures with a Knudsen cell and a quartz crystal microbalance: New data for SiO. *J. Chem. Eng. Data* **57,** 1594–1601 (2012).

150. Kanai, H. *et al.* Wetting and reaction between Si droplet and SiO2 substrate. *J. Mater. Sci.* **42,** 9529–9535 (2007).

151. Yuan, Z. F., Mukai, K. & Huang, W. L. Surface Tension and Its Temperature Coefficient of Molten. 2054–2062 (2002).

152. Komarov, S. V., Kuznetsov, D. V., Levina, V. V. & Hirasawa, M. Formation of SiO and Related Si-Based Materials Through Carbothermic Reduction of Silica-Containing Slag. *Mater. Trans.* **46,** 827–834 (2005).

153. Yuan, Z., Huang, W. L. & Mukai, K. Wettability and reactivity of molten silicon with various substrates. *Appl. Phys. A Mater. Sci. Process.* **78,** 617–622 (2004).

154. Mukai, K. & Yuan, Z. Wettability of ceramics with molten silicon at temperatures ranging from 1693 to 1773 K. *Mater.Tr.JIM* **41,** 338–345 (2000).

155. Li, J. G. & Hausner, H. Wetting and adhesion in liquid silicon/ceramic systems. *Mater. Lett.* **14,** 329–332 (1992).

156. Drevet, B. & Eustathopoulos, N. Wetting of ceramics by molten silicon and silicon alloys: A review. *J. Mater. Sci.* **47,** 8247–8260 (2012).

157. Li, R., Liu, J., Shi, Y., Wang, L. & Jiang, W. Balling behavior of stainless steel and nickel powder during selective laser melting process. *Int. J. Adv. Manuf. Technol.* **59,** 1025–1035 (2012).

Marie Le Dantec

27 years old
B Swiss residence permit
Single

Contact

Oberlandstrasse 20
3700 Spiez
Switzerland

Tel. 0041 76 632 08 81
Email. Marie.ledantec9@gmail.com

PhD in Materials Science and Engineer in Micro- and Nanotechnologies

Last Position

11.2013 – 06.2018	**EMPA (Swiss Laboratories for Material Science and Engineering), Thun, Switzerland** PhD graduate student enrolled at EPFL, Lausanne, Switzerland Dept. Photonics, Thesis title: Additive Fabrication of Silicon Pillars on Monocrystalline Silicon by Direct Laser Melting

Education

2010 - 2013	**M.Sc. in Micro and Nanotechnologies for Integrated Systems – joint degree** Phelma – Grenoble INP, France Politecnico di Torino, Italy Ecole Polytechnique Fédérale de Lausanne (EPFL), Switzerland

Professional Experience and Internships

2014	**Organization of EMPA PhD Symposium** Internal EMPA conference – Responsible for Sponsors
2014-2016	**Teaching Assistant -** Chemistry of Surfaces, 2nd year Bachelor in Microtechnique, EPFL
2013	**Plus Mat AG and ZHAW, Winterthur, Switzerland** Master Thesis (6 months) – Recycling of Silicon Powder from Diamond Sawing Wastes
2012	**CNRS, Gif-sur-Yvette, France** Master 2 Internship (3 months) – Study of Formin Action on Actin Polymerization with Microfluidics Channels
2011	**RATP, Paris, France** Internship (2 months) – Maintenance of Buses and Tramways of RATP Network

Professional Skills

Materials Processing
Additive Manufacturing Techniques: Direct Energy Deposition, Selective Laser Melting
Microwave processing

Materials Characterization Techniques
UV-vis-NIR and IR Spectroscopy (especially DRIFTS, but also liquids, integrating sphere, ATR), SEM/EDX, EBSD, Raman Spectroscopy, XRD, Fluorhydric Acid (HF) handling, powder handling

Computer MS Office, Origin, Basics in Comsol Multiphysics, VHDL, C++

Publication

- **Additive Manufacturing of Semiconductor Silicon on Silicon by Direct Laser Melting**, M. Le Dantec, M. Abdulstaar, M. Leistner, M. Leparoux, P. Hoffmann, *Industrializing Additive Manufacturing - Proceedings of Additive Manufacturing in Products and Applications – AMPA 2017*, pp. 104-116

Conferences

- **Microwave Processing of Silicon Wafers and Powder: Effect of Size and Impurities**, M. Le Dantec, A. Dubach, P. Unifantowicz, S. Vaucher*,* Poster*, Crystalline Silicon for Solar Cells (CSSC-8*), Bamberg, Germany

- **Micron-sized silicon powder layers for selective laser melting,** M. Le Dantec, F. Vakili Farahani, M. Leistner, L. Güniat, P. Hoffmann, Talk, *EMRS Spring Meeting 2016*, Lille, France

- **Additive Manufacturing of Silicon using Direct Laser Melting,** M. Le Dantec, M. Abdulstaar, M. Leistner, M. Leparoux, P. Hoffmann, Talk, *Additive Manufacturing in Products and Applications – AMPA 2017, Zürich, Switzerland*

Languages

French – Mother language, English – Fluent speaking and writing, German – B2, Spanish and Italian – Basic knowledge

Personal Interests

Arts and Crafts (actively taking drawing and painting courses, clay modelling, jewelry making), Music (Classical guitar, singing), Photography (Analog, Digital), Hiking, Reading